

STUDIES OF STRONGLY-CORRELATED FERMIONS IN AN OPTICAL LATTICE

BY

WILLIAM NATHAN MORONG

DISSERTATION

Submitted in partial fulfillment of the requirements
for the degree of Doctor of Philosophy in Physics
in the Graduate College of the
University of Illinois at Urbana-Champaign, 2019

Urbana, Illinois

Doctoral Committee:

Assistant Professor Bryce Gadway, Chair
Professor Brian DeMarco, Director of Research
Professor Nadya Mason
Associate Professor Vito Scarola, Virginia Tech

Abstract

Ultracold fermionic atoms in a disordered optical lattice can realize the disordered Fermi-Hubbard model, allowing investigations of the nature of strongly-correlated fermions in a minimal setting. This thesis describes two such studies. In the first, we observe the momentum relaxation of strongly-correlated fermions in the absence of disorder. We find a violation of the weak-scattering prediction for the scaling with temperature, which is analogous to the linear-in-temperature scaling of resistivity in substances called “bad metals.” In the second, we probe a disordered and strongly-correlated system using quenches of the interaction strength that take it far from equilibrium. We find that the relaxation of double occupancies following the quenches has distinct dynamical regimes controlled by the interplay of interactions and disorder. We present a minimal picture of the relaxation process that illustrates the origin of these regimes, which are related to the Mott–metal–Anderson transitions of the ground state at half-filling.

To my teachers

Acknowledgments

The rest of this thesis, by necessity, will present my work as if it is only *my* work, when in reality nothing could be further from the truth. It is therefore my pleasure to recognize here a few of the people who helped this document see the light of day.

The most important decision a graduate student can make is in their advisor, and we seldom know as much as we should in making it. Therefore, I feel not only grateful but incredibly fortunate to have ended up with Brian, who is both a fantastic scientist and a dedicated mentor. More than anything, I'm thankful to him for putting process above results, always pushing me to think harder but also to be the best version of myself in all aspects.

I benefitted greatly from the work of those who came ahead of me on the potassium apparatus: Stan Kondov, Will McGehee, Josh Zirbel, and Wenchao Xu. Will and Wenchao in particular were both fantastic scientific role models and also directly important to much of the work presented here. A number of younger students have also contributed to the apparatus or studies, including Pei-Wen Tsai, Nathan Fredman, Lucas Slattery, Chuankun Zhang, and Wilbur Shirley. Pei-Wen and Nathan have been a pleasure to train and work with, and I'm excited to see what they do with our machine next.

I'm also grateful to our theoretical collaborators on two projects. Vito Scarola and Hoi-Yin Hui helped us analyze correlated spin-flip tunneling, described in Appendix D. Sean Muleady, Itamar Kimchi, Ana Maria Rey, and Rahul Nandkishore deepened my understanding of the doublon decay measurement described in Chapter 4 through numerical and theoretical models.

The ultracold atom community at Illinois have been the source of many fun discussions, journal club talks, and DAMOP memories. This includes the rubidium half of the DeMarco group: David Chen, Carrie Meldgin, Phil Russ, Laura Wadleigh, and Nicholas Kowalski; and Prof. Bryce Gadway and his students: Eric Meier, Alex An, Jackson Ang'ong'a, Michael Highman, Zejun Liu, Sai Paladugu, Shraddha Agrawal, and Garrett Williams.

I would like to thank Alexander Hill for helping me polish an optical fiber tip when I really needed it, as well as for being a great roommate for most of our graduate school lives.

I am indebted to our administration and staff for keeping everything running so that I could focus on the science. Betsy Greifenkamp, Cheryl Sabas, Lisa Selle, and Jerry Cook in particular were always helpful and accommodating in arranging travel, facilitating purchases, and keeping our lab running.

The Illinois physics graduate department was, to me, a model for academia: perpetually buzzing with new ideas, lively with camaraderie, and open to all. Probably no person is more responsible for this than Prof. Lance Cooper. I would also like to thank everyone who helped to organize or participate in Illinois GPS.

Finally, thanks to the people who have meant everything to me here: my wonderful friends and family, and you, Jillian.

Table of Contents

List of Tables	viii
List of Figures	ix
Chapter 1 Introduction	1
1.1 Ultracold Atomic Gases: A Great Way to Study Many-Body Physics	2
1.2 The Disordered Fermi-Hubbard Model	3
1.3 Outline of Manuscript	7
Chapter 2 The Experimental Apparatus	8
2.1 Overview: What's Not New	8
2.1.1 Evaporation Sequence	8
2.1.2 Disordered Optical Lattice: A Real-Life DFHM System	10
2.1.3 Experimental Determination of DFHM Parameters	14
2.1.4 Manipulation and Probing	16
2.1.5 Imaging	18
2.2 Feshbach Resonances	22
2.2.1 Model of a Feshbach Resonance	22
2.2.2 Feshbach Resonance in Harmonically Trapped Gas	25
2.2.3 Feshbach Resonance in a Lattice	28
2.2.4 Molecule Lifetime Limitations	30
2.3 Local Raman Setup	33
2.3.1 Introduction	33
2.3.2 Experimental Implementation	33
2.3.3 Parameters and Rabi Rate	35
2.3.4 Early Results	38
2.4 Science Cell MOT and All-Optical Evaporation	38
2.4.1 Strategies for All-Optical Evaporation	40
2.4.2 The Science Cell MOT	43
2.4.3 All-Optical Evaporation	46
2.5 Looking Forward	48
Chapter 3 Bad-Metal Relaxation Dynamics	50
3.1 Good Metals and Fermi Liquid Theory	50
3.2 Non-Fermi Liquids	52
3.2.1 Bad Metals	52
3.2.2 Strange Metals	53
3.3 Our Measurement	54
3.3.1 Experimental Procedure	54
3.3.2 Causes of Momentum Relaxation	55
3.3.3 Our Results	57
3.4 Some Theories of Bad and Strange Metals	62

3.4.1	Comparison to Numerics	62
3.4.2	Universal Planckian Scattering	65
3.4.3	Resistivity from Entropy	66
3.4.4	Others: Marginal Fermi Liquids, Unparticle Phenomenology, Hidden Fermi Liquid	68
3.4.5	Comment on the Bakr Group Result	69
3.5	Outlook	70
Chapter 4	Signatures of Mott and Anderson Transitions Far from Equilibrium	72
4.1	Introduction	73
4.2	Background: Anderson and Mott Transitions	73
4.2.1	Anderson Localization Transitions	73
4.2.2	Mott Transitions	75
4.2.3	The Anderson-Mott Crossover and Many-Body Localization	76
4.2.4	Previous Experiments with Ultracold Atoms	77
4.3	Doublon Decay	78
4.3.1	The Non-Equilibrium Frontier	78
4.3.2	Understanding Doublon Decay	79
4.4	Experimental Setup	79
4.4.1	Initial Conditions	80
4.4.2	Lattice Load	81
4.4.3	Interaction Quench and t_{hold}	81
4.4.4	Doublon Selection and Readout	82
4.5	Model and Fitting	84
4.6	τ in the Absence of Disorder	86
4.7	Regimes of τ in Disorder	87
4.8	A Simple Model (and Why it Doesn't Work)	89
4.9	Dynamical Doublon Regimes and the LDOS	90
4.10	Doublon Relaxation Phase Diagram	92
4.11	Equilibrium Doublon Population	93
4.12	Conclusion and Outlook	95
Chapter 5	Conclusion	97
5.1	A Composite Picture of the DFHM	97
5.2	The Promise of Ultracold Atoms	99
Appendix A	List of Programs Used to Control Experimental Subsystems	101
Appendix B	Code for Brillouin Zone Visualization	103
Appendix C	Reprint: Simulation of Anderson Localization in Two-Dimensional Ultra-cold Gases for Pointlike Disorder	114
Appendix D	Reprint: Correlated Spin-Flip Tunneling in a Fermi Lattice Gas	124
References	136

List of Tables

2.1	Parameters used in existing implementations of all-optical evaporation of potassium	42
4.1	Data used to create doublon relaxation phase diagram	94

List of Figures

1.1	Flow of ideas between topics within quantum many-body physics	3
1.2	Ground-state phase diagram of the DFHM.	6
2.1	Pictures of our experimental apparatus	9
2.2	A sample evaporation trajectory	10
2.3	Probability distribution of DFHM parameters in speckle disorder	14
2.4	Lattice calibration using amplitude modulation	15
2.5	Measurements of the size of our disorder beam	17
2.6	Spin transfer using the rf coil	18
2.7	Cross-talk between the rf coil and magnetic field controls.	19
2.8	Raman laser setup	19
2.9	Applications of the Raman lasers.	20
2.10	Enhanced inelastic loss near a Feshbach resonance	25
2.11	Creation of Feshbach molecules with a magnetic field ramp	26
2.12	Lifetime of Feshbach molecules	28
2.13	RF spectroscopy of Feshbach molecules	29
2.14	Energy levels of two atoms in a deep lattice site.	30
2.15	RF spectroscopy of Feshbach molecules in a lattice	31
2.16	Loss of Feshbach molecules from our dipole laser	32
2.17	Setup for local Raman transitions.	34
2.18	AC Stark shift for local Raman beams.	35
2.19	Alignment of local Raman beam	39
2.20	Layout of sciMOT optics	43
2.21	Image of the sciMOT	44
2.22	Optimized parameters for sciMOT	45
2.23	Lifetime of sciMOT	46
2.24	MOT beam profile	47
2.25	Layout of high-power dipole beam optics	48
3.1	Setup of momentum relaxation measurement	54
3.2	Sample momentum relaxation data	56
3.3	Fit values of Ω and q_0	58
3.4	Temperature dependence of τ_t	60
3.5	Resistivities determined from τ_t	63
3.6	$1/\tau_t$ compared to Planckian scaling	65
3.7	$1/\tau_t$ compared to holographic scaling	66
4.1	Experimental setup for doublon decay measurement	72
4.2	Anderson localization	74
4.3	Density of states in Anderson transition	75
4.4	Density of states in Mott transition	76
4.5	Experimental procedure	80

4.6	Details of the doublon readout procedure	83
4.7	Sample doublon and single decays	84
4.8	Loss rates	85
4.9	Doublon lifetimes without disorder	86
4.10	Dynamical regimes of doublon relaxation in a 12 E_R lattice ($U/12t = 1.8$)	88
4.11	Average of local doublon decays	89
4.12	Effect of LDOS on doublon lifetime	91
4.13	Doublon relaxation phase diagram	92
4.14	Equilibrium doublon population	95
5.1	Composite picture of the DFHM	98
B.1	Examples of BZ visualizations	113

Chapter 1

Introduction

In a way, my path to this thesis began in my second year of undergraduate studies when I read, on the suggestion of professor Xiaosheng Huang, the article *More is Different* by P. W. Anderson [1]. This article makes a powerful case that emergent phenomena, appearing only in systems of a certain scale or complexity, are just as scientifically, intellectually, and philosophically significant as the fundamental phenomena from which they are generated.

As I would soon discover, quantum many-body physics is a particularly rich field in examples of emergence. Ideas originally formulated to describe collections of quantum particles, such as the organization of these collections by their symmetries, systematic coarse-graining with a renormalization group flow, and the classification of phases and phase transitions, have burst from their original contexts to become not just techniques but more like guiding philosophies for the study of complex phenomena.

Why has quantum many-body physics specifically been so successful at generating these ideas? One reason, I think, is that the general problem is *hard*—it is about as difficult as anything can be without being actually impossible. Complete theories of some systems do exist, in a sense that is not possible in, say, a complex biological or social setting. Furthermore, the laws describing the individual units and their compositions are often very well known. As we will see, this is particularly true for the systems studied in this thesis. However, the general case is far too complex to simulate without approximations, and the appropriate emergent laws can be completely different depending on the microscopic details. As a result, there are many topics that remain shrouded in mystery and controversy. A theory of the normal state of high-temperature superconductors, to be discussed later in this thesis, is a prominent example that has challenged many deep thinkers (including Prof. Anderson himself) for a generation.

1.1 Ultracold Atomic Gases: A Great Way to Study Many-Body Physics

The subject of this thesis is the study of a dilute collection of potassium atoms, held and shaped by the force of light at the center of an ultrahigh vacuum chamber, less than a millionth of a degree above absolute zero. What makes this system, which might sound very obscure, worth studying? Any two people in this field might give two different answers to this question, but this is my thesis so here is mine. But first, here are two reasons for studying this system that, while perfectly respectable, are *not* why I do it:

Reason #1:

There is a long and storied tradition in physics of progression from examination of systems closer at hand to those in more and more extreme conditions. Some examples include the high energies probed in particle accelerators, the extreme spacetime curvature of black holes, and very rare processes such as the posited neutrinoless double beta decay. This is partly because we have gotten very good at explaining everyday phenomena and need to look farther and farther afield to find new puzzles, and partly because extreme conditions usually provide the most stringent tests of theory. Ultracold atoms, which are the coldest substances that we know of in the entire universe, represent another such frontier.

This is perfectly true, yet not primarily what interests me.

Reason #2:

Through either a remarkable accident or powerful display of the universality of physical law, certain ultracold atomic systems have behavior analogous to materials, and as a result study of them might help us design materials with desired properties. This idea is often called “quantum simulation” [2], and it traces its origins back to Richard Feynman and the birth of quantum computing [3]. What more could you want?

This is getting closer, and I will use the language of quantum simulation at times in this document, but it doesn't quite do the job for me. Here is the real answer:

Ultracold atoms represent a new, simple, and controllable many-body quantum system. In the past, studies of other such quantum many-body systems have led to new insights and general concepts that are not only useful for that particular system, but find a life far beyond it [Fig. 1.1]. Fermi liquid theory, originally formulated for superfluid Helium-3, was quickly found to be relevant to the study of metals, and now forms the foundation of our understanding of them.

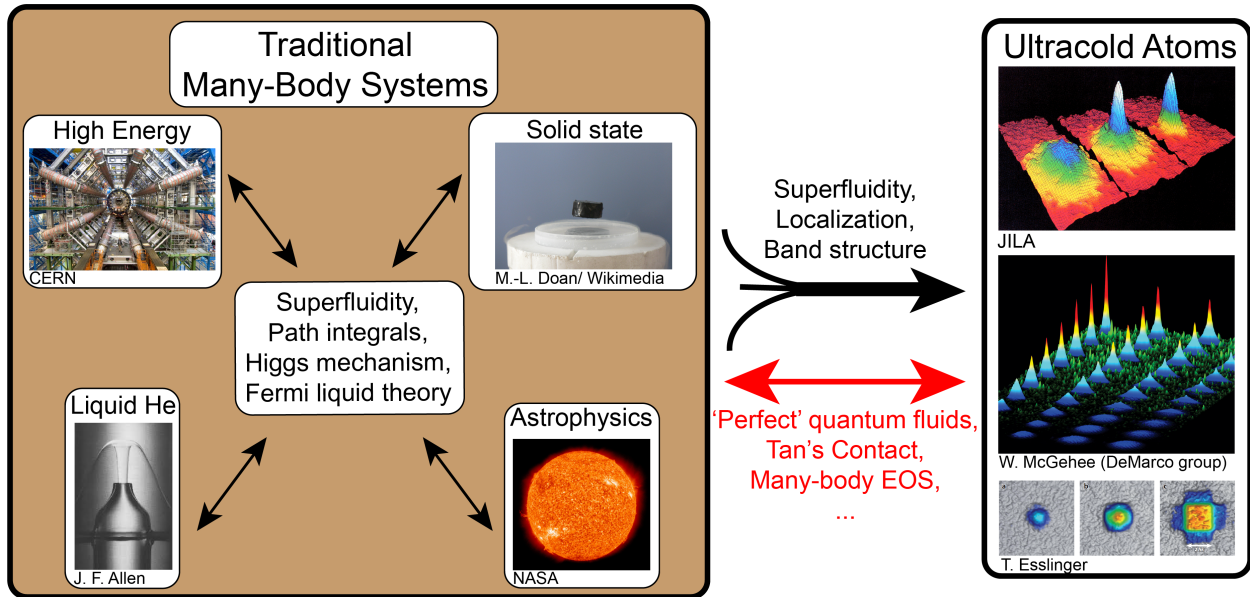


Figure 1.1: Flow of ideas between topics within quantum many-body physics. All images are copyright to their respective owners. Only a few example subfields and concepts are shown. Ultracold atoms, the newest of these subfields, have adapted many ideas from the others and are also beginning to contribute to the development of broadly applicable concepts, some of which (beyond those to be discussed in this thesis) are shown in red. However, it will take the perspective of future generations to know which of these concepts prove most important.

Similarly, the Anderson-Higgs mechanism was originally used to describe the conditions inside a superconductor, and later was realized to be a crucial part of our understanding of the vacuum of space itself. Ultracold atoms hold great potential, only beginning to be realized, to be a new model many-body system whose study shines light not only on what can be done with them, or what happens in materials, but on the organizing principles of nature itself.

1.2 The Disordered Fermi-Hubbard Model

A general recipe for an interesting quantum many-body problem is to have a system in which two or more energy scales are comparable, so that neither of the effects associated with these energies can be neglected. Many such energy scales may exist in one context or another, but three are very common:

- The average kinetic energy of particles. We will mostly consider particles with a band structure, in which case there is also a maximum kinetic energy of the bandwidth, W . For fermionic particles, the subject of this thesis, unless the system is nearly empty these energy scales will be comparable to each other, so we can consider them together.

- The characteristic energy of the interparticle interactions, U .
- The characteristic energy of random disorder in the system, Δ . This could be, for example, the standard deviation of the energy shifts from one location to another.

To these scales we can also add the thermodynamic energy scales, $k_B T$ and μ .

To study the general effects that might result when these scales are comparable, it is helpful to choose a minimal model that incorporates these effects without any complications. Specializing to fermions with two spin species $|\uparrow\rangle$ and $|\downarrow\rangle$, here is a Hamiltonian of a famous model, the *disordered Fermi-Hubbard model* (DFHM):

$$\hat{H} = \sum_{\langle i,j \rangle, \sigma} -t \left(\hat{c}_{j\sigma}^\dagger c_{i\sigma} + h.c. \right) + U \sum_i n_{i\downarrow} n_{i\uparrow} + \sum_i \epsilon_i . \quad (1.1)$$

The first term describes hopping between adjacent sites i and j , with the angled brackets $\langle i, j \rangle$ representing a sum over nearest-neighbor locations. t determines the bandwidth (for a 3D cubic lattice $W = 12t$), and therefore the typical kinetic energies as well. The second term is a contact interaction U between two particles on the same site. We will mostly consider the case in which it is positive, signifying repulsive interactions. The final term, ϵ_i , is a random disorder that varies from site to site, which might be drawn from a probability distribution characterized by some parameter Δ . Although this model neglects many effects that might occur in condensed matter systems, it is believed to capture the essential physics of strongly-correlated materials such as the cuprate high-temperature superconductors [4]. By *strongly-correlated* materials I will mean materials in which the interactions are sufficiently strong that a perturbative treatment (such as Fermi liquid theory, to be described in Chapter 3) fails.

Two limiting cases of this Hamiltonian have been extensively studied. The first is the case in which $\epsilon_i = 0$, so there is no disorder, $U, W \gg k_B T \gg t^2/U$,^a and $\mu = W/2$, which results in a half-filled band (one particle per site) as is typical for metals. Then the interesting thing to study is how the behavior changes as the ratio U/t is varied. This was the situation originally considered by Hubbard [5], and he argued (reinforced by subsequent work [6]) that there is a change—a quantum phase transition—at a critical value of U/t between conducting (or metallic) and insulating behaviors. If the model is applied to electrons, this results in a change in the electronic material from a conductor of current to an insulator, but the transition can be formulated in a more general way by the localization or delocalization of the single-particle states. For $U/t \ll 1$ the single-particle states are roughly states of definite quasimomentum that are delocalized across the system, resulting in a conductive or metallic response, while for $U/t \gg 1$ the single-particle states are

^aFor $U \gg t$ and temperatures below $\sim t^2/U$, the DFHM can have a magnetic phase transition to an antiferromagnetic phase, and may even have a superconducting phase transition away from half-filling. There are many interesting questions about this regime; unfortunately it is below the accessible temperatures for experiments described in this thesis, so I will largely ignore the possibility of magnetic ordering.

confined to specific sites, localized by the strong interactions, resulting in a state known as a Mott insulator [6, 7]. Already in this case many interesting questions arise, about problems such as the order of the phase transition and behavior of the metallic state near the transition [8].

The second limiting case is $U = 0$ and $T = 0$. In this case, the interesting competition is between the disorder scale Δ and the kinetic energy (KE). This model, too, turns out to have a localization transition, now at a critical Δ/KE . This is known as an *Anderson localization transition*, with the disordered state an *Anderson insulator* [9–13]. The localization has a very different mechanism from a Mott transition. It is the result of random wave scattering resulting in destructive interference of paths propagating outward, and as a result it can also occur in classical wave systems of sound or light [14, 15]. One interesting aspect of Anderson localization is that it is strongly dependent on the dimensionality of the system. Any disorder results in localization at all energies for $d \leq 2$, but for three and higher dimensions mobility edges that separate localized and delocalized states appear at critical kinetic energies.

For any more complicated situation than these two limits, it quickly becomes difficult to answer even the most basic questions about the possibilities of the DFHM. Calculations for half-filling ($\mu = W/2$) and variable U , Δ , and W have been performed using statistical dynamical mean field theory by the group of W. Hofstettler [16, 17] (see also Refs. [18–21]). An example of the resulting phase diagram (for speckle disorder, the case that will be most relevant to our experiments) is shown in Fig. 1.2. It consists of three regions, which are extensions of the Mott Insulator, Anderson Insulator, and metallic phases. Each of these phases is robust against small perturbations (and finite temperatures), but the interplay of the three energy scales results in interesting paths of the phase boundaries. However, while it provides a valuable guide, this phase diagram is calculated with significant uncontrolled approximations and largely untested experimentally.

This is where we come in. As I will explain, with our ultracold Fermi gas we are able to make a nearly ideal realization of the DFHM and study its properties. In this thesis I will explain how we do this, and describe two such studies in detail.

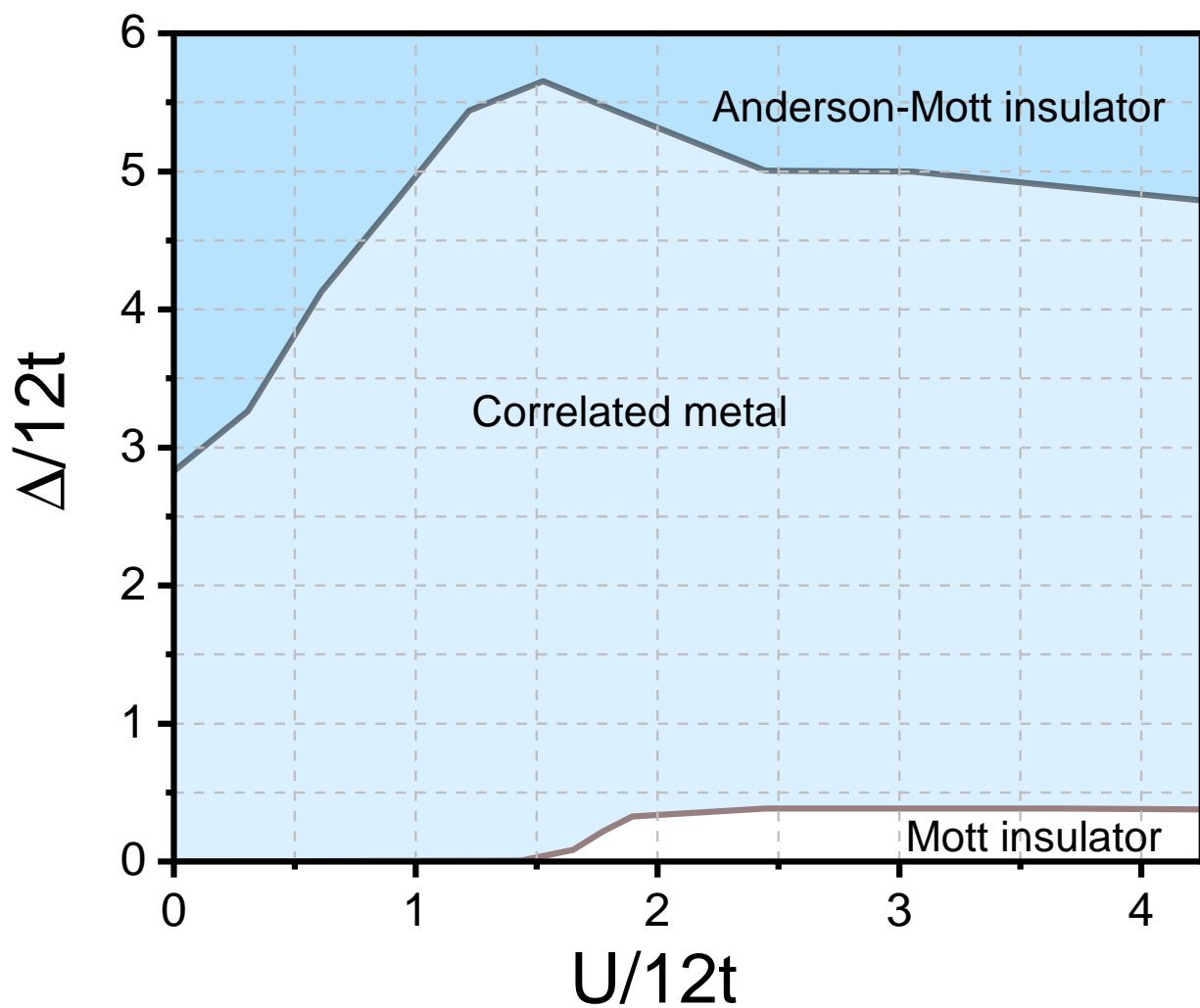


Figure 1.2: Ground-state phase diagram of the disordered Fermi-Hubbard model with speckle disorder at half-filling, as calculated by Hofstetter et al using statistical dynamical mean field theory and adapted from Ref. [17]. Energies are shown scaled by the bandwidth in 3D of $W = 12t$.

1.3 Outline of Manuscript

- **Chapter 2:** The apparatus. I explain how we realize, manipulate, and measure our disordered fermionic system, and give a small window into some of the practical challenges involved in these experiments. In addition to setting the stage for the results in Ch. 3 and 4, I describe some upgrades we are currently making to improve our capabilities going forward.
- **Chapter 3:** Bad-metal relaxation dynamics. We examine momentum relaxation dynamics properties in the correlated metal phase of the DFHM, and compare our findings to a number of theories for one of the thorniest problems in condensed matter physics.
- **Chapter 4:** Signatures of Mott and Anderson transitions far from equilibrium. We use the relaxation of a non-equilibrium density distribution to study the interplay of interactions and disorder over a wide range of parameters that correspond to all three phases in Fig. 1.2.
- **Chapter 5:** Conclusion.

The appendices include two studies that I contributed to earlier in my graduate work, as well as some information about our experimental controls and visualization code that might be useful to future students.

Chapter 2

The Experimental Apparatus

When I began to work with the potassium apparatus, it was already a complete device capable of performing interesting investigations into strongly correlated and disordered fermions in an optical lattice. Many aspects of the apparatus have barely changed since then, such as the initial trapping and cooling of atoms in a dark spot magneto-optical trap, transfer to the science cell by the cart-mounted quadrupole coils, and the way in which we generate our lattice and disorder light. Therefore, for many elements I will only provide the minimum details needed to set the stage for our experiments, and refer the reader to previous theses for more information [22–25]. I will discuss in greater depth the experimental capabilities that I helped to add: first, modifications needed to access the useful Feshbach resonance near 202 G to tune our interparticle interactions, and second, an all-optical evaporation scheme that we are implementing to improve our cooling procedure.

2.1 Overview: What’s Not New

2.1.1 Evaporation Sequence

The starting place for all of our experiments is a dilute gas of ^{40}K atoms, near or below the Fermi temperature (T_F) that signifies the onset of quantum degeneracy, held in a far off-resonant optical dipole trap. To prepare this system from a room-temperature potassium vapor takes us a little over a minute and two Nobel prize-winning experimental techniques^a.

Our source of atoms is an isotopically enriched potassium dispenser, held inside a glass chamber (our *collection cell*), which under an applied current leads to a low vapor pressure within the cell [Fig. 2.1]. Each experiment begins with atoms from this vapor being cooled, trapped, and gathered in a dark spot magneto-optical trap (MOT) [23, 24]. Once this MOT reaches its equilibrium number of atoms, it is loaded into a magnetic trap formed by quadrupole coils mounted on a translatable cart. The coils then move about

^aThat would be the 1997 prize, awarded for development of the MOT, and the 2001 prize, awarded for the magnetic trapping and cooling techniques used to achieve quantum degeneracy.

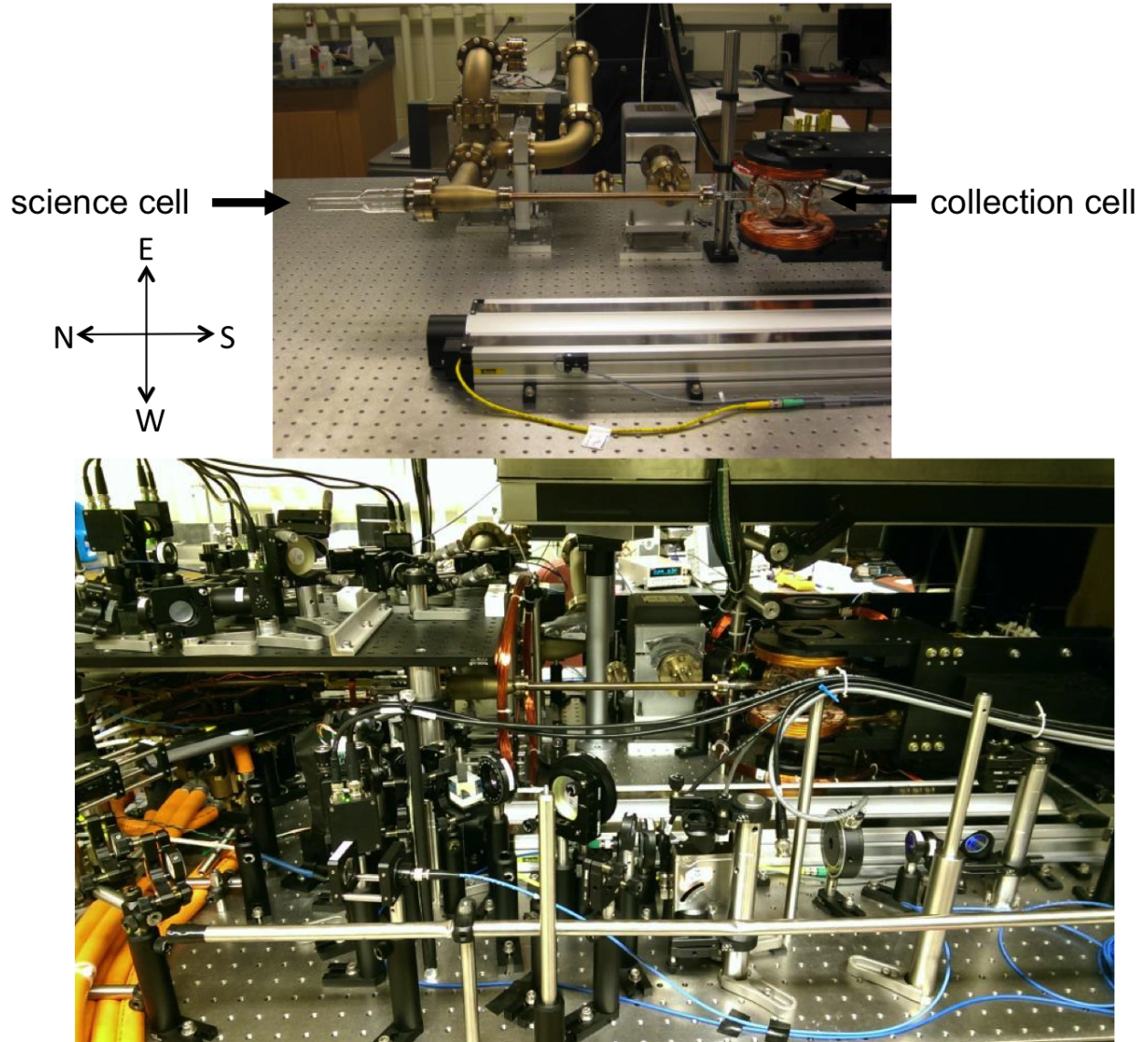


Figure 2.1: Pictures of our experimental apparatus. North is to the left. Top: Experimental apparatus circa 2009, at beginning of construction, showing exposed vacuum chamber with collection and science cells indicated. The cart-mounted quadrupole coils are also visible above and below the collection cell. Bottom, experimental apparatus at present day, in which the cells are obscured by a thicket of optical, magnetic, and rf elements.

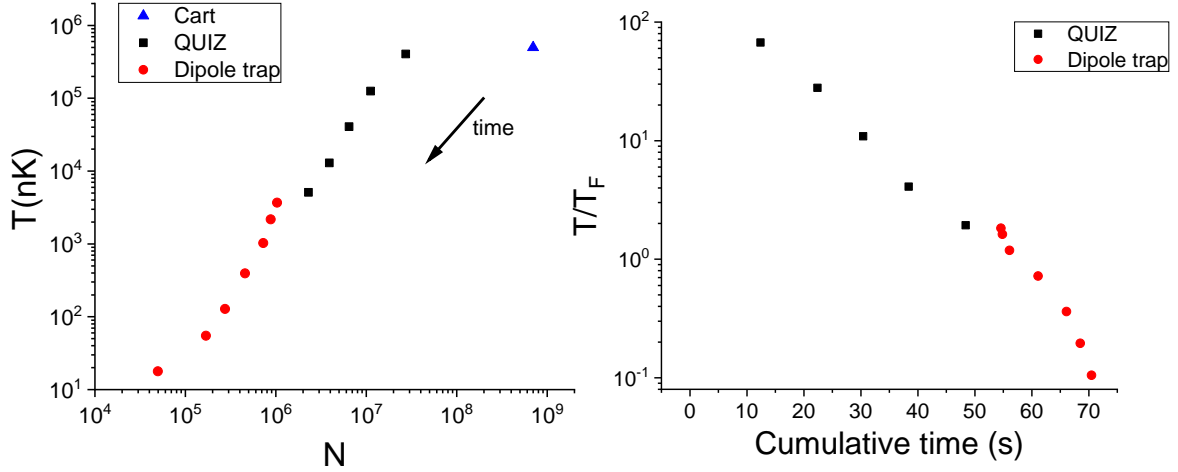


Figure 2.2: Our evaporation trajectory on an exemplary day (June 29, 2016). Left: log-log plot of the evaporation trajectory in terms of temperature drop versus number lost. The QUIZ evaporation manages moderate but consistent efficiency, while in the dipole trap evaporation stage the evaporation is initially more efficient due to the tighter confinement but gets worse as the confinement is reduced to remove atoms and as Fermi degeneracy sets in. The temperature at the end of evaporation is roughly $0.1 T_F$. Right: Semilog plot of the progression towards degeneracy as a function of elapsed time. Note the very long time that this procedure takes, compared to the ~ 10 s evaporation times routinely achieved by other groups. Most of this time is spent in the QUIZ evaporation.

one meter, bringing the atoms to a very isolated portion of the vacuum chamber (the *science cell*), in which the subsequent cooling and experimentation occurs.

There are two cooling stages in the science cell, both of which involve holding the atoms in yet another two traps [Fig. 2.2]. First, they are transferred to a modified Quadrupole-Ioffe trap, which we call a Quadrupole-Ioffe-Zirbel or QUIZ trap, in which forced radiofrequency (rf) evaporation takes place. Then, the remaining atoms are transferred to the dipole trap, in which more forced evaporation is performed by reducing the trapping potential and letting the hottest atoms escape. When we’ve cooled enough, we have exactly what we need—a quantum degenerate gas to which we can easily add additional potentials such as a lattice or disorder.

2.1.2 Disordered Optical Lattice: A Real-Life DFHM System

The Hamiltonian for atoms in the dipole trap is:

$$\begin{aligned} \hat{H}_1 = & \sum_{\sigma} \int d\vec{x} \hat{\psi}_{\sigma}^{\dagger}(\vec{x}) \left(\frac{-\hbar^2}{2m} \nabla^2 + V_0 e^{-2x^2/w_x^2 - 2y^2/w_y^2 - 2z^2/w_z^2} \right) \hat{\psi}_{\sigma}(\vec{x}) \\ & + \int d\vec{x} d\vec{x}' \hat{\psi}_{\uparrow}^{\dagger}(\vec{x}) \hat{\psi}_{\downarrow}^{\dagger}(\vec{x}') \left(\frac{4\pi\hbar^2 a}{m} \delta(\vec{x} - \vec{x}') \frac{\partial}{\partial(\vec{x} - \vec{x}')} (\vec{x} - \vec{x}') \right) \hat{\psi}_{\downarrow}(\vec{x}') \hat{\psi}_{\uparrow}(\vec{x}) . \end{aligned} \quad (2.1)$$

Here $\hat{\psi}$ is a fermionic destruction operator, σ indexes the two spin species of interest (our hyperfine ground state has ten spin states, but we typically only populate two), V_0 is the peak AC Stark shift from the crossed dipole beams, a is the scattering length, and we have assumed the Lee-Huang-Yang pseudopotential as the interatomic interaction form [26]. There is also, not shown, a bias magnetic field which creates an energy offset between the spin species. In all the work described in this thesis the offset is large enough (> 3 G) that we can neglect its effects on the dynamics and just consider each spin population as conserved in the absence of an external coupling. The Gaussian waists w_x , w_y , and w_z are determined by the dipole beam waist $w = 100 \mu\text{m}$ and the crossing geometry. Their ratio $1/w_x^2 : (1/w_y^2 = 1/w^2) : 1/w_z^2$ is measured, from measurements of oscillation frequency of the atoms following a kick, as $0.385 : 1 : 0.894$. Here I use the convention that +x is east, +y is up, and +z is south (away from the main imaging camera).

At the end of evaporation we typically have a dipole laser power of around 1 W per beam. The resulting trapping potential is determined using the peak intensity of a Gaussian beam $\mathcal{I} = 2P/\pi w^2$, with P the total power, and the AC Stark shift (including counter-rotating terms) [27]:

$$U(r, \omega) = -\frac{\pi c^2}{2} \left[\frac{\Gamma_{D2}(2 + \mathcal{P}g_F m_F)}{\omega_{D2}^3} \left(\frac{1}{\omega - \omega_{D2}} + \frac{1}{\omega + \omega_{D2}} \right) + \frac{\Gamma_{D1}(1 - \mathcal{P}g_F m_F)}{\omega_{D1}^3} \left(\frac{1}{\omega - \omega_{D1}} + \frac{1}{\omega + \omega_{D1}} \right) \right] \mathcal{I}(r). \quad (2.2)$$

Here \mathcal{P} is ± 1 for σ^\pm -polarized light and 0 for π -polarized light, \mathcal{I} is the intensity, and $\Gamma_{(D1/D2)}$ and $\omega_{(D1/D2)}$ are the linewidths and resonant frequencies of the D1 and D2 transitions. Values for these parameters are conveniently compiled in Ref. [28] and reprinted here for convenience: $\Gamma_{D1} = 2\pi \cdot 5.956$ MHz, $\Gamma_{D2} = 2\pi \cdot 6.035$ MHz, $\omega_{D1} = 2\pi \cdot 389.2862$ THz, $\omega_{D2} = 2\pi \cdot 391.0163$ THz, and $g_F = 2/9$. This leads to a potential minimum of $V_0/h = -350$ kHz, which is much larger than the thermal kinetic energy of the atoms on the order of $k_B \cdot 300$ nK $= h \cdot 6.25$ kHz.

Our optical lattice consists of three retro-reflected pairs of orthogonal beams, all at $\lambda = 782.2$ nm (with small offsets on the order of 80 MHz to wash out any interference between the different directions), and in a rotated coordinate frame relative to the trap:

$$V_L(\vec{x}') = -s \left(e^{-2x'^2/w_L^2} \cos^2 k_L x' + e^{-2y'^2/w_L^2} \cos^2 k_L y' + e^{-2z'^2/w_L^2} \cos^2 k_L z' \right), \quad (2.3)$$

where s is the lattice depth, usually specified in units of the recoil energy, $E_R = \frac{h^2}{8md^2}$, $k_L = 2\pi/\lambda$, and d the lattice spacing is $\lambda/2$. The relation between the lattice coordinates and the lab coordinates, as measured using the separation between lattice diffraction peaks as projected into the imaging plane, is:

$$\begin{bmatrix} x' \\ y' \\ z' \end{bmatrix} = \begin{bmatrix} -0.667 & 0.536 & -0.518 \\ 0 & 0.736 & 0.677 \\ 0.644 & 0.550 & -0.532 \end{bmatrix} \begin{bmatrix} x \\ y \\ z \end{bmatrix}. \quad (2.4)$$

Our lattice is generated from a Ti:sapphire laser, and using all the available power we reach a lattice depth of about $s = 30 E_R$ in all three directions, or a total depth ($= 3s$) of $h \cdot 731$ kHz. This is enough that the tunneling time between sites becomes about 40 ms, and the atoms are effectively frozen on timescales shorter than this.

We can add disorder to this by superimposing a speckle field generated by light passed through a holographic diffuser attached to a high-NA lens [23, 29]. The light for this speckle field comes from a 532 nm diode-pumped solid state laser (Coherent Verdi V18), which is also used to pump the lattice Ti:sapphire. This generates a pattern with an autocorrelation length of approximately one lattice site in the transverse directions, and about five lattice sites in the direction of propagation (along $-z$). The precise intensity distribution of the resulting field has been characterized ex-situ and is understood well [23]. The maximum AC Stark shift from this beam, at 1 W power, is estimated at $h \cdot 24.9$ kHz (see next section). The disorder beam creates the weakest potential in absolute terms of the DFHM elements, but it only needs to be comparable to the kinetic energy to see localization effects.

The total Hamiltonian for atoms in our disordered lattice is therefore:

$$\begin{aligned} \hat{H} = & \sum_{\sigma} \int d\vec{x} \hat{\psi}_{\sigma}^{\dagger}(\vec{x}) \left(\frac{-\hbar^2}{2m} \nabla^2 + V_L(\vec{x}) + V_d(\vec{x}) + V_0 e^{-2x^2/w_x^2 - 2y^2/w_y^2 - 2z^2/w_z^2} \right) \hat{\psi}_{\sigma}(\vec{x}) \\ & + \int d\vec{x} d\vec{x}' \hat{\psi}_{\uparrow}^{\dagger}(\vec{x}) \hat{\psi}_{\downarrow}^{\dagger}(\vec{x}') \left(\frac{4\pi\hbar^2 a}{m} \delta(\vec{x} - \vec{x}') \frac{\partial}{\partial(\vec{x} - \vec{x}')} (\vec{x} - \vec{x}') \right) \hat{\psi}_{\downarrow}(\vec{x}') \hat{\psi}_{\uparrow}(\vec{x}), \end{aligned} \quad (2.5)$$

where V_d is the disordered potential.

For a sufficiently deep lattice, the full Hamiltonian 2.5 can be simplified considerably in the limits of low energy and for atoms near the origin. Following Jaksch et. al in the clean case [30], and the generalization to disorder of Zhou and Ceperley [31], we construct a tight-binding representation for the ground band using a generalized Wannier basis. We also assume that the pair wavefunctions are not singular at zero separation, in which case the interaction reduces to a simple contact interaction. The resulting Hamiltonian,

$$\hat{H} = \sum_{\langle i,j \rangle, \sigma} \left(-t_{ij} \hat{c}_{j\sigma}^{\dagger} c_{i\sigma} + h.c. \right) + \sum_i U_i n_{i\downarrow} n_{i\uparrow} + \sum_{i,\sigma} \left(\frac{1}{2} m (\omega_x^2 x_i^2 + \omega_y^2 y_i^2 + \omega_z^2 z_i^2) n_{i\sigma} + \epsilon_i \right), \quad (2.6)$$

is simply the disordered Fermi-Hubbard Hamiltonian (Eq. 1.1) with a confinement term. Note that we

have added a constant energy shift relative to Eq. 2.5 to set the center of the trap at zero energy. Here \hat{c}_i is the destruction operator for a fermion in the maximally localized Wannier orbital centered on site i , $n_{i\sigma} = \hat{c}_{i\sigma}^\dagger \hat{c}_{i\sigma}$, and $\langle i, j \rangle$ represents a sum over nearest-neighbor lattice sites. The trap frequencies $\omega_{x/y/z}$ combine the anisotropic trapping from the dipole trap, the isotropic trapping from the lattice beams (coming from two beams per direction), and a second-order correction due to the Gaussian lattice beam profile [32]. The expression for ω_x is

$$\omega_x = \sqrt{\frac{4V_0}{mw_x^2} + \frac{4s}{mw_L^2} \left(2 - \sqrt{E_R/s}\right)} \quad (2.7)$$

and likewise for ω_y and ω_z (make sure to note the difference between the trapping frequencies $\omega_{x/y/z}$ and the Gaussian beam waists $w_{x/y/z}$). There is also a contribution to the overall confinement from the disorder beam, but it is smaller (no more than a 2% shift for the studies in this thesis) and usually neglected.

The Hubbard parameters t_{ij} , U_i , and ϵ_i are all disordered parameters which differ from site to site. Their precise distributions and correlations can be determined numerically [31], and are shown in Fig. 2.3. In the clean limit t and U have simple expressions in terms of the Wannier orbitals:

$$t = - \int d\vec{x} \mathcal{W}^*(\vec{x} - \vec{x}_i) \left(\frac{-\hbar^2}{2m} \nabla^2 + V_L(\vec{x}) \right) \mathcal{W}(\vec{x} - \vec{x}_{i+1}) \quad (2.8)$$

$$U = \frac{4\pi\hbar^2 a}{m} \int d\vec{x} |\mathcal{W}(\vec{x})|^4, \quad (2.9)$$

where \mathcal{W} is the Wannier orbital corresponding to \hat{c} , $\hat{c}_{i\sigma} = \int d\vec{x} \hat{\psi}_\sigma(\vec{x}) \mathcal{W}(\vec{x} - \vec{x}_i)$. Note that the formula for t is often written without the overall sign, which seems to be a widespread error. Finally, the on-site disorder ϵ_i follows a simple exponential distribution for speckle: $P(\epsilon) = \frac{1}{\Delta} e^{-\epsilon/\Delta}$, where Δ is the average potential of the disorder beam at the atoms.

Putting this all together, we have a system whose effective Hamiltonian is a minimal model for competing interactions, kinetic energy, and disorder in fermions. Furthermore, we have a great deal of control over each individual term: adjusting the lattice depth s allows us to change U and t through their dependence on the Wannier orbitals, while the disorder is directly controlled by Δ . As we will discuss shortly, we can also vary a (and thus U) through use of a Feshbach resonance. Combining these effects lets us study many regimes of behavior, which can be probed either through direct variation of the Hamiltonian parameters (such as rapid changes to perform a quench), or using other dedicated probes.

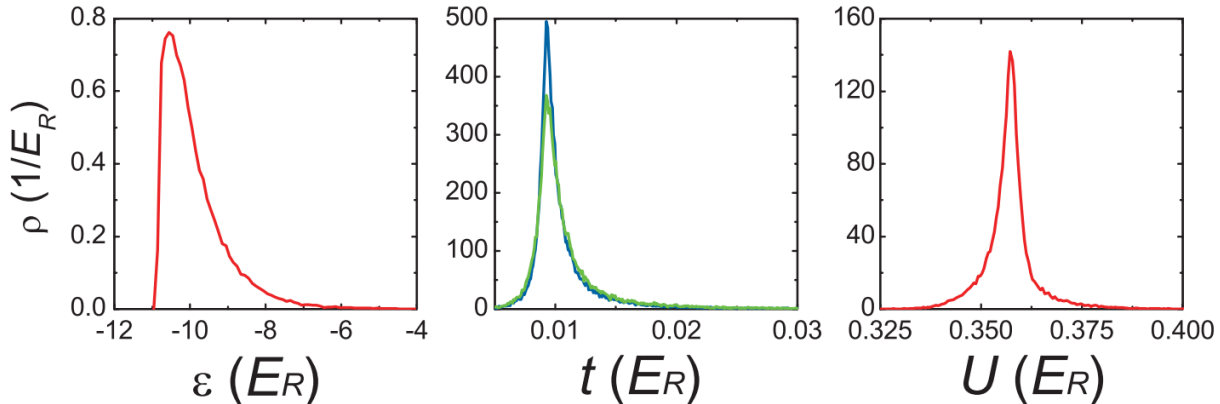


Figure 2.3: Probability distribution of DFHM parameters in speckle disorder, from Ref. [33]. The distributions shown are for $s = 14 E_R$ ($U = 0.360 E_R$, $t = 0.0095 E_R$ without disorder) and $\Delta = 1 E_R$. The curve for t shown in blue corresponds to a 60° angle between the lattice and speckle beams, while the curve in green corresponds to a 45° angle, which span the range of angles in the experimental setup. The clean value for ϵ is set at $-10.85 E_R$.

2.1.3 Experimental Determination of DFHM Parameters

To study the different regimes of this DFHM realization, it is important that we know our Hubbard parameters precisely. Fortunately, they can all be determined with straightforward independent calibrations.

Far from the Feshbach resonance, and in the absence of disorder, t and U are uniquely determined by the lattice depth s . By numerically diagonalizing the lattice potential (Eq. 2.3, usually in the $w_L \rightarrow \infty$ limit) plus kinetic energy, we can solve for the full band structure. This allows us to find t , most easily from its relation to the ground band width, and to determine the Wannier functions which along with a can be used to calculate U using Eq. 2.9. Therefore, we measure the lattice depth by mapping out the band structure, then use calculation to determine the Hubbard parameters at a given lattice depth. We map the band structure by measuring the band gap at zero quasimomentum to the second excited band, determined by driving interband transitions using lattice amplitude modulation with one lattice beam at a time [Fig. 2.4]. It is easy to get an accuracy of around 1% in the lattice depth with this technique. In practice, we also find that the long-term drift of s over a typical period of data acquisition is at the few percent level. In the measurements described in Ch. 4, this leads to a statistical uncertainty in the lattice depth of 3%, and corresponding uncertainty in t of around 4% and U of 1%.

Near the Feshbach resonance, we also must know the magnetic field accurately to determine the value of U . We calibrate the magnetic field using rf spectroscopy, as shown in Fig. 2.6. The main limit to the accuracy of this calibration is slow drifts in the environmental magnetic field, at around the 10 mG level. These lead to an additional uncertainty in U that is usually negligible unless we are within 1 G of the

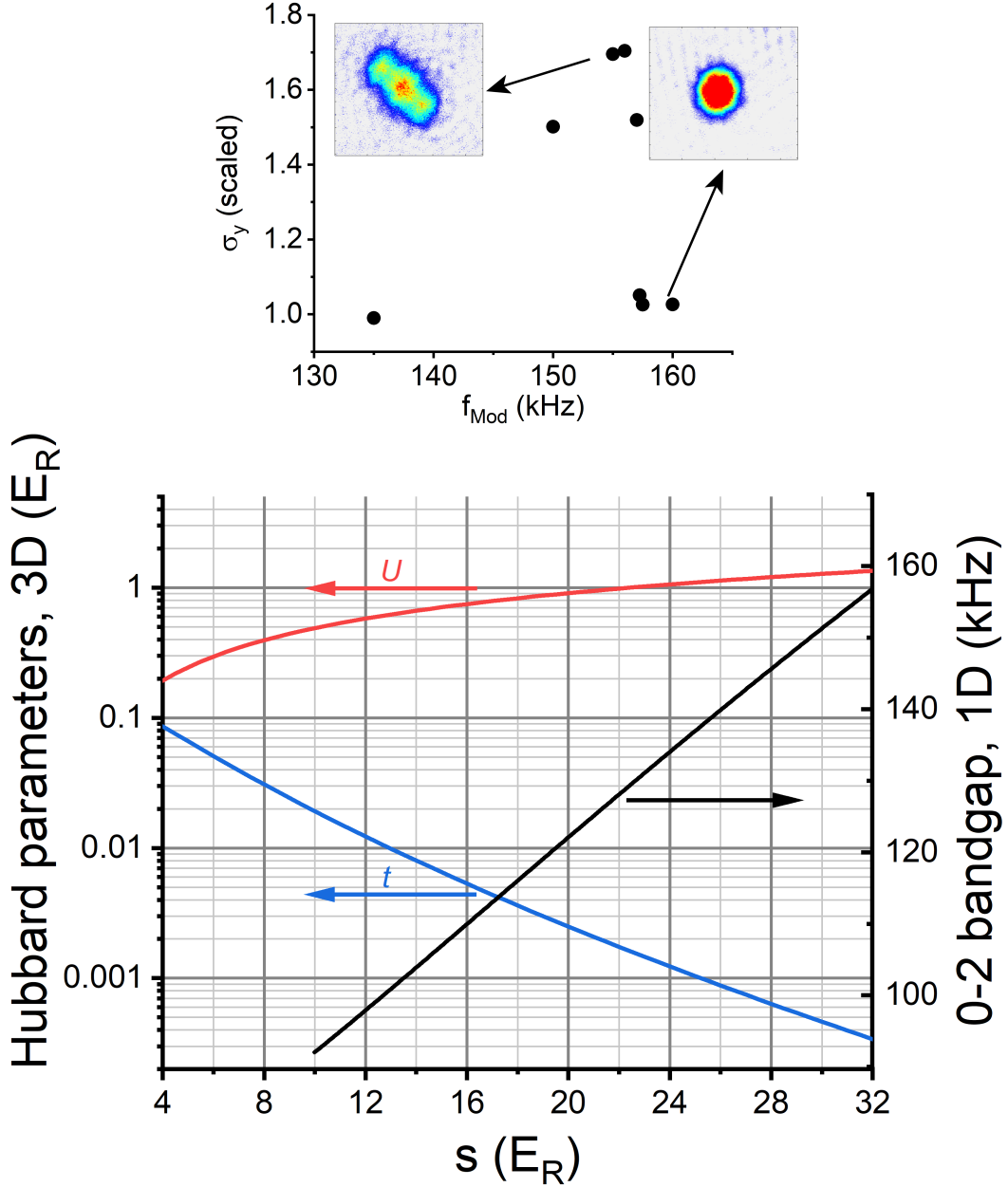


Figure 2.4: Top: Lattice calibration using amplitude modulation. Each image is the average of several experimental runs, corresponding to slightly different modulation frequencies. When a 1D lattice is applied to the gas and modulated at f_{Mod} (typically for 5% of the amplitude and 200 ms), it can resonantly drive band excitations which appear as density lobes along the modulated direction spaced by $2q_B$. These are conveniently measured by the change in the size of the gas using a Gaussian fit, with the onset of transfer at zero quasimomentum appearing as the sharp rise at the high end of the transfer feature. In this case, the onset frequency is determined as 157.25 ± 0.5 kHz, corresponding to $32.1 \pm 0.15 E_R$. This is a spin-polarized gas of approximately 200k atoms and $0.5 T_F$. Bottom: Hubbard t and U for a three-dimensional lattice, and the 0-2 band transition at zero quasimomentum for a 1D lattice, as a function of lattice depth s . Typically we will use a 1D lattice in the range of 15-35 E_R to calibrate the lattice depth, and a 3D lattice in the 4-15 E_R range in experiments. In the large- s limit, t decreases exponentially with s while U increases as $s^{0.75}$ [24].

resonance. There are also systematic contributions to our uncertainty in U from uncertainties in the known values of the scattering length a and the parameters characterizing the Feshbach resonance, but these are small—no more than 0.3% for the data presented here.

Finally, the disorder beam is difficult to calibrate absolutely because it does not cause any simple physical effect similar to a band gap. In principle it could be calibrated by measurements of localization, but the precise onset of localization in a realistic anisotropic speckle field is nontrivial both theoretically and experimentally, especially since we are not working with a BEC but a Fermi gas that always has a large number of energy states populated. We determine our speckle strength instead by measurements of the beam power and waist. We measure the beam power before the cell and assume that 8% is lost on each of the two (uncoated) surfaces of the cell. The beam waist is difficult to measure accurately, and we have seen a wide variety of incompatible results using different measurement methods [Fig. 2.5]. The measurements that we trust the most are measurements of the motion of the gas after a kick from the speckle, in which we use a two-component fit for the mobile and localized components of the atoms, and compare only the mobile atoms with a control set of atoms expanding without disorder. Following our previous publications, I take a waist value of $170 \mu\text{m}$ determined from these as the accepted value, resulting in an overall calibration of $\Delta/h = 24.9 \text{ kHz}/W_{\text{before cell}}$. Because of the disagreement between beam measurements, the systematic uncertainty of Δ is large (typically reported as 40%), and reconciliation of these measurement techniques is needed for us to report precise values. However, past agreement of our measurements with ab initio calculations [24, 34, 35] gives us some confidence that our calibration is approximately correct and that these statistical uncertainties may be on the conservative side.

2.1.4 Manipulation and Probing

We have a number of tools to manipulate our atomic system. Two of the most flexible are coils designed to drive magnetic dipole transitions between different spin states, and a pair of beams that drive two-photon Raman transitions.

Microwave and RF coils

Our microwave and rf coils are designed to work at around 1 GHz and 5-50 MHz, respectively. The first frequency corresponds to the ground state hyperfine splitting (1.2 GHz at zero magnetic field), while the second frequency corresponds to the Zeeman splitting for the two lowest spin states at fields between 17 and 200 G. Both of these coils are put to use during the course of our evaporation sequence. The microwave coil is used to remove high-energy atoms during the forced rf evaporation in the magnetic trap, while the rf coil

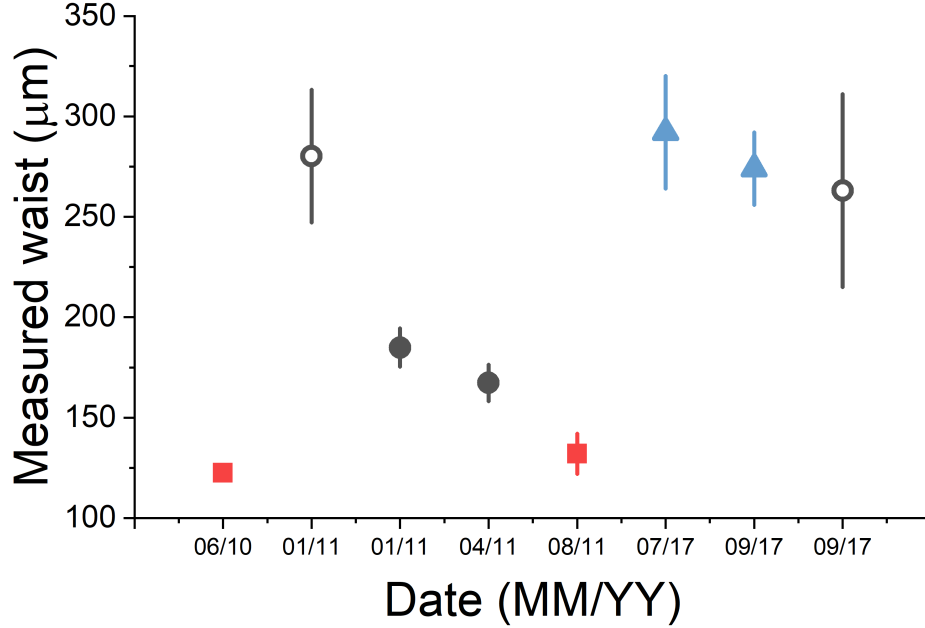


Figure 2.5: Measurements of the size of our disorder beam, which are used for calibration of Δ . The measurement techniques are: ex-situ images of the beam profile (red square), kicks of the atoms (black hollow circles), kicks of the atoms with separate analyses of the mobile and localized components (black solid circles), and fluorescence images (blue triangles).

is used to bring the spin state from $|9/2, 9/2\rangle$, the state that is primarily used for magnetic trapping and cooling, to $|9/2, -9/2\rangle$ and $|9/2, -7/2\rangle$, the states involved in the Feshbach resonance that we use. These coils are also commonly used for magnetic field calibration, as in Fig. 2.6.

While the microwave coil has been in this experiment since the inception, I helped to set up the rf coil as part of our upgrade to use the Feshbach resonance. It is a simple design that does not use any resonant impedance matching. This has the virtue of allowing the coil to work over a wide frequency range, but the downside is that the maximum achievable Rabi rate is currently only $\Omega = 2\pi \times 6$ kHz near the Feshbach resonance. Another unexpected challenge after this coil was installed was the appearance of severe cross-talk between the rf coil and the current servos used to stabilize the magnetic field. Our understanding is that some of the rf was picked up by magnetic trap coils, leaked into the servo analog electronics, and rectified, resulting in a large DC shift in the magnetic field that depended on the strength and frequency of the rf. Unfortunately, this pickup seemed to have a resonance near 50 MHz—exactly the frequency used for atoms near the Feshbach field. We had to use a number of strategies to reduce this pickup, such as shielding the magnetic trap wires and servo input and output cables with aluminum foil and metallic jackets, connecting all the sensitive electronics on a pristine ground path with low impedance, and adding choke beads to certain wires. The combined effect of all these improvements greatly reduced the crosstalk (see Fig. 2.7), but it still

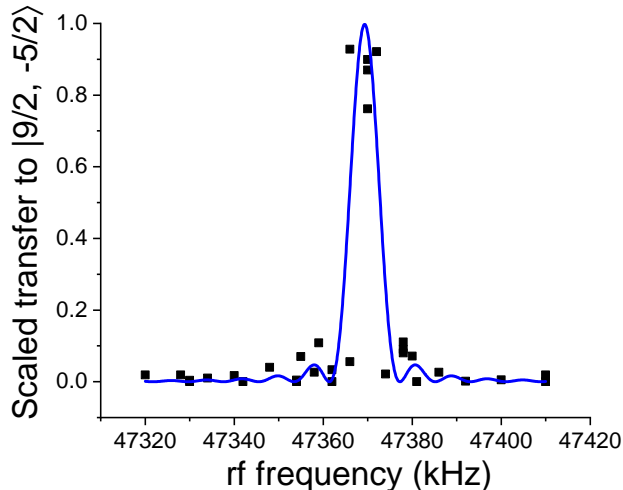


Figure 2.6: Spin transfer using the rf coil. The atoms were initialized in the $|9/2, -7/2\rangle$ state, and the y-axis shows the fraction of atoms transferred to $|9/2, -5/2\rangle$ by an approximate π -pulse. The curve is a sinc function with a width determined by the pulse time of 0.12 ms; the approximate agreement of this width with the actual transfer indicates that we are near the Fourier-limited regime. We can use measurements of this type to precisely calibrate the magnetic field; in this case it is 202.954 ± 0.002 G.

likely limits our ability to drive multiple coherent Rabi flops.

Raman Lasers

The Raman lasers are set up to give a momentum kick of about $q_B/2$ ($= \hbar k_L/2$) for atoms in our optical lattice [23] [Fig. 2.8]. These can be operated in several regimes: we can use a fast, spectrally broad pulse to make a momentum kick that is resonant for all the atoms equally, or a slow and narrow pulse that selects out a class of atoms for which the energy and momentum matching conditions are satisfied. Additionally, while we typically use these lasers for Zeeman or hyperfine-changing Raman transitions, by setting the two-beam detuning near one of these transitions, but we can also set the two-beam transition near zero and drive internal state-preserving Bragg transitions. Fig. 2.9 shows some of these possibilities, many of which we have yet to take use in experiment.

2.1.5 Imaging

At the end of each experimental run, we take an absorption image. We shine a brief pulse of resonant light through the atoms and onto a camera, and compare this to a reference pulse without atoms and a measurement of the background light. In this way we image the shadow of the atoms, quantified by the fraction of light scattered out of the resonant beam. This is conventionally measured in terms of an optical density (OD), using the relationship $e^{-OD} = (\text{atom} - \text{background})/(\text{reference} - \text{background})$. Using the

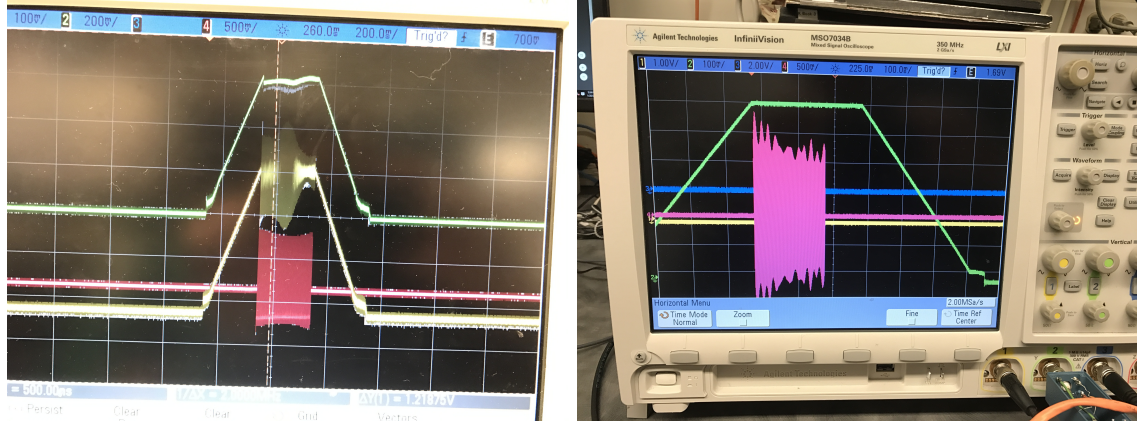


Figure 2.7: Oscilloscope traces showing cross-talk between the rf coil and magnetic field controls. Left: before shielding improvements, showing rf pulse (magenta), magnetic field control voltage (yellow), and magnetic field current witness (green). The yellow trace is 100 mV/div, the green trace is 200 mV/div, the red trace is 500 mV/div, and the horizontal axis is 200 ms/div. In the central region the magnetic field should remain steady, but it is disrupted by the rf. Right: after improvements, showing rf pulse (magenta), and magnetic field witness (green). The green trace is 100 mV/div, the red trace is 500 mV/div, and the horizontal axis is 100 ms/div. Both images show a ramp up to 200 A of the coil which is held for 300 ms.

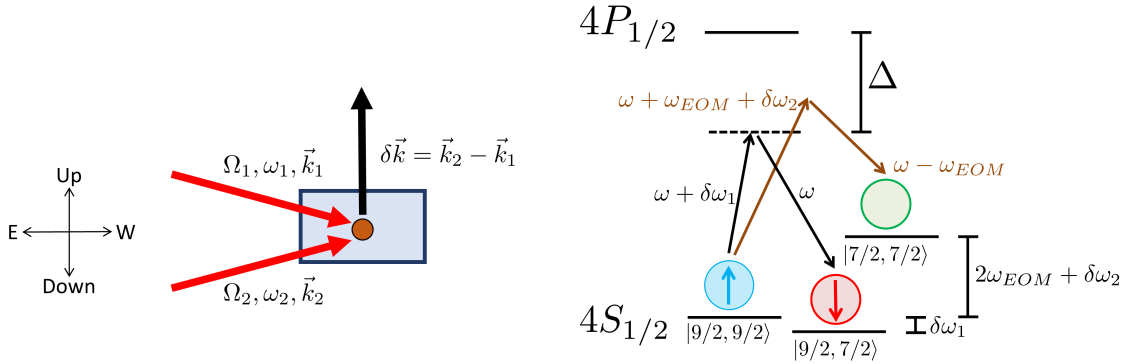


Figure 2.8: Raman laser setup. Left: Geometry of the raman lasers. The two beams have an angle of 30° , leading to a fixed momentum kick in the vertical direction, and adjustable frequencies (ω_1, ω_2) and single-beam Rabi rates (Ω_1, Ω_2). When these match the momentum and energy of an available final state, they drive a transition with a Raman Rabi rate of $\Omega_R = \Omega_1\Omega_2/2\Delta$ [36]. The final state may either be the same internal state (a Bragg transition) or a different one. Right: level diagram of internal states connected by the Raman lasers to the $|9/2, 9/2\rangle$ state. Level spacings are not to scale. The Raman lasers are individually detuned from the $D1$ transition. They may be used to drive a transition to the $|9/2, 7/2\rangle$ state by setting the frequency difference to $\delta\omega_1$ (black arrows). Alternatively, with the addition of sidebands from an electro-optic modulator, they can drive transitions to the $|7/2, 7/2\rangle$ state (brown arrows). The detunings are $\Delta = 40\text{--}80$ GHz, $\delta\omega_1 = 1$ MHz, $\omega_{EOM} = 632.2$ MHz, and $\delta\omega_2 = 13.4$ MHz.

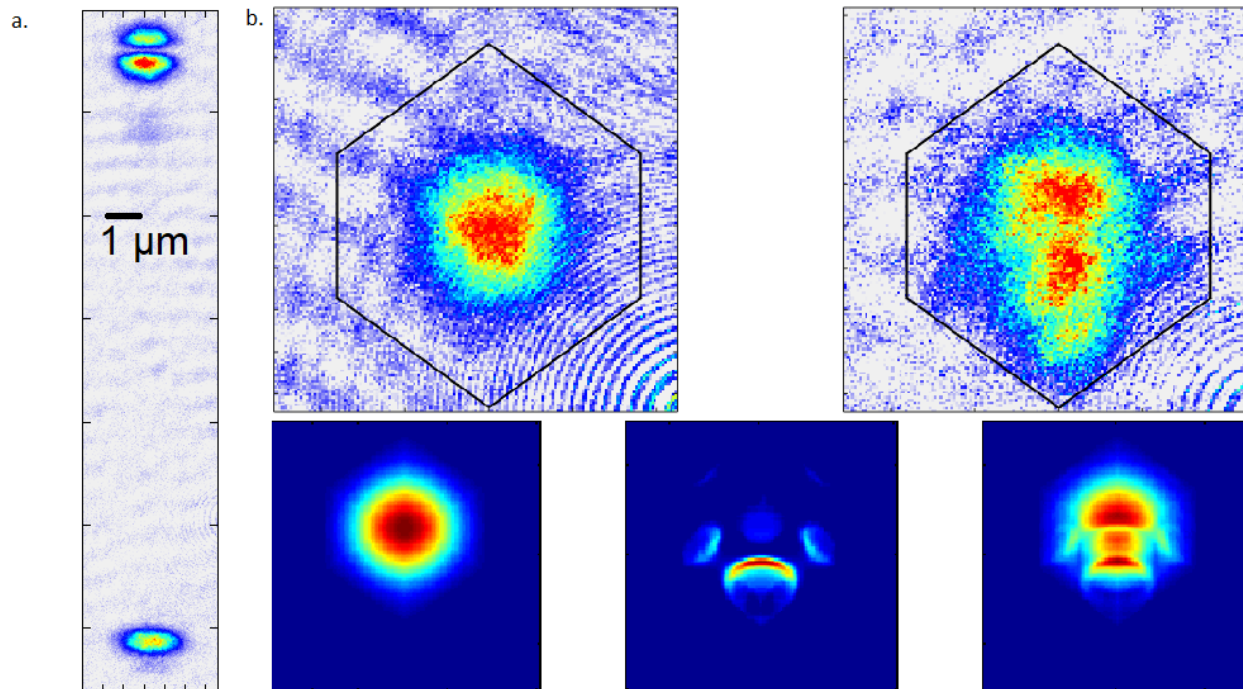


Figure 2.9: Applications of the Raman lasers. a.: A long pulse driving a hyperfine-changing Raman transition, which selects out a slice of the gas in momentum. This image is taken after a time-of-flight expansion and application of a magnetic gradient to separate spins. Atoms in the upper (divided) cloud have spin $|9/2, 9/2\rangle$ and the bottom cloud is the slice transferred to $|7/2, 7/2\rangle$. Faint traces of population in other states, such as $|9/2, 7/2\rangle$, are also visible. This data was taken in a harmonic trap, whose parabolic dispersion makes the energy and momentum matching conditions fairly simple. b.: A Bragg transition in a lattice. The top panel shows the experimentally measured cloud, after bandmapping and time-of-flight, before and after the Bragg pulse. The black hexagons show the outline of the first Brillouin Zone, which is a cube, as viewed from our imaging direction. The bottom panels show sample calculations of the absorption profile, showing the initial atoms, the atoms that are shifted by the Bragg pulse (determined by identifying the atoms for which the transition satisfies energy and momentum conservation, and shifting these atoms by the appropriate quasimomentum), and the resulting total absorption profile. The combined effects of the lattice dispersion, the possibility of the momentum kick to drive atoms across the edge of the Brillouin zone, and the angle of imaging relative to the lattice axes result in an interesting “tadpole” appearance. The code used in the calculations is reproduced in Appendix B.

resonant atom-light cross section σ_λ for a particular transition this allows us to extract the density profile integrated along the imaging beam by applying Beer’s Law: $OD = \sigma_\lambda \int n(z)dz$.

We can take images either at low field (about 3.2 G) or around 200 G, which as described in the next section is near a useful Feshbach resonance. At low field, we can send imaging light along the magnetic field axis. By adjusting a set of waveplates in the front imaging path, we can either image with σ^+ light, and use the closed cycling transition for $|9/2, 9/2\rangle$ atoms, or image with σ^- light on the corresponding transition for $|9/2, -9/2\rangle$. For these transitions, $\sigma_\lambda = 3\lambda^2/2\pi = 0.281 \mu m^2$. In either case many spin states are simultaneously near-resonant with the imaging pulse, and as the imaging pulse is long enough to absorb and emit several dozen photons the atoms are optically pumped toward the cycling transition. The result is that we can image several spin states simultaneously with nearly the same scattering rate. If desired, we can also apply a magnetic field gradient during time-of-flight expansion to spatially separate these spin components. To detect atoms in the $F = 7/2$ manifold we can follow this gradient with a pulse of repump light, the same used in the MOT, to repump these atoms into the 9/2 manifold for imaging without substantially modifying their trajectory. This is the process used to create the image shown in the first panel of Fig. 2.9.

At high fields, our imaging changes in a number of ways. First, the transitions for each spin are frequency resolved, so that we only see one spin at a time. The only closed transition we can access is for $|9/2, -9/2\rangle$, but for $|9/2, -7/2\rangle$ and $|9/2, -5/2\rangle$ the branching ratios are favorable enough that we can still perform imaging with a mild reduction in the signal to noise. Second, due to our coil geometry the field is oriented vertically, perpendicular to the imaging direction (North-South). This means that we cannot drive $\sigma^{+/-}$ transitions. Instead, we use linearly polarized light (along the East-West axis) to drive a σ transition. In practice, this means that σ_λ is reduced by one-half, to $3\lambda^2/4\pi$, which appears as a reduction in the apparent atom number [22]. Also, the changing curvature of the magnetic field along the vertical direction leads to a significant distortion of a cloud falling in time-of-flight, which limits the maximum useful expansion time to around 7 ms. This could potentially be alleviated by using another magnetic coil (the “anti-gravity” coil) to provide a gradient that balances the downward forces on the atoms, but this has not been explored extensively. The end result is that time-of-flight expansion is much less useful near the Feshbach field than at lower fields. All of these problems could be alleviated in a future redesign of the QUIC/Feshbach coils, which would ideally orient the field along the imaging direction and also circumvent current technical limitations that prevent us from quickly lowering the magnetic field during time-of-flight expansion.

2.2 Feshbach Resonances

One of the great advantages of studying many-body physics with ultracold atoms is the ability to use collision resonances to tune the interatomic interaction strength. The most common example is a *Feshbach resonance*, a scattering resonance between a weak molecular bound state and two free atoms. ^{40}K has a Feshbach resonance between the $|9/2, -9/2\rangle$ and $|9/2, -7/2\rangle$ states at 202.1 G, which was originally characterized by the Jin group and has since become a workhorse for studies of strongly-correlated Fermi gases [37]. In the course of this thesis work I helped to make upgrades to our apparatus to access this resonance, and I applied it to study the lifetime of doublons in a disordered lattice (Chapter 4). I will now summarize the theoretical and experimental background needed to apply this resonance to studies of interacting fermions.

2.2.1 Model of a Feshbach Resonance

The following simple model of a Feshbach resonance is adapted from Ref. [38]. I consider two atoms in a magnetic field, which have a continuum of scattering states and a molecular state near this continuum (possibly above or below). Why should such a situation arise? Well, for two atoms that have different spins when far separated, there can be various Van der Waals potentials due to the spin-spin coupling when they are brought together. For example, there might be one potential for a singlet coupling, and another for a triplet coupling. These potentials can have different shapes and offsets, so that a molecular bound state of one is at a comparable energy to scattering states in the other.

We can define projection operators, \hat{P} and \hat{Q} onto the scattering and molecule subspaces. As is usual for such operators, $\hat{P} + \hat{Q} = I$, the identity operator, $\hat{P}\hat{P} = \hat{P}$ and likewise for \hat{Q} , and $\hat{P}\hat{Q}\hat{O} = 0$ for any operator \hat{O} . Our goal will be to determine the effective Hamiltonian when confined only to the scattering subspace,

$$\hat{H}\hat{P}|\psi\rangle = E\hat{P}|\psi\rangle . \quad (2.10)$$

This is a sensible thing to do if we assume that the probability amplitude in the molecular state is low relative to the amplitude in the scattering states, but that it can still influence the evolution. This is the same spirit as the adiabatic elimination procedure often used to find an effective Hamiltonian of a reduced subspace, as in the two-photon Raman transition problem [36]. Whether this condition is met depends on the particular Feshbach resonance, with those in which it is (such as the resonance of interest to this thesis) termed *broad* Feshbach resonances (or *entrance-channel dominated* resonances [39]).

We will take the diagonal subspaces as:

$$\begin{aligned}\hat{P}\hat{H}\hat{P} &= E_1 + E_2 + \frac{4\pi\hbar^2}{m}a\delta(\vec{r}) , \\ \hat{Q}\hat{H}\hat{Q} &= E_n .\end{aligned}\tag{2.11}$$

Here we have $E_{1(2)}$, the energy of atom 1(2), and the molecular energy E_n . We need not assume any specific form for $\hat{P}\hat{H}\hat{Q}$ and its transpose.

We now apply these projectors to the Schrodinger equation:

$$\hat{H}|\psi\rangle = E|\psi\rangle\tag{2.12}$$

$$\hat{P}\hat{H}|\psi\rangle = E\hat{P}|\psi\rangle,$$

$$\hat{Q}\hat{H}|\psi\rangle = E\hat{Q}|\psi\rangle\tag{2.13}$$

$$\hat{P}\hat{H}(\hat{P} + \hat{Q})|\psi\rangle = E\hat{P}(\hat{P} + \hat{Q})|\psi\rangle,$$

$$\hat{Q}\hat{H}(\hat{P} + \hat{Q})|\psi\rangle = E\hat{Q}(\hat{P} + \hat{Q})|\psi\rangle\tag{2.14}$$

$$(\hat{P}\hat{H}\hat{P} + \hat{P}\hat{H}\hat{Q})|\psi\rangle = E\hat{P}|\psi\rangle,$$

$$(\hat{Q}\hat{H}\hat{P} + \hat{Q}\hat{H}\hat{Q})|\psi\rangle = E\hat{Q}|\psi\rangle .\tag{2.15}$$

We then rearrange the second expression of Eqs. 2.15: $\hat{Q}\hat{H}\hat{P}|\psi\rangle = (E - \hat{Q}\hat{H})\hat{Q}|\psi\rangle = (E - \hat{Q}\hat{H}\hat{Q})\hat{Q}|\psi\rangle$ and substitute $\hat{Q}|\psi\rangle = \hat{Q}(E - \hat{Q}\hat{H}\hat{Q})^{-1}\hat{Q}\hat{H}\hat{P}|\psi\rangle$ into the first expression for:

$$\left[\hat{P}\hat{H} + \hat{P}\hat{H}\hat{Q}(E - \hat{Q}\hat{H}\hat{Q})^{-1}\hat{Q}\hat{H} \right] \hat{P}|\psi\rangle = E\hat{P}|\psi\rangle .\tag{2.16}$$

The term in brackets in Eq. 2.16 is now our effective Hamiltonian for the scattering subspace.

We evaluate the perturbative expression for the energy of this Hamiltonian, for a scattering state with zero relative momentum $|k_1k_2\rangle = |K\rangle$:

$$E^{(1)}(K) = \langle K|\hat{P}\hat{H}\hat{P}|K\rangle + \langle K|\hat{P}\hat{H}\hat{Q}(E^{(0)} - \hat{Q}\hat{H}\hat{Q})^{-1}\hat{Q}\hat{H}\hat{P}|K\rangle .\tag{2.17}$$

We next introduce a resolution of the identity, $I = \sum_k |k\rangle\langle k| + \sum_n |n\rangle\langle n|$, use the property that $\hat{P}I =$

$\sum_k |k\rangle\langle k|$ and $\hat{Q}I = \sum_n |n\rangle\langle n|$, and apply the expressions for the diagonal elements from Eqs. 2.11:

$$E^{(1)}(K) = E_1 + E_2 + \frac{1}{V} \frac{4\pi\hbar^2}{m} a + \langle K | \hat{P} \hat{H} \hat{Q} \sum_n |n\rangle\langle n| (E^{(0)} - \hat{Q} \hat{H} \hat{Q})^{-1} \sum_n |n\rangle\langle n| \hat{Q} \hat{H} \hat{P} |K\rangle \quad (2.18)$$

$$= E_1 + E_2 + \frac{1}{V} \frac{4\pi\hbar^2}{m} a + \sum_n \frac{|\langle K | \hat{P} \hat{H} \hat{Q} |n\rangle|^2}{E_1 + E_2 + \frac{1}{V} \frac{4\pi\hbar^2}{m} a - E_n} . \quad (2.19)$$

Eq. 2.19 has the familiar form for a second-order perturbative expression. Finally, we assume that for one molecular state n' and at some magnetic field B_0 the denominator of the last term in Eq. 2.19 vanishes, and that near this divergence the contribution of the other states is much smaller. This is generically possible if the energies of the atoms and the molecule do not scale the same with magnetic field. We can expand the denominator around this critical magnetic field value:

$$(E_1 + E_2 + \frac{1}{V} \frac{4\pi\hbar^2}{m} a - E_{n'})_{B_0} \approx (B - B_0) \left(\frac{\partial E_1}{\partial B} + \frac{\partial E_2}{\partial B} - \frac{\partial E_{n'}}{\partial B} \right) \quad (2.20)$$

$$= (B - B_0) (-\mu_1 - \mu_2 + \mu_{n'}) \quad (2.21)$$

resulting in the interaction energy:

$$E_{int}^{(1)} = \frac{1}{V} \frac{4\pi\hbar^2}{m} a + \frac{|\langle K | \hat{P} \hat{H} \hat{Q} |n\rangle|^2}{(-\mu_1 - \mu_2 + \mu_{n'})(B - B_0)} , \quad (2.22)$$

which we can repackage as a new effective scattering length:

$$a(B) = a \left(1 - \frac{\Delta B}{B - B_0} \right) , \quad (2.23)$$

$$\Delta B = \frac{m}{4\pi\hbar^2 a} \frac{V |\langle K | \hat{P} \hat{H} \hat{Q} |n\rangle|^2}{-\mu_{n'} + \mu_1 + \mu_2} . \quad (2.24)$$

In this context a is called the *background scattering length*.

Eq. 2.23 is the normal functional form for a Feshbach resonance. It shows the key characteristics: by tuning the magnetic field around B_0 , one can set the scattering length between atoms to be, in principle, any value from $-\infty$ to $+\infty$. The Feshbach parameters can be determined by computation or experiment; we will use the most recent and precise measurements: $a=169.7 \pm 0.4 a_0$, $B_0=202.14 \pm 0.01$ G, and $\Delta B=6.70 \pm 0.03$ G. [40, 41].

2.2.2 Feshbach Resonance in Harmonically Trapped Gas

Once we can access a Feshbach resonance, we must make sure we understand the physics around it. Therefore, I first did a number of simple measurements that largely recreated the pioneering experiments studying this resonance from the Jin group [37]. This section serves as a quick tour of those results, which confirm our ability to tune interactions and form Feshbach molecules.

The simplest signature of a Feshbach resonance, often used to discover new ones, is enhanced loss in the vicinity of the resonance with the relevant spin mixture [Fig. 2.10]. The experiment to observe this is straightforward: prepare a mixture of $|9/2, -9/2\rangle$ and $|9/2, -7/2\rangle$ atoms away from the resonance, ramp the magnetic field close to resonance, and hold for some time (for our parameters, one second gives a large signal) before returning to the initial field for imaging. For a more precise loss measurement this procedure could be improved by preparing a spin-polarized state, then shifting to the target field and spin-mixing with an RF sequence to guarantee that losses during the ramp or association of Feshbach molecules do not affect the result. For a coarse first identification of the resonance, these steps are unnecessary.

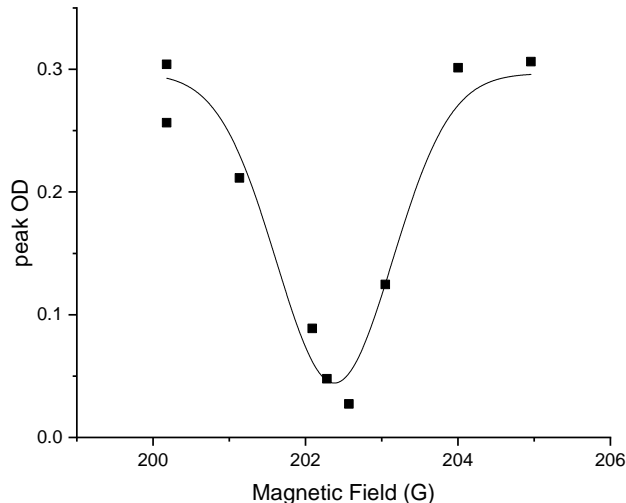


Figure 2.10: Enhanced inelastic loss near a Feshbach resonance. A mixture of atoms in spin states $|9/2, -9/2\rangle$ and $|9/2, -7/2\rangle$ is held at the indicated field for one second, which results in enhanced three-body loss near the Feshbach resonance. The line is a fit to a Gaussian. The value of the magnetic field is calibrated in separate measurements of rf transitions. The center of the feature as extracted from the fit is at 202.38 ± 0.10 G. The difference between this and the accepted value of 202.14 G may be due to changes in the calibration of our magnetic field (see also Fig. 2.11, measured around the same time), although the center of this loss feature is also expected to be slightly shifted from the resonance [42].

The next step to identifying a Feshbach resonance is to create molecules by an adiabatic ramp of the magnetic field [43]. In this measurement, we ramp the Feshbach mixture from above the resonance to some final field near the resonance, with typical ramp speeds of 1-10 G/ms. Then the trap is snapped off and the gas is allowed to freely expand. After a few ms of expansion, with the density sufficiently low that

many-body effects are negligible, we jump the field far below resonance, so that Feshbach molecules have a large binding energy that shifts them off-resonant for imaging light tuned to the single atoms, and take an image to count the single atoms remaining. The signature of this measurement [Fig. 2.11] is an apparent sharp loss of some fraction of the atoms in a narrow region around the resonance.

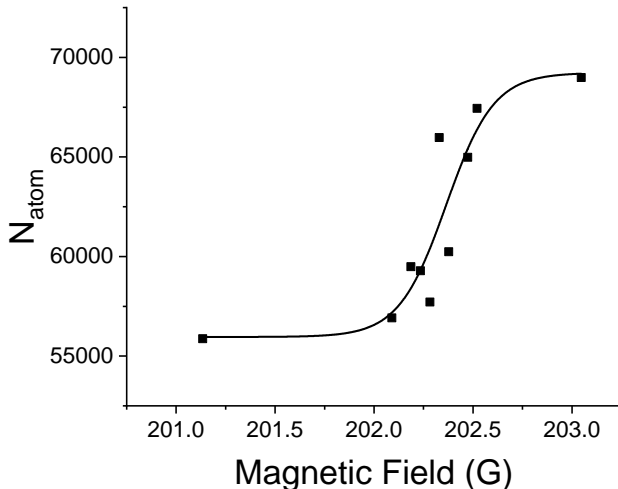


Figure 2.11: Creation of Feshbach molecules by ramping the magnetic field through the resonance. After a ramp from well above the resonance to the indicated field, the trap is snapped off for a time-of-flight expansion. During the expansion, the field is reduced to ~ 150 G for imaging, so that the molecular binding energy is comparable to the imaging linewidth and the molecules are imaged with reduced efficiency when the atoms are on-resonance. Therefore, molecular formation appears as a sharp step-function loss feature in the number of atoms. The black line is a fit to a phenomenological logistic curve. The extracted center value is 202.364 ± 0.08 G; the difference between this and the accepted value of 202.14 G may be due to changes in the calibration of our magnetic field (see also Fig. 2.10, measured around the same time).

The drop in the number of measured atoms crossing over the resonance provides an estimate of the fraction of atoms associated into molecules. Naively, because only the lowest two-body harmonic trap state is adiabatically connected to the Feshbach molecule, it might seem that for a Fermi gas only one pair of atoms should be converted into a molecule [44], however, the actual process is intrinsically many-body and requires multiple thermalizing collisions. Fortunately, the production efficiency in an adiabatic ramp can be understood as being simply related to phase space density, for either fermions or bosons [45], and therefore to T/T_F in a harmonically trapped Fermi gas. For the molecular fraction of 18% of Fig. 2.11 this would suggest a temperature of $0.8 T_F$, far above the temperature according to other methods such as fits to the momentum profile of a weakly interacting Fermi gas. As I will discuss later, we believe this is in part due to effects limiting the lifetime of molecules in our system.

To further confirm that the loss feature that we see is associated with Feshbach molecules, we study the lifetime dependence on magnetic field. Feshbach molecules have a finite lifetime, due to eventual decays into more tightly bound molecular states. However, unlike the overall atom number loss, this decay becomes

longer as one approaches the Feshbach resonance, because the wavefunction overlap between the Feshbach molecular state and lower-lying molecular states decreases [37]. In this experiment, similar to the inelastic loss study, we ramp over the Feshbach field to associate molecules, wait a variable time, and then dissociate molecules again before imaging. Close to the resonance the lifetime of molecules and atoms will be similar, but far away the timescales are well-separated and the loss we see should be dominated by the molecular lifetime [42]. Accordingly, while we see a smaller amount of fractional loss farther away from resonance, the loss occurs faster. We can compare the loss rates to previous measurements, and we find similar scaling with $a(B)$ [Fig. 2.12].

The most conclusive signature of Feshbach molecule formation is to spectroscopically resolve them. We do this by ramping a Feshbach mixture over the resonance from above, then applying an rf pulse nearly resonant with the $|9/2, -7/2\rangle \rightarrow |9/2, -5/2\rangle$ transition. This can flip the spin of either an atom that is unbound or one that is part of a Feshbach molecule, but in the latter case the rf frequency must have enough energy to break apart the molecular bond. Furthermore, there is a range of possible final states corresponding to the two atoms either being released at rest or with equal and opposite momenta, resulting in a characteristic asymmetric transfer peak [43]. When final-state effects can be neglected, and the spectral width of the rf pulse is negligible, this peak follows a simple analytical form [46]:

$$N(-5/2)(f) \sim \Theta[h(f - f_c) - E_B] \frac{\sqrt{h(f - f_c) - E_B}}{(h(f - f_c))^2}. \quad (2.25)$$

Here f is the frequency of the applied rf field, f_c is the frequency of the single-atom spin flip transition, $\Theta[x]$ is the Heaviside function, and E_b is the molecular binding energy. A measurement of molecular dissociation is shown in Fig. [2.13]. We can clearly see the asymmetric molecular dissociation peak, visible as an excess spectral weight on the positive side of the main single-atoms feature which moves away from it as the field decreases away from the resonance.

One difference between this and previous molecular dissociation measurements in similar systems [43, 46–48] is that the size of the molecular dissociation signal is quite small. This was unexpected, and made this measurement much more difficult than anticipated. The molecular conversion efficiency is predicted to be purely dependent on T/T_F [45], and at the typical values of 0.2-0.3 for this data we would expect around 70% of the atoms to be converted to molecules in an adiabatic sweep, far short of the observed signal even accounting for the finite molecular lifetime and reduced Rabi rate. We were unable to understand this until we studied Feshbach molecules in an optical lattice, which allowed us to separate out effects from our dipole laser as described below.

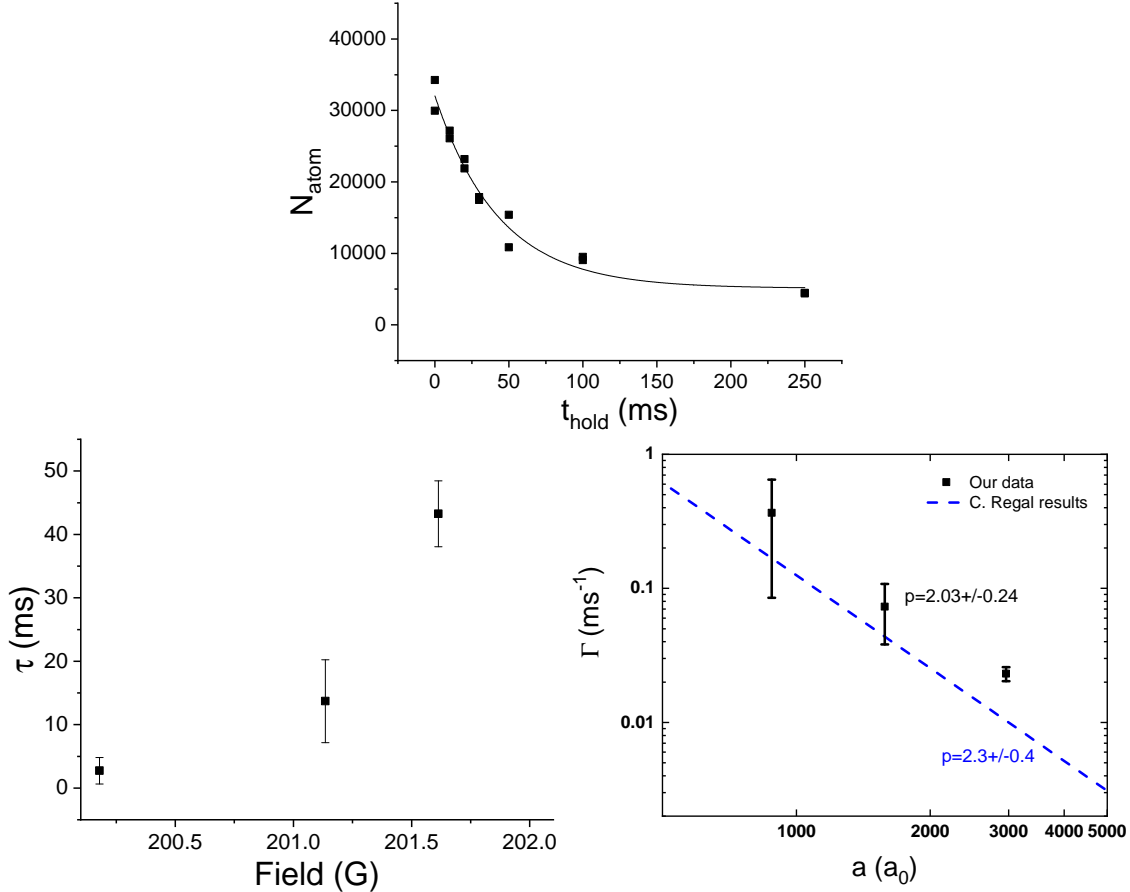


Figure 2.12: Lifetime of Feshbach molecules. Top: Population in a spin-mixed gas after ramping over the Feshbach resonance (here to 201.6 G), holding for a variable time, and then ramping back above the resonance to dissociate any remaining molecules before imaging. Points are individual data runs. Conversion of some of the atoms into unstable molecules results in a fast (typically ~ 10 s of ms) decay. Bottom left: dependence of lifetime on field value. Error bars reflect fit uncertainty. As field values approach the resonance, the molecules become increasingly weakly bound and have smaller overlap with lower-lying molecular states, resulting in a longer lifetime. This is a key signature distinguishing this loss from the inelastic loss of Fig. 2.10. Bottom right: The loss rate is conveniently plotted as a decay rate $\Gamma = 1/\tau$ versus scattering length a , with a functional form $\Gamma(B) = Ca(B)^{-p}$. Our lifetimes are found to obey similar scaling to the best fit of measurements by the Jin group [37], but with a systematic shift towards faster decay. For this plot only we have used the same calibration values for a , B_0 and ΔB as were used in Ref. [37], to facilitate comparison between these two measurements.

2.2.3 Feshbach Resonance in a Lattice

Our main application of the Feshbach resonance is to tune interactions in a 3D lattice. The presence of a lattice substantially modifies the Feshbach physics. An instructive limit is the deep lattice, in which each site can be considered as a decoupled harmonic potential with at most two atoms. The problem of two atoms in a harmonic potential with a contact interaction can be solved exactly, leading to the spectrum shown in

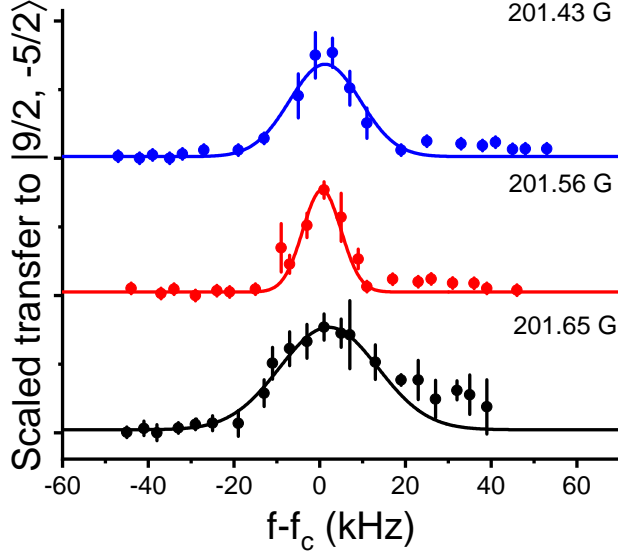


Figure 2.13: RF spectroscopy of a mixture of free atoms and molecules at varying fields. Error bars represent the standard error on the mean (s.e.m.). Lines are Gaussian fits to points below 15 kHz, to capture the main peak. The molecular signal appears as an additional asymmetric peak at positive frequencies.

Fig. 2.14 [49, 50]. The energy levels are given by an analytical formula:

$$\frac{\Gamma(-E/2\hbar\omega - 1/2)}{\sqrt{2}\Gamma(E/2\hbar\omega)} = \frac{a(B)}{a_{ho}}. \quad (2.26)$$

Here ω is the harmonic trap frequency, a_{ho} is the characteristic harmonic oscillator length $a_{ho} = \sqrt{\hbar/m\omega}$, and Γ is the Gamma function. As the magnetic field is swept up from far below the Feshbach resonance, a deeply bound state, which is the state corresponding to the Feshbach molecule in free space, moves up towards the ladder of harmonic oscillator states. The energy of this state saturates when $a(B)$ becomes comparable to a_{ho} . At the Feshbach resonance, which corresponds to $\pm\infty$ on the horizontal axis, the levels are smoothly connected and the states cross over from the left side of the plot to the right. In contrast to free particles, in this problem there is no singularity at the resonance. The finite extent of the system, characterized by a_{ho} , acts as a spatial cutoff. This limit also corresponds to a maximum repulsive Hubbard U that can be generated using the Feshbach resonance, of order the size of the band gap, although of course in this regime the single-band approximation required to realize the Hubbard model breaks down.

Fig. 2.15 shows an example of rf spectroscopy in a lattice and near the Feshbach resonance. For a spin-mixed gas, two peaks appear, corresponding to flipping a spin from $|9/2, -7/2\rangle$ to $|9/2, -5/2\rangle$ that is either in a singly-occupied site or a doubly-occupied site (doublon) with a $|9/2, -9/2\rangle$ atom. The frequency separation between the peaks is the difference of the on-site energy shift between the two spin mixtures: $\hbar\delta\omega = U_{97}(B) - U_{95}$, where U_{ij} is the interaction between atoms of $m_F = i/2, j/2$, equivalent to the binding

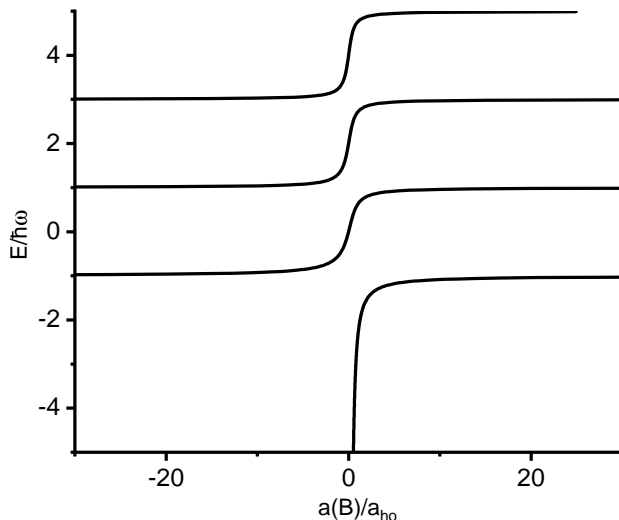


Figure 2.14: Energy levels of two atoms in a deep lattice site in three dimensions [49]. ω is the harmonic oscillator frequency for the single site, which corresponds to the bandgap in a deep lattice system, and a_{ho} is the corresponding harmonic oscillator length, $a_{ho} = \sqrt{\hbar/m\omega}$. The Feshbach resonance is at $\pm\infty$ on this plot, so a sweep over the resonance can connect the left- and right-hand sides. The lowest eigenvalue for $a(B) > 0$ corresponds to the Feshbach molecule in free space, while the rest of the states correspond to free atom pairs. In contrast to free particles, in this problem there is no singularity at the resonance. The finite extent of the system, characterized by a_{ho} , acts as a spatial cutoff.

energy when it is negative. Away from the Feshbach resonance these two spin mixtures have the same scattering length and thus the same U , so the shift seen is a direct measurement of the interaction change induced by the Feshbach resonance. This peak is absent for a spin-polarized $|9/2, -7/2\rangle$ initial state, which is a nice demonstration of Fermi statistics. Comparing the measured binding energies to the two-site model, we see that they are in good agreement for lattice depths greater than $10 E_R$ [Fig. 2.15, right]. The ability to selectively address only atoms in singly or doubly occupied sites with an rf pulse will be crucial for the study described in Chapter 4, which is concerned with doublon dynamics in a disordered lattice. It also allows us to directly observe the doublon lifetime, and in doing so helped to resolve a key question about our system.

2.2.4 Molecule Lifetime Limitations

After observing persistently shorter molecule lifetimes and smaller molecule fractions, we asked whether some mechanism was causing enhanced loss of molecules in our system. In general, molecules have loss channels not available to weakly-interacting atoms, which can be driven by external forces. For example, the JILA KRb experiment found that enhanced loss of their heteronuclear Feshbach molecules was caused by the presence of light from their broadband 1075 nm optical dipole laser, which was attributed to driven bound-bound transitions [51]. We became concerned that our broadband 1064 nm laser might be causing

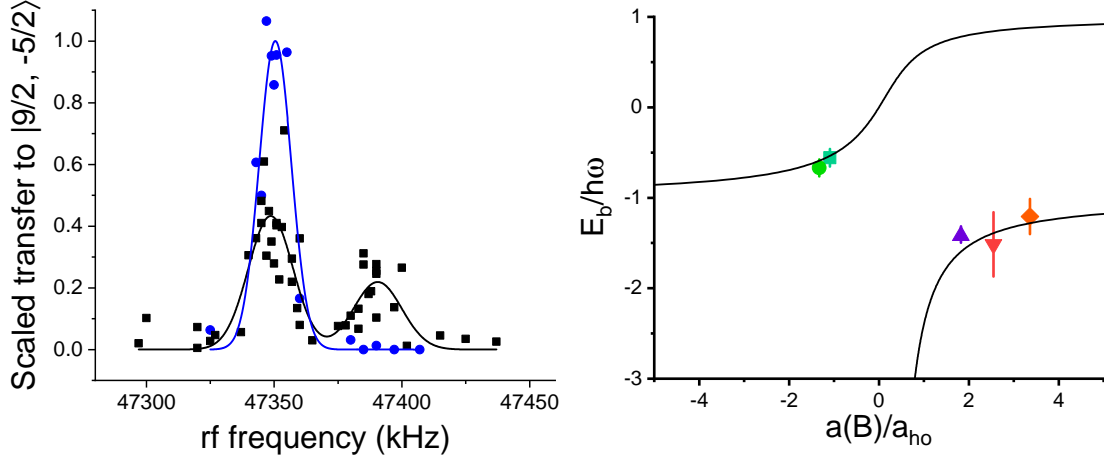


Figure 2.15: RF spectroscopy of Feshbach molecules in a lattice. Left: atoms transferred from $|9/2, -7/2\rangle$ to $|9/2, -5/2\rangle$ by a short rf sweep for an initial state that is an even mixture of $|9/2, -9/2\rangle$ and $|9/2, -7/2\rangle$ (black squares) or that is polarized $|9/2, -7/2\rangle$ (blue circles). Points are individual data runs. When the two spins experiencing the Feshbach resonance are present, a sidelobe appears due to the large on-site interaction shift. Since we are transferring atoms to a spin state with a higher energy, the higher resonant frequency of the side peak corresponds to a lower energy of the initial state, resulting from attractive interactions. Fits are to a sum of Gaussian peaks. These data are taken at fields higher than the Feshbach resonance ($B=203.25$ G), so the doublon states are adiabatically connected to free particles with an attractive interaction in the absence of a lattice. Similar spectroscopy can be performed below the Feshbach resonance, in which the attractive doublon are adiabatically connected to free Feshbach molecules (see. Fig. 4.6). Right: Comparison of measured binding energy with theoretical calculation for isolated sites [50]. Points are at a lattice depth of $10 E_R$ (violet up triangle), $18 E_R$ (turquoise square), $20 E_R$ (green circle, corresponding to the data at left), $25 E_R$ (orange diamond), and $30 E_R$ (red down triangle). Error bars reflect fit uncertainty.

similar processes, and decided to test this by varying its power. By trapping atoms in a strong lattice, which is sufficiently confining on its own, we were able to vary the dipole power without significantly changing the environment of the atoms. Our sequence was as follows: we loaded a relatively shallow $10 E_R$ lattice above the Feshbach resonance, so that the attractive interactions would result in an appreciable fraction of doublons. Then we ramped into a deep lattice of $25 E_R$, which effectively decouples the individual sites and freezes the density distribution. At this point the dipole force has little effect on the atoms, so we ramp the dipole power to some variable power between zero and 2.7 W per beam, ramp across the Feshbach resonance to associate molecules, then after a variable wait time apply an rf pulse resonant with the doublon peak and read out the transferred atoms to infer the number of molecules. The results of this measurement are shown in Fig. 2.16. The solid points show that increasing dipole power causes a rapid decreasing molecule lifetime. For the hollow points, we instead turn on the dipole beam 30 ms into the hold time, and see an abrupt drop in the molecule number immediately following. Thus, we conclude that our dipole laser is driving Feshbach molecule loss.

The reduced molecule lifetime from the dipole beam is a significant constraint on our capabilities, es-

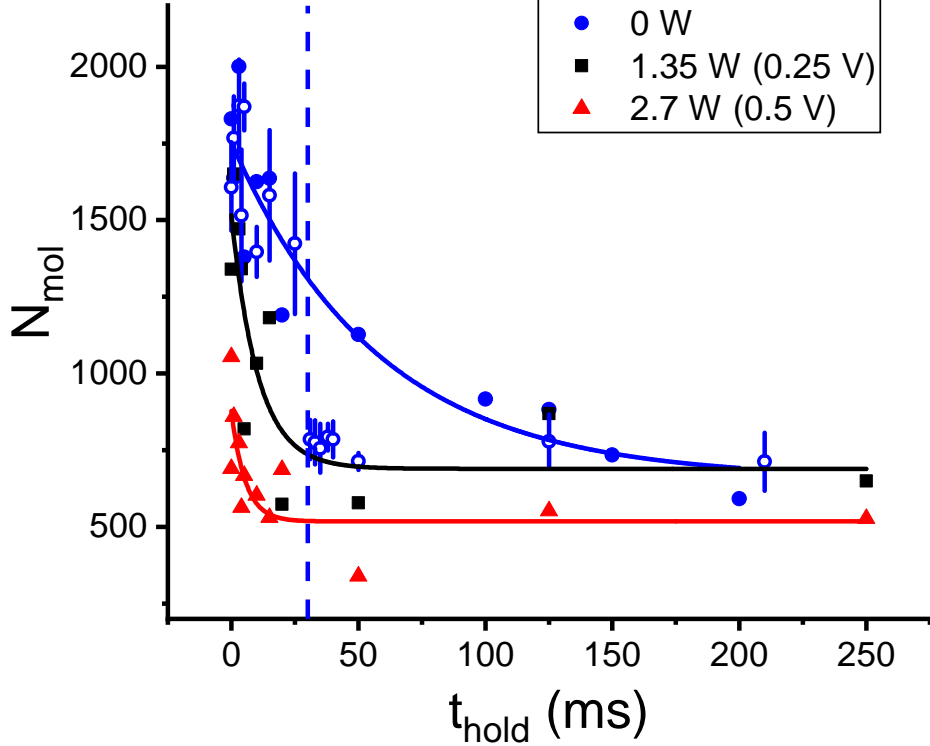


Figure 2.16: Loss of Feshbach molecules from our dipole laser. For the solid points, the dipole laser was ramped to the indicated power per beam (or servo voltage) with the atoms in a deep $25 E_R$ lattice. Then Feshbach molecules were created by an adiabatic magnetic field ramp, and after t_{hold} the molecule number was read out using rf spectroscopy and spin-selective imaging. Solid lines are fits to an exponential decay. The time constant steadily decreases with increasing dipole power. The initial measured molecule number also decreases, suggesting that the decay is really beginning before the hold, during the ramp across the Feshbach resonance. The hollow points correspond to a sequence in which the dipole beam was initially off, but was turned on to 2.7 W at the time marked by the dashed line, which results in an initial longer lifetime that abruptly decreases. The solid points are single experimental runs, while the hollow points show the mean and s.e.m. of 4 runs.

pecially if we want to investigate BEC-BCS crossover physics with and without a lattice. We currently circumvent this problem by studying doublon dynamics farther away from the Feshbach resonance, and by turning off the dipole beam when we want to ramp over the resonance to measure doublon number. Looking ahead, one of our upgrades in progress is installation of a single-frequency dipole laser that should remove this effect. In the final two sections of this chapter I will describe two more upgrades in progress: one that will enhance our science capabilities by allowing us to perform locally resolved probes of the atoms, and one that will modernize our evaporation sequence and make data taking faster and more efficient.

2.3 Local Raman Setup

2.3.1 Introduction

Historically, the most common measurements of ultracold gases have been those which involve a period of free expansion, effectively mapping the momentum distribution before expansion to the imaged density distribution. This has two primary advantages. First, it greatly reduces the density of the gas, which is helpful in an absorption image since imaging a very dense and opaque gas with this technique tends to lead to a signal dominated by systematic errors such as any residual changes in background light. Second, many interesting properties of a quantum degenerate gas are often best revealed by the momentum distribution. This includes the sharp momentum peak that was the crucial signature of the creation of a BEC [52], and band populations in a lattice which may be mapped to the momentum distribution with the bandmapping technique [53, 54].

However, in systems with strong correlations, disorder, or both, the physics is often highly local and real-space measurements become valuable. Similarly, any transport process that involves diffusion, or localization, both of which are at the heart of extremely interesting questions about the DFHM, is most naturally studied without a period of free expansion. Quantum gas microscope apparatuses, which typically image single atoms *in situ*, have begun to explore real-space correlations and diffusive transport in strongly-correlated fermions [55–59], but they are typically limited to low dimensionalities and small system sizes, making the classification and delineation of disordered phases challenging.

In this section I will describe a modification to our apparatus to directly measure diffusion, relaxation, and transport processes in real space. We achieve this by combining a tightly focused beam that can drive spatially selective co-propagating Raman transitions with the high imaging resolution needed to study the subsequent dynamics. I will focus on the goals and design considerations, and then describe progress towards implementation.

2.3.2 Experimental Implementation

Although our system is in some ways like a solid material, the differences in length scales open up new possibilities. Unlike a solid, ultracold atoms have a lattice spacing comparable to the imaging resolution, and our atoms are sufficiently dilute that we image the entire bulk of the cloud. As a result, it is natural to consider the possibility of probing transport and correlations on the smallest characteristic length scales of the system, as opposed to only macroscopic response functions. This would allow for very direct measurement and characterization of fundamental transport properties, such as diffusive relaxation of spin and density

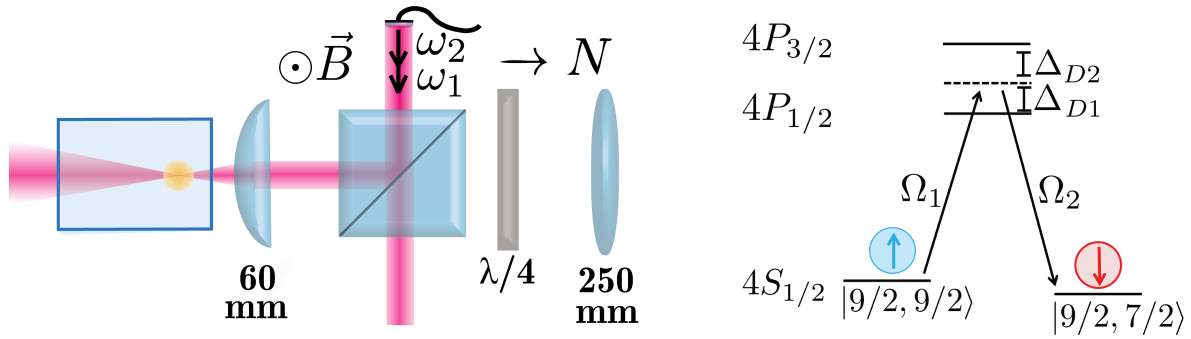


Figure 2.17: Setup for local Raman transitions. Left: Our main imaging pathway (from above). The imaging beam (not pictured) travels from left to right, and is collected by the high-NA 60 mm lens. The proposed local Raman probes with frequencies ω_1 and ω_2 co-propagate, and both are coupled in on a non-polarizing beamsplitter. Right: level diagram for the Raman transition. The single-photon detunings Δ_{D1} and Δ_{D2} are 0.6 and -1.1 THz, respectively, while the Raman detuning is near the Zeeman splitting of 1-50 MHz. N indicates North.

gradients and momentum relaxation rates.

We propose a straightforward modification to our apparatus that will allow us to perform this type of experiment. We will couple two additional co-propagating Raman beams into our system with a very tight focus, centered on the gas with a beam waist much smaller than its spatial extent [Fig. 2.17]. These beams will have two possible roles. They may be used to change between internal atomic states in a spatially selective manner, allowing us to create, e.g., a minority spin component that we can observe diffuse through the majority gas using spin-resolved imaging. Because the beams are co-propagating, the Raman transition would not impart any momentum to the atoms, and in effect would only act to “tag” a spatially-localized subensemble with the internal spin degree of freedom. With a slightly different configuration, one of these beams may also be used to create a localized force on the atoms, which we can use to study relaxation of density perturbations.

To generate a tightly focused beam without losing any optical access, we send this Raman beam backwards through our high-NA primary imaging lens (GPX 30-60, NA=0.23). This drives transitions within a narrow, roughly elliptical region of the intersection of the Raman beam and atomic density profile, which in the front imaging plane appears as an initial spot of minority spins that diffuses into the surrounding majority component.

We will also increase the magnification of our system to resolve the in-situ dynamics. We currently image at $3.1 \mu\text{m}$ per CCD pixel, but for these measurements it will be advantageous to increase this to the optics-limited $1.7 \mu\text{m}/\text{pix}$. This can be done most simply by exchanging the 250 mm imaging lens (see Fig. 2.17) for a 400 mm lens and moving the camera appropriately. Or, we may break the magnification into two

stages instead, which has the advantage of allowing us to easily switch back to lower-magnification imaging. Given the typical $20 \mu\text{m}$ diameter of the gas, this means we will observe the spin-flipped atoms diffusing from a single pixel in about 12 pixels in each direction.

2.3.3 Parameters and Rabi Rate

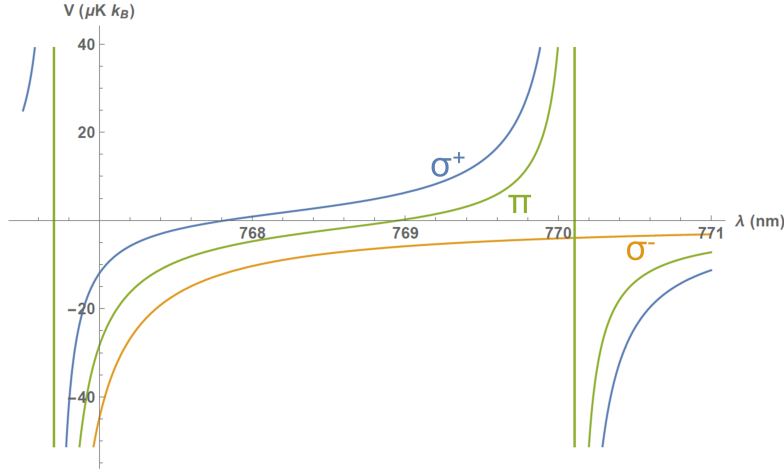


Figure 2.18: AC Stark shifts V for $|9/2, 9/2\rangle$ atoms and σ^+ , σ^- , and π -polarized light (blue, orange, and green), for a Gaussian beam with waist $1.7 \mu\text{m}$ and power $10 \mu\text{W}$. The D1 transition occurs at roughly 770.1 nm , and D2 at 766.7 nm , while between them there is a point at which σ^+ and σ^- have equal shifts.

The parameters of the local Raman beam are optimized to efficiently drive a spin-flip transition without producing any other effects on the atoms, so that effects of excitations of different types can be cleanly separated. Because of this, it is important that the beams not impart any momentum on the atoms. By using co-propagating Raman beams, we are guaranteed that the momentum transfer from the Raman process itself will vanish, so the only remaining effect to consider is the AC Stark force on the atoms from the beam. We can accomplish this by clever choices of polarization and wavelength. The AC Stark shift (Eq. 2.2), in the rotating-wave approximation and neglecting the small difference between the D1 and D2 linewidth, is

$$U(\vec{r}, \omega) = -\frac{\pi c^2 \Gamma}{2} \left[\frac{2 + \mathcal{P} g_F m_F}{\omega_{D2}^3 (\omega - \omega_{D2})} + \frac{1 - \mathcal{P} g_F m_F}{\omega_{D1}^3 (\omega - \omega_{D1})} \right] \mathcal{I}(\vec{r}). \quad (2.27)$$

It is evident that for $\mathcal{P} = 0$, or an equal sum of $\mathcal{P} = \pm 1$ polarizations, this potential will vanish at $\omega = (\omega_{D2}^4 + 2\omega_{D1}^4)/(\omega_{D2}^3 + 2\omega_{D1}^3)$, which corresponds to about 769 nm [Fig. 2.18]. Therefore, we will operate our Raman lasers at this wavelength and with an even balance of σ and π polarizations. In the case where the magnetic field is vertical (satisfied for our apparatus near the Feshbach resonance at 202 G), this condition

corresponds to a linear polarization that is at 45 degrees relative to horizontal.

Given this wavelength choice, we must show that the Rabi rate can be made reasonably fast, ideally faster than the atomic dynamics in a lattice of order 1 ms, without challenging power requirements. For a general laser field $\vec{E}(\vec{x}, t)$, with frequencies near ω , and taking the dipole approximation, the Raman Rabi rate is

$$\Omega = \sum_i \langle 1 | -e\vec{E} \cdot \vec{r} | i \rangle \langle i | -e\vec{E} \cdot \vec{r} | 2 \rangle \frac{2}{\hbar^2(\omega - \omega_i)}, \quad (2.28)$$

where ω_i is the detuning between states 1 and 2 and the intermediate state i . We assume that the difference between these is negligible; in our case $\delta\omega_i/\omega_i \approx (40 \text{ MHz})/(390 \text{ THz}) \approx 10^{-7}$. We will consider all intermediate states in the $P_{1/2}$ and $P_{3/2}$ manifolds.

The amplitude-modulated electric field is taken to be:

$$\vec{E}(\vec{x}, t) = E(x, t)\hat{e} = (A \cos \omega_M t + A_0) \cos(\vec{k} \cdot \vec{x} - \omega_L t) \left(\sqrt{\frac{2}{3}}\hat{y} + \frac{1}{\sqrt{3}}\hat{z} \right) \quad (2.29)$$

Here A and ω_M are the amplitude and frequency of the amplitude modulation and ω_L is the carrier frequency.

We will re-write this in a more revealing form using the product-to-sum rule:

$$\vec{E} \left(\sqrt{\frac{2}{3}}\hat{y} + \frac{1}{\sqrt{3}}\hat{z} \right) \left(A_0 \cos(\vec{k} \cdot \vec{x} - \omega_L t) + \frac{1}{2}A \cos(\vec{k} \cdot \vec{x} - \omega_L t - \omega_M t) + \frac{1}{2}A \cos(\vec{k} \cdot \vec{x} - \omega_L t + \omega_M t) \right) \quad (2.30)$$

The electric field has three components separated by ω_M , which have the possibility to drive transitions if this is near an atomic transition. Specifically, we will consider the case in which $2\omega_M \approx \omega_{12}$, in which the transition is driven between the two sidebands at $\pm\omega_M$. However, it must still be demonstrated that the transition rate does not vanish due to some subtle selection rule. For example, for a purely phase-modulated electric field of the form $A_0 \cos(\vec{k} \cdot \vec{x} - \omega_L t + \phi_M \cos(\omega_M t))$, it may superficially appear that similar frequency components exist that could drive transitions, but in fact they do not [60].

The main task is to evaluate the matrix elements $\langle 1 | \hat{e} \cdot \vec{r} | i \rangle \langle i | \hat{e} \cdot \vec{r} | 2 \rangle$. In our real atom, $|1\rangle$ is $|\frac{9}{2}, \frac{9}{2}\rangle$, $|2\rangle$ is $|\frac{9}{2}, \frac{7}{2}\rangle$, and $|i\rangle$ is really 54 intermediate states in the $P_{3/2}$ and $P_{1/2}$ manifolds, although fortunately due to selection rules only a handful of these states will lead to nonzero matrix elements for both initial states.

We write $\hat{e} \cdot \vec{r}$ in the appropriate spherical tensor basis (using the convention of Ref. [61]):

$$\hat{\epsilon} \cdot \hat{r} = \epsilon_x x + \epsilon_y y + \epsilon_z z \quad (2.31)$$

$$= -\epsilon_+ r_- - \epsilon_- r_+ + \epsilon_z z, \quad (2.32)$$

$$\epsilon_+ = -\frac{1}{\sqrt{2}}(\epsilon_x + i\epsilon_y), \quad (2.33)$$

$$\epsilon_- = \frac{1}{\sqrt{2}}(\epsilon_x - i\epsilon_y) \quad (2.34)$$

$$= \frac{1}{\sqrt{3}}(r_- - r_+) + \frac{1}{\sqrt{3}}z \quad (2.35)$$

The first component can drive $\Delta m = \pm 1$ transitions, while the second component is limited to $\Delta m = 0$. Now we're ready to evaluate the matrix elements for either the D1 or D2 transition:

$$\sum_i \langle 1 | \hat{\epsilon} \cdot \vec{r} | i \rangle \langle i | \hat{\epsilon} \cdot \vec{r} | 2 \rangle \quad (2.36)$$

$$= \sum_F \sum_{m_F} \langle \frac{9}{2}, \frac{9}{2} | \hat{\epsilon} \cdot \vec{r} | P_j, F, m_F \rangle \langle P_j, F, m_F | \hat{\epsilon} \cdot \vec{r} | \frac{9}{2}, \frac{7}{2} \rangle \quad (2.37)$$

$$= \sum_F \langle \frac{9}{2}, \frac{9}{2} | \epsilon_z z | P_j, F, \frac{9}{2} \rangle \langle P_j, F, \frac{9}{2} | (-\epsilon_- r_+) | \frac{9}{2}, \frac{7}{2} \rangle + \langle \frac{9}{2}, \frac{9}{2} | (-\epsilon_- r_+) | P_j, F, \frac{7}{2} \rangle \langle P_j, F, \frac{7}{2} | \epsilon_z z | \frac{9}{2}, \frac{7}{2} \rangle \quad (2.38)$$

$$= -\epsilon_- \epsilon_z \sum_F \langle \frac{9}{2}, \frac{9}{2} | z | P_j, F, \frac{9}{2} \rangle \langle P_j, F, \frac{9}{2} | r_+ | \frac{9}{2}, \frac{7}{2} \rangle + \langle \frac{9}{2}, \frac{9}{2} | r_+ | P_j, F, \frac{7}{2} \rangle \langle P_j, F, \frac{7}{2} | z | \frac{9}{2}, \frac{7}{2} \rangle \quad (2.39)$$

$$= -\frac{1}{3} \sum_F \langle \frac{9}{2}, \frac{9}{2} | z | P_j, F, \frac{9}{2} \rangle \langle P_j, F, \frac{9}{2} | r_+ | \frac{9}{2}, \frac{7}{2} \rangle + \langle \frac{9}{2}, \frac{9}{2} | r_+ | P_j, F, \frac{7}{2} \rangle \langle P_j, F, \frac{7}{2} | z | \frac{9}{2}, \frac{7}{2} \rangle \quad (2.40)$$

With the last expression we have two simple combinations of standard dipole integrals (which have the same value) that we can easily calculate using following the prescription laid out, for example, by Steck [62]. This makes the full result for the Rabi rate take the following form, given in experimentally relevant quantities:

$$-\frac{1}{3} \frac{2P_A}{\pi w^2} \frac{1}{2\epsilon_0 c} \left[\frac{2}{\hbar^2(\omega - \omega_{D2})} \sum_F \langle \frac{9}{2}, \frac{9}{2} | z | P_{3/2}, F, \frac{9}{2} \rangle \langle P_{3/2}, F, \frac{9}{2} | r_+ | \frac{9}{2}, \frac{7}{2} \rangle + \langle \frac{9}{2}, \frac{9}{2} | r_+ | P_{3/2}, F, \frac{7}{2} \rangle \langle P_{3/2}, F, \frac{7}{2} | z | \frac{9}{2}, \frac{7}{2} \rangle + \frac{2}{\hbar^2(\omega - \omega_{D1})} \sum_F \langle \frac{9}{2}, \frac{9}{2} | z | P_{1/2}, F, \frac{9}{2} \rangle \langle P_{1/2}, F, \frac{9}{2} | r_+ | \frac{9}{2}, \frac{7}{2} \rangle + \langle \frac{9}{2}, \frac{9}{2} | r_+ | P_{1/2}, F, \frac{7}{2} \rangle \langle P_{1/2}, F, \frac{7}{2} | z | \frac{9}{2}, \frac{7}{2} \rangle \right]. \quad (2.41)$$

Here we have P_A as the sideband beam power, $P_A = |A|^2 \epsilon_0 c$, and w the Gaussian beam waist. The result

for the full Rabi rate, given a power P_A in μW and waist size w in μm , is

$$\Omega = 2.8 \cdot 10^5 \frac{P_A}{w^2} \text{Hz} . \quad (2.42)$$

For a $1.7 \mu\text{m}$ and $10 \mu\text{W}$, this results in a π -time of about $3.2 \mu\text{s}$.

This looks good, but in practice there is another constraint on the power to consider: we will be able to tune to the desired wavelength approximately but not exactly. How precise must we be? The maximum force imparted by a Gaussian beam with center AC Stark shift U_0 is $4U_0e^{-2}/w$. Meanwhile, the peak AC Stark shift at a deviation $\delta\omega$ away from the ideal frequency ω is:

$$U_0 = \frac{-\pi c^2 \Gamma}{2} \frac{2P}{\pi w^2} \frac{2\omega_{D1}^3 + \omega_{D2}^3}{\omega_{D1}^3 \omega_{D2}^3 (\omega - \omega_{D2})(\omega - \omega_{D1})} \delta\omega . \quad (2.43)$$

For, again, $w = 1.7 \mu\text{m}$ and power $P = 10 \mu\text{W}$, this all works out to be 3.6 GHz detuning (in linear frequency) for each mg of force, meaning that we would want to stay within a few hundred MHz of the ideal frequency. This is well within the capabilities of a passively stable ECDL, although we may need to regularly tweak the frequency to compensate for slow drifts.

2.3.4 Early Results

As of summer 2019, this upgrade is in progress. We have added the optics needed to couple a beam backward through the imaging lens, and using light from a lattice beam we have aligned this to the atoms, effectively demonstrating the ability to apply a localized force [Fig. 2.19]. We are now implementing the Raman light needed to drive local spin flips, along with an increase in our imaging magnification needed to take full advantage of this capability.

2.4 Science Cell MOT and All-Optical Evaporation

An undesirable aspect of our experimental apparatus is the very long time it takes to prepare a quantum degenerate sample for study. As seen in Fig. 2.2, our evaporation takes about 70 seconds, in addition to a MOT filling time of about 20 seconds. Informal surveys suggest that this is well outside the norm; in fact I am not sure if I have ever met anyone working on a modern ultracold atom experiment of this type who claimed to have a slower experimental cycle.

A few of the contributing factors to this slowness are:

- Our MOT loading is slow in part because we use a dark spot MOT, which gives an increase in number

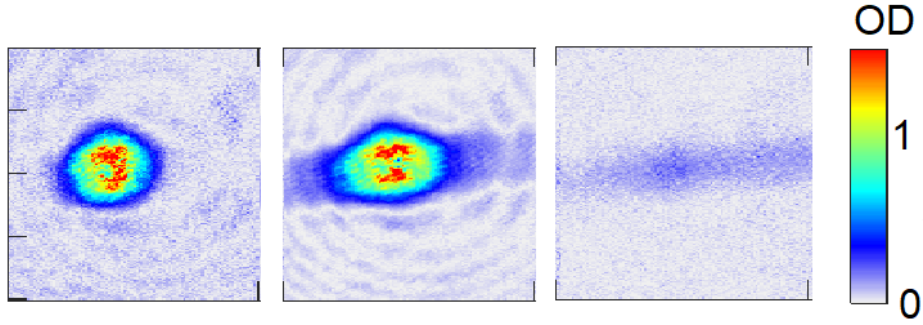


Figure 2.19: Alignment of local Raman beam pathway, using the AC Stark shift from detuned light (coupling from one of the lattice beams). All images are averages of at least ten shots. Left: atoms in the harmonic trap, viewed from the side imaging pathway. Center: addition of the tightly-focused beam with blue detuning ($\lambda = 753$ nm, $P = 100$ mW). Atoms are forced out of the trap center and into the wings of the crossed dipole trap. Right: addition of the tightly-focused beam with red detuning ($\lambda = 800$ nm, $P = 250$ mW), and 5 ms after snapping off the main optical trap.

and density at the expense of a slower capture rate [24, 63]. This is particularly helpful for potassium, which in the absence of a dark spot suffers from substantial inelastic collisions stemming from the small excited state fine structure splitting, which ends up enhancing loss and reducing the peak MOT density.

- We transport our MOT atoms quite far before evaporation, down the ~ 1 m transfer tube connecting our collection and science chambers. This large separation and narrow transfer tube provides a large differential pressure, giving our science cell a slow vacuum-limited lifetime of around ten minutes [24]. But, this good vacuum comes at the cost of more heating during loading and transport, resulting in a relatively hot and dilute initial gas.
- Our QUIC coils are only weakly confining along the N/S direction, with a trap frequency of only about 40 Hz, an order of magnitude lower than the other two directions [23]. This also leads to a low initial density for forced rf evaporation, resulting in initial evaporation stages that must be very slow due to the low collision rate. This is partly a legacy of the history of this experiment, which was originally designed to evaporate in a quadrupole field and had the QUIC coils added when this was found to be ineffective [24].
- Finally, near the end of evaporation, after the onset of quantum degeneracy, the evaporation efficiency of fermions becomes increasingly low, as a Fermi surface forms and the phase space for rethermalizing collisions steadily vanishes.

We can imaging trying to mitigate each of these problems in various ways:

- To speed up the MOT loading somewhat, we can optimize a MOT loading sequence that quickly captures atoms in a bright MOT before switching to the dark MOT.
- To remove the heating caused by transfer, we can recapture into a MOT in the science cell before further evaporation.
- To avoid the problems with the QUIC coils, we can switch to an all-optical evaporation scheme in which we load directly into a high power optical trap.
- We can use our Feshbach resonance to increase the collision rate near the end of evaporation.

We have implemented or are working on all of these changes, but the switch to all-optical evaporation, starting from a science cell MOT, involves both the greatest effort and greatest potential reward. In the following section, I will describe the plan and progress of this upgrade.

2.4.1 Strategies for All-Optical Evaporation

All-optical evaporation, in which atoms from a MOT or optical molasses are loaded directly into a far-detuned optical trap for evaporative cooling, is an increasingly popular choice for new experiments. Here I briefly summarize a few such setups that have been successfully used by other groups, focusing on the cases of ^{40}K and ^{39}K most relevant to us.

A summary of these can be found in Table 2.1. Generally speaking, in the existing potassium experiments either D1 or D2 grey molasses are used to cool the atoms and increase phase space density after the MOT. Furthermore, a dipole beam is used that is optimized for capture, with a trap depth several times larger than the temperature of the atoms and a shallow crossing to maximize trap volume.

Comparing these parameters to those of our experiment immediately after transport to the science cell, as shown in column DeMarco(1), it is clear that we are starting in an unfavorable regime for loading an optical dipole trap. In contrast to these experiments, we start with a temperature above the Doppler temperature for potassium, $T_D = 144 \mu\text{K}$, and a correspondingly lower density. In addition, our dipole trap is designed to have comparable trap frequencies in each direction, helpful for studying 3D lattice physics but not for a large loading volume. Experimentally, we find that the number of atoms loaded directly into the optical trap under these conditions is too small to detect.

In contrast, the column DeMarco(2) shows expected and measured parameters after recapturing into a MOT in the science cell, following by loading into a large-volume and high-power dipole trap. Recapturing into a MOT provides a substantial cooling and increase in density, and a high-power dipole beam allows us

to reach the regime in which the dipole depth is much larger than the temperature of the atoms, common to all successful loading schemes.

Unlike the other potassium apparatuses here, we have chosen not to implement sub-Doppler cooling initially. This choice was made in part to avoid extra complexity, and in part because, as detailed below, we are using an unconventional MOT geometry in which the effectiveness of sub-Doppler cooling is less well-established. However, this would be a natural extension for the future if we find that the loading efficiency is not sufficient, or want to boost it even higher so that we can tolerate a shorter MOT loading period and speed up the cycle time even further. In the absence of sub-Doppler cooling, it is useful to compare our plans to parameters used for ^6Li , which has no such mechanism available. Therefore, we also show for comparison the loading parameters used by the Bakr group. Loading an optical dipole trap from a MOT is a complex dynamical process [70], making it difficult to predict exactly how many atoms we should expect to capture with these parameters, but these upgrades will put us within reach of other successful designs in terms of the important figures of merit: initial density, trap volume, and ratio of atom temperature to trap depth.

Group	Kuhr ([64])	Grimm ([65])	Bourdel ([66])	Marcassa ([67])	Bakr ([68])	DeMarco(1)	DeMarco(2)
Species	⁴⁰ K	⁴⁰ K	³⁹ K	³⁹ K	⁶ Li	⁴⁰ K	⁴⁰ K
MOT T (μ K)	80	30	6	40	400	600	330
MOT N *10 ⁶	130	2	2000	30	100	700	140
MOT n_{pk} * 10 ¹⁰ (cm ⁻³)	1.4	-	10	-	-	0.1	2
Dipole depth (μ K)	180	260	40	4200	1700	230	2800
Dipole power (W)	100	11.5	30	40	112	13.5	120
Dipole waist (μ m)	300	86	150	40	70	100	85
Dipole λ (nm)	1070	1070	1550	1071	1070	1064	1070
Dipole geometry	17°	18°	one beam	68°	11°	54°	20°
Fraction loaded	0.07	0.2	0.015	0.07	0.003	0	-

Table 2.1: Parameters used in select implementations of all-optical evaporation. Blank spaces indicate parameters that could not be determined with published information. Numbers given for a MOT refer to the final stage of laser cooling, which in some cases is an optical molasses stage to achieve sub-Doppler temperatures. Dipole power refers to the power of a single beam when a crossed trap is used, at the highest power used for initial loading, and angles refer to the full angles between the two crossed beams. Fraction loaded refers to the number of atoms various groups reported as being captured in their optical traps, but these numbers are not necessarily directly comparable as the observed number may depend on how long the atoms are held in the optical trap and evaporate. The parameters DeMarco(1) correspond to our initial evaporation sequence, where the numbers listed as the MOT are instead the parameters in the quadrupole trap after transfer to the science cell. The temperature in the cart is taken from Ref. [23], and the peak density is calculated according to equation 2.3 of that source. The parameters DeMarco(2) correspond to design parameters after implementation of the science cell MOT and high-power dipole beam described in this chapter. The MOT temperature is calculated by suddenly turning off the light and fields, allowing the atoms to expand for a variable time, and taking a fluorescence images on the auxiliary Point Grey camera. The central density is estimated using the laser parameters, MOT number and transfer efficiency from [23, 24], and the MOT model of Steane et al [69] which accounts for the effects of radiation pressure. Many of these systems have specific idiosyncrasies that are not easily captured in a chart—for example, the Grimm experiment is a dual-species apparatus for potassium and dysprosium, complicating the cooling and trapping sequences—but I have attempted to give numbers for each that can be sensibly compared.

2.4.2 The Science Cell MOT

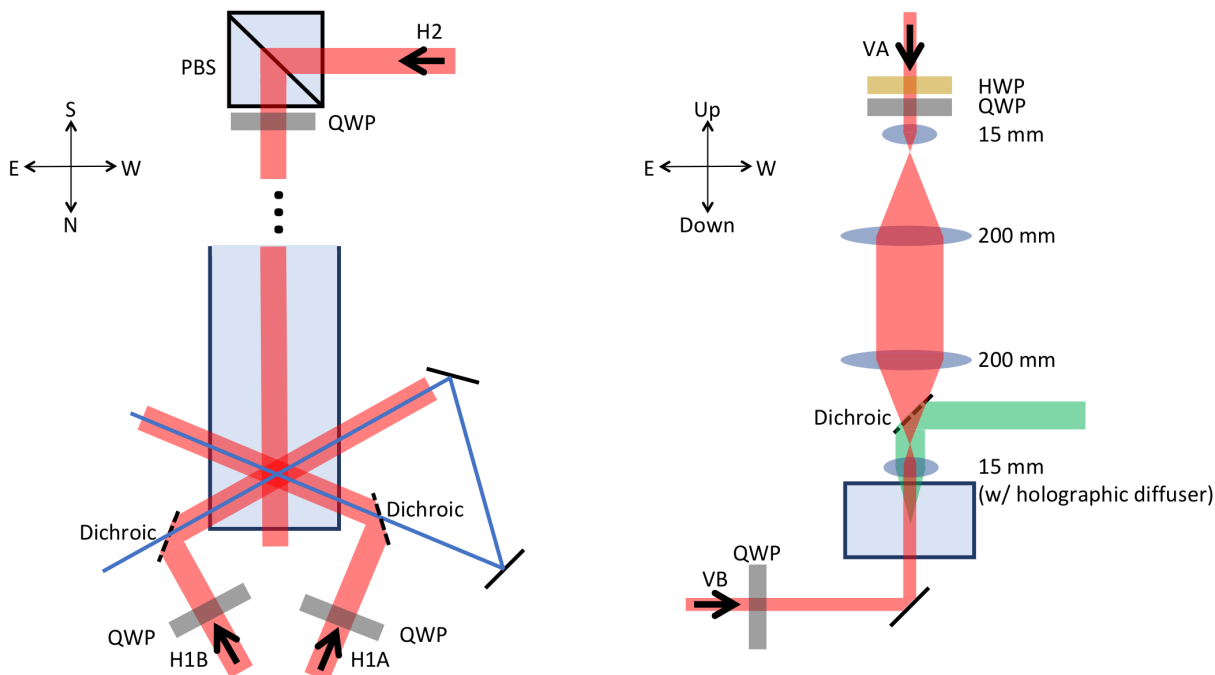


Figure 2.20: Layout of sciMOT optics. Distances are not to scale. Left: view from above (top is South). Two of the transverse MOT beams (red) are co-propagating with the lower-power dipole beam (blue), coupled in by dichroic mirrors (dashed lines). The third beam travels down the transfer tube along the main imaging pathway. Quarter waveplates (grey boxes) set the polarizations. Not shown are an initial PBS and expanding telescope, the same for each beam. Right: view from North (top is up). The vertical beams are half the size of the transverse beams, and share the pathway of the disorder beam (green). A half waveplate (yellow) is required in VA to adjust for the birefringence of the diffuser.

The goal of the science cell MOT (sciMOT) is to recapture and collect atoms from the cart quadrupole, and provide a suitable starting point to load the high-power dipole trap. The cart quadrupole itself provides a convenient magnetic gradient, so we only need turn its current down while turning on the appropriate light. Because of constraints on optical access, and because it only needs to capture atoms that are already relative cold, the design is somewhat different from a typical MOT such as the one in our collection cell.

Due to optical access constraints, we use a five beam MOT [71], with three transverse beams (H1A, H1B, H2) and two counterpropagating vertical beams (VA, VB) [Fig. 2.20]. This is not a commonly used geometry, but it can be thought of as an intermediate case between the normal six beam cubic MOT and a four beam tetrahedral MOT [72]. Four of the five beams share a pathway with another beam. H1A and H1B are along portions of the (lower-power) dipole pathway, coupled in by dichroic mirrors (Thorlabs DMLP950), H2 is joined with the imaging light on a cube, and VA shares a path with the disorder, coupled in on another dichroic (Thorlabs DMLP605L). Because it must go through the GPX 15-15 lens and holographic diffuser

directly above the cell, the downward beam also has a series of lenses to create a pair of telescopes. These consist of another GPX 15-15, followed by two large 200 mm achromats (Thorlabs AC508-200-B), before the final GPX 15-15. Because the MOT beam is not focused at the atoms, the holographic diffuser does not create fine-grained speckle as it does for the green disorder beam. However, we found experimentally that the diffuser used (a holographic diffuser from Luminit) is strongly birefringent. Therefore, we have a half and quarter waveplate to compensate for its effect on the polarization, which we determine by analyzing the beam after the cell.

While this setup works, it can be cumbersome. Because the transverse beams are not precisely at 120° , we must adjust their powers individually to suitably balance the forces on the atoms. Both H2 and VA are tightly constrained, making alignment tedious. Most importantly, the beams are all rather small, with diameters ranging from around a quarter to half inch. This makes alignment much more sensitive than typical for a MOT, and places significant constraints on the parameters required to maximize lifetime.

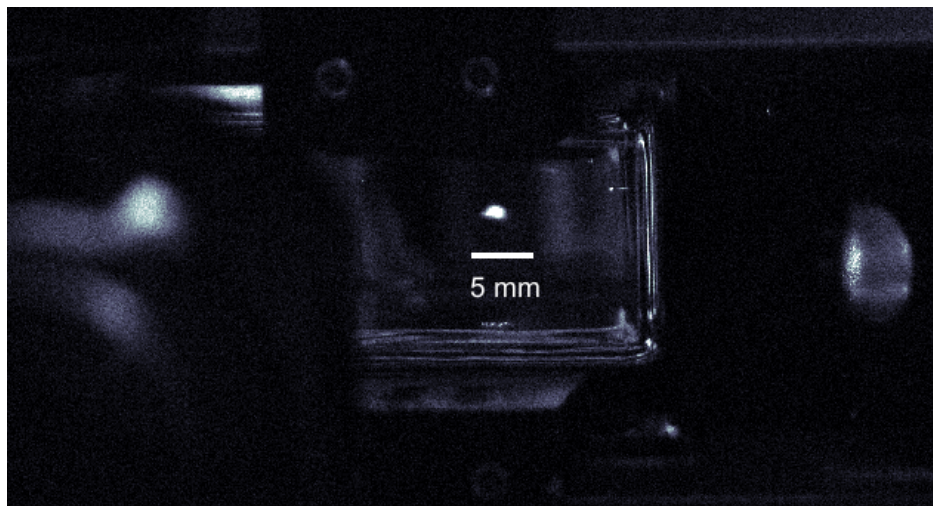


Figure 2.21: Image of the sciMOT, taken with an auxiliary camera (Point Grey CMLN-13S2M) from the side pointing west. The edges of the science cell are clearly visible, as are the brackets used to mount the QUIC/Feshbach coils. This is a composite of two images to show the MOT and background. The MOT is shown 50 ms after recapture, with a 1 ms exposure.

The optimized parameters for the MOT detuning and cart current are shown in Fig. 2.22. In these measurements, the atoms were released from the cart quadrupole into the sciMOT, held for 50 ms, and then the sciMOT light was turned off and the cart current was turned back up to recapture atoms back into the quadrupole trap. After a brief hold to allow any transient atoms to leave the cart was shut off and the atoms were counting with an absorption image. Compared to a typical MOT, such as the one used in our collection cell, the optimum parameters for a long-lived MOT require much stronger inward forces—a fairly small trap detuning of around -10 MHz (compared to -30 MHz for our collection MOT), and a very high

quadrupole current of around 50 A (compared to 8 A for our collection MOT).

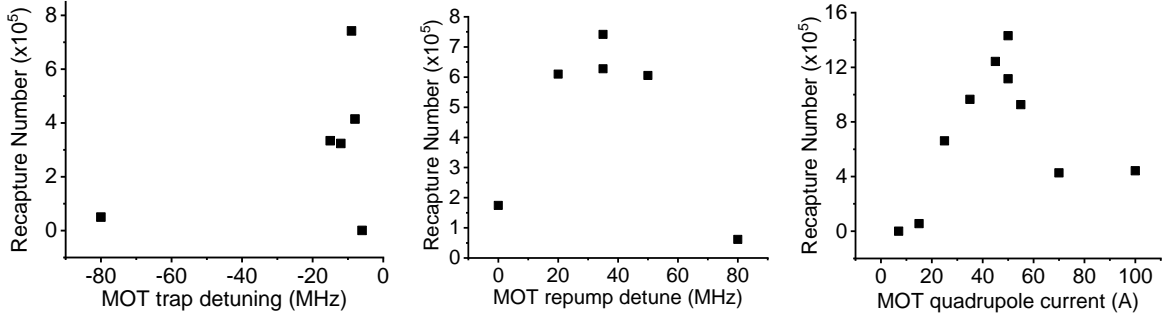


Figure 2.22: Optimization of the sciMOT parameters. The number of atoms in the MOT is determined by the number of atoms recaptured into the cart quadrupole after 50 ms, measured with absorption imaging. Compared to a typical MOT the optimum parameters are for a small trap detuning (around -10 MHz) and high cart quadrupole (around 50 A, corresponding to ~ 50 G/cm vertically)- parameters closer to what one would typically use in a compressed MOT (cMOT) stage.

We can get some insight into these optimum parameters by looking at the decay of the MOT. Figure 2.23 shows this decay, measured by the integrated fluorescence at variable times from images like Fig. 2.21. Two curves are shown, at the optimum trap detuning of -10 MHz and a more conventional detuning of -25 MHz. They are compared to two models: one-body exponential decay, modeled as $\dot{N} = -N/\tau$, and two-body decay, modeled as $\dot{N} = -bN^2$. For the optimized parameters the decay is better described by the two-body formula, with a loss constant of $\beta = 4 * 10^{-9}/(\text{atoms*s})$, about 20 times larger than a typical value for a potassium MOT [25]. For the larger detuning the decay is much faster and more consistent with one-body loss, with $\tau = 11$ ms.

My best guess at what is happening here is the following: because of our relatively small and inhomogeneous beams, only a small region near the intersection of the beams has sufficient balancing of the light forces for stability. When the natural size of the MOT is larger than this, as set by the detunings, the magnetic field gradient, and the outward force of light pressure [69, 73], our atoms quickly explore the allowed region and find places where they can be pushed out of the trap, which proceeds at a rate independent of the density for most of the relevant time (although in principle there should eventually be a crossover between the radiation pressure-dominated regime and the regime in which the density is set by the single-particle laser cooling dynamics [69]). When the MOT is sufficiently compressed, this loss is reduced, but at the expense of much higher two-body losses than one would normally encounter. Fortunately, this loss is sufficiently slow that it shouldn't pose a major problem over the tens of ms time for the dipole loading stage. Implementation of a dark spot MOT, as in our collection cell, would likely help to alleviate this problem. However, this would come at the cost of making the MOT beam alignment even more sensitive, and would

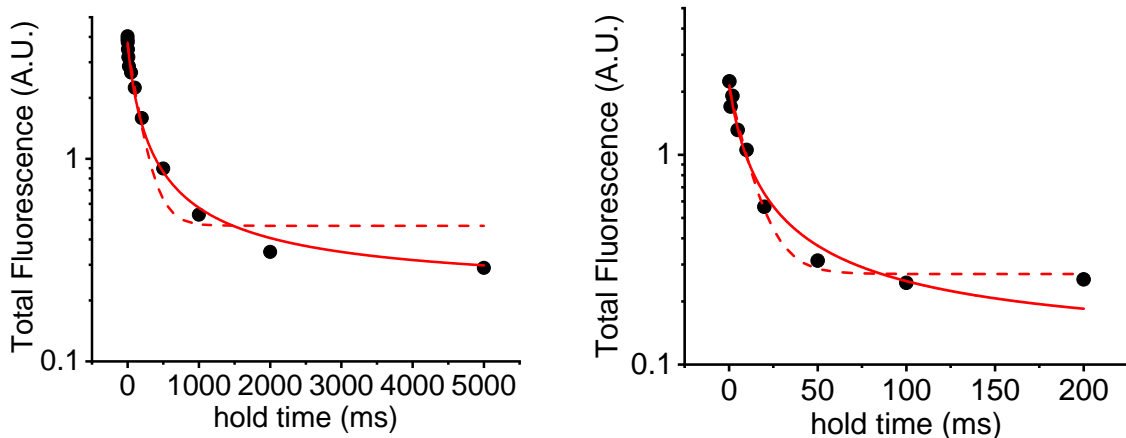


Figure 2.23: Lifetime of sciMOT. After a variable delay, fluorescence was measured by summing the counts within a region of an image on the auxiliary side camera as in Fig. 2.21. The left panel shows the optimized parameters, while the right panel has a trap detuning of -25 MHz rather than -10 MHz. Note the different horizontal scales. The dashed line is a fit to a simple exponential, while the solid line is a fit to two-body loss. For the optimized parameters the decay is best described by two-body loss, while for a larger detuning the exponential is a better fit. This indicates a crossover of the dominant loss mechanism (see text).

require substantial changes from our current setup in which the trap and repump beams are jointly coupled into fibers that deliver them to the science cell. Therefore, I believe that this limited lifetime is unavoidable given the constraints of our current setup.

As a side note, this project had some instructive lessons in proper design of optical systems. The path VA, which goes through the high-NA GPX lens for disorder, must be appropriately magnified and shrunk back down to exit this lens collimated, effectively making it the last element in a $4f$ telescope. However, because of the large beam divergences involved, this system is sensitive to non-idealities. Fig. 2.24 shows an example of what I saw when I initially found that this beam wasn't working and decided to look at it ex-situ. An amount of clipping in the intermediate stages that naively seemed tolerable resulted in a complete distortion of the beam profile, with most of the light being concentrated in a ring at the size set by the NA of the system. Reducing the intermediate magnification solves this issue, but limits how large a beam we can create at the atoms.

2.4.3 All-Optical Evaporation

To achieve the strong trapping forces needed to load a gas with temperatures in the several hundreds of μK , we are installing a high-power dipole laser (IPG YLR-200-LP-AC-Y14). We will run this at no more than 60% of the design power, or 120 W. The idea is for this laser to be used for initial trapping and cooling,

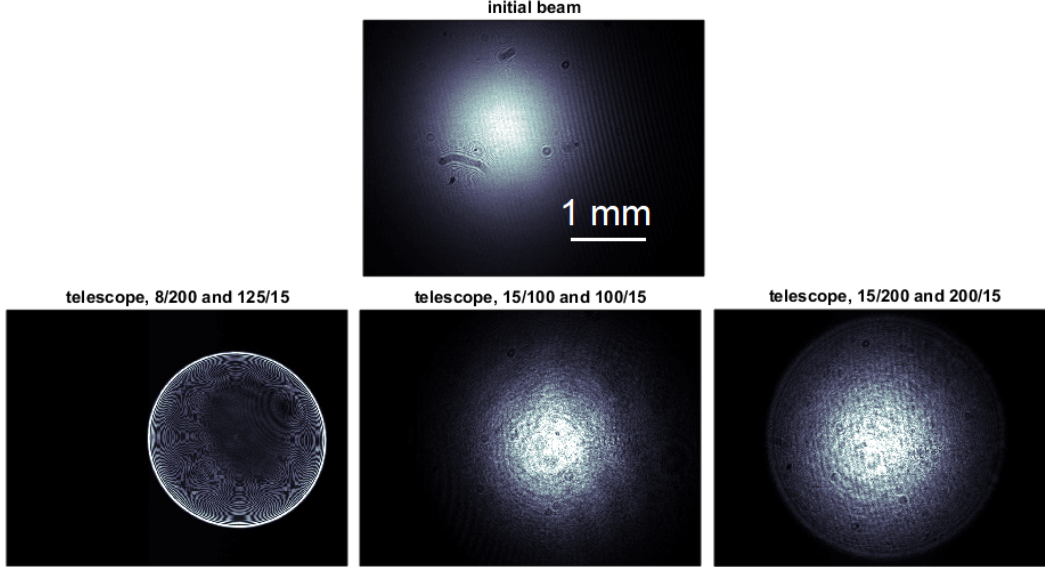


Figure 2.24: Profile of MOT beam VA before and after telescoping optics, imaged ex-situ. The top panel shows the initial beam, the output of the fiber collimator (Thorlabs TC25APC-780), which has a $1/e^2$ diameter of 2.8 mm. The bottom panel shows the beam after three progressive sets of $4f$ telescopes, with the indicated focal lengths. The second and third lenses in all of these systems have 2 inch (50.8 mm) diameters. Severe distortion is evident in the first telescope, due primarily to clipping of the beam on these lenses. This problem is largely removed by decreasing the magnification of the intermediate stage, as in the center pane, but results in lens distances incompatible with our setup. The right pane shows the lens arrangement that was chosen, which has an acceptable amount of clipping. The field of view of is 4.8 mm x 3.6 mm.

before the atoms are passed to a weaker dipole beam (the current one, or a single-frequency replacement to improve performance with Feshbach molecules) with more uniform confinement for the final stages of cooling and experimentation.

The layout for the high-power beam will be similar in many ways to the current dipole laser [Fig. 2.25]. After some initial lenses to shrink down the large fiber output, the beam will pass through a TeO_2 AOM (Gooch and Housego AOMO 3110-197) before further lenses arrange for the beam to come to a focus of 80 μm at the atoms. A half waveplate will set the polarizations of the two crossed beams to be orthogonal, to avoid interference. Both the zeroth and first AOM orders will be routed to water cooled beam dumps (Kentek ABD-2CNP). A pickoff (not shown) early in the path will send a small amount of light to the intensity servo to stabilize the power. The lenses are all laser-line YAG coated, with reflections of $< 0.1\%$, and are made of fused silica, which is known to have tolerable thermal effects at high power [74].

The use of such a powerful NIR beam requires special safety precautions. First, the beam path is kept as short and simple as possible, to reduce any possible failure points (and, additionally, thermal lensing effects). A beam block (Thorlabs LB1) is positioned behind each mirror as a precaution against the beam burning

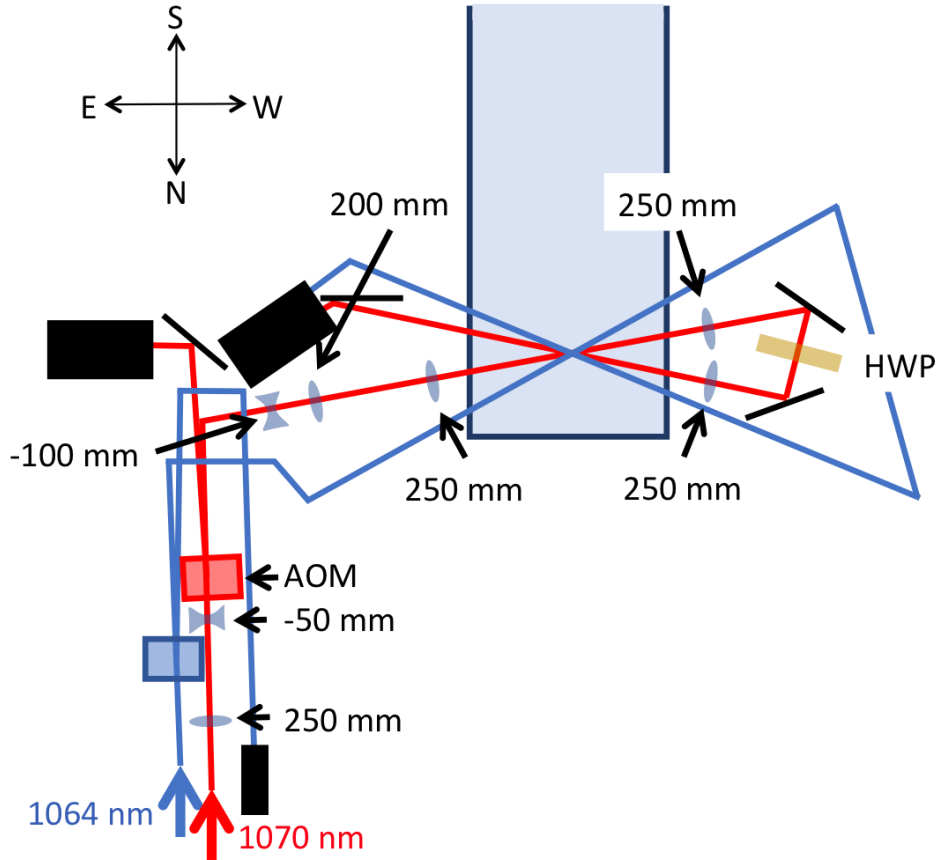


Figure 2.25: Layout of high-power dipole beam (red) and optics, as shown from above. The current low-power dipole beam (blue, optics not shown) is included for reference. Beam paths are approximately to scale, with elements enlarged for ease of viewing. The angle between the crossed beams is approximately 20° .

through the mirror surface. The beam path is shielded in several ways—where possible, by an aluminum box and tubes covering initial parts of the path, and as an additional precaution by a heavy-duty laser curtain (Kentek Everguard, rated for 1200 W/cm^2 for 100 s) that will completely enclose the north side of the table. Interlocks will also automatically turn the beam off when the curtains are open or when the water to the beam dumps is not flowing.

2.5 Looking Forward

Our apparatus is already distinguished by being among a small list of machines designed to study ultracold fermions in three-dimensional disordered lattices, and is quite versatile in its manipulation and measurement capabilities. Upgrades currently in progress should add even more tools to our kit and, by improving our data acquisition rate, enable sensitive or data-intensive measurements that are not currently feasible. A

natural next direction with these capabilities would be the comparison of transport of different quantities, such as spin, charge, and momentum. Different scalings of these excitations are widely predicted to occur in the strongly-correlated regime of the DFHM, and are related to interesting questions such as the possibility of spin-charge separation [75] and violation of the Wiedemann-Franz law [76, 77]. These upgrades should also allow us to make full use of our Feshbach resonance to study Fermi superfluids in disorder, a largely unexplored field in ultracold gases [78] with interesting possibilities such as the disorder-mediated enhancement of pairing [79].

Chapter 3

Bad-Metal Relaxation Dynamics

One of the great promises of studying strongly-correlated fermions in an optical lattice is the ability to recreate phenomena that are poorly understood or controversial in models of condensed matter systems and to perform experiments that illuminate new observables or remove usual limitations. In this chapter I will describe one such experiment, in which we realized a minimal model of materials known as *bad metals*, which have been a subject of long-standing theoretical and experimental interest. I will provide a brief review of previous studies of bad (and strange) metals, intended especially as a short orientation for students new to the study of these systems. Then I will describe our results, comment on how they fit into the overall picture, and mention some future directions.

Portions of this chapter are adapted from *Bad-metal relaxation dynamics in a Fermi lattice gas*, Nature Communications, **10**, 1588 [80].

3.1 Good Metals and Fermi Liquid Theory

To understand a bad metal, it helps to first define a *good* (or *conventional*) *metal*. A canonical good metal has several related properties:

- It is accurately described by Fermi liquid theory. This theory is based upon the existence of long-lasting states, the *Fermi liquid quasiparticles*, that are adiabatically connected to the bare, noninteracting electron states and have a nonzero overlap with them [81–83]. As one imagines adiabatically turning on the electron interactions, in a Fermi liquid there is a smooth mapping from the non-interacting states to the interacting ones. Quantum numbers such as the quasimomentum, charge, and spin are preserved, and the mass is renormalized.
- T/T_F is low, and the electrical resistivity due to electron-electron interactions scales as T^2 . This can be shown, under certain conditions, to be a natural result of quasiparticles scattering near a Fermi surface [82, 84].

- The resistance is controlled by the *momentum relaxation rate* $1/\tau_t$. τ_t itself is commonly called the transport time, but I will favor the former name for clarity. The momentum relaxation rate can equivalently be seen as the inverse lifetime of a Fermi liquid quasiparticle [85]. From this perspective, a condition for Fermi liquid theory to be valid is that $\epsilon\tau_t/\hbar \gg 1$, where ϵ is the excitation energy of the quasiparticle. A quasiparticle which damps away before its phase can evolve a full 2π cannot really be said to be a quasiparticle at all.
- The mean free path of quasiparticles is much larger than the lattice spacing d . This condition is the most common form of the *Mott-Ioffe-Regel (MIR) Limit* [86, 87]. If it is violated, the quasiparticles are plainly not long-lived, and a Fermi liquid description is impossible. The MIR limit is also commonly formulated in terms of a maximum electrical resistivity^a. Indeed, a saturation of electrical resistivity, corresponding to a calculated mean free path near the MIR limit, is seen in certain good metals [89]. However, it is very important to remember that this formulation assumes a specific relation between resistivity and mean free path, which often has some of the following assumptions: that the system is semiclassical, that the system can be described with Fermi liquid quasiparticles, or that the relaxation time and effective mass are constants.

To relate resistivity and mean free path, it is convenient to start with a simple formula for the resistivity generated from scattering quasiparticles:

$$\rho = \frac{m^*}{ne^2\tau} . \quad (3.1)$$

This is known as the Drude formula for resistivity. Here τ is the quasiparticle scattering rate, n is the density, and m^* is the quasiparticle effective mass. While originally found from classical models, the Drude formula can be derived as the resistivity of a Fermi liquid using the Kubo formalism with some assumptions about the nature of the quasiparticles [22, 90, 91]. To connect to the MIR limit, in electronic metals one can typically make the additional assumptions that the density is uniform and that $T \ll T_F$, so the mean free path $l_s = v_F\tau$ and (in 3D) $n = k_F^3/3\pi^2$, resulting in [89, 92]

$$\rho = \frac{m^*}{ne^2\tau} = \frac{3\pi^2\hbar}{e^2k_F^2l_s} \quad (3.2)$$

and thus making the MIR limit

$$\rho_{MIR} = \frac{3\pi^2\hbar}{e^2k_F^2d} . \quad (3.3)$$

Eqs. 3.2 and 3.3 express everything in terms of properties (ρ , k_F , and d) that can be measured in

^aHistorically, the question of a maximum resistivity (or minimum conductivity) in metals was the original motivation for Mott [88].

electronic materials, so they are the most common way to identify a bad metal. Eq. 3.1, in contrast, makes no additional assumptions beyond the existence of Fermi liquid quasiparticles, and is easily generalized to a varying density, so it will be more useful for ultracold atoms.

The MIR limit is an argument, not a theorem, and it does not include constant factors. Therefore, it should be thought of not as a bright line that some materials cross, but more of a fuzzy region. Far above the MIR limit a quasiparticle description is (possibly) sensible, and far below the limit it is not, but as a material crosses it there is not one point at which quasiparticles stop being present.

3.2 Non-Fermi Liquids

Fermi liquid theory has been successfully applied to a vast variety of metals, so the discovery of classes of strongly-correlated materials for which this description fails spurred efforts to understand what alternative organizing principles emerge in these cases [83]. These materials are variously called bad metals and strange metals, with some authors using these terms interchangeably. However, each phase as originally coined emphasizes different phenomena that in principle need not coincide, so I will define them as specifically as possible.

3.2.1 Bad Metals

The term *bad metal* was first introduced by Emery and Kivelson [93] to describe a metal which has a high enough electrical resistivity that, when the mean free path is calculated in the simple quasiparticle picture, this calculated mean free path exceeds the MIR limit. Typically this happens at some elevated temperature, and the resistivity continues to rise far beyond this value as the temperature is raised without any indication that this limit is relevant to the material behavior. Furthermore, bad metals generally have resistivity that does not scale as T^2 , but often scales linearly with T instead. The slope of the T -linear resistivity also seems to have a universal value, in the appropriate rescaled units [92, 94]. This slope corresponds to taking the quasiparticle calculation for the scattering rate τ , and setting $\tau \approx \hbar/k_B T$. Interestingly, this universal slope also applies to materials which are not bad metals, such as conventional metals at temperatures where the scattering is determined by electron-phonon coupling. This leads to a mechanism for T -linear resistivity that, unlike bad metal resistivity, is well-understood. It also appears that the resistivity of some bad metals may also scale linearly with other parameters, such as magnetic field [95].

Along with their unusual DC resistivity, bad metals display spectral weight transfer [96]. As the temperature is increased, the AC conductivity is reduced at lower frequencies, but correspondingly increases at

higher frequencies. This spectral weight transfer is enabled by the strong interactions, and is believed to be a key characteristic of bad metals [87].

It is important, at this point, to state clearly two things that are not necessarily true about bad metals. The mean free path (of quasiparticles if they exist, or more generally defined as the length scale over which a momentum impulse travels before it is dissipated away) may not actually be smaller than the lattice spacing. Rather, some other aspect of the derivation of Eq. 3.2 may have failed [87]. As I will discuss later, this is the picture suggested by numerical and experimental evidence. Also, while the system must be a non-Fermi liquid at the temperatures for which the MIR limit is violated, it does not necessarily follow that the system cannot be a Fermi liquid at lower temperatures [97]. Regardless of the ultimate resolutions of these issues, it is safe to say that bad metals represent a violation of the most simple theory of a metal in some way, and are therefore an interesting subject of study.

3.2.2 Strange Metals

The term *strange metal*, probably due to Anderson [98], is most often applied to the normal state of a cuprate high- T_c superconductor. Unlike a bad metal, which might begin at high temperature, it refers to a non-Fermi liquid ground state (neglecting a possible superconducting transition, which might be suppressed with a magnetic field) [99, 100]. This state features non-Fermi liquid scaling of the resistivity with temperature, which approaches T -linear resistivity at optimal doping [101]. It also has other interesting properties, such as a Hall current scattering rate which scales differently than the resistivity, and power law scaling of the optical conductivity [83, 98, 102]. One proposed explanation for these phenomena (hotly debated) is that they are the result of proximity to a quantum critical point that is hidden by the superconducting transition [103]. Since a material would arguably need to exhibit several of these properties to qualify as a strange metal, this name is, as far as I know, usually only applied to the cuprate superconductors and models designed to explain them.

The cuprates near optimal doping are strange metals, and at sufficient temperature they also become bad metals. Other bad metals exist that are not strange metals. An example is vanadium dioxide, which shows the T -linear scaling and violation of the quasiparticle-derived MIR limit required for a bad metal, but has a metal-insulator transition as temperature is lowered and therefore does not have a strange metal ground state [104]. Similar statements apply to the rare-earth nickelates [96]. However, as neither strange nor bad metals are well understood, the precise relation between them is also not clear. I will be careful to delineate between them throughout this chapter, but the reader should remember that it may really be a distinction without a difference.

3.3 Our Measurement

3.3.1 Experimental Procedure

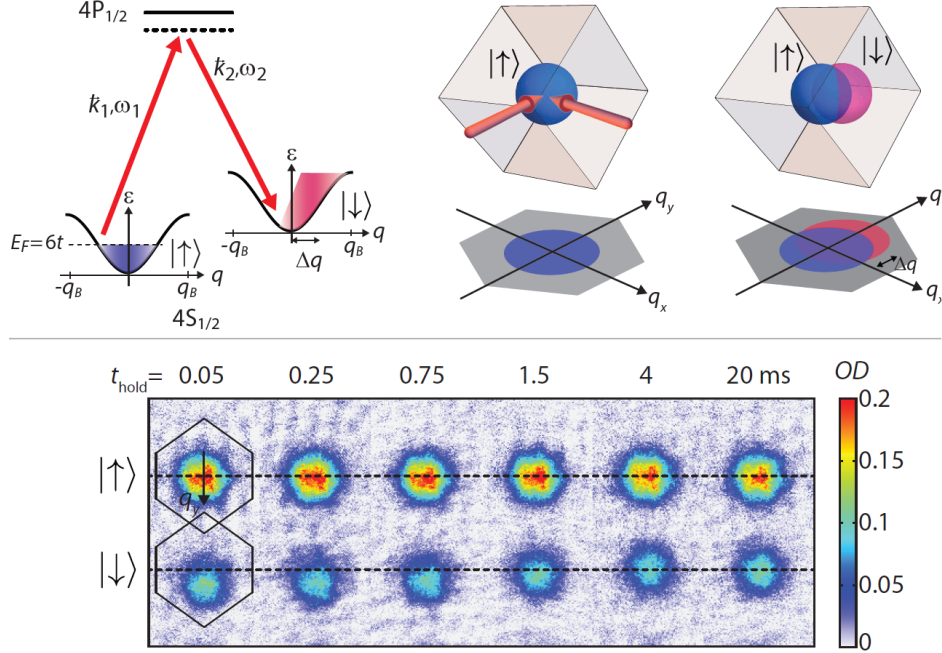


Figure 3.1: Setup of momentum relaxation measurement. Top: Schematic of the two-photon Raman transition used to introduce a second spin with a momentum current. Each beam is detuned 40 GHz from the optical transition to $4P_{1/2}$ (the $D1$ transition), and the two-photon Raman detuning is 1 MHz to match the Zeeman splitting between the two spins. Both the imaging direction and the direction of the Raman kick, which is set by $(\vec{k}_1 - \vec{k}_2)$, are not aligned with the lattices axes. Bottom: sample momentum relaxation data. About 30% of the atoms are transferred to the $|\downarrow\rangle$ ($|9/2, 7/2\rangle$) spin, which within 0.1 ms begin to collide with the majority $|\uparrow\rangle$ ($|9/2, 9/2\rangle$) component and experience damping. After applying the momentum impulse, we wait a variable time t_{hold} , then read out the quasimomentum of each component using bandmapping [54] and spin-resolved imaging. The $|\downarrow\rangle$ component relaxes to zero net quasimomentum, while the $|\uparrow\rangle$ component stays largely stationary. Hexagonal lines represent the outline of the Brillouin zone for each spin as projected onto the imaging plane.

To investigate the relaxation dynamics of a correlated metal, we initially loaded a spin-polarized (non-interacting) gas into an optical lattice [Fig. 3.1]. By varying the efficiency of the final evaporation stages, we could adjust the final temperature (between 0.22 to 1.2 T_F before turning on the optical lattice) while fixing the number such that $E_F = 6t$. This sets the filling so that the ground state is not a band insulator. We then apply a short (25 μs) pulse of two lasers driving a stimulated Raman transition, which does two things: it transfers a fraction (roughly 1/3) of the atoms to a second spin state, effectively turning on interactions, and also gives those particles a momentum impulse, which is set by the frequency of the two beams and the angle between them: $|\vec{\Delta p}| = 2\hbar\omega \sin(\theta/2)/c$, which for $\theta = 30^\circ$ and $\omega = 2\pi c/(770 \text{ nm})$ is about $|\vec{\Delta p}| = q_B/2$. We

chose optical lattice depths of 4 to 7 E_R , which is deep enough that the system is described by the (clean) Hubbard Hamiltonian, but sufficiently shallow that a Mott insulator does not form in any part. Nonetheless, $U > t$ over all the data, putting us in the regime in which a weak-scattering theory may be expected to break down.

By applying a magnetic gradient during time-of-flight expansion we can spatially separate the spin components and watch the motion of each subsystem of spins independently. We see that the momentum impulse of the minority spin relaxes back to zero, while the majority spin remains largely stationary. The momentum relaxes back to zero with a characteristic time, which we extract and write as τ_t , the inverse momentum relaxation rate.

3.3.2 Causes of Momentum Relaxation

Why does momentum relax at all? In a translationally invariant system, momentum is conserved. As a result, a free Fermi gas, whether interacting or not, has a vanishing DC resistivity. A nonzero resistivity requires some source of translational symmetry breaking. In a solid this comes from the ions. Since their masses are $\approx 10^4$ times larger than electrons, we can usually ignore their response to an applied current and treat them as a fixed background. Doing so results in a system that only has discrete translational symmetry, with physical consequences that are encapsulated by Bloch's theorem and the band physics familiar from a first condensed matter course (see, for example, Ref. [106]). This is one reason that understanding resistivity which is due to interparticle interactions, such as that of a bad metal, is challenging, both conceptually and computationally. It results from a subtle interplay of the translationally invariant interactions and translation breaking effects, and requires both to be present [84].

In our system, we have multiple sources of translational symmetry breaking, all of which can lead to momentum relaxation, and we must understand each of them to isolate the effects we are interested in. The first source is the overall harmonic trap, which makes the trap center a special place. For a perfectly harmonic trap this is only a minor concern: the momentum p is no longer conserved, but $p^2 + x^2$ (in rescaled units) is, and a current without dissipation just changes into an oscillation at the trap frequency without dissipation. However, in practice our trap is not perfectly harmonic, meaning that the frequency of oscillation is not fully independent from the amplitude, and this leads to momentum relaxation due to dephasing after many oscillations.

The second source of translational symmetry breaking is the lattice. Of course, the discrete symmetry breaking from the lattice is precisely what we want to emulate materials, but it also makes the momentum relaxation due to dephasing much faster. Now not only is the energy dependence on position non-quadratic,

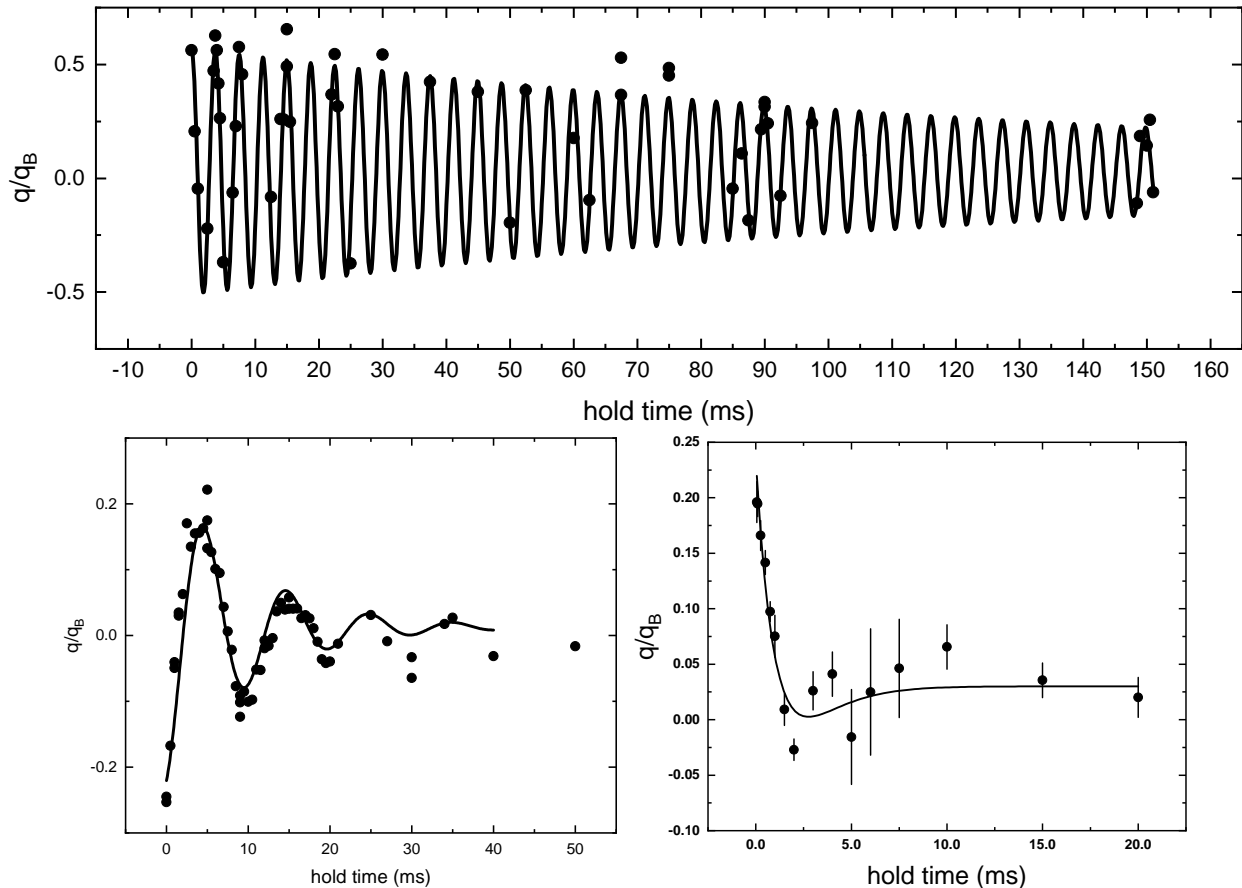


Figure 3.2: Momentum relaxation in different regimes. The momentum is scaled by q_B in a lattice. Note the different horizontal scales. Lines are fits to equations describing damped harmonic motion. Top: Momentum relaxation of the $|\downarrow\rangle$ component from a Raman kick in a harmonic trap. The $|\uparrow\rangle$ component (not shown) remains largely stationary. Points are the results of individual runs. Although this is a spin-mixed interacting gas, the interactions are so weak in the absence of a lattice that the momentum impulse relaxes primarily due to anharmonicity of the trap over ≈ 100 ms. In a more harmonic trap, we would expect to see even slower collisional relaxation described by quasiparticle theory, as in Ref. [105]. Bottom left: Momentum relaxation of a spin-polarized gas in an optical lattice ($s = 4 E_R$). Points are the results of individual runs. In this case, the momentum impulse was caused by a magnetic field gradient. Because this system is non-interacting, relaxation is due to dephasing from the band dispersion, which has a timescale of several ms. Bottom right: Relaxation of the $|\downarrow\rangle$ component of a strongly interacting and high-temperature ($4 E_R$ and $1.3 T_F$) gas after a Raman kick, which happens over only a few tunneling times ($\hbar/t = 0.23$ ms). The $|\uparrow\rangle$ component (not shown) remains largely stationary. Points are the mean and s.e.m. of at least five runs. This is the relaxation process that we are interested in characterizing.

because of the higher-order terms in the confining potential, but the energy dependence on momentum is also non-quadratic because of the modified dispersion relation of particles in a lattice relative to free particles. This makes the dephasing effects much faster; nonetheless we can at least observe several oscillations in the trapping potential before a momentum current is damped away. Furthermore, since this is a non-interacting effect, we are able to understand it by numerical simulation and to measure it in isolation by kicking a spin-polarized gas with a brief magnetic force. As a result, we have a good understanding of this timescale

and how it is determined.

Fig. 3.2 shows a summary of measured momentum relaxation in three cases. The first, a weakly interacting gas in a trap, relaxes due to the anharmonic potential. The second, a noninteracting gas in a lattice, relaxes due to the dephasing resulting from the band dispersion. In the third panel we have turned on strong interactions, by doing a Raman pulse in the lattice, and we see such an increase in the momentum relaxation rate that the gas can no longer even make one oscillation—the motion is overdamped. We now know that this momentum relaxation rate is due to the strong interactions, aided by the translational symmetry breaking of the lattice, in exact analogy with a strongly-correlated material. Now that we have isolated this interaction-driven momentum relaxation, we may study it.

3.3.3 Our Results

Fitting Procedure

We extract τ_t from the data with a fit to the solution of the differential equations:

$$\frac{\partial}{\partial t} q_{\downarrow}(t) = -m\Omega^2 y_{\downarrow}(t) - \frac{q_{\downarrow}(t)}{\tau_t}, \quad (3.4)$$

$$\frac{\partial}{\partial t} y_{\downarrow}(t) = \frac{q_{\downarrow}(t)}{m}, \quad (3.5)$$

in which q_{\downarrow} is the average quasimomentum of the $|\downarrow\rangle$ atoms in the direction of the Raman kick (which coincides with the vertical axis of the imaging plane). This is a solution to the Boltzmann equation [82], which has been used successfully to model the momentum relaxation of a weakly-interacting Fermi gas in a harmonic trap [105]. We fit the solution of these equations for the evolution of $q_{\downarrow}(t)$, with initial conditions $y_{\downarrow}(0) = 0$ and $q_{\downarrow}(0) = q_0$, and fit parameters τ_t , the inverse momentum relaxation rate, Ω , the averaged trap frequency, and q_0 , the averaged initial impulse. We also add an overall offset to the functional form for fitting, to remove any small errors in our determination of the resting center of the gas, but this is very small throughout the data. These equations describe damped harmonic oscillatory motion. It is an approximation, and leaves out the anharmonic dephasing discussed in the previous section. Nevertheless, because our data is all in the slightly underdamped to very overdamped regime, we expect and find that it fits the data well. Reassuringly, there is also no structure evident in the residuals, which suggests that our model captures the most important effects. The fit values for Ω and q_0 do show some systematic trends that are not straightforward to extract information from; as a result we did not use them in our analysis. Plots of their temperature dependences can be seen in Fig. 3.3.

Finally, at $4 E_R$ we varied the temperature before loading the lattice between 0.2 and 1.2 T_F . We

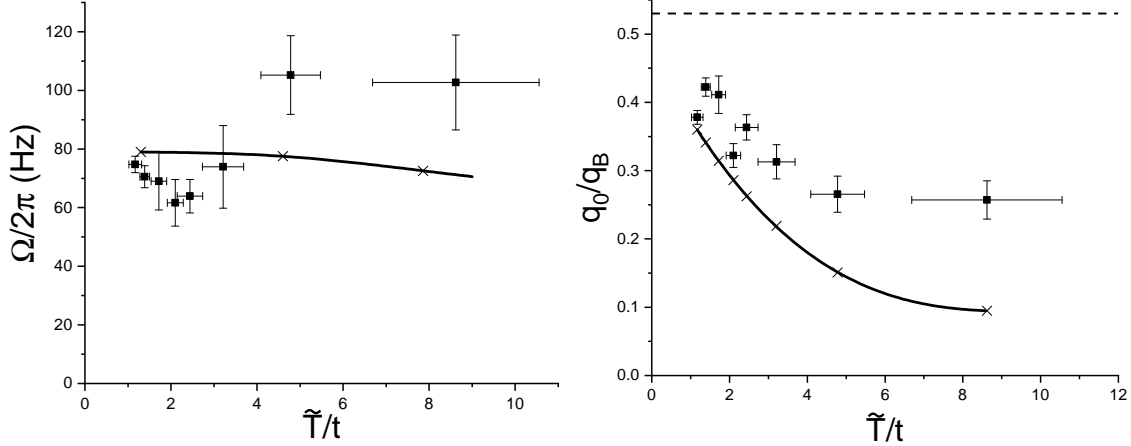


Figure 3.3: Fit values of other parameters in momentum relaxation data. Vertical error bars reflect fit uncertainty, and horizontal error bars represent s.e.m. from temperature measurements. The x-axes are effective temperature in the lattice \tilde{T}/t , as described in Sec. 3.3.3. Left: fit values to $\Omega/2\pi$ as a function of temperature. The x's represent calculated variation in Ω for a polarized gas due to the change in momentum occupations, with the line as a guide to the eye. The explanation for this trend is not evident. It may reflect temperature-dependent changes in the shift of the the oscillation frequency due to interactions, similar to effects seen in mixed-species experiments [107], and therefore contain interesting information about the changing quasiparticles. However, the higher-temperature points are quite overdamped (see the bottom right of Fig. 3.2, which corresponds to the highest temperature point), and as a result the accuracy of the fit to Ω is questionable. Right: Fit values for the initial quasimomentum q_0 for the same data, compared to the single-particle Raman momentum given by $|\Delta p| = 2\hbar\omega \sin(\theta/2)/c$ (dashed line), and the calculated q_0 for a thermodynamic distribution with \tilde{T} and $\tilde{\mu}$ (x's, with solid line interpolation as a guide to the eye). The decrease of the effective kick with increasing temperature is due to increasing population near the edge of the Brillouin Zone. The increasing disagreement with temperature may reflect a failure of our procedure to determine \tilde{T} and $\tilde{\mu}$ in this regime (see SM of [80]), or limits of bandmapping near the Brillouin zone edge [54].

also varied, at low temperature, the lattice depth from 4 to 7 E_R to study the interaction dependence. Because the density and thus signal size decreases rapidly both with increasing lattice depth and increasing temperature, we were not able to get high-quality data at both elevated temperatures and deeper lattice depths.

Comparison to Quasiparticle Calculation

The momentum relaxation rate is compared to a calculation based on Fermi's golden rule (FGR) and Boltzmann transport. This calculation was developed by Brian DeMarco, and is described in more detail in Refs. [22, 80].

To calculate the predicted scattering, we must know the density and quasimomentum distributions in the lattice. We take advantage of our initial non-interacting state. Before the lattice is turned on the atoms are at equilibrium, with occupations of each harmonic oscillator state that are determined by the measured T/T_F . We then map these harmonic oscillator eigenstates to the corresponding combined lattice-trap eigenstates

[54] to determine the predicted distribution after an adiabatic lattice turn-on. Note that this procedure is adiabatic at the level of individual eigenstates, in the sense of the adiabatic theorem of quantum mechanics, but *not* adiabatic in the thermodynamic sense. Because the population of each state cannot change in the absence of interactions, the state in the lattice is generically not at thermodynamic equilibrium. Fortunately, we find that in all cases we can find an effective temperature \tilde{T} and effective chemical potential $\tilde{\mu}$ which do a good job of capturing the overall density and quasimomentum distributions. Therefore, we characterize the initial state with these effective thermodynamic parameters. In practice, \tilde{T} and $\tilde{\mu}$ are not very different than the expected thermodynamic parameters if the gas did remain in thermodynamic equilibrium during the lattice load, with the entropy per particle conserved. We also benchmarked this procedure by comparing observed and predicted in-trap density distributions and found reasonable agreement.

With the initial state in hand, we calculate the scattering rate as:

$$\begin{aligned}
\frac{1}{\tau_t} &= -\frac{1}{\langle \vec{Q}_\downarrow \cdot \delta \hat{k} \rangle} \times \left\langle \frac{\partial (\vec{Q}_\downarrow \cdot \delta \hat{k})}{\partial t} \right\rangle \\
&= \frac{1}{\langle \vec{Q}_\downarrow \cdot \delta \hat{k} \rangle} \frac{1}{2} \frac{2\pi}{\hbar} \frac{U^2}{2t} \int d^3 \vec{\mathcal{R}} \int \frac{d^3 \vec{Q}_{1\downarrow}}{(2\pi)^3} \int \frac{d^3 \vec{Q}_{2\uparrow}}{(2\pi)^3} \int \frac{d^3 \vec{Q}_{3\downarrow}}{(2\pi)^3} \\
&\times \tilde{\rho}_\downarrow (\vec{Q}_{1\downarrow}, \vec{\mathcal{R}}) \tilde{\rho}_\uparrow (\vec{Q}_{2\uparrow}, \vec{\mathcal{R}}) \left[1 - \tilde{\rho}_\downarrow (\vec{Q}_{3\downarrow}, \vec{\mathcal{R}}) \right] \left[1 - \tilde{\rho}_\downarrow (\vec{Q}_{4\uparrow}, \vec{\mathcal{R}}) \right] (\vec{Q}_{3\downarrow} - \vec{Q}_{4\downarrow}) \cdot \delta \hat{k} \\
&\times \delta \left[\tilde{\epsilon} (\vec{Q}_{1\downarrow}) + \tilde{\epsilon} (\vec{Q}_{2\uparrow}) - \tilde{\epsilon} (\vec{Q}_{3\downarrow}) - \tilde{\epsilon} (\vec{Q}_{4\uparrow}) \right].
\end{aligned} \tag{3.6}$$

Here $\langle \cdot \rangle$ denotes a thermodynamic average, \mathcal{Q} and \mathcal{R} are dimensionless quasimomentum and position variables, $\tilde{\rho}$ is a semiclassical Fermi-Dirac phase space distribution determined by $\tilde{\mu}$ and \tilde{T} , and $\tilde{\epsilon}$ is the non-interacting band dispersion. This is a generalization of the Fermi liquid procedure applied to good metals, which gives a $1/\tau_t \sim T^2$ dependence at low temperature and small kicks ($\hbar^2 \delta k^2 / 2m \ll T \ll T_F$), and uniform density, but also incorporates effects beyond this model, such as the crossover to the classical limit in which the scaling is $\tau_t \sim T^{3/2}$ [22]. However, this model is perturbative in U/t , which means that it, like normal Fermi liquid theory, requires that the eigenstates be quasiparticles with definite quasimomenta that are only mildly affected by isolated scattering events.

The observed scaling with temperature is found to be completely different from this calculation [Fig. 3.4]. The scattering at high temperature is much stronger than predicted, and approaches the tunneling time \hbar/t . This brings us into a regime in which weak-scattering descriptions should not be expected to be valid. We can see this in a number of ways, using the criteria for a Fermi liquid quasiparticle description mentioned earlier. For example, if we use a semiclassical calculation for the velocities of the $|\downarrow\rangle$ atoms, which is close to $2t\pi/\hbar q_B$ [22], the predicted mean free path l_s at the highest temperature is about four times

the lattice spacing d , and roughly the same as the average spacing between scatterers $n^{-1/3}$, suggesting an approach to the MIR limit. Similarly, the average excitation energy ϵ , calculated in a simple approximation that only considers the kinetic energy added by the Raman kick, is of order t , which also suggests that the damping rate of the excitations is comparable to their energies, $\epsilon\tau_t/\hbar \sim 1$, and that as a result Fermi liquid quasiparticles do not survive long enough to be well-defined. Most directly, an inverse momentum relaxation rate that approaches \hbar/t suggests a quasiparticle that is scattering roughly as often as it travels to a new site, which is plainly the maximum rate that could be consistent with a quasiparticle description.

In summary, seeing relaxation near this scale is an important indication that we are in the strong-scattering regime in which a bad metal might be expected. Furthermore, it might not be a coincidence that our fastest observed momentum relaxation is near the MIR limit. As we will discuss (in Sec. 3.4.1), a substantial class of theories about bad metal states predict that while their resistivities goes straight through the calculated MIR limit of Eq. 3.2, the momentum relaxation rates themselves do saturate at around the MIR value [87].

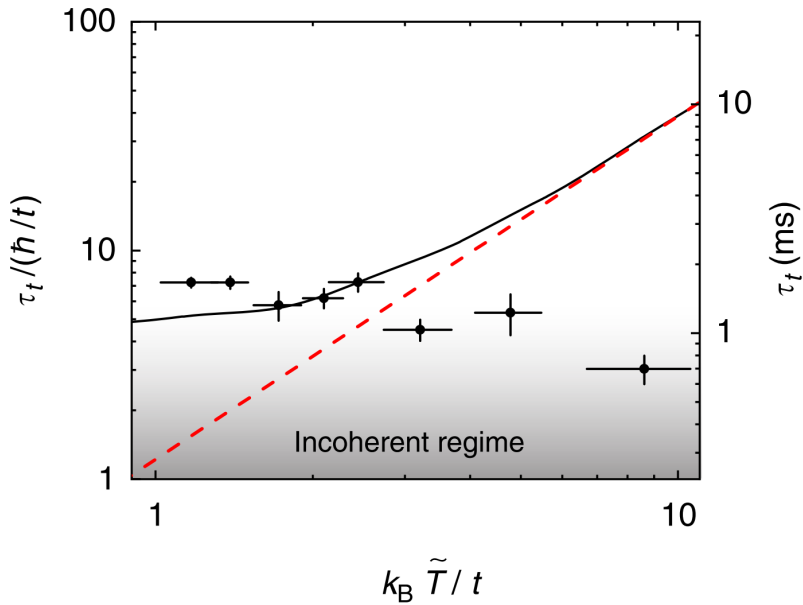


Figure 3.4: Temperature dependence of τ_t . Points are experimental data, with y-error corresponding to fit uncertainty and x-error the s.e.m. error from temperature measurements. The solid line is the FGR calculation, and the red dashed line is the scaling prediction of $T^{3/2}$ in the Maxwell-Boltzmann limit. The data strongly disagree with the weak-scattering theory scaling, and when τ_t is comparable to the tunneling time \hbar/t the system crosses over into the incoherent regime.

Because our Fermi gas is at a much higher temperature relative to T_F than most materials, some of the typical condensed matter intuition has to be rethought. For this reason, a useful point of comparison

for our measured relaxation comes from a recent study of the behavior of a good metal, liquid metallic deuterium, up to the Fermi temperature [108]. The relaxation time in this system, as determined from optical reflectivity measurements, initially decreases with temperature until saturating at a value near the expected MIR limit. Once the temperature is sufficient to break up the Fermi surface, at around $T/T_F = 0.4$, the relaxation time increases again, crossing over to the scaling expected for a classical plasma of $\tau \sim T^{3/2}$. This regime is analogous to the high-temperature regime of our FGR calculation, which also approaches a classical temperature scaling of $\tau \sim T^{3/2}$ (the fact that these scalings have the same numerical power, though, is purely a coincidence). While a complete theoretical picture of this good metal in the crossover regime, in which it is a strongly coupled plasma, is not available, both high and low temperatures show behavior consistent with a theory based on Boltzmann transport of quasiparticles. In contrast, the radical disagreement of our system with quasiparticle scaling highlights what an unusual metal we have created.

Effective Resistivity

To more clearly illustrate the relation between our system and measurements of resistivity in traditional bad metals, we calculate a dimensionless effective resistivity using this measured τ_t and the quasiparticle relation: $\rho/\rho_0 = \hbar/(n_{dwd}d^3\tau_t t)$ [Fig. 3.5]. This is a simple generalization of the Drude formula (Eq. 3.1), to allow for an average over a locally varying n , τ , and ρ . n_{dwd} is the density-weighted density, or average density of scatterers:

$$n_{dwd} = N_{\uparrow} \frac{\int d^3x d^3q w_{\downarrow}(\vec{x}, \vec{q}, \tilde{\mu}, \tilde{T}, t, \omega) w_{\uparrow}(\vec{x}, \vec{q}, \tilde{\mu}, \tilde{T}, t, \omega)}{\int d^3x d^3q w_{\downarrow}(\vec{x}, \vec{q}, \tilde{\mu}, \tilde{T}, t, \omega) \int d^3x d^3q w_{\uparrow}(\vec{x}, \vec{q}, \tilde{\mu}, \tilde{T}, t, \omega)} \quad (3.7)$$

where $w_{\uparrow(\downarrow)}$ is the semiclassical probability distribution for an atom in spin up (down):

$$w_{\uparrow(\downarrow)}(\vec{x}, \vec{q}, \tilde{\mu}, \tilde{T}, t, \omega) = \frac{1}{2q_B^2} \frac{{}^3N_{\uparrow(\downarrow)}}{N_{tot}} \frac{1}{e^{\epsilon(\vec{\tau}, \vec{q}, \tilde{\mu}, \tilde{T}, t, \omega)} + 1}. \quad (3.8)$$

Here ϵ is the energy of a single non-interacting particle in the band, which depends on the band dispersion and harmonic trapping. This procedure is precisely the inverse of the derivation of the scattering time for materials summarized in Eq. 3.2, and the same limitations apply. Therefore, this calculation can be considered as the resistivity that we would observe if our momentum relaxation were generated by collisions between scattering quasiparticles. By comparing these results to the Fermi liquid T^2 scaling of resistivity, we test the null hypothesis that our system is a good metal described by binary collisions of Fermi-liquid quasiparticles. This effective resistivity also has the virtue of taking out, within a quasiparticle framework, the trivial effects of changing density in our system. Since our system grows more dilute with increasing

temperature, even a constant momentum relaxation rate due to scattering quasiparticles would lead to a higher resistivity.

Our calculated resistivity displays strong anomalous scaling, growing without bound while the FGR calculation quickly saturates to its high-temperature limit. The observed scaling agrees reasonably well with the T -linear scaling predicted for the resistivity from DMFT, with the best linear fit giving a slope of 1.79 ± 0.37 and an intercept consistent with zero, -0.23 ± 0.53 .

Taking this all together, we have created a system of strongly-correlated fermions featuring momentum relaxation that scales very differently from a generic expectation for a system with quasiparticles and approaches the maximum rate that is consistent with a quasiparticle description. We therefore claim that this system displays all the defining characteristics of a bad metal. What can we learn from our new bad metal, in a radically different physical system from all previous examples?

3.4 Some Theories of Bad and Strange Metals

The past thirty years have seen many attempts to extract general principles from bad and/or strange metallic behaviors, which range from purely phenomenological descriptions to microscopic models. Unfortunately, it is often difficult to find a clear enumeration or comparison of these theories. In the following subsections, I will try to fill that gap by providing brief summaries of these approaches, focusing on their application to our measurements. It is important to remember that while these are to some extent competing explanations for bad or strange metals, they are not necessarily mutually exclusive. They vary in the level of abstraction and the specific limits in which they are predicted to apply.

3.4.1 Comparison to Numerics

One longstanding path of theoretical study of bad metals has been numerical investigations, using dynamical mean field theory (DMFT) [97, 110–112], and more recently using finite temperature Lanczos [113], quantum Monte Carlo [114], and high-temperature expansion [109] methods. These investigations paint a largely consistent picture of the basic mechanism behind the T -linear resistivity of bad metals: the strong interactions result in a temperature-dependent single-particle density of states, which coincides with a spectral function that redistributes weight away from the quasiparticle peak as temperature is increased and eventually destroys it entirely. In the quasiparticle picture, this is sometimes referred to as a “temperature-dependent effective carrier density” [96, 109]. This effective density is able to shrink without bound while the momentum relaxation rate saturates at around the MIR limit. As a result, in this picture the resistivity

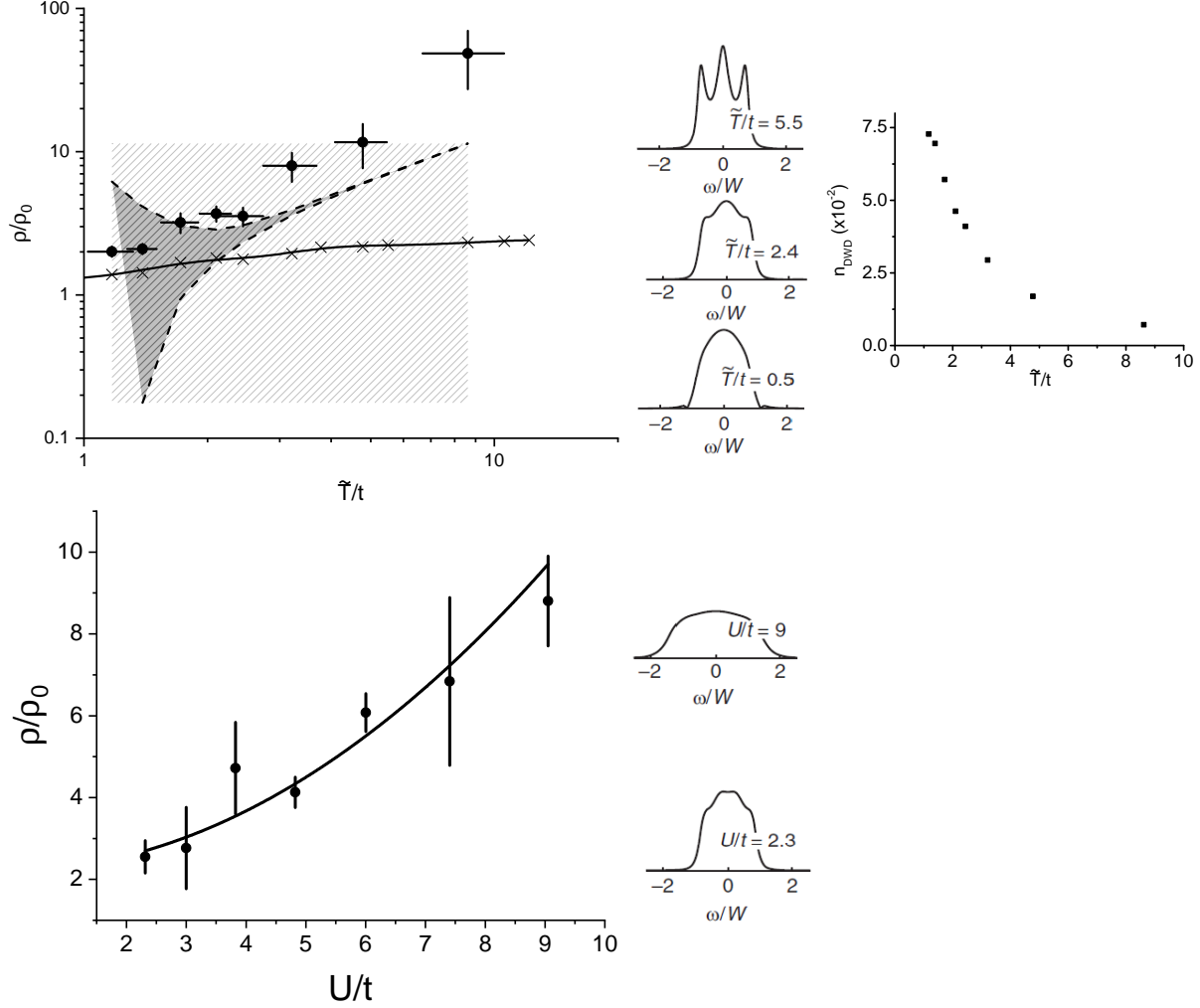


Figure 3.5: Resistivities determined from τ_t . Top left: Temperature dependence of calculated resistivity derived from experimental data (black points), compared with resistivity from the weak-scattering FGR calculation (x's, with solid line interpolation as a guide to the eye) and resistivity from the high-temperature series expansion for the Hubbard Hamiltonian of Ref. [109] (see Sec. 3.4.1) (shaded region, lower bound is 3rd order and upper bound is 5th order). Vertical error bars reflect fit uncertainty, and horizontal error bars represent s.e.m. from temperature measurements. Both calculated resistivities have no free parameters. At the right are three representative results for the spectral function of this system at half-filling, $U/t = 2.3$, and the given temperature, calculated with DMFT (see Sec. 3.4.1). The resistivity determined from these spectral functions (not shown) scales linearly with \tilde{T} over the experimental temperature regime [22]. Top right: density-weighted densities n_{dwd} used to determine ρ . Bottom: Interaction dependence of calculated resistivity derived from experimental data (black points), compared with the best-fit for the U^2/t scaling predicted by both DMFT and weak-scattering theory (black line). Error bars reflect fit uncertainty. At the right are representative spectral functions, again from DMFT at half-filling and with $\tilde{T}/t = 1.5$.

becomes independent of the relaxation rate at high temperatures.

Although it was challenging to make an exact comparison, these calculations seem to show some consistency with our data. Our calculated resistivities show good agreement with the scaling predicted by DMFT, both with temperature ($\rho \sim T$) and with interaction strength ($\rho \sim U^2$, which is not strongly modified

from the weak-scattering theory) [Fig. 3.5]. We did not attempt to compare the absolute magnitude of these measurements with prediction, in part because the DMFT calculations are performed at half-filling, where they are simplified by particle-hole symmetry. Another comparison, not necessarily more accurate but with different limitations, can be made using the high-temperature expansion technique [109], which admits simple analytical expressions for ρ in certain limits. Fig. 3.5 also shows the comparison between our data and the calculated temperature dependence results from the high-temperature expansion for a d -dimensional hypercubic lattice, in the large- d , strongly-interacting ($U \rightarrow \infty$), and low ($n = 0.1$) filling regime, compared to the resistivity from τ_t and n_{dwd} . We can approximate $n \sim 0.1$ over our data because of an interesting prediction of this model, that resistivity should be independent of n in the limit $n \rightarrow 0$. The form of this expansion is

$$\frac{\rho(T)}{\rho_0} = d \frac{T}{D} \left[c_1(n) + c_3(n) \left(\frac{D}{T} \right)^2 + c_5(n) \left(\frac{D}{T} \right)^4 \right], \quad (3.9)$$

in which $d = 3$ is the spatial dimension, D is the characteristic width of the hypercubic density of states, $D = 2\sqrt{d}t$, and the coefficients c_i are given by Table VII of Ref. [109]: $c_1(0.1) = 1.56337$, $c_3(0.1) = -0.228875$, and $c_5(0.1) = 0.0849724$. The two curves of the high-temperature expansion are the resulting expression to third and fifth orders; the difference between them gives an indication of the regime of convergence. Unlike the FGR calculation, this high-temperature calculation gets the magnitude and scaling of our observed resistivity approximately right, with an apparent disagreement by a constant factor of order two that may be explained in part by the large-dimensional limit.

Fig. 3.5 also shows the calculated spectral functions, from DMFT at half-filling, for a system with our U , t , and \tilde{T} . These were calculated by Wenchao Xu [22] using the TRIQS toolbox [115, 116], which employs a Bethe lattice geometry and uses simplifications that occur due to the particle-hole symmetry at half-filling. This exposes the mechanism, within this approximation, for the anomalous temperature-dependence of resistivity. As the temperature is raised, the density of states changes markedly, with weight shifted into the two Hubbard bands located at roughly $\pm U$. This reflects an effect that is widely seen in this type of simulation: increasing temperature, perhaps counterintuitively, can actually enhance Mott localization effects by driving a crossover from Fermi liquid quasiparticle excitations to local magnetic moments [112]. Interestingly, we do not see this effect when we instead change the interactions at fixed $\tilde{T}/t = 1.5$. In that case, we see a broadening of the density of states from the interactions but no marked shift of spectral weight into the Hubbard sidebands. This may be related to the experimental observation that the scaling with interactions at low temperature, unlike the temperature dependence, does not depart strongly from the weak-scattering prediction.

3.4.2 Universal Planckian Scattering

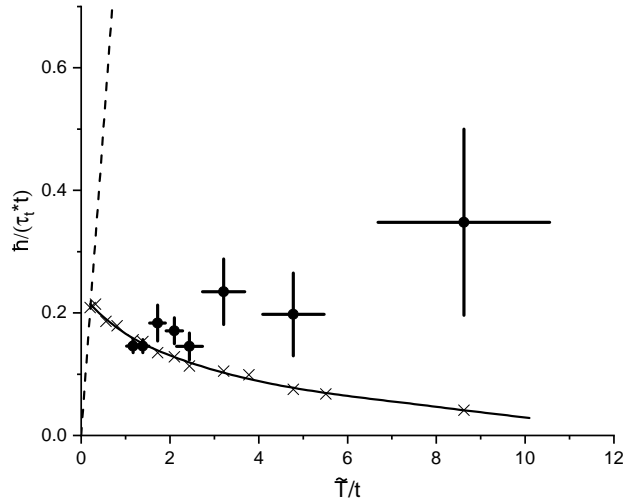


Figure 3.6: Comparison of the momentum relaxation rate $1/\tau_t$ to Planckian scaling. Points are experimental data, with vertical error bars reflecting fit uncertainty and horizontal error bars representing s.e.m. from temperature measurements. X's and solid line are FGR weak-scattering calculation with interpolation (b-spline) as a guide to the eye. Dashed line is Planckian scaling, $1/\tau_t = T/\hbar$.

Another line of inquiry about bad metals has developed to attempt to explain the seeming universal scaling of T -linear resistivity. As mentioned above in Sec. 3.2.1, in a variety of T -linear materials, including both good metals (in the regime where ρ is determined by coupling to phonons) and bad metals, it has been found that when resistivity and Fermi surface measurements are used to extract a scattering rate, following Eq. 3.2, $1/\tau \approx T/\hbar$. Among the attempts to explain this theoretically is Hartnoll's proposal of a bound on diffusion in strongly interacting systems [77].

Although these bounds have taken different forms, we are ideally positioned to evaluate the claim that for bad metals $1/\tau_t \approx T/\hbar$. As shown in Fig. 3.6, our measured relaxation rates are far below the T/\hbar line, and do not change nearly enough with temperature. The best-fit line for our momentum relaxation rate versus temperature has a slope of $0.02 T/\hbar$, rather than $\mathcal{O}(1)$. This is in general agreement with the picture from the numerics described above, which predict a saturation of τ_t .

That said, the observed universal T -linear scaling still cries out for an explanation. It is natural to ask whether we are really comparing the same observables. The quantity that is observed to obey scaling laws in materials is, roughly, $ne^2\rho/m^*$. In the weak-scattering, quasiparticle limit, in which $\rho = m^*/ne^2\tau_t$, this is equivalent to the momentum relaxation rate, $1/\tau_t$, but as I have stressed this may not be true in general. Therefore, let us give this quantity a new name, such as the *resistance rate*, and make the following claim: for T -linear materials, the inverse resistance rate $\tau_{res} \equiv ne^2\rho/m^*$ obeys $\tau_{res} = \hbar/T$, while the inverse momentum relaxation rate τ_t , in general, does not. As temperature is raised τ_{res} crosses over from being

nearly the same as τ_t to being independent of it, corresponding to two distinct regimes that both display the same smooth T-linear resistance [109, 117].

It remains to find a simple physical interpretation of τ_{res} that is valid both when there are quasiparticles and when there are not. I should hasten to add that this is not necessarily a unique insight- some other authors, such as Hartnoll (Ref. [77]), are careful to distinguish between the characteristic times for momentum relaxation, momentum diffusion, energy transport, and quasiparticle scattering, and discuss the relevance of each to resistivity in bad metals. The τ_{res} suggested here may also be related to other proposed timescales bounding diffusive transport, such as a Lyapunov time [118] (however, see Ref. [119] for limits on this interpretation). However, it is often the case in the literature that the characteristic relaxation time of the system is only defined by the quasiparticle relation $\rho = m^*/ne^2\tau$, or $\tau_{res} = \tau_t$ is implicitly assumed. To move beyond the paradigm of colliding Fermi liquid quasiparticles we will need to develop a consistent language and set of organizing principles that is not valid only in that limit, and experiments such as ours that access previously hidden observables can help to highlight that need.

3.4.3 Resistivity from Entropy

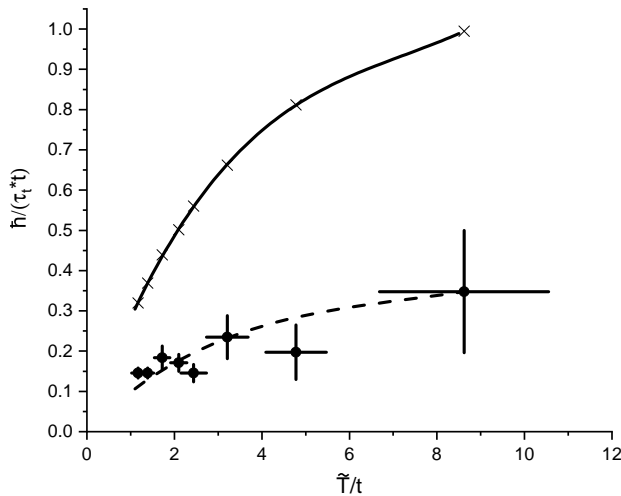


Figure 3.7: Comparison of the momentum relaxation rate $1/\tau_t$ to holographic scaling with entropy per particle. Points are experimental data, x’s are calculations based on scaling with entropy per particle, with solid line an interpolation as a guide to the eye. The dashed line is the solid line scaled by 0.35.

A related but distinct set of ideas to explain T-linear resistivity have been developed by Davison [120] and Zaanen [121], among others. These ideas have developed out of bounds observed in gravitational systems, which are mapped to strongly-coupled conformal quantum field theories using the AdS-CFT mapping. As such, I will refer to them for convenience as “holographic scaling.” As I understand, the logic goes something

like the following: among strongly interacting quantum field theories that are dual to gravitational systems, there is an observed bound (the *KSS Bound*) on the ratio of shear viscosity to entropy density, and the quantum systems saturating this bound, sometimes called *perfect quantum fluids*, are dual to gravitational systems with black holes [122]. Kovtun et al. made the further conjecture that this bound is universal to systems without such a dual. This conjecture has been tested in two radically different environments: in an ultracold unitary Fermi system in a harmonic trap [123], and in studies of quark-gluon plasmas [124]. To make the connection with strange metals, Davison and Zaanen further postulate that electrons in these systems are also perfect quantum fluids, which leads to a bound on resistivity determined from shear viscosity in the presence of translation invariance breaking. The resulting prediction is appealingly simple:

$$\frac{1}{\tau_t} = \frac{\hbar A}{l^2 m^*} \frac{S}{N}. \quad (3.10)$$

In other words, the momentum relaxation rate is proportional to the entropy per particle S/N , with $A \approx 1/4\pi$ as a universal constant and l as the length scale associated with translational symmetry breaking. If $S/N \sim T$, as is the case in most metals, this results in T -linear resistivity.

This theory is mainly intended for good strange metals rather than bad metals: that is, for strange metals at relatively low temperature so that they still feature a sharp peak in measurements of AC conductivity. Thus, it is not clear *a priori* that our system is within its domain of validity, but with that qualification we will look at the comparison anyway. For our system, both quantities of interest are readily determined: τ_t has been directly measured and S can be estimated by, for example, measuring the degeneracy before the lattice is loaded using the fit to the momentum distribution of a free Fermi gas, and assuming an adiabatic loading process. Taking $l = d$ and, as before, $m^* = \hbar^2/(2td^2)$, this results in a prediction of $\hbar/(\tau_t t) = S/2\pi N$. This comparison is shown in Fig. 3.7. The prediction with no free parameters clearly disagrees with the data, but if one permits one overall scaling factor of order unity it can be quite consistent. As this argument ignores prefactors, this is the most one could reasonably hope for. However, more interesting than the comparison itself is its implications for future measurements: because of our harmonic trap, and the resulting modification to the density of states, this theory predicts a non-linear scaling of $1/\tau_t$ with temperature. Therefore, a refinement of our technique, with small enough error to make an unambiguous determination of the linearity of τ_t with temperature, might be able to distinguish convincingly between this and other theories of T -linear resistivity.

3.4.4 Others: Marginal Fermi Liquids, Unparticle Phenomenology, Hidden Fermi Liquid

I will mention three other theories of strange metals for completeness. The Marginal Fermi Liquid theory, mainly associated with Varma [125], represents an early attempt to find a unified phenomenological framework for (primarily) strange metals. It unifies ARPES measurements of the spectral function with transport measurements to provide a form of the spectral function that gives the correct scalings for these behaviors, while also predicting other observables. We first attempted to interpret our measurements using this framework, but we found that because it is phenomenological it was difficult to tell unambiguously how to adapt it for the differences between our system and metals. The utility of this theory is more in suggesting what the effective excitations of the strange metal might be, which a more complete theory could try to derive.

Unparticle theory, associated with Phillips, attempts to describe a strange metal as a system in which the effective excitations are, instead of Fermi liquid quasiparticles, “unparticles” with a continuously varying mass [102]. This gives rise to incoherent, non-quasiparticle behavior that may be a suitable starting point for a description of strongly interacting quantum liquids. This is similar to Marginal Fermi liquid theory in that it attempts to find a consistent phenomenological framework to describe many observations of strange metals. However, studies using this framework, to date, have focused on observables besides the DC resistivity.

Finally, Hidden Fermi liquid theory, due to Anderson, uses a technique based on Gutzwiller projection to determine the effective excitations for a doped Mott insulator and predicts that they are a sort of quasiparticle that, unlike the Fermi liquid quasiparticle, has zero overlap with the bare electrons [126]. The prediction for metals is that the resistivity is determined by two decays: first, the coupling to the electric field excites quasiparticles that do overlap with the physical electrons, as in a Fermi liquid quasiparticle, but since these are not approximate eigenstates of the system they quickly decay into the excitations of the hidden Fermi liquid. These hidden Fermi liquid “pseudoparticles” are not adiabatically connected to the physical electrons but otherwise behave as a Fermi liquid, and in particular have a momentum relaxation rate that goes as T^2 . The total relaxation time is determined by the sum of these two decay processes, and either can serve as a bottleneck. The result is that the momentum relaxation rate from a conductivity measurement is

$$\frac{1}{\tau_t} = \left(\frac{\hbar}{p\pi T} + \frac{2\hbar W_{HFL}}{T^2} \right)^{-1}, \quad (3.11)$$

leading to T -linear scaling at high temperature. Here W_{HFL} is the bandwidth of the hidden Fermi liquid, which is not directly observable but can be inferred from ARPES measurements, and p is, for materials, a function of the hole doping x away from half-filling: $p = (1 - x)^2/4$.

An interesting question that arises when considering this theory is how, in our case, the physical impulse couples to the fundamental excitations of the system. An electrical field clearly couples to eigenstates of electric charge, regardless of whether these are the fundamental excitations of the system, but we instead use a Raman transition. Because we start with a non-interacting Fermi gas, the eigenstates of the system at this point, as mentioned in Sec. 3.3.3, are very well understood. In a uniform system they would be the quasimomentum states of a free Fermi gas in a lattice, while the addition of our trap results in a modification from this that can be analytically determined [54]. Furthermore, because our atoms are all initially in the same spin state, if each experiences the same Raman pulse with the same effect then they remain spin-polarized (with a spin that is now tilted in a Bloch sphere representation), and thus non-interacting, immediately after the Raman transition. Interactions can only have an effect once there is some decoherence, so that the system can be considered as a statistical mixture of $|\uparrow\rangle$ and $|\downarrow\rangle$ atoms rather than each atom as an identical superposition between these states. In practice, this decoherence appears to happen fast enough that we can neglect this consideration. We have measured the decoherence rate in the absence of a lattice, using a Ramsey sequence, and found it to be around $100 \mu\text{s}$. Summarizing, we should expect that the evolution of our system proceeds something like this: first, the atoms are all in an equal superposition of spins, and a corresponding superposition between the quasimomentum states of a equilibrium non-interacting Fermi gas and the states shifted by the Raman kick $|\vec{\Delta p}\rangle$. After a short time, this superposition dephases into a statistical mixture of atoms in $|\uparrow\rangle$ and atoms in $|\downarrow\rangle$, each still in spatial eigenstates that correspond to the non-interacting gas. Finally, the strong interactions cause these states to evolve in some way away from the non-interacting states of definite quasimomentum, and the coupling to the lattice finally dissipates away the momentum through Umklapp scattering. In the limit in which the initial decoherence is fast enough to be ignored, this is exactly analogous to the decay into hidden Fermi liquid states postulated by this theory.

Having satisfied ourselves on that point, we can estimate the prediction this model gives for our system by taking $x = (1 - n)$ and $W_{HFL} \approx t$, the order of magnitude suggested by the authors of Ref. [126]. This leads to a predicted relaxation rate that is strongly density-dependent, and which decreases with increasing temperature—in contrast to our measurements. However, it would be very interesting to see a full application of this theory to ultracold Fermi gases.

3.4.5 Comment on the Bakr Group Result

While our ultracold atomic bad metal was very different from every previous type, it has a contemporary counterpart, from the group of Waseem Bakr [59]. This study employs a similar system (in 2D rather than

3D) and explores a similar parameter range to our own. The measurement method is somewhat different. Rather than creating a momentum current, the authors watch the relaxation of a non-equilibrium density pattern, and extract from this a diffusion constant which can be related, when combined with a separately measured compressibility, to resistivity through the Nernst-Einstein equation. This allows for a direct, albeit unconventional, determination of the resistivity, in contrast to our calculation from a quasiparticle framework. The momentum relaxation rate also comes out of their fit, but it is a somewhat auxiliary quantity in contrast to our measurement in which it is the main observable of interest. Two more minor differences are that we, unlike them, measured the scaling of the relaxation with interaction as well as temperature, making for a nice additional comparison to theory, but they, unlike us, were able to simplify their system considerably by engineering a flat potential and thus a region of constant density near half-filling.

The authors compare their results to numerical methods (DMFT and finite temperature Lanczos calculations), and find reasonable agreement. While they do not explicitly compare to any other theories, the inverse momentum relaxation rate they extract from their data does not appear to follow the Planckian scaling $1/\tau_t = T/\hbar$, falling below this at high temperatures, while the resistivity slope is consistent with my conjecture for the scaling of τ_{res} in Sec. 3.4.2. Therefore, the general picture painted by our results and theirs seem to be consistent with each other.

3.5 Outlook

I believe that the study of bad metallic behavior in ultracold atomic systems is an exciting frontier that still has a lot of unanswered questions. It would be very interesting to characterize this system across the expected interaction-driven good metal to bad metal transition, which should be possible by pushing the lower limits of temperature and tuning the interactions with a Feshbach resonance. Measurement of static properties, such as the density of states revealed by RF spectroscopy [127] or the spectral function with momentum resolution [128, 129], could be a nice point of comparison with numerical techniques such as DMFT. Techniques for measuring the AC conductivity of an ultracold gas, previously applied to the weak-scattering regime [130], could enable observation of the expected spectral transfer accompanying low DC conductivity. Finally, measurement of relaxation or transport of other quantities, such as heat or spin, might also be illuminating. A recent experiment looking at spin transport in strongly-correlated lattice fermions represents a step in this direction [58]. Heat transport measurements might be especially interesting, because they could be combined with our momentum relaxation technique to look for violation of the neutral equivalent of the Wiedemann-Franz law. This is predicted by various theories (for example, in Ref. [77]), and has been reported in a

unitary Fermi gas without a lattice [76], but is unstudied as of yet in an ultracold Fermi-Hubbard system. As experiments develop, it will also be exciting to see careful applications of the various theoretical frameworks described above to these systems, rather than the crude ones I have attempted.

One organizing question for these possible experiments goes back to the distinction previously drawn between a bad and strange metal. Now that we have evidence that bad metal behavior is possible in a Fermi-Hubbard system, can it also realize strange metal behavior such as power law scaling of AC conductivity? Understanding the relationship between these two sets of behavior in a simple Hubbard system, which does not have complications such as structural transitions, might help to clarify the exact relationship between these two phenomena. It will also be a big step towards answering a key question driving studies of the Hubbard model: whether it is a suitable minimal model for high- T_c superconductors such as the cuprates [4, 131].

Chapter 4

Signatures of Mott and Anderson Transitions Far from Equilibrium

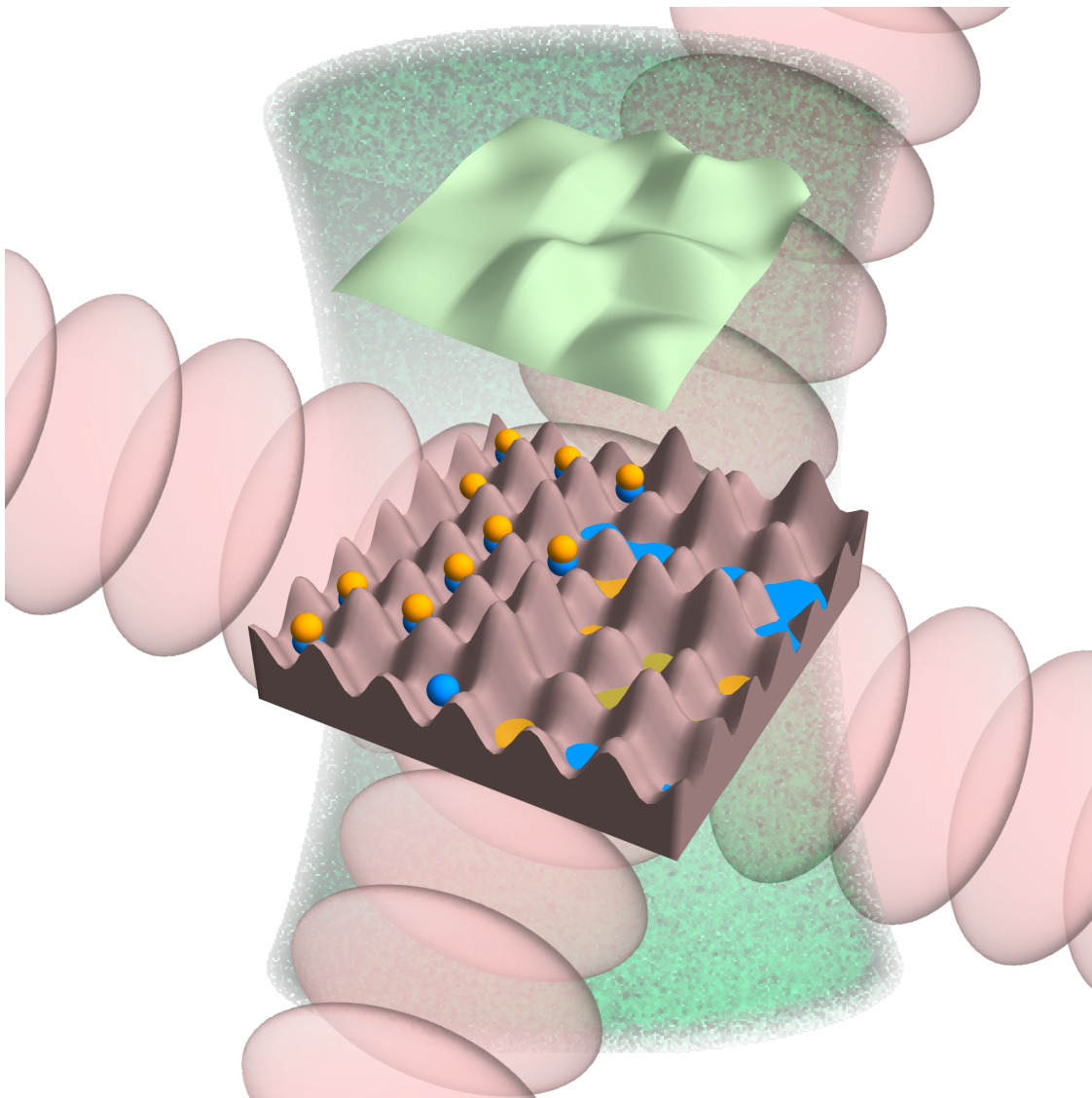


Figure 4.1: Experimental setup. For clarity, a lower-dimensional representation of our 3D lattice is shown. Lattice beams (red, diagonal) are combined with a speckle beam (green, vertical) to create a disordered lattice potential. Depending on the system parameters, a non-equilibrium population of doublons may persist due to localization, or delocalization may cause a fast equilibration of the doublon population.

4.1 Introduction

Questions about the nature of many-body quantum systems with interparticle interactions and disorder go to the heart of condensed matter physics. Beginning with a system of weakly-interacting fermions in a periodic potential, which populate delocalized Bloch wave states, it is well understood that sufficiently strong repulsive interactions or disorder can each result in a quantum phase transition to localized states, which cause metal–insulator transitions of the linear-response properties such as DC conductivity [8]. These metal–insulator transitions due to interactions or disorder are respectively termed a Mott transition [6, 7, 132] and an Anderson transition [9, 12, 13, 133], and they individually represent paradigmatic examples of strongly correlated and strongly disordered systems. What happens when both effects are large, as in an initial Mott insulator that is subjected to increasing disorder?

The measurements described in this chapter address one aspect of this question. We study the dynamics of perturbed fermions realizing the disordered Fermi-Hubbard model (DFHM), a paradigmatic model for disordered many-body systems. Applying a quench of the interactions, we take the system far out of equilibrium and study the relaxation in a regime in which the linear-response formalism no longer applies. The observable we study, the population of double occupancies (doublons), is attuned to be highly sensitive to both the interactions and disorder, revealing the competition between their effects. In regions with individually strong interactions and disorder, we see each result in a persistent non-equilibrium doublon population, while in a crossover region featuring both influences the population can quickly equilibrate. Finally, we provide a qualitative explanation for the observed behavior by considering the predicted changes in the density of states associated with the Mott and Anderson transitions.

4.2 Background: Anderson and Mott Transitions

4.2.1 Anderson Localization Transitions

A non-interacting wave system, when subjected to disorder, can undergo a disorder-driven phase transition, known as *Anderson localization*. Below the critical disorder, states are extended, and resemble plane waves (or Bloch waves if a lattice is present), with slight modifications due to isolated scattering from the disorder that has a characteristic length scale of l_s , the mean free path. Above the critical disorder, they are localized, with an exponential overall envelope $e^{-x/\xi}$ that has a characteristic localization length, ξ [Fig. 4.2]. If the waves in question are electrons, and the states at the Fermi surface become localized, this results in a metal–insulator transition. However, Anderson localization is more clearly seen in non-interacting or weakly

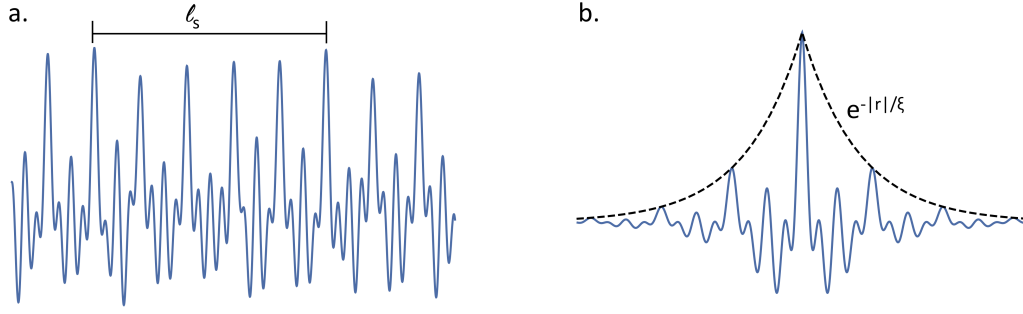


Figure 4.2: Anderson localization. a) In a lattice with weak disorder, the non-interacting eigenstates may be modified from periodic Bloch waves on the scattering length scale l_s without losing their extended character. b) In sufficiently strong disorder, the eigenstates will become exponentially localized with localization length ξ .

interacting wave media, such as light [15], ultrasound [14], and, of course, ultracold atoms [134–136].

Anderson localization can intuitively be thought of as the result of a coherent random walk resulting from scattering. Provided that this random walk is in a time reversal-invariant environment with static disorder, the amplitude for paths staying near the origin will constructively interfere while those propagating away will be reduced. Like a classical random walk, this makes Anderson localization highly dependent on the dimensionality of the system. In a classical random walk, the probability of returning to the origin approaches unity as the number of steps increases for $d \leq 2$, but for $d > 2$ it is finite, as shown originally by Polya [137]. Correspondingly, one-dimensional disordered quantum systems become localized at infinitesimal uncorrelated disorder. In contrast, in three dimensions for a given disorder strength there are states that are localized by the disorder and those that are not, separated by a *mobility edge*. Two dimensions is marginal, and an important advance in the understanding of Anderson localization was the “Gang of Four” scaling argument that two dimensional systems should be localized by any disorder, as in the one-dimensional case, but with a localization length that grows very rapidly with energy [10, 138].

Anderson localization does not leave any experimental signature in the density of states for a large system. However, in a disordered system a more meaningful quantity is the local density of states (LDOS), defined (at zero temperature) as $\rho(E, x) = \sum_n |\langle \Phi_0 | [\hat{c}(x) + \hat{c}^\dagger(x)] | \Phi_n \rangle|^2 \delta(E - E_n + E_0)$, where Φ_n is the quantum state with energy E_n , $E_0 = E_F$, and $\hat{c}(x)$ is the fermionic destruction operator at position x [106]. The LDOS changes at the mobility edge from being continuous to pointlike discrete [Fig. 4.3]. Correspondingly, the Green’s function for the system changes from having a branch cut to dense discrete poles [17]. Detailed calculations for localization due to correlated speckle disorder, performed by the group of S. Pilati, predict

that for the disorder used in our experiment complete localization of the ground band should take place around $\Delta/12t = 2$, where Δ is the characteristic disorder strength and $12t$ is the 3D bandwidth [139].

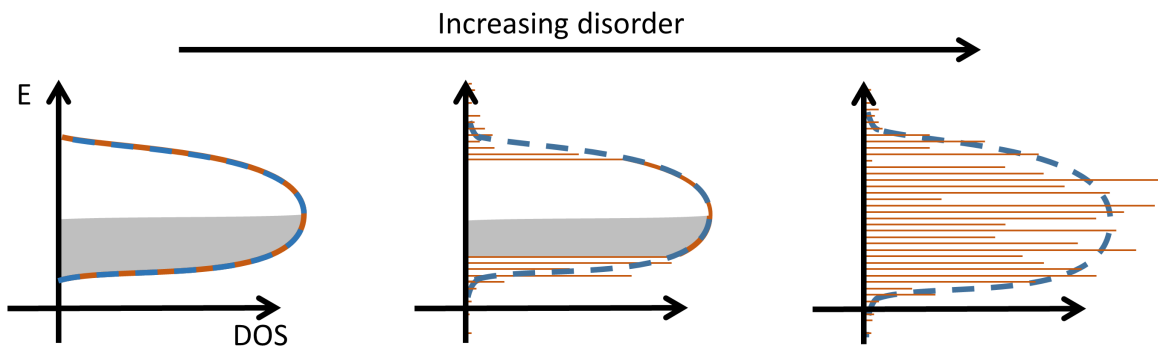


Figure 4.3: Cartoon of the density of states in the Anderson transition for the Hubbard model in 3D, showing a typical local density of states (orange solid lines) and average density of states (blue dashed lines). At low disorder, the local and average densities of states coincide, and the states form a band that is filled up to the Fermi level. As disorder increases, states near the edges of the band become localized, resulting in two mobility edges near the top and bottom of the band that separate the continuous region of the LDOS from the discrete region. The averaged density of states does not show a sharp change. At a critical disorder all the states in the band become localized.

4.2.2 Mott Transitions

A strongly interacting lattice system also has a localization transition, a *Mott transition*. This transition occurs when short-range repulsive interactions are sufficiently strong that it is energetically favorable for particles to become localized, and pay the increase in kinetic energy rather than overlapping. Unlike an Anderson transition, this is a transition between two ergodic phases. The Mott transition also features an obvious change in the density of states, which in the simplest case such as the Hubbard model splits into two sub-bands, with the upper band corresponding to double occupancies [Fig. 4.4]. This justifies the terminology “doublon:” double occupancies make up a distinct sector of quasiparticle-like excitations in this regime.

The Mott transition only occurs for an integer number of particles per site, and it is only in that special case that the picture presented above is valid. For other densities, there is no sharp transition but instead a crossover to a gapless, strongly-correlated *doped Mott insulator*. This state, which is not fully understood, is of high interest as the possible model for high-temperature superconductors [4], and as an environment in which the bad and strange metals discussed in Ch. 3 are realized.

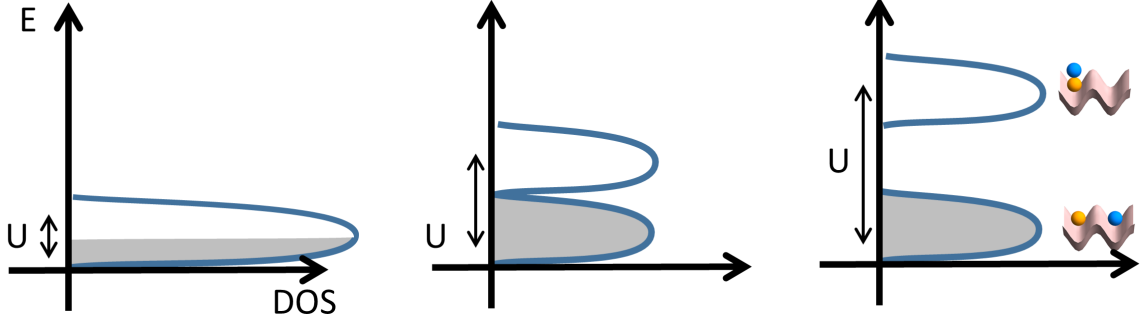


Figure 4.4: Cartoon of the density of states in the Mott transition for the Hubbard model. In the non-interacting limit, the states form a single band, and for two spin states and $\langle n \rangle = 1$ the Fermi level is at the midpoint of the band. As interactions increase they split the band into two Hubbard bands, consisting of states with single and double occupancies and separated by U , the interaction strength. The system becomes a gapped insulator. Although the real picture is more complicated, and can involve deformations of the Hubbard bands and hybridization between them near the transition, the general features of this cartoon are consistent with calculations of the transition [6, 16, 112].

4.2.3 The Anderson-Mott Crossover and Many-Body Localization

The effect of interactions on Anderson localization was left as an open problem in Anderson’s original paper, and it remained so for decades afterward. Increasingly sophisticated simulations lead to predictions that interactions could either increase or decrease the conductivity of disordered fermions. This is because, depending on the ratio of disorder and interaction strengths, they could either weaken Anderson localization effects or cause Mott localization [16, 140–143]. However, these calculations did not address the problem in full generality, usually being limited to some combination of idealized models, limited dimensionalities, perturbative interactions, and either near-ground state behavior or a high-temperature expansion. Experimental study of this problem in a condensed matter setting without any complicating factors is also challenging. Notable experiments in this arena include controversial reports of a localization transition in two-dimensional materials, in tension with the scaling theory for non-interacting Anderson localization [144], and limited observations of disorder-induced Mott gap breaking [145, 146].

Among the predictions of near ground state behavior I will highlight one with special applicability to our experiments: the calculation of the phase diagram of the Hubbard model with speckle disorder performed by the group of W. Hofstetter [17], already introduced in Ch. 1 [Fig. 1.2]. The ground state at half-filling ($\langle n_i \rangle = 1$) in this calculation features a metal-Mott insulator transition at critical interaction strength $U/12t = 1.4$, a metal-Anderson insulator transition at $\Delta/12t = 2.7$, and a complex interplay of these three phases in regions where U and Δ are both nonzero. The states are classified based on the average LDOS at the Fermi level: for the Mott insulator it is gapped when arithmetically averaged, for the Anderson-Mott insulator it is not gapped when arithmetically averaged but is gapped when geometrically averaged, and

for the metal it is gapless. The technique used, statistical dynamical mean field theory (DMFT), is exact for $d \rightarrow \infty$ but is believed to be accurate for $d = 3$ above the Néel temperature. The phase diagram 1.2 is specifically relevant for speckle disorder—other types of disorder statistics result in a different phase diagram topology [16]. While this phase diagram provides a valuable road map, it is largely unconfirmed experimentally.

New life was breathed into this venerable subject beginning in 2006 with the development of the theory of *many-body localization* [147, 148]. While a clear understanding of this phenomenon is still limited to particular models and low dimensions, it has exposed some features that seem to be generally applicable. We now know that, in certain idealized models such as 1D spin chains or localized systems with weak interactions, Anderson-like localization can persist with interactions, not only near the ground state but for a generic excited state (and, in some models with bounded spectra, even at infinite temperature). Furthermore, within these tractable models, we know something about the structure of these many-body localized states. An Anderson localized state has an extensive number of local conserved quantities, which are the occupations of the localized eigenstates. In fully localized 1D systems with interactions this characteristic is preserved: the local quantities are modified by interactions but persist [149, 150]. As a result, these MBL state can be thought of as a generic integrable system, unlike typical integrable systems which require fine-tuned parameters. However, it is unclear at present whether this is still a valid picture in higher dimensions [151]. Interactions also have the consequence that the MBL state, unlike an Anderson localized state, is not a product state of single-particle wavefunctions, but instead features entanglement. However, each particle is mostly entangled with those nearby; for an initial product state entanglement spreads logarithmically away from a given site and the eigenstates only have area-law entanglement entropy, unlike the volume-law entanglement entropy of an ergodic thermal system [148].

Many questions related to many-body localization are still quite open. A brief list: whether MBL can occur in translationally invariant systems, the dependence of MBL on dimensionality, the precise behavior at the MBL transition, and the robustness of MBL states to dissipation, thermal baths, or loss. Since every true system exhibits these properties, the real-world existence of many-body localization is still up for debate. Therefore, experiments have a very important role to play.

4.2.4 Previous Experiments with Ultracold Atoms

The potential for ultracold atoms in optical lattices to study interactions and disorder was quickly recognized, and a number of studies of this type have already been performed. One series of experiments has studied the relaxation of fermions in quasi-disorder generated by incommensurate optical lattices [152–155]. These

experiments were argued to show evidence of many-body localization because of the persistence for many tunneling times, in sufficient disorder, of the initial non-equilibrium density distribution. Additionally, a previous study by our group has examined the interplay of interactions and disorder with fermions in a three-dimensional lattice with speckle disorder [156]. This study, which was limited to interactions too weak to form a Mott insulator, measured the response to an impulse of a DFH system. In general agreement with the phase diagram of Fig. 1.2, a localization transition was seen requiring stronger disorder with increasing $U/12t$. Furthermore, the response in the localized state was shown to be consistent with zero over an extended temperature range. This is also in general agreement with the MBL paradigm, but note that we don't have a concrete prediction for this model, and questions such as whether it features a many-body mobility edge in analogy to the Anderson localization limit are unknown. An alternative, possibly complementary picture is provided by the localization of renormalized Hubbard band quasiparticles, and remarkably a model of this type was used to find agreement with experiment without any free parameters [35].

For completeness, I note that another extensive series of experiments has investigated the properties of interacting bosons in disordered lattices. A full survey of these is beyond our scope, but they include experiments near equilibrium in one-dimensional quasi-disorder [157–159], one-dimensional impurity disorder [160], and three dimensional speckle disorder [34, 161]; and far from equilibrium to investigate many-body localization [162, 163]. At zero temperature the bosonic case differs from fermions because of the possibilities of superfluid order and a Bose glass [164]. However, for strong interactions and finite temperatures it is likely that the physics does not depend strongly on statistics. Some evidence for this comes from calculations of doublon lifetime in the absence of disorder which compare bosonic and fermionic contributions [165].

4.3 Doublon Decay

4.3.1 The Non-Equilibrium Frontier

Metal–insulator transitions, such as Mott and Anderson transitions, are formulated within a linear response framework. A small force (or DC voltage for electronic materials) is applied to the equilibrium system, and classification as a metal or insulator is determined by whether it responds to this perturbation. While classification of systems near equilibrium based on transport measurements has a long history, the isolation and slow characteristic dynamics of ultracold atomic systems have allowed the increasing exploration of far-from-equilibrium systems, for which the organizing principles are much less clear [166–170].

We know that in the DFHM the interplay between disorder, interactions, and tunneling gives rise to

interesting ground-state transitions and linear-response behavior. What happens to far-from-equilibrium systems in this regime? Can interesting transitions still occur?

We will give an answer to this by looking at the relaxation of a non-equilibrium population of doublons.

4.3.2 Understanding Doublon Decay

There are many ways one could conceivably take a gas of ultracold atoms out of equilibrium, but in the context of a strongly-correlated lattice gas exciting doublons is a particularly natural choice. As we saw in Sec. 4.2.2, doublons are the fundamental excitation of a Mott insulator, and in a doped Mott insulator they still make up a distinct high-energy sector. In addition, we know something about doublon relaxation in the absence of disorder. This process was studied previously in a joint theory–experiment collaboration, with the experiment performed by the Esslinger group [165, 171]. For strong interactions, and in the absence of disorder, a non-equilibrium population of doublons is highly stable due to the scarcity of energy-conserving decay processes. The Mott gap in the density of states prevents a two-body decay that conserves energy, and higher-order processes become necessary for a finite decay, leading to a doublon lifetime scaling of

$$\tau \sim \frac{t}{\hbar} e^{\alpha U/12t} \quad (4.1)$$

where α is scaling parameter that depends on parameters such as density. This scaling has also been predicted in other theoretical studies [172–174]. Doublon decay can also be observed in condensed matter systems using ultrafast pump-probe spectroscopy [175]

Because a Mott gap can stabilize doublons, they are a great way to look for the effect of disorder on the system. We saw (in Fig. 1.2) that in the ground state, sufficient disorder can destroy the Mott insulator by redistributing states into the gap. The clean doublon decay results suggest that this will also have an effect on the doublon lifetime.

4.4 Experimental Setup

To probe doublon relaxation, we use an interaction quench to take the system out of equilibrium [Fig. 4.5]. Interaction quenches to create out-of-equilibrium doublons have been previously considered in theoretical and numerical studies [176–178] and were experimentally performed in a Bose-Hubbard system [179]. By quenching from attractive to repulsive interactions, we create an unstable population of doublons. Then, after a variable hold, we use the Feshbach resonance to read out the doublon population by spectroscopically resolving them from single sites.

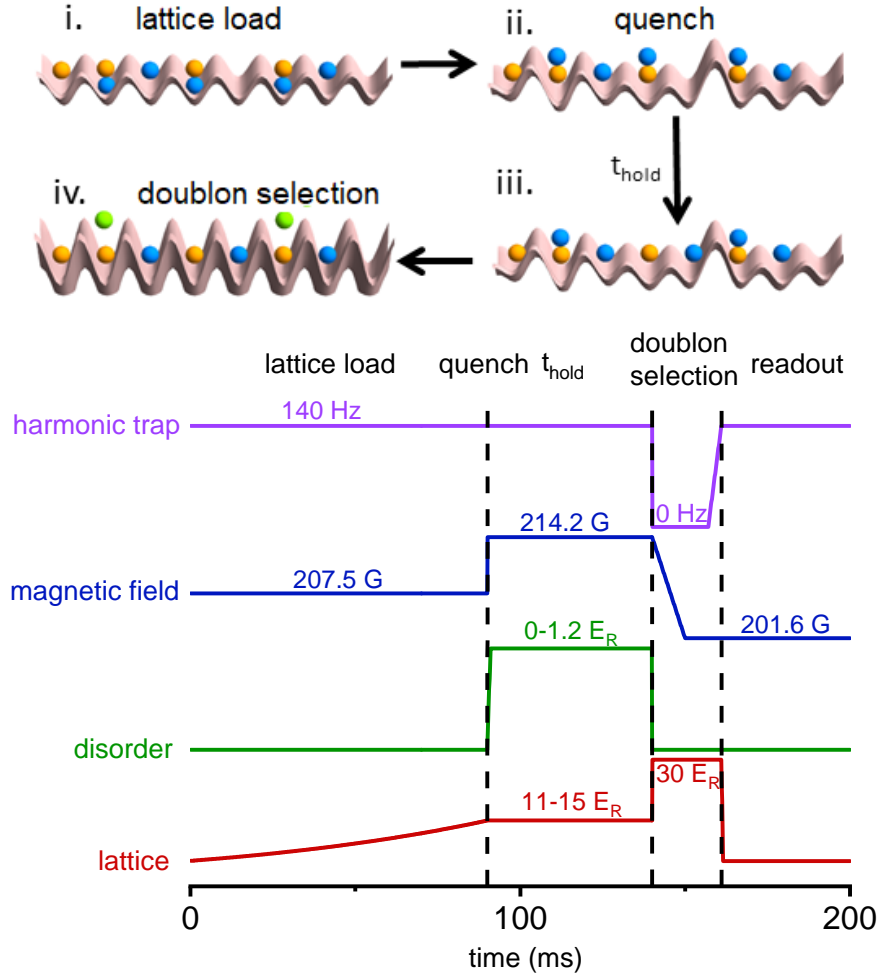


Figure 4.5: Experimental procedure. Top: i: Two fermionic spin states are initialized in an optical lattice with attractive interactions, so that doublons are energetically favorable. ii: An interaction quench takes the system out of equilibrium by changing the sign of the interactions, and a disordered potential is added. iii: After a variable evolution time t_{hold} , part of the doublon population has decayed. iv: The site populations are frozen by a sudden increase of the lattice, and one atom in each doublon is selectively mapped to an ancillary spin state that is subsequently imaged. Alternatively, the single occupancies of one spin can instead be imaged (not shown). Bottom: traces of signals corresponding to procedure. These traces represent the control signals, and neglect the effects of finite servo bandwidth and eddy currents in the magnetic field. To avoid reductions in the doublon lifetime near the Feshbach resonance due to the dipole laser, as discussed in Chapter 2, it is turned off during the doublon selection stage. The readout procedure involves a series of resonant light pulses and rf sweeps, which remove all atoms except those in the ancillary spin state and then image those on a closed transition. This is shown in detail in see Fig. 4.6.

4.4.1 Initial Conditions

Our initial trapping and cooling follows the procedures described in Ch. 2. Before the measurement, we have $N = (110 \pm 21) \times 10^3$ atoms at $T/T_F = (0.43 \pm 0.09)$ in an equal mixture of $|9/2, -9/2\rangle$ and $|9/2, -7/2\rangle$. We are capable of evaporating further and reducing T/T_F by another factor of 2–3, but experimentally

we have found that the largest signal and best long-term stability for our measurement is in this regime. These atoms are held in a trap made from a crossed far-detuned 1064 nm laser, with trapping frequencies $\omega_{x,y,z} = 2\pi \times (49, 103, 112)$ Hz. The magnetic field is above the Feshbach resonance, so that the atoms have weakly attractive interactions ($a = -41.1 a_0$).

4.4.2 Lattice Load

We begin the experimental procedure by slowly loading the atoms into a 3D cubic optical lattice with a lattice depth $s = 11\text{--}15 E_R$. For this interaction strength, and taking into account the typical geometric average harmonic confinement (including contributions from the lattice) $\omega = 2\pi \cdot 140$ Hz and entropy per particle $S/N = 3.8$, the initial state of the system has $(15 \pm 3)\%$ of the atoms in doubly-occupied sites, in reasonable agreement with an equilibrium atomic limit calculation. The average filling at the center of the system is calculated as $\langle n_i \rangle = 0.48$, or near quarter-filling, which smoothly decreases toward zero away from the center due to the harmonic confinement.

4.4.3 Interaction Quench and t_{hold}

At this point the interaction quench is performed. The system is taken out of equilibrium by an abrupt change of the interaction strength from attractive to repulsive ($a_s = 75.3 a_0$), realized with an increase of the magnetic field by 7 G over 100 μs . This results in values of $U/12t$ between 1.2 and 4.2. Immediately after the interaction quench, variable disorder is added over 1 ms, with a strength ranging from 0 to 1.2 E_R . These timescales are chosen to make the changes adiabatic relative to the band gap, but fast compared to the doublon decay rate in the absence of disorder.

Our disordered speckle field is generated with a tightly-focused 532 nm laser passed through a holographic diffuser, which results in autocorrelation lengths of $\zeta_r = 270$ nm and $\zeta_z = 1600$ nm along the directions perpendicular and parallel to its propagation, respectively [135]. The disordered beam is not oriented along any of the lattice directions and has a nearly equal projection along all three.

The Hamiltonian after the quench is the disordered (repulsive) Fermi-Hubbard Hamiltonian with confinement:

$$H = \sum_{\langle i,j \rangle, \sigma} \left(-t_{ij} \hat{c}_{j\sigma}^\dagger c_{i\sigma} + h.c. \right) + \sum_i U_i n_{i\downarrow} n_{i\uparrow} + \sum_{i,\sigma} \left(\epsilon_i + \frac{1}{2} m \omega^2 r_i^2 \right) n_{i\sigma} .$$

Here σ indexes the two spin states ($|\uparrow\rangle = |9/2, -9/2\rangle$, $|\downarrow\rangle = |9/2, -7/2\rangle$), t_{ij} controls hopping between nearest-neighbor sites i and j , and U_i is the on-site interaction energy between particles of different spin.

Two terms contribute to the local energy offset: a disordered on-site energy controlled by ϵ_i , and an overall harmonic confinement term with frequency ω . The speckle field results in disorder in each of the t , U , and ϵ terms with known distributions and correlations [31, 33]. For simplicity, we have assumed a spherically symmetric overall confinement with the geometric mean trapping frequency

To adjust the Hubbard parameters, we fix the magnetic field values across all data and tune the ratio U/t by changing the lattice depth, while the disorder strength is controlled by the speckle field. This ensures that, for a given lattice depth, we are preparing exactly the same average initial state each time and performing the same interaction quench, and any differences in evolution are due to the changing parameters following the quench. This procedure is also designed to minimize overall forces on the atoms while still producing a large enough quench that the change in doublon population can be readily monitored. One compromise is that changes in the doublon decay between different lattice depths may potentially combine the effects of lattice depth on both the initial and final states.

4.4.4 Doublon Selection and Readout

After a variable hold time t_{hold} , we perform the doublon selection and readout [Fig. 4.6]. We quickly ramp the lattice to $30 E_R$ to freeze the density distribution, and turn off the speckle field. Then we read out the doublon population by ramping the magnetic field over the Feshbach resonance to associate doublons into Feshbach molecules [180], which have a binding energy of $h \cdot 110$ kHz and are thus spectroscopically resolved from the single occupancies. We apply a radiofrequency (rf) pulse to transfer the $|\downarrow\rangle$ atom in each doublon to an adjacent unpopulated spin state, $|9/2, -5/2\rangle$, and selectively image only those atoms. To do this, we use a combination of light pulses resonant with the ${}^2S_{1/2}|9/2, -9/2\rangle \rightarrow {}^2P_{3/2}|11/2, -11/2\rangle$ imaging transition and radio-frequency sweeps to remove all the atoms remaining in $|9/2, -9/2\rangle$ and $|9/2, -7/2\rangle$, before transferring the atoms in $|9/2, -5/2\rangle$ back to $|9/2, -9/2\rangle$ and imaging them on the same transition. Alternatively, by only changing the rf frequency, we can image the $|\downarrow\rangle$ atoms in single sites instead of doublons. By comparing these populations as doublons decay into singles, we estimate that about 50% of the doublons are imaged, with the rest lost due to either the reduced Rabi rate for dissociation of molecules relative to singles or decay into more tightly bound molecular states (see Fig. 4.7).

Repeating this procedure while varying t_{hold} , we build up a plot of the time dependence of the doublon (and possibly single occupancy) population [Fig. 4.7]. To extract useful information, we fit these curves to a minimal model.

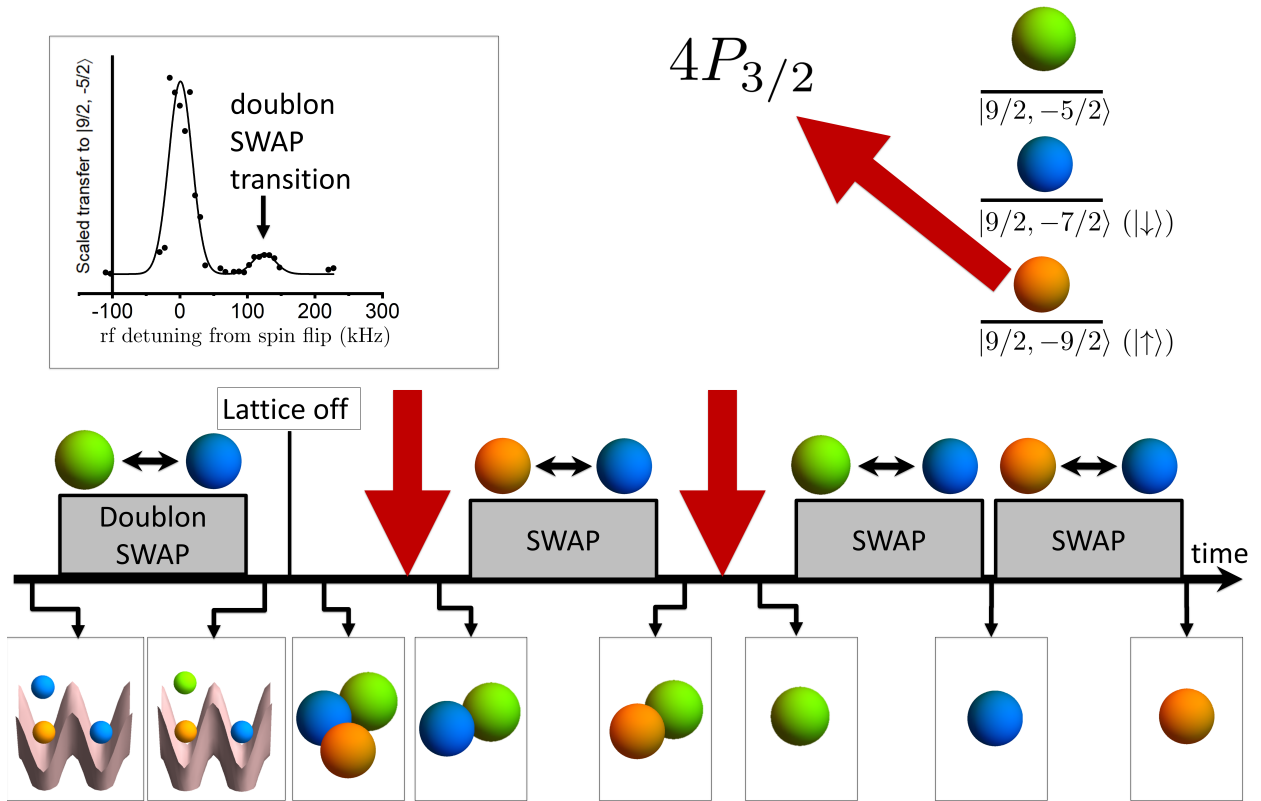


Figure 4.6: Details of the doublon readout procedure. We initially use a doublon-selective rf swap in the lattice to selectively map each $|9/2, -7/2\rangle$ atom in a doublon to spin $|9/2, -5/2\rangle$, with a transition that is 125 kHz detuned from the main transition due to the Feshbach molecule binding energy. Following this, we turn off the lattice and use a series of light pulses resonant only with $|9/2, -9/2\rangle$ and rf swaps to remove all the atoms except the ones that were transferred to $|9/2, -5/2\rangle$. Finally, we transfer these atoms with two swaps to $|9/2, -9/2\rangle$ for imaging on a closed cycling transition. By changing the rf frequency of the initial swap, we can instead selectively image the single atoms instead of the doublons. This procedure was inspired by readout sequences used in past atomic photoemission measurements [46].

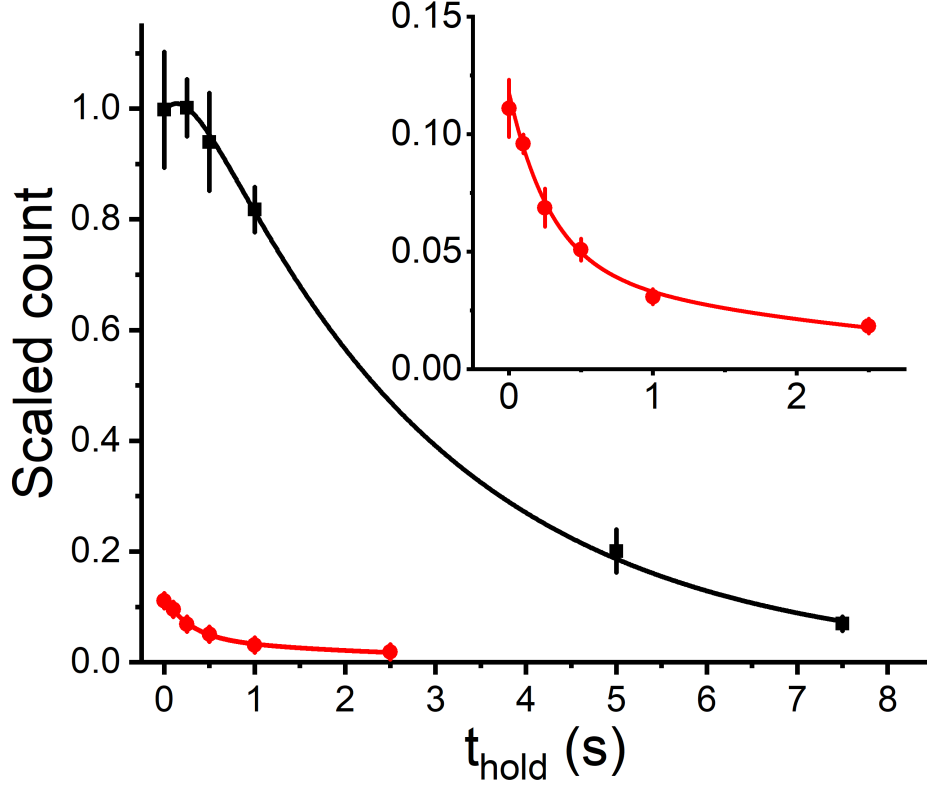


Figure 4.7: Sample doublon (red point) and single (black point) decays. Error bars are the s.e.m. of at least four measurements. Fits are to the model described in Section 4.5. The inset is a magnified look at the doublon decay. This data is taken for a 15 E_R lattice ($U/12t = 4.15$) without disorder. In these measurements, the fit value for the population of doublons as determined by the increase in singles is consistently larger than the population of doublons directly observed, by an average factor of 2.6. We attribute this to reduced efficiency in the doublon readout and use it to calibrate the absolute doublon fraction.

4.5 Model and Fitting

We extract the doublon lifetime τ using a fit to a simple rate model for the imaged $|\downarrow\rangle$ atoms that takes into account doublon decay into single atoms as well as the slower overall number loss. The model used is:

$$\dot{N}_{d\downarrow} = \dot{N}_{d\downarrow,neq} + \dot{N}_{d\downarrow,eq}, \quad (4.2)$$

$$\dot{N}_{d\downarrow,neq} = -\frac{1}{\tau}N_{d\downarrow,neq} - \frac{1}{\tau_{loss}}N_{d\downarrow,neq}, \quad (4.3)$$

$$\dot{N}_{d\downarrow,eq} = -\frac{1}{\tau_{loss}}N_{d\downarrow,eq}, \quad (4.4)$$

$$\dot{N}_{s\downarrow} = -\frac{1}{\tau_{loss}}N_{s\downarrow} + \frac{1}{\tau}N_{d\downarrow,neq}. \quad (4.5)$$

This describes a non-equilibrium population of doublons that dissociates into single atoms at a rate of $1/\tau$, an equilibrium population of doublons, and overall number loss of both doublons and singles at the same

single-particle loss rate of $1/\tau_{loss}$. It is very similar to the model used in the previous study of doublon lifetime (Ref. [171]), but without an inelastic loss term. It appears that this was only relevant when those authors used a $|9/2, -9/2\rangle$ and $|9/2, -5/2\rangle$ spin mixture, which has been found by multiple groups (including us) to have a reduced lifetime near 200 G [37, 165].

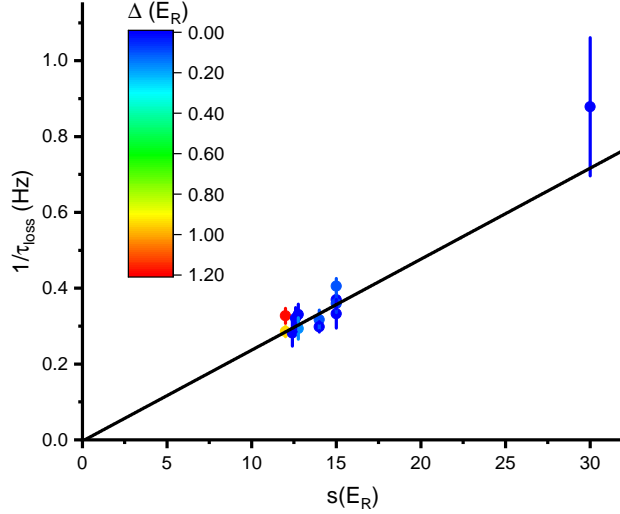


Figure 4.8: Measured loss rates at various lattice depths and disorder strengths, with linear fit. The fit slope is 0.024 ± 0.006 Hz/ E_R , with an intercept consistent with zero. We use this fit to determine the average τ_{loss} to be used for datasets in which we do not measure loss directly. The linear scaling of loss with lattice depth suggests that the dominant mechanism is off-resonant scattering.

The solution to Eqs. 4.2–4.5 is:

$$N_{d\downarrow}(t) = N_{d\downarrow,eq}(t) + N_{d\downarrow,neq}(t) = N_{d\downarrow,eq,0}e^{-t/\tau_{loss}} + N_{d\downarrow,neq,0}e^{(-t/\tau - t/\tau_{loss})} \quad (4.6)$$

$$N_{s\downarrow}(t) = N_{s\downarrow,0}e^{-t/\tau_{loss}} + N_{d\downarrow,neq,0}(e^{-t/\tau_{loss}} - e^{(-t/\tau - t/\tau_{loss})}). \quad (4.7)$$

These equations can be fit to find τ , τ_{loss} , $N_{d\downarrow,eq,0}$, $N_{d\downarrow,neq,0}$, and $N_{s\downarrow,0}$, as shown in Fig. 4.7. For the longest doublon lifetimes ($\tau > 100$ ms) we perform a simultaneous fit to the changes in the doublon and singles populations to extract all these parameters, while for the shorter lifetimes we find that the singles equation (Eq. 4.7) provides no additional constraint, so we fit the doublon population to Eq. 4.6, fixing the much slower τ_{loss} according to the value determined from the fit to all the loss data shown in Fig. 4.8. For the data in which we measure both populations, τ as determined by a fit to both equations and τ as determined by a fit to Eq. 4.6 alone are consistent within their mutual uncertainties throughout the data. For the short-time measurements, the fractional uncertainty in τ_{loss} due to the fit uncertainty is less than 4%, which leads to an additional uncertainty in the measured τ of less than 1% that has not been propagated in the error bars.

It is not obvious that the loss rate should be the same for a doublon and a single. We test this by loading into a $30 E_R$ lattice, so that elastic doublon decay is negligibly slow. In this case we see behavior best described by a simple exponential decay for both doublons and singles, with consistent time constants of (1310 ± 210) and (1040 ± 300) ms. A uniform loss rate per site was also found by the authors of Ref. [171].

4.6 τ in the Absence of Disorder

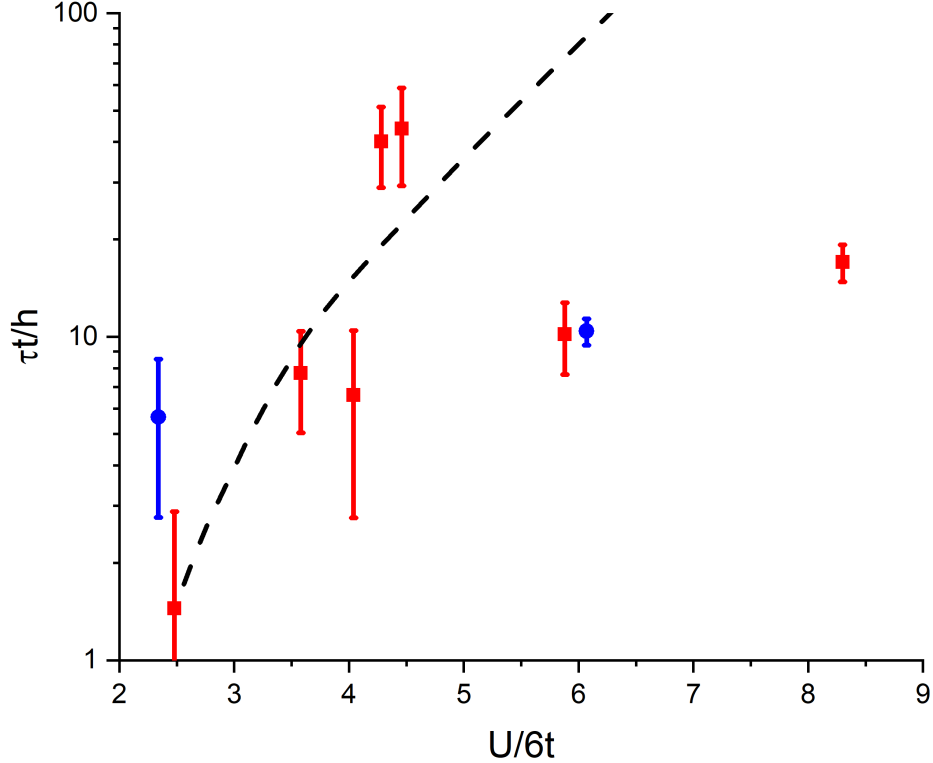


Figure 4.9: Doublon lifetimes measured without disorder, compared with the theoretical scaling at half-filling calculated in Ref. [165, 171] (dashed line). Red squares correspond to data used in the main text, with U/h ranging from 1.8–2.4 kHz, while blue circles correspond to measurements at different lattice depths and interaction strengths, such that $U/h = 2.7$ and 3.8 kHz respectively. Note that this plot uses the scalings of the interactions ($U/6t$) and lifetime ($\tau t/h$) of Ref. [171], differing by a factor of 2π and 2, respectively, from the units used in the rest of the chapter.

In the absence of disorder, the doublon population decays to a new equilibrium of $(9.0 \pm 2.5)\%$ over scales of 10–300 times the tunneling time, \hbar/t . For the lower range of interactions studied ($U/12t$ from 1.0–2.5) we observe scaling with the interaction strength that is similar to the exponential dependence found in the previous study [171], while for our largest interactions ($U/12t$ from 2.5–4.2) we observe a saturation in the observed lifetime that may be due to technical limitations.

Fig. 4.9 shows the doublon lifetimes measured without disorder. These are compared to the calculation

of doublon lifetime at half-filling reported in [165, 171]. While our results are comparable in the range $2 < U/6t < 5$, there is a clear disagreement for higher values, at which the observed lifetime is far below the predicted value. Even in absolute terms, the two final red points represent shorter lifetimes than the two points before them.

The most straightforward explanation for this disagreement is that something else is limiting our observed doublon lifetime in this stronger interaction regime. This is not surprising, because the predicted lifetimes grow extremely quickly with lattice depth, as $e^{1/t} \sim \exp(e^{\sqrt{s}})$. In real units, the predicted decay time for the point at $U/6t = 6$ is about one second, and for the highest point at $U/6t = 8.5$ it is around nine seconds, which is much longer than our loss rates. Therefore, even a very slow neglected process could limit our ability to observe the desired decay in this regime. Because we can measure both the disappearance of doublons and corresponding appearance of singles, this limiting process would have to also cause elastic decay into singles. A natural possibility is a small amount of noise on the lattice beams with a frequency near U/h . One challenge to this explanation is that measurements taken at different individual values of U and t (blue points in Fig. 4.9) appear to show that the observed lifetimes are a function of $U/6t$ and h/t rather than the individual values of the parameters.

As we will see, for the interaction strengths at which large deviations are evident, the clean value is also the slowest relaxation observed. Therefore, while it is unclear that we are always seeing the true doublon lifetime in this regime, we do not believe that this saturation affects the disordered physics of interest.

4.7 Regimes of τ in Disorder

The addition of disorder dramatically changes τ from its clean value [Fig. 4.10, left panel]. In a $12 E_R$ lattice, which has $U/h = 2.0$ kHz and $t/h = 100$ Hz, $\tau = (47 \pm 16) \hbar/t$ in the absence of disorder. For a small amount of disorder the doublon lifetime does not change, but at a critical disorder value near $0.04 E_R$ it abruptly becomes much faster, decreasing to a minimum of $(2.5 \pm 1.6) \hbar/t$ and staying near this value over an extended range of disorder values. At around $0.4 E_R$ the lifetime begins to steadily increase, and grows far beyond the initial lifetime until reaching a maximum of $(430 \pm 240) \hbar/t$ at the highest disorder strength. As such, three regimes of doublon lifetime behavior are naturally identified by the system: the initial long lifetime of the clean system, which is robust to small disorder, the short lifetime that appears at a first critical disorder value Δ_{c1} , and the continuously increasing lifetime that sets in at a second critical disorder value Δ_{c2} . Relative to the clean, non-interacting case, in which the doublon decay is of order \hbar/t , this system therefore demonstrates one regime in which the relaxation is much slower because of the strong interactions,

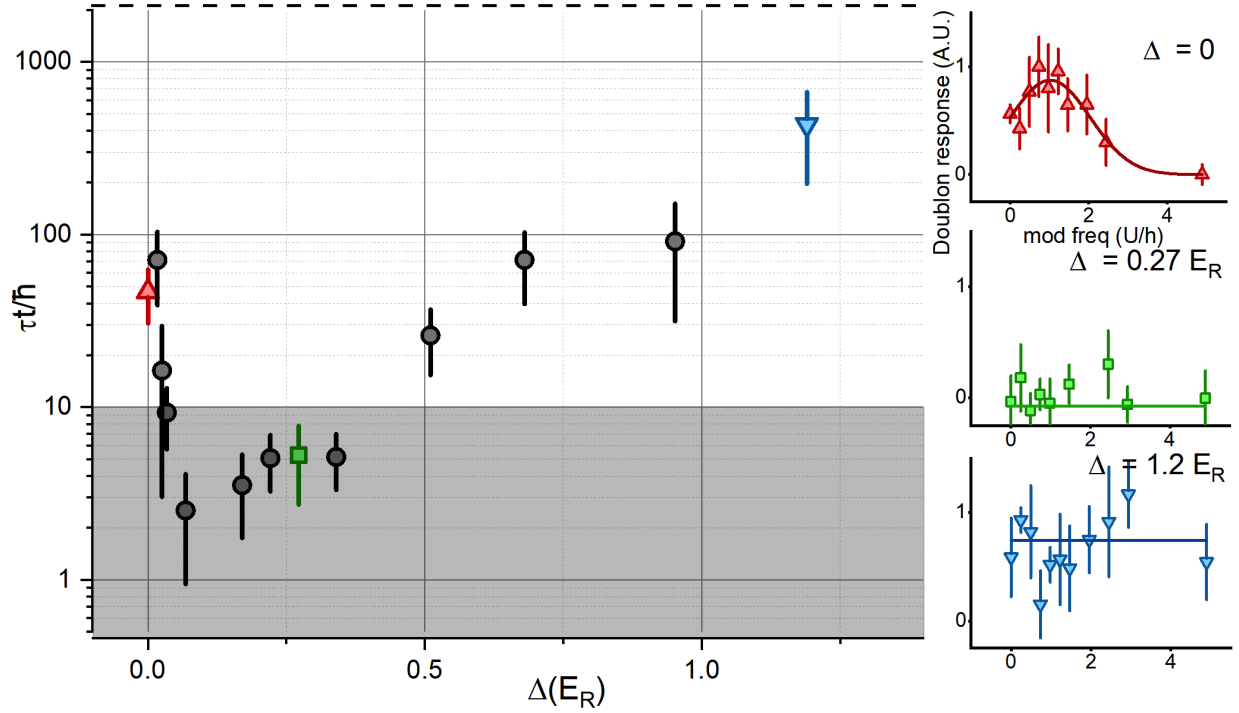


Figure 4.10: Dynamical regimes of doublon relaxation in a $12 E_R$ lattice ($U/12t = 1.8$). Left: Extracted doublon lifetimes for varied disorder. Δ is measured in units of the lattice recoil energy E_R . Error bars represent the fit uncertainty. The resulting lifetime has a strong, non-monotonic dependence on disorder and varies over two order of magnitude. The dashed line indicates the single-particle loss rate, which is nearly constant across all values of disorder. Taking $10 \hbar/t$ as a convenient dividing line separating doublons that are long-lived relative to single-particle tunneling versus those that are not (unshaded vs shaded region), three regimes can be distinguished: the initial clean behavior, an abrupt change to much smaller τ at moderate disorder ($\Delta_{c1} \sim 0.04 E_R$), and a progressively rising τ beyond a critical disorder ($\Delta_{c2} \sim 0.4 E_R$). Right: Doublon creation by lattice modulation at three disorder values, corresponding to the three lifetime regimes. The x-axis is scaled by $U/h = 2.0$ kHz, as determined by a single-band tight-binding calculation. The y-axis is a scaled response with the minimum doublon fraction subtracted, which is the same for all three figures. Error bars represent the s.e.m. from 4-6 measurements. The solid line is the fit to a Gaussian peak. In the “Mott insulator” regime a doublon creation peak centered near $f = U/h$ is evident, while in the “metallic” regime this response has vanished. In the “disordered insulator” regime a spectrally flat response is again observed, on average, which appears to have significantly more weight than in the “metallic” regime.

one regime in which it is much slower because of the strong disorder, and an intermediate regime in which the relaxation is again comparable to \hbar/t . Therefore, in analogy to the ground state phases, we call these regimes the “Mott insulator,” “metallic,” and “disordered insulator” regimes. How can we understand these changes?

4.8 A Simple Model (and Why it Doesn’t Work)

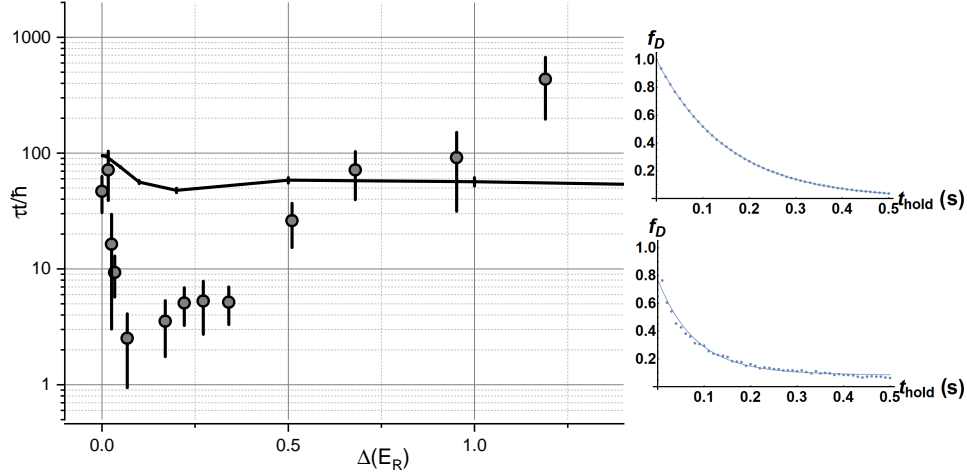


Figure 4.11: Model using an average of local doublon decays. Left: Doublon decay data compared to a model using an average of local doublon decays. The model has no free parameters. Vertical lines represent fit uncertainty. Right: sample calculated decay curves, with fits, at $s = 12E_R$ and $\Delta = 0.001E_R$ (top) and $\Delta = 0.2E_R$ (bottom). Each has been disorder averaged 1000 times. The horizontal axis is time in seconds, and the vertical axis is $N_{d\downarrow}(t)/N_{d\downarrow}(0)$.

As a simple check, the first model we will consider is one in which the observed doublon decay is a disordered average over many local decays, each obeying a different exponential time constant. We take the form as the minimal generalization of the clean decay formula:

$$N_{d\downarrow}(t)/N_{d\downarrow}(0) = e^{-t/\langle\tau_{ij}\rangle}, \quad (4.8)$$

$$\tau_{ij} = c \frac{\hbar}{t} e^{\alpha|U+\epsilon_i-\epsilon_j|/6t}. \quad (4.9)$$

Here $\epsilon_{i,j}$ are randomly drawn from the appropriate exponential disorder, $P(\epsilon_i) = (1/\Delta)e^{-\epsilon_i/\Delta}$. We take $c = 0.5$ and $\alpha = 1.0$, the best-fit values for our spin mixture found in the Esslinger group study [181]. For each site i , we consider the decay to six nearest neighbors, and combine these decays using the approximation, valid at short times, of parallel processes: $\tau_{ij} = (1/\tau_{ij1} + 1/\tau_{ij2} + \dots + 1/\tau_{ij6})^{-1}$. Effectively, this means that the decay is dominated by whichever of the six nearest neighbor sites has an offset closest to U . The idea

of this model is that the doublon decay is a local process determined by the energy difference between the initial and final two-body states. In the absence of disorder, this reduces to the known exponential scaling of the lifetime with U .

In this model, the decay takes a stretched exponential form, which is often seen in the relaxation of disordered glassy systems [182]. However, under our experimental conditions the slow tail of the decay would quickly become indistinguishable from single-particle loss. When fit to our normal functional form combining a fast and slow decay, the resulting fit gives a short-time decay that gets continuously faster but has a decreasing amplitude. Both these observations strongly disagree with the data. The comparison of this time constant with measurement is shown in Fig. 4.11, where it is evident that it does not capture any of the observed behavior beyond the clean limit. As we will show later, the amplitude of the fast decay relative to the slow decay, from which the equilibrium doublon fraction is determined, also does not show a substantial disorder dependence.

The failure of this local site model suggests that the physics controlling the doublon decay changes cannot be simply ascribed to the fairly trivial effect of the disorder shifting the offset between sites to be closer and then further from U . A key physical effect that this model is potentially missing is the possibility for localization and delocalization transitions, either of the doublons themselves or the surrounding medium. We can begin to understand these by considering the predicted changes in the local density of states.

4.9 Dynamical Doublon Regimes and the LDOS

I have named the dynamical regimes that we have observed as “Mott insulator,” “metallic,” and “disordered insulator” regimes. But are these actually related to the different equilibrium states, and if so, how? One simple picture is that they are caused by the same changes in the local density of states [Fig. 4.12]. The doublon decay process is sensitive to overall changes in the structure of the local density of states, and each ground-state transition at half-filling entails such a change. At $U/12t > 1.4$, the ground state is predicted to have two changes with applied disorder. First there is a Mott insulator to metal transition, in which the gap at the Fermi level closes, and second, a metal to Anderson (or Anderson-Mott) insulator transition, in which a gap at the Fermi level is restored. A local gap which initially closes and then reopens with increasing disorder is expected to lead to a doublon decay lifetime that decreases and then increases, as we observe. This is due to the changes in the availability of final states for the doublon decay. When there are few or no states present near $U/2$, as is the case in the “Mott regime,” two-body doublon decay is suppressed. This leads to a slow decay controlled by higher-order processes, as described in Sec. 4.3.2. Disorder redistributes

states into the Mott gap, which can drive the equilibrium insulator-metal transition and also can re-enable fast two-body doublon decay. This causes the dynamical crossover to the “metallic regime.” However, strong disorder can also drive a localization transition to a pointlike spectrum. When this occurs, decay is again suppressed in most places since there will not typically be a state at the final energy needed for decay. This is the dynamical regime that we have called the “disordered insulator.”

In a strongly-correlated system the density of states generally depends on the filling and temperature, but numerical studies suggest that these features persist away from zero temperature and half-filling [6, 17, 174]. However, we are not aware of any numerical technique capable of fully capturing the regime in which our experiments are performed.

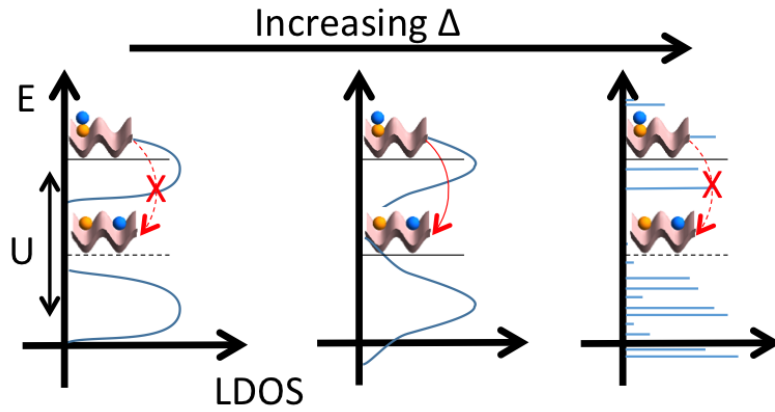


Figure 4.12: Sketch of doublon relaxation dependence on local density of states (LDOS). Left: In a system with strong interactions, which forms a Mott insulator at half filling, there is no two-body decay from a doublon that conserves energy. Decay is suppressed as a result. Center: moderate disorder creates mid-gap states, restoring fast two-body decay. Right: strong disorder drives a localization transition, in which the LDOS bands are replaced by a discrete spectrum. As a result, two-body decay is again suppressed.

To help us understand the doublon lifetime regimes, we also characterized the response of this system to lattice amplitude modulation [Fig. 4.10, right panel]. Lattice modulation is a well-established tool for probing the Mott insulating state in clean fermions [180] and clean and quasi-disordered bosons [157, 183–185]. We modify the experimental sequence described above to instead load the lattice at the final magnetic field, without the interaction quench. We then wait for 100 ms ($= 2.1\tau$) to allow the doublon population to equilibrate, before turning on the disorder over 1 ms as before. Next, amplitude modulation (typical 15% for 200 ms) is applied on all three beams, resulting in an increase of the doublon fraction to a new, driven steady-state value, which is then read out as before. Similar to previous measurements, in the absence of disorder we see a peak in doublon creation near $hf = U$ that is characteristic of the Mott gap. However, in both the “metallic” regime in which doublon lifetime is short and the “disordered insulator” regime in which it grows long, this peak vanishes in favor of a flat spectral response, which has an integrated weight that

increases in the “disordered insulator” regime. This confirms that we observe three qualitatively different regimes of behavior with increasing disorder: slow doublon relaxation with a gapped response, fast relaxation without a gap, and slow relaxation without a gap. These are the traits expected from the picture in terms of the LDOS presented above, in which the response is controlled by disorder-driven transitions between a uniform gap, no gap, and a non-uniform gap.

4.10 Doublon Relaxation Phase Diagram

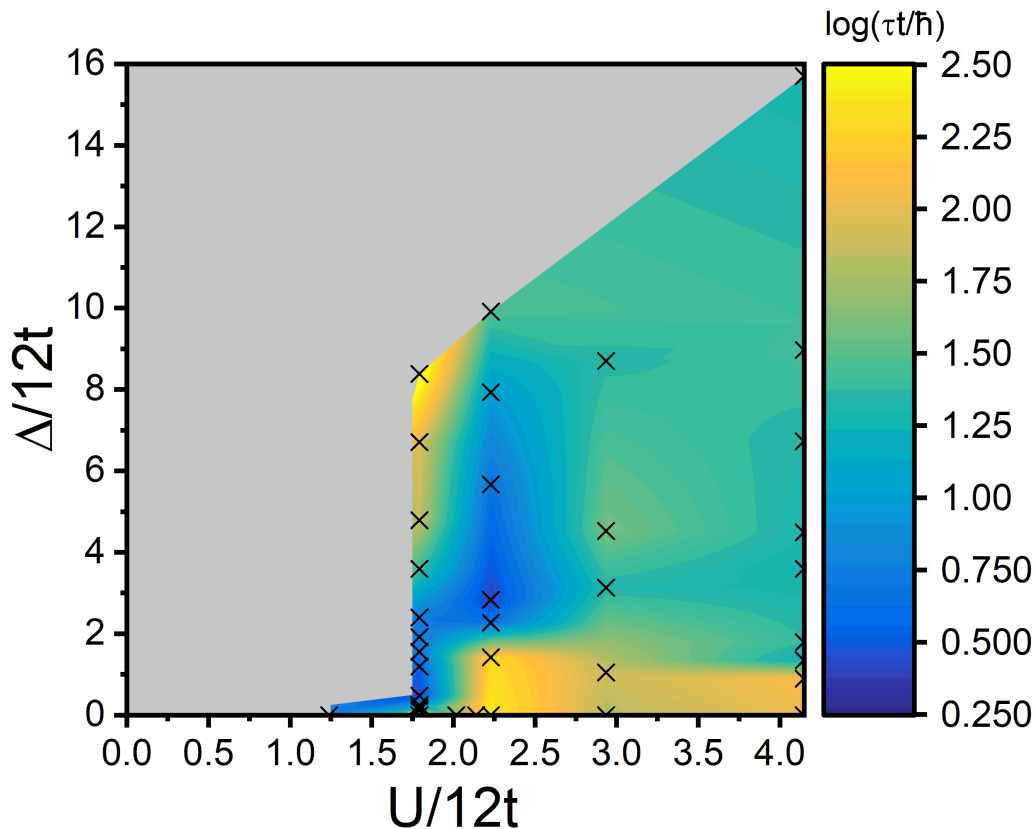


Figure 4.13: Relaxation phase diagram resulting from measurement of τ across different values of U and Δ , scaled by the bandwidth $12t$. Black x’s represent measured data points, which have been linearly interpolated to make a smooth colormap. Near zero disorder, the onset of slow dynamics due to a Mott gap can be seen beginning near $U/12t = 1.5$. Elsewhere, the complex interplay between interactions and disorder is evident; for strong interactions this results in the destruction of the “disordered insulator regime” (yellow region at high disorder) within the measured parameter regime in favor of a wide region in which relaxation is moderately fast and constant.

To further study the interplay of interactions and disorder in this system, we varied the lattice depth and repeated the measurement to explore a wide region of parameter space [Fig. 4.13]. This allows us

to construct a relaxation phase diagram, which is a type of non-equilibrium phase diagram [167, 186]. To create a smooth colormap, we first linearly interpolated between our four families at data at different interaction strengths, as well as the clean data, to make five smooth curves. Then these were themselves linearly interpolated to create Fig. 4.13. This two stage procedure resulted in the most physically-motivated plot because, once the general shape of the curves were determined, we sampled each interaction strength selectively to find important features such as transition points. Therefore, a naive interpolation without physical understanding would sometimes fill in these less sampled regions in ways that are not physically motivated, such as adding spurious features. The colormap is adapted from the Parula map developed by MATLAB, which is designed to faithfully represent data and avoid the apparent boundaries that can appear in a rainbow mapping. The raw data for these points is provided in Table 4.1.

At zero disorder, slow dynamics due to the opening of the Mott gap are clearly visible near $U/12t = 1.75$. Our lowest interaction strengths are also near a predicted transition between dynamical regimes at $U/12t = 0.8$, at which the clean relaxation time reaches an absolute minimum [178]. As the interactions are increased, the Mott insulator regime initially expands, reflecting the ability of stronger interactions to stabilize the system against disorder, before reaching a wide regime of parameter space over which the critical disorder required for the “metallic” regime stays near $\Delta_{c1}/12t \sim 1$. The onset of the “disordered insulating” regime, on the other hand, quickly increases with disorder until it is beyond the maximum disorder accessible to us. This leaves most of the parameter space in the “metallic regime”, in which the interactions and disorder mutually destroy insulating effects. However, the relaxation here is of order $20 \hbar/t$, which is significantly faster than in the initial “Mott insulator” regime, but slower than in the “metallic” regimes at lower $U/12t$.

It is interesting to compare our observed relaxation phase diagram with the predicted DMFT ground state phase diagram [17]. At lower interaction energies ($U/12t \leq 2$) the boundaries separating our dynamical regimes occur at disorder values comparable to the predicted ground-state transitions. At stronger interactions, the “metallic” transition still occurs at a comparable disorder, but our observed disappearance of the “disordered insulator” state up to very strong disorder is not predicted by the ground-state calculation. This may reflect the relative fragility of the localized state with respect to temperature in this regime.

4.11 Equilibrium Doublon Population

In principle, the steady-state doublon population in a disordered Mott system carries information about its nature. At low and moderate disorder, the ground-state doublon fraction is predicted to increase as disorder

$U/12t$	$\Delta/12t$	$\log_{10}(\tau t/\hbar)$	$\delta\tau/\tau$	$U/12t$	$\Delta/12t$	$\log_{10}(\tau t/\hbar)$	$\delta\tau/\tau$
1.24	0	0.846	0.991	2.23	2.27	0.66	0.627
1.79	0	1.67	0.346	2.23	2.83	0.40	0.343
1.79	0.12	1.85	0.454	2.23	5.67	0.67	0.634
1.79	0.18	1.21	0.815	2.23	7.93	0.98	0.624
1.79	0.24	0.97	0.388	2.23	9.91	1.48	0.503
1.79	0.48	0.40	0.626	2.94	0	1.81	0.250
1.79	1.20	0.55	0.505	2.94	1.04	1.88	0.504
1.79	1.56	0.70	0.359	2.94	3.13	1.33	0.446
1.79	1.92	0.72	0.484	2.94	4.52	1.58	0.591
1.79	2.39	0.71	0.357	2.94	8.70	1.35	0.481
1.79	3.59	1.42	0.413	4.15	0	2.01	0.132
1.79	4.79	1.85	0.445	4.15	0.90	2.10	0.384
1.79	6.70	1.96	0.656	4.15	1.35	1.23	0.868
1.79	8.38	2.64	0.547	4.15	1.79	1.38	0.333
2.02	0	1.64	0.583	4.15	3.59	1.26	0.276
2.14	0	2.44	0.280	4.15	4.49	1.31	0.596
2.23	0	2.43	0.336	4.15	6.73	1.34	0.395
2.23	1.42	2.30	0.546	4.15	8.97	1.43	0.653
				4.15	15.70	1.28	0.405

Table 4.1: Data used to create doublon relaxation phase diagram (Fig. 4.13), along with the fractional fit error $\delta\tau/\tau$.

breaks the Mott gap. This effect has been observed in previous studies with this experimental apparatus [24], and used to characterize the ground state transition in bosons [187]. However, the equilibrium change in doublon fraction is sharply reduced with increasing temperature, and at our temperature it is a small effect [Fig. 4.14]. In strong disorder, on the other hand, the steady-state doublon population could deviate from thermal equilibrium due to ergodicity breaking, similar to the lack of density-wave relaxation seen in other experiments [152–155, 163].

Fig 4.14 shows fit values for the steady-state doublon fraction $N_{d\downarrow,eq,0}/N_{\downarrow}$ for $s = 12 E_R$. It is compared to the result from an atomic limit calculation, for which we assume an adiabatic lattice load and neglect the entropy generated by the quench. In general, the measured values do not show much variation, which is striking given the large changes in doublon lifetime that occur over this data set. In particular, the most straightforward expectation for many-body localization, a doublon population that only relaxes slightly from the initial value before remaining largely constant, is clearly not present. We conclude that as far as we can determine, the doublon population approaches a similar equilibrium value across all disorder strengths sampled. This is not necessarily uncommon—all experiments (to my knowledge) that have claimed to observe MBL observe thermalization at long times, and base their claims on the behavior at some truncated time.

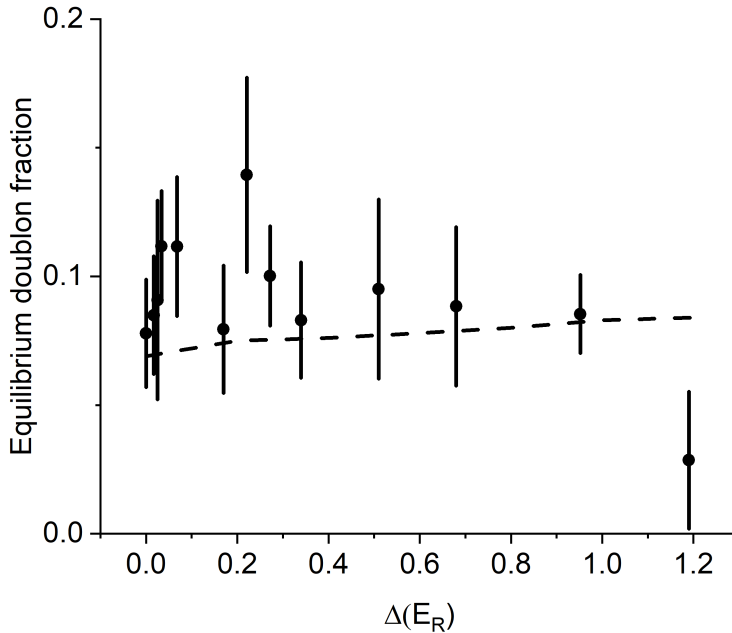


Figure 4.14: Equilibrium doublon population for $U/12t = 1.5$ ($s = 12 E_R$). Error bars represent the fit uncertainty. The dashed line is the result of an atomic limit calculation for the averaged parameters.

4.12 Conclusion and Outlook

A natural extension to this work is to attempt to develop a more detailed model of the doublon decay process, to try to get a more precise and quantitative picture of the physics behind the decay regimes we have observed. While this is a formidable problem, collaborators at JILA have made impressive progress in this direction, combining sophisticated numerics based on the discrete truncated Wigner approximation, a semiclassical approach that has been shown to reproduce MBL dynamics [188], and phenomenological models that incorporate the energetics of disordered doublon decay and diffusion suppression by many-body localization [189]. In both cases the general trends of the data appear to be captured, giving us some confidence that we understand the basic mechanics behind both the increase and decrease in the decay rates.

Each of the disordered regimes that we have found is predicted to have interesting properties that could be the subject of future experimental studies. The intermediate disorder “metallic” regime is likely to show characteristics of a bad metal, evidence for which, as discussed in chapter 3, has already been seen in similar systems with weaker interactions and no disorder [59, 80]. Under certain conditions, the doublon occupancy following a quench is directly related to the quasiparticle residue Z [177], suggesting that our measurement technique might be adapted to directly study this state. Spectroscopic measurements could also look for the

presence of a pseudogap in this regime [190], which was observed in a disorder-driven metallic phase in a condensed matter system [145].

As for the high-disorder “disordered insulator” regime, it is natural to ask the question of whether this system is in a many-body localized (MBL) phase. It is difficult to make such a determination based purely on dynamics, as many effects can result in a system with slow dynamics. To accurately characterize the dynamical regimes of our system, we have monitored the doublon population over sufficiently long timescales ($t_{hold,max} = 1500 \hbar/t$) to see relaxation towards a small thermal doublon population in all cases. In the “disordered insulator” regime, this relaxation is potentially consistent with a number of effects, such as the remnant of MBL in a system with loss [153, 191], glassy dynamics [192], subdiffusive behavior due to the vicinity of an MBL transition [154, 193–195], or thermalization due to rare “avalanche” processes [196]. As previous experiments claiming to show MBL in more than one dimension may also have competing explanations in terms of glassy dynamics [197], this ambiguity highlights the need for a greater theoretical understanding of MBL in this setting.

In summary, by taking a disordered Fermi-Hubbard system out of equilibrium and watching the subsequent relaxation of the doublon population, we have observed two crossovers between dynamical regimes with increasing disorder: first, a crossover from slow relaxation controlled by a uniform Mott gap to fast, gapless “metallic” relaxation dynamics, followed by a change to increasingly slow gapless dynamics at high disorder. Evidence that these changes in relaxation correspond to different regimes of behavior was also found through lattice modulation spectroscopy, and related to general changes predicted in the local density of states. Further study of both crossovers as well as the intervening disordered regimes should provide a valuable new front in the study of strongly interacting and disordered phenomena.

Chapter 5

Conclusion

5.1 A Composite Picture of the DFHM

The two studies described in detail in this thesis gave evidence for the following behaviors of the DFHM:

- In the clean, correlated metal regime, momentum relaxes very quickly and scales anomalously with temperature, showing signs of bad metallic relaxation that is not generated by scattering of Fermi liquid quasiparticles.
- At higher interactions, doublons become protected from decay by the Mott gap.
- However, disorder can modify this, first by destroying the Mott gap, and secondly by causing the emergence of a state that has the hallmarks of a disordered insulator—it does not have a distinct gap, but features slow relaxation.

It is convenient to discuss these results along with one more—the first experimental study of the 3D DFHM with ultracold atoms, which occurred in our group shortly before I joined [156]. In this study, the relevant observable was something I will call *mobility*—we applied a force to the atoms, using a magnetic gradient, and looks at the magnitude of the shift in momentum that developed after a fixed time. This mobility decreases with disorder, and the point at which it reaches zero can be interpreted as a dynamic signature of a localization transition. We characterized the dependence of this mobility on disorder, interactions, and temperature.

These dynamical measurements of the DFHM can be combined in a composite picture that shows behavior across a wide range of parameter space. Figure 5.1 shows the result. The doublon relaxation data is shown as before in a colorscale, while the mobility data at lower interaction strengths is shown as a red gradient, with a dotted line indicated where the mobility transition reported in the paper was identified. Two insets show representative temperature dependence. In the absence of disorder, the bad metallic scaling of relaxation with temperature is shown, while at high disorder a mobility consistent with zero is shown across a significant temperature range, suggesting a robust localized regime.

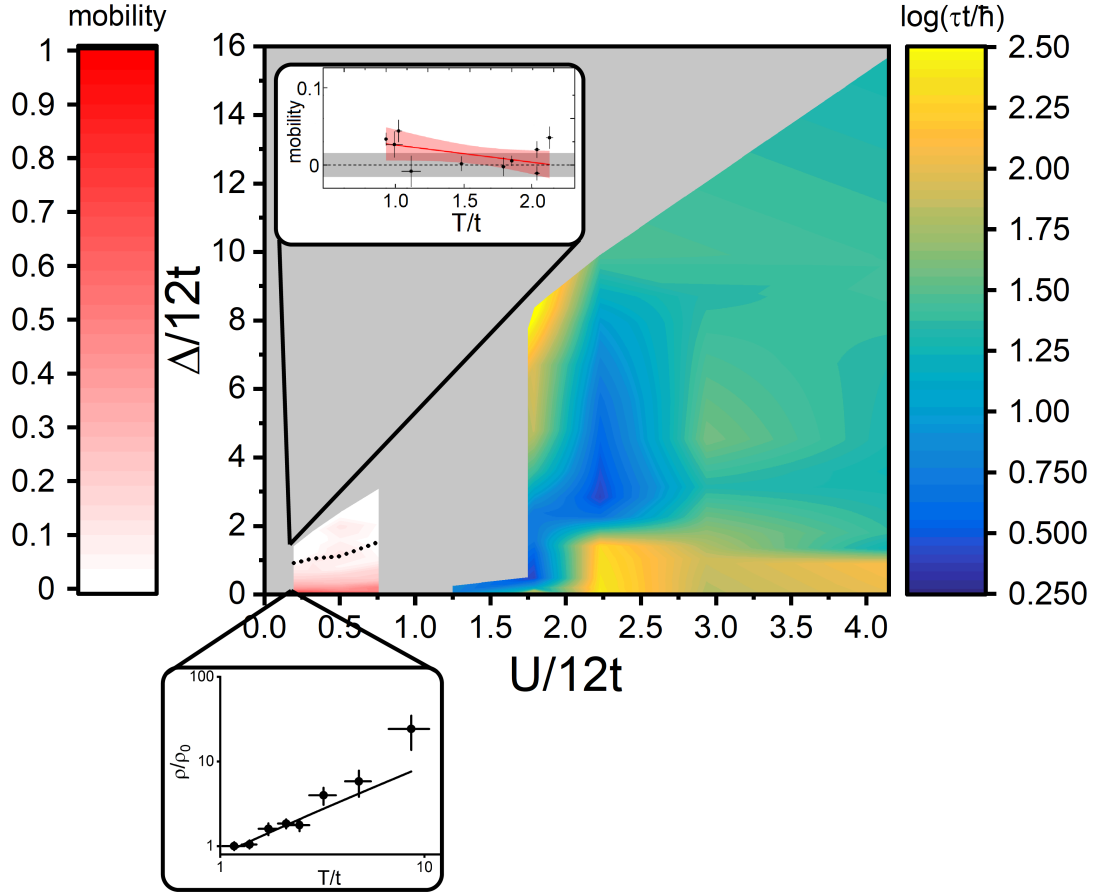


Figure 5.1: Composite picture of the DFHM, from the experiments described in Ch. 3 and Ch. 4 and from Ref. [156]. The colored region is the doublon lifetime phase diagram from Ch. 4. The red gradient colormap is the mobility extracted from Ref. [156], defined as $v_{COM}/v_{COM,max} \times t_{4E_R}/t_s$. The black dotted lines show the critical disorder for localization extracted from the mobility measurements, as described in Ref. [156]. The insets show two measurements of the temperature: the linear temperature dependence of ρ/ρ_0 seen for the clean bad metal in Ch. 3, and the lack of change in mobility over temperature in the localized phase as reported in Ref. [156].

Reassuringly, these very different dynamical measurements seem to tell a consistent story about the regimes of this model and their transitions. At lower disorder and interactions, we have a correlated bad metal. Atoms can tunnel about relatively freely, making doublons unstable and allowing a current to develop in response to an applied force. Sufficient disorder causes a transition to a ‘frozen’ localized phase, which seems to persist well into the excited state spectrum as evidenced by its resilience to temperature and to probes using high-energy doublons. Strong interactions, on the other hand, can both introduce slow dynamics of their own at low disorder and increase the disorder required for localization.

This picture is suggestive, but requires further validation. In the vicinity of the Mott transition, it

appears that neither doublons nor momentum currents are even approximately conserved, making it difficult to create and study an excitation of either type and leaving a conspicuous grey region in the center of Fig. 5.1. The nature of the large region at high interactions and disorder is also unclear—should it be thought of as a ‘bad metal,’ or a ‘bad insulator,’ or something else entirely? These questions and other await further studies. Nevertheless, the ability to reveal, through dynamical measurements, the different emergent behaviors resulting from competition of kinetic energy, interactions, and disorder shows the utility of the minimal physical model realized by ultracold atoms.

5.2 The Promise of Ultracold Atoms

As I said in the introduction, my hope for ultracold atoms is that they might contribute widely-applicable concepts to the pantheon of organizing concepts for complex systems. How does the work presented in this thesis fare in this regard? I certainly won’t claim that it originates any such idea, but maybe it can help to nurture some that are already taking root. Here are what I see as the three best candidates for these kinds of ideas:

- *Many-body localization* seems like a good candidate for a general phenomenon that is most purely realized in ultracold atoms (along with other isolated quantum systems such as trapped ions [198]). Although we cannot make an unambiguous determination of whether we have (or anyone has) realized a many body localized system, we do unambiguously see a dramatic slowdown of dynamics due to disorder, which should be investigated in future studies.
- The possibility that bad metals and other strongly relaxing systems are controlled by a simple *Planckian dissipation* rule, a question partially addressed by our measurements, seems to point to a powerful organizing principle in these systems. Whether this can be understood as the saturation of some bound on dissipation remains to be seen.
- Finally, our doublon relaxation measurement fits into a general trend of understanding many-body systems through their *far from equilibrium properties*. Studies of this type are by no means unique to ultracold atoms, but the isolation and control of these systems makes far from equilibrium behavior almost the norm, rather than a challenge to realize. The best way to understand such systems are still quite unclear. In this thesis, we have attempted to use the connection to the equilibrium phase diagram to provide some unified view, but this may be an example of the “Streetlight Effect;” we use this language only because few alternatives are available.

It will be exciting to see how these ideas, and others like them, develop in the coming years.

Appendix A

List of Programs Used to Control Experimental Subsystems

The following is a list of computer programs used to control or initialize different experimental subsystems, with the computer they live on (as of 08/2019) and a brief description. Brief reference guides to many of these programs are located on walls near the computers in the DeMarco lab.

- Wireshark (demarco-40kexp): Packet analyzer, used to verify communication with FPGA. Used only for troubleshooting, typically in the case that FPGA loses power.
- TFTP32 (demarco-40kexp): Programs FPGA. Used only for troubleshooting, typically in the case that FPGA loses power.
- out_fpga (demarco-40kexp): Sends compiled sequence to FPGA. Must be run upon restart.
- SciTE (demarco-40kexp): Text editor used to write and compile sequence. Must be reset upon restart.
- Motion Planner (demarco-40kexp): Used to communicate with cart. Required to resend normal cart program (TESTWRM) in event of interruption, or to bring cart under manual control for troubleshooting.
- AD9516 Eval (demarco-40kexp): Used to reset clock distribution controlling many DDSes in experiment. Must be reset upon restart.
- ADF4360-5 Eval (demarco-40kexp): Used to control PLL for EO in Raman beams, to provide offset of 1.2 GHz for hyperfine-changing transitions. Must be reset upon restart.
- TortoiseHG Workbench (demarco-40kexp): Front end for Mercurial version control software, used to browse versions of sequence.
- Winview (Demarco imaging): Camera control and image acquisition.
- Matlab (Demarco imaging): Fitting data.
- Origin (Demarco imaging): Visualize data.

- Demarco imaging (Demarco imaging): Visual Basic program used to interface between Winview, Matlab, Origin, and sequencer (via Seq40K.exe). Must be reset upon restart.
- Synergy (Demarco imaging): Allows for remote control of sequence and monitor computers through imaging computer. Typically runs fine automatically, needed if computers replaced or computer names or IP addresses change.

Appendix B

Code for Brillouin Zone Visualization

Here is an example of the Matlab code used to generate quasimomentum distributions of atoms in the ground band along our imaging direction, as used in Fig. 2.9. This code is stored locally at:

'Z:\Pubs\Will Morong\Numerical OD Simulations'. A few examples of the resulting images follow.

```
1 % makes a classical thermal 3D distribution of quasimomentum w/ correct
2 % imaging direction
3 % ignores trap effects
4
5 close all
6
7 %the size of the system.
8 %Start small for reasonable computation time- goes as ~n^6.
9 thesize=60/2*(120/60);
10
11 bz=24/2*(120/60); %the size of the Brillouin Zone.
12 pulse=round(0.5*bz); %the size of the kick, set by the Raman beam geometry
13 Bt=1/2; %inverse temperature scaled by t.
14 rotate=diag([1 1 1]);
15 [X1 Y1 Z1]=ndgrid(-thesize:thesize,-thesize:thesize,-thesize:thesize);
16 A=zeros(2*thesize+1,2*thesize+1,2*thesize+1);
17
18 %Here's where we set the imaging direction. There are several options:
19 % lattice axis, as measured by me using images of atoms
20 %(see Mathematica notebook 'Brillouin Zone Orientation'):
21
22 %my measurement of lattice axis
```

```

23 xp=[-0.679;-0.545;0.492];
24 yp=[0;-0.722;-0.692];
25 zp=[0.680;-0.544;0.491];
26
27 %imaging along (1,1,1) (close to what we do):
28 % xp=[1/sqrt(2); -1/sqrt(6);1/sqrt(3)];
29 % yp=[0;sqrt(2/3);1/sqrt(3)];
30 % zp=[-1/sqrt(2);-1/sqrt(6);1/sqrt(3)];
31
32 %arbitrary rotation:
33 % th1=0;
34 % th2=0;
35 % th3=0;
36 % rotate=[cos(th1), sin(th1),0;-sin(th1), cos(th1),0;0,0,1]...
37 %      * [cos(th2),0,sin(th2);0, 1,0;-sin(th2),0,cos(th2)]...
38 %      * [1,0,0;0,cos(th3), sin(th3);0,-sin(th3), cos(th3)];
39 % xpypzp= [rotate*diag([1 1 1])]';
40 % xp=xpypzp(:,1);
41 % yp=xpypzp(:,2);
42 % zp=xpypzp(:,3);
43
44 %this is the equilibrium classical thermal distribution
45 A0=exp(-2*Bt*(3-cos(pi.*((xp(1).*X1+xp(2).*Y1+xp(3).*Z1))/bz)-...
46      cos(pi.*((yp(1).*X1+yp(2).*Y1+yp(3).*Z1))/bz)-...
47      cos(pi.*((zp(1).*X1+zp(2).*Y1+zp(3).*Z1))/bz)));
48
49 %It's not difficult to make a variety of other quasimomentum distributions.
50 %For example: here's a uniformly filled band instead:
51 % A0=ones(size(X1));
52
53
54 %the next two parameters set the energy matching condition for the

```

```

55 %Raman/Bragg pulse:
56 %the kinetic energy difference between the beams, in units of t.
57 center=2.56;
58 % center=3.56;
59 % center=0;
60 %a finite broadening parameter,
61 %so the matching condition is not a perfect delta function.
62 width=0.2;
63
64 %this creates a landscape of the energy matching condition
65 %for each initial quasimomentum triple, how far from the energy matching
66 %condition it is to give the atom at the quasimomentum a vertical kick with
67 %strength 'pulse.'
68 Ediff=2*(3-cos(pi.*((xp(1).*X1+xp(2).*Y1+xp(3).*Z1))/bz))-...
69     cos(pi.*((yp(1).*X1+yp(2).*Y1+yp(3).*Z1))/bz))-...
70     cos(pi.*((zp(1).*X1+zp(2).*Y1+zp(3).*Z1))/bz))-...
71     2*(3-cos(pi.*((xp(1).*X1+xp(2).*(Y1-pulse)+xp(3).*Z1))/bz))-...
72     cos(pi.*((yp(1).*X1+yp(2).*(Y1-pulse)+yp(3).*Z1))/bz))-...
73     cos(pi.*((zp(1).*X1+zp(2).*(Y1-pulse)+zp(3).*Z1))/bz))+center;
74 %use a Gaussian broadening of the delta function. Assumes pi-pulse for
75 %resonant atoms:
76 mask=exp(-(Ediff/(width)).^2);
77
78 %here we ensure that only the first BZ is occupied
79
80 indxplus=find((X1*xp(1)+Y1*xp(2)+Z1*xp(3))>bz);
81 A0(indxplus)=0;
82 indxminus=find((X1*xp(1)+Y1*xp(2)+Z1*xp(3))<-bz);
83 A0(indxminus)=0;
84 indyplus=find((X1*yp(1)+Y1*yp(2)+Z1*yp(3))>bz);
85 A0(indyplus)=0;
86 indyminus=find((X1*yp(1)+Y1*yp(2)+Z1*yp(3))<-bz);

```

```

87 A0(indyminus)=0;
88 indzplus=find((X1*zp(1)+Y1*zp(2)+Z1*zp(3))>bz);
89 A0(indzplus)=0;
90 indzminus=find((X1*zp(1)+Y1*zp(2)+Z1*zp(3))<-bz);
91 A0(indzminus)=0;
92
93 %This creates the distribution of atoms resonant with the Raman pulse.
94 A1=A0.*mask;
95 A=A1;
96
97 % We then shift it in quasimomentum with a coordinate change
98 X=X1;
99 Y=Y1-pulse;
100 Z=Z1;
101
102 %the next six loops take atoms that were brought outside the Brillouin Zone
103 %by the momentum kick, and maps them back into the first BZ.
104
105 % %%
106 tic
107 indxplus=find((X*xp(1)+Y*xp(2)+Z*xp(3))>bz & A>0.001);
108 if numel(indxplus)>0
109     bzscaleplus=mod((X(indxplus)*xp(1)+Y(indxplus)*xp(2)+...
110         Z(indxplus)*xp(3))+bz,2*bz);
111     indxbzplus=[];
112     for iii=1:numel(bzscaleplus);
113         temp1=round(xp*(bzscaleplus(iii)-bz)+yp*(X(indxplus(iii))*yp(1)+...
114             Y(indxplus(iii))*yp(2)+Z(indxplus(iii))*yp(3))+...
115             zp*(X(indxplus(iii))*zp(1)+Y(indxplus(iii))*zp(2)+...
116             Z(indxplus(iii))*zp(3)));
117         indxbzplus(iii,1)=find(X==temp1(1)&Y==temp1(2)&Z==temp1(3));
118     end

```

```

119
120 A(indxbzplus)=A(indxbzplus)+A(indxplus);
121 A(indxplus)=0;
122 end
123
124 fprintf('Progress: 1/6\n');
125
126 indxminus=find((X*xp(1)+Y*xp(2)+Z*xp(3))<-bz & A>0.001);
127 if numel(indxminus)>0
128     bzscalexminus=mod((X(indxminus)*xp(1)+Y(indxminus)*xp(2)+...
129         Z(indxminus)*xp(3))-bz,-2*bz);
130     indxbzminus=[];
131     for iii=1:numel(bzscalexminus);
132         temp2=round(xp*(bzscalexminus(iii)+bz)+yp*(X(indxminus(iii))*yp(1)+...
133             Y(indxminus(iii))*yp(2)+Z(indxminus(iii))*yp(3))+...
134             zp*(X(indxminus(iii))*zp(1)+Y(indxminus(iii))*zp(2)+...
135             Z(indxminus(iii))*zp(3)));
136         indxbzminus(iii,1)=find(X==temp2(1)&Y==temp2(2)&Z==temp2(3));
137     end
138
139 A(indxbzminus)=A(indxbzminus)+A(indxminus);
140 A(indxminus)=0;
141 end
142
143 fprintf('Progress: 2/6\n');
144 %% %%
145 indyplus=find((X*yp(1)+Y*yp(2)+Z*yp(3))>bz & A>0.001);
146 if numel(indyplus)>0
147     bzscaleyplus=mod((X(indyplus)*yp(1)+Y(indyplus)*yp(2)...
148         +Z(indyplus)*yp(3))+bz,2*bz);
149     indybzplus=[];
150     for iii=1:numel(bzscaleyplus);

```

```

151     temp3=round(yp*(bzscaleyplus(iii)-bz)+xp*(X(indyplus(iii))*xp(1)+...
152         Y(indyplus(iii))*xp(2)+Z(indyplus(iii))*xp(3))+...
153         zp*(X(indyplus(iii))*zp(1)+Y(indyplus(iii))*zp(2)+...
154         Z(indyplus(iii))*zp(3)));
155     indybzplus(iii,1)=find(X==temp3(1)&Y==temp3(2)&Z==temp3(3));
156     end
157
158 A(indybzplus)=A(indybzplus)+A(indyplus);
159 A(indyplus)=0;
160 end
161
162 fprintf('Progress: 3/6\n');
163
164 indyminus=find((X*yp(1)+Y*yp(2)+Z*yp(3))<-bz & A>0.001);
165 if numel(indyminus)>0
166     bzscaleyminus=mod((X(indyminus)*yp(1)+Y(indyminus)*yp(2)+...
167         Z(indyminus)*yp(3))-bz,-2*bz);
168     indybzminus=[];
169     for iii=1:numel(bzscaleyminus);
170         temp4=round(yp*(bzscaleyminus(iii)+bz)+xp*(X(indyminus(iii))*xp(1)+...
171             Y(indyminus(iii))*xp(2)+Z(indyminus(iii))*xp(3))+...
172             zp*(X(indyminus(iii))*zp(1)+Y(indyminus(iii))*zp(2)+...
173             Z(indyminus(iii))*zp(3)));
174         indybzminus(iii,1)=find(X==temp4(1)&Y==temp4(2)&Z==temp4(3));
175     end
176
177 A(indybzminus)=A(indybzminus)+A(indyminus);
178 A(indyminus)=0;
179 end
180
181 fprintf('Progress: 4/6\n');
182 % %%

```

```

183 indzplus=find((X*zp(1)+Y*zp(2)+Z*zp(3))>bz & A>0.001);
184 if numel(indzplus)>0
185     bzscalezplus=mod((X(indzplus)*zp(1)+Y(indzplus)*zp(2)+...
186         Z(indzplus)*zp(3))+bz,2*bz);
187     indzbzplus=[];
188     for iii=1:numel(bzscalezplus);
189         temp5=round(zp*(bzscalezplus(iii)-bz)+xp*(X(indzplus(iii))*xp(1)+...
190             Y(indzplus(iii))*xp(2)+Z(indzplus(iii))*xp(3))+...
191             yp*(X(indzplus(iii))*yp(1)+Y(indzplus(iii))*yp(2)+...
192             Z(indzplus(iii))*yp(3)));
193         indzbzplus(iii,1)=find(X==temp5(1)&Y==temp5(2)&Z==temp5(3));
194     end
195
196 A(indzbzplus)=A(indzbzplus)+A(indzplus);
197 A(indzplus)=0;
198 end
199
200 fprintf('Progress: 5/6\n');
201
202 indzminus=find((X*zp(1)+Y*zp(2)+Z*zp(3))<-bz & A>0.001);
203 if numel(indzminus)>0
204     bzscalezminus=mod((X(indzminus)*zp(1)+Y(indzminus)*zp(2)+...
205         Z(indzminus)*zp(3))-bz,-2*bz);
206     indzbzminus=[];
207     for iii=1:numel(bzscalezminus);
208         temp6=round(zp*(bzscalezminus(iii)+bz)+xp*(X(indzminus(iii))*xp(1)+...
209             Y(indzminus(iii))*xp(2)+Z(indzminus(iii))*xp(3))+...
210             yp*(X(indzminus(iii))*yp(1)+Y(indzminus(iii))*yp(2)+...
211             Z(indzminus(iii))*yp(3)));
212         indzbzminus(iii,1)=find(X==temp6(1)&Y==temp6(2)&Z==temp6(3));
213     end
214

```

```

215 A(indzbzminus)=A(indzbzminus)+A(indzminus);
216 A(indzminus)=0;
217 end
218
219 toc
220 %% Find the edges of the first BZ, and display them if desired:
221
222 edge1=find((abs(X*xp(1)+Y*xp(2)+Z*xp(3))>.97*bz &...
223     abs(X*xp(1)+Y*xp(2)+Z*xp(3))<1.03*bz)&(abs(X*yp(1)+Y*yp(2)+Z*yp(3))>.97*bz...
224     & abs(X*yp(1)+Y*yp(2)+Z*yp(3))<1.03*bz));
225 edge2=find((abs(X*xp(1)+Y*xp(2)+Z*xp(3))>.97*bz &...
226     abs(X*xp(1)+Y*xp(2)+Z*xp(3))<1.03*bz)&(abs(X*zp(1)+Y*zp(2)+Z*zp(3))>.97*bz...
227     & abs(X*zp(1)+Y*zp(2)+Z*zp(3))<1.03*abs(bz)) &...
228     abs(X*yp(1)+Y*yp(2)+Z*yp(3))<bz);
229 edge3=find((abs(X*zp(1)+Y*zp(2)+Z*zp(3))>.97*bz &...
230     abs(X*zp(1)+Y*zp(2)+Z*zp(3))<1.03*bz)&(abs(X*yp(1)+Y*yp(2)+Z*yp(3))>.97*bz...
231     & abs(X*yp(1)+Y*yp(2)+Z*yp(3))<1.03*bz)& abs(X*xp(1)+Y*xp(2)+Z*xp(3))<bz);
232 % A(edge1)=2*10^10;
233 % A(edge2)=2*10^10;
234 % A(edge3)=2*10^10;
235 %%
236
237 %Make another thermal distribution in the shifted coordinates, and do the
238 %energy matching conditions here as well, to combine with the shifted atoms
239 %for the total picture. Not a very elegant way to implement this,
240 %but it was the easiest thing to do at the time.
241
242 A0=exp(-2*Bt*(3-cos(pi.*((xp(1).*X+xp(2).*Y+xp(3).*Z))/bz)-...
243     cos(pi.*((yp(1).*X+yp(2).*Y+yp(3).*Z))/bz)-...
244     cos(pi.*((zp(1).*X+zp(2).*Y+zp(3).*Z))/bz)));
245
246 %uniform filling instead (must match A0 above)

```

```

247 % A0=ones(size(X1));
248 Ediff=(-cos(pi.*((xp(1).*X+xp(2).*Y+xp(3).*Z))/bz)-...
249     cos(pi.*((yp(1).*X+yp(2).*Y+yp(3).*Z))/bz)-...
250     cos(pi.*((zp(1).*X+zp(2).*Y+zp(3).*Z))/bz))-...
251     (-cos(pi.*((xp(1).*X+xp(2).*(Y-pulse)+xp(3).*Z))/bz)-...
252     cos(pi.*((yp(1).*X+yp(2).*(Y-pulse)+yp(3).*Z))/bz)-...
253     cos(pi.*((zp(1).*X+zp(2).*(Y-pulse)+zp(3).*Z))/bz))+center/2;
254
255 mask=exp(-(Ediff/(width)).^2);
256
257
258 indxplus=find((X*xp(1)+Y*xp(2)+Z*xp(3))>bz);
259 A0(indxplus)=0;
260 indxminus=find((X*xp(1)+Y*xp(2)+Z*xp(3))<-bz);
261 A0(indxminus)=0;
262 indyplus=find((X*yp(1)+Y*yp(2)+Z*yp(3))>bz);
263 A0(indyplus)=0;
264 indyminus=find((X*yp(1)+Y*yp(2)+Z*yp(3))<-bz);
265 A0(indyminus)=0;
266 indzplus=find((X*zp(1)+Y*zp(2)+Z*zp(3))>bz);
267 A0(indzplus)=0;
268 indzminus=find((X*zp(1)+Y*zp(2)+Z*zp(3))<-bz);
269 A0(indzminus)=0;
270
271 A1=A0.*mask;
272
273 total=(A0-A1+A); %combined density distribution
274
275 figure
276 subplot(1,3,1)
277 imagesc(imrotate(sum(A0,3),90))
278 colormap('jet')

```

```

279 % colorbar
280 colorscale=caxis;
281 axis image
282 subplot(1,3,2)
283 imagesc(imrotate(sum(A,3),90))
284 colormap('jet')
285 caxis(colorscale)
286 axis image
287 subplot(1,3,3)
288 imagesc(imrotate(sum(total,3),90))
289 colormap('jet')
290 caxis(colorscale)
291 axis image
292
293 %Plot vertical slices through center of figures
294 % figure
295 % plot(temp(60/2,:), 'r')
296 % hold on
297 % temp2=sum(A0,3);
298 % plot(temp2(60/2,:), 'b')

```

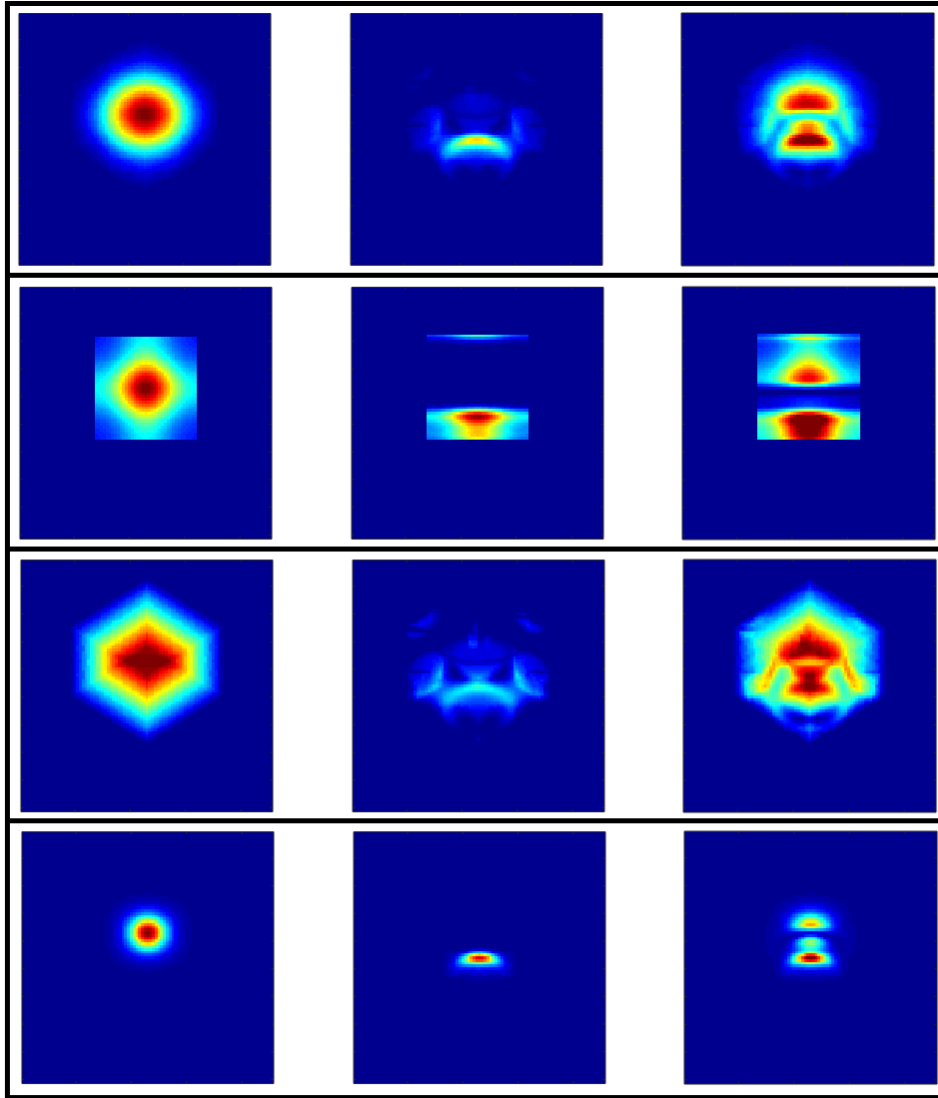


Figure B.1: Examples of BZ visualizations. Each panel consists of an initial distribution, the atoms transferred by a resonant kick, and the combined distribution after the kick is applied. Top: results for normal imaging direction and $\beta t = 1/3$. Second: the result if the lattice were aligned with the imaging and Raman directions ($\theta_1 = \theta_2 = \theta_3 = 0$). Third: same as top, but for uniform initial filling (or, equivalently, $\beta t = 0$). Bottom: same as top, but for $\beta t = 1$. A number of interesting distributions can result, ranging from the ‘tadpole’ to the ‘penguin’ to the ‘pteradactyl.’

Appendix C

Reprint: Simulation of Anderson Localization in Two-Dimensional Ultracold Gases for Pointlike Disorder

The following is a reprint of W. Morong and B. DeMarco, *Simulation of Anderson localization in two-dimensional ultracold gases for pointlike disorder*, Physical Review A, **92**, 023625 [199].

Simulation of Anderson localization in two-dimensional ultracold gases for pointlike disorder

W. Morong and B. DeMarco

Department of Physics, University of Illinois at Urbana-Champaign, 1110 West Green Street, Urbana, Illinois 61801, USA

(Received 20 May 2015; published 17 August 2015)

Anderson localization has been observed for a variety of media, including ultracold atomic gases with speckle disorder in one and three dimensions. However, observation of Anderson localization in a two-dimensional geometry for ultracold gases has been elusive. We show that a cause of this difficulty is the relatively high percolation threshold of a speckle potential in two dimensions, resulting in strong classical localization. We propose a realistic pointlike disorder potential that circumvents this percolation limit with localization lengths that are experimentally observable. The percolation threshold is evaluated for experimentally realistic parameters, and a regime of negligible classical trapping is identified. Localization lengths are determined via scaling theory, using both exact scattering cross sections and the Born approximation, and by direct simulation of the time-dependent Schrödinger equation. We show that the Born approximation can underestimate the localization length by four orders of magnitude at low energies, while exact cross sections and scaling theory provide an upper bound. Achievable experimental parameters for observing localization in this system are proposed.

DOI: [10.1103/PhysRevA.92.023625](https://doi.org/10.1103/PhysRevA.92.023625)

PACS number(s): 03.75.-b, 71.23.An, 67.85.-d

I. INTRODUCTION

Anderson localization (AL) [1,2]—the preclusion of wave propagation in a disordered medium by interference—has been observed in many settings, including, e.g., light and sound [3,4]. Recent experiments observing AL for ultracold atomic gases expanding in disordered optical speckle potentials show promise for gaining enhanced understanding of how microscopic disorder characteristics affect localization and the interplay with interparticle interactions. In particular, these systems allow for independent control of interatomic interactions and the disorder strength and correlation length. Localization has been observed and its dependence on these disorder parameters studied for gases confined to one-dimensional geometries [5,6] and in three dimensions [7–9]. In two-dimensional gases, however, the classical diffusive regime [10] and the impact of disorder on superfluids have been explored [11,12], but AL has not yet been observed. The study of localization in two dimensions using ultracold gases is especially desirable given the many outstanding questions regarding localization in two-dimensional electronic solids [13–15].

In this paper, we discuss how classical trapping effects complicate the observation of AL for speckle disorder in two dimensions. We demonstrate how pointlike disorder (Fig. 1) avoids these problems. Through a combination of analytical and numerical simulation, we show that a disordered potential of this type would enable experimental observation of two-dimensional AL for ultracold gases. Pointlike, two-dimensional disorder and time-dependent simulations of localization have not been considered in previous theoretical studies of ultracold systems [16–18]. Like previous studies, we consider an ideal two-dimensional geometry and ignore interparticle interactions and quantum statistics. As our focus is on realistic experimental conditions, we have limited our investigation to experimentally accessible disorder strengths and energy scales for ultracold, spin-polarized ^{40}K atoms. We expect that this technique can be straightforwardly extended to other experimental configurations.

This paper is organized as follows: in Sec. II, we describe classical trapping in two-dimensional speckle potentials using percolation theory, and we show how pointlike disorder can

avoid this problem for realistic experimental parameters. In Sec. III, we identify experimentally accessible parameters for localization in pointlike disorder using scaling theory and the Born approximation, which we show may fail in this regime. Therefore, in Sec. IV, we calculate exact differential cross sections using numerical simulations to more accurately determine localization lengths via scaling theory. We also use exact time-dependent simulations of wave-packet propagation in pointlike disorder to determine localization lengths as would be observed in an experiment that allows a gas to expand into a disordered potential.

II. PERCOLATION IN SPECKLE AND POINTLIKE DISORDER

In this section, we examine the classical trapping properties of speckle and pointlike disorder potentials in two dimensions using percolation theory, which is the study of the random growth of interconnected regions in networks. These regions grow in size as a parameter is varied until a transition at the percolation threshold, at which a connected region spanning the system is formed [19,20]. In the context of atom transport in a two-dimensional disordered potential, the problem is easily visualized in this way: the disorder potential forms a potential landscape that constrains the atomic motion. Atoms with kinetic energy higher than the percolation threshold will travel freely through the potential, but below a critical fraction of the average potential energy atoms will be trapped in potential minima of finite size [21]. If this percolation threshold occurs near the same energy scale as Anderson localization, AL may not be detectable or experimentally distinguishable from classical trapping.

Because of their ease of creation and simple statistical properties, optical speckle fields [22] have been used to generate disorder in virtually all ultracold atom experiments exploring disorder-induced effects; see, e.g., Refs. [5,7,8,10–12,23,24]. A notable exception is disorder generated by impurity atoms [25]. Optical speckle is produced by focusing a laser beam that has passed through a diffuser. The atoms experience a potential-energy shift proportional to the optical

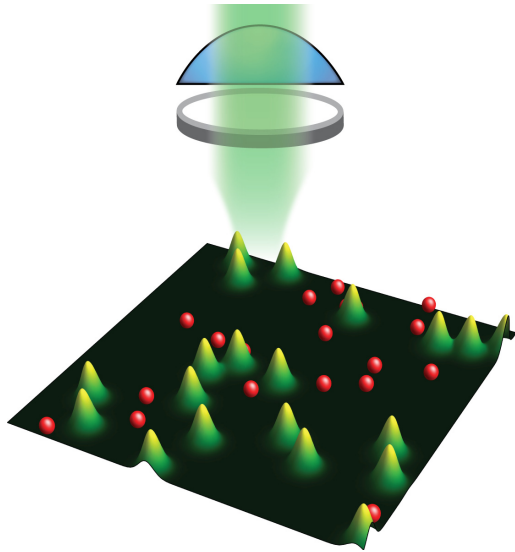


FIG. 1. (Color online) Schematic representation of experimental implementation of pointlike disorder. Ultracold atoms are confined to a quasi-two-dimensional geometry using a sheet of far-detuned light (not shown). The disordered potential is generated by an additional laser beam (green shaded region) that passes through a holographic optic (disc) and is focused on the atoms (red spheres). The atoms experience a disorder potential consisting of a random arrangement of Gaussian barriers.

intensity of this light. Speckle disorder has an exponential distribution of potential energies and a spatial autocorrelation that is approximately Gaussian. While in three dimensions the percolation threshold for a blue-detuned speckle field is negligible [26,27], potential minima appear in one and two dimensions that can classically trap the atoms. As a result, the percolation characteristics of a speckle potential become a significant constraint on attempts to observe Anderson localization in reduced dimensions.

This limitation is in part due to scaling symmetries unique to speckle disorder. A distinctive feature of a speckle field is that it has only one adjustable length scale, i.e., the correlation length ζ . This characteristic leads to a simple scaling symmetry of the field: any change in scale of the system is equivalent to a suitable change in ζ . The percolation threshold is necessarily scale invariant, and as a result it must be independent of ζ . Thus, the critical energy for a percolation transition in a speckle field is always at a fixed fraction of the average potential energy Δ , which simulation shows to be roughly 52% in two dimensions [27–29]. This dependence complicates observing AL in two dimensions using ultracold atoms. In an infinitely sized two-dimensional system, infinitesimal disorder will localize atoms with any kinetic energy [30]. The localization length grows exponentially with the particle energy [31], and thus relatively strong disorder is required to localize atoms on experimentally accessible length scales. This leads to classical trapping of a wide range of particle energies, which may be difficult to separate from AL.

In light of this high, fixed percolation threshold, an alternative form of disorder that does not cause classical

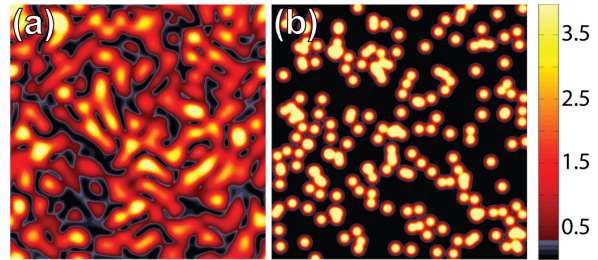


FIG. 2. (Color online) Comparison of percolation in (a) a speckle potential and (b) a sparse pointlike disordered potential (b). Here, images of disorder potentials are shown in a scale-free fashion. The disorder potential energy is shown in false color. The color bar shows the potential energy in units of Δ . Regions in grayscale correspond to energies that are less than 30% the average disorder energy. A classical particle with this energy would be trapped in a finite-size region in the speckle potential, but able to propagate indefinitely for the pointlike disorder case.

trapping is desirable. The pointlike disorder we investigate consists of individual Gaussian potential barriers with randomly distributed locations \vec{x}_i ,

$$V(\vec{x}) = \sum_i V_0 e^{-|\vec{x}-\vec{x}_i|^2/w^2}, \quad (1)$$

where V_0 is the peak disorder energy, i indexes the individual Gaussian potentials, and $w/\sqrt{2}$ is the rms width of an individual barrier. This type of disordered potential was chosen for its simplicity and straightforward experimental realization in a cold-atom experiment using holographic techniques [32–34]. As shown in Fig. 1, a random array of blue-detuned focused Gaussian laser beams can produce potential barriers as in Eq. (1). The advantage of pointlike disorder over a speckle potential is that the freedom to tune the density n of potential barriers introduces a second length scale $n^{-1/2}$, and varying the ratio of w and the average distance between scattering sites $n^{-1/2}$ allows the percolation threshold to be tuned.

The impact of this tunability is shown visually in Fig. 2. Potential landscapes are displayed for speckle and pointlike disorder with the same average potential energy. While the percolation threshold for this finite-size realization of speckle disorder is 0.39Δ , the pointlike disorder parameters were chosen to set the percolation threshold for the realization shown in Fig. 2(b) to approximately 0.06Δ . Thus, particles with small kinetic energies compared with the disorder energy are free to propagate in the pointlike disorder, while particles with relatively high kinetic energies are classically trapped by the speckle disorder.

We used a standard technique to calculate the dependence of the percolation threshold on the pointlike disorder parameters. Disorder potentials were numerically simulated, and the percolation threshold was determined by detecting the formation of a connected region spanning the simulation space by points below a threshold potential energy. The percolation threshold E_{th} was determined by averaging over independent realizations of the disorder potential. While only approximating the percolation threshold, which is defined in the limit of an infinite system, this method gives excellent

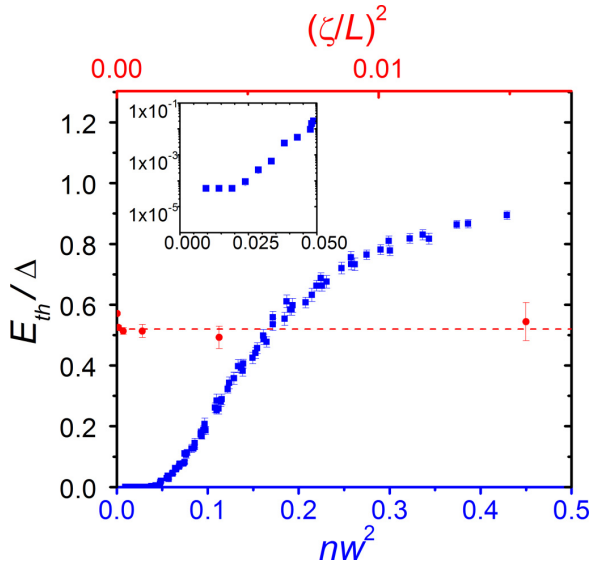


FIG. 3. (Color online) Percolation threshold for pointlike (blue squares) and speckle (red circles) disorder potentials. The dashed line is the known percolation threshold for speckle disorder, and the points are results of our simulation. For pointlike disorder, n and w are independently varied, and for speckle disorder, the correlation length was changed. Inset: The onset of significant percolation for pointlike disorder. The minimum detectable threshold level is 5×10^{-5} in our simulation. The error bars show the standard error of the mean for the average taken over 50 disorder realizations at each pointlike disorder point and eight realizations for each speckle disorder case.

agreement with the known value for speckle disorder (Fig. 3). In our simulation, a fixed system size L is used and the number of Gaussian potential barriers and w are independently varied.

As shown in Fig. 3, the percolation threshold was found to be a function of only the dimensionless combination nw^2 , as expected from simple space-filling considerations [35]. For sufficiently dilute disorder (i.e., low nw^2), the percolation threshold is arbitrarily close to zero and monotonically increases with nw^2 towards the limit of the average disorder energy. Our interest is in the regime where the percolation threshold is lower than that of a speckle potential and ideally negligible, while maintaining sufficient density of scattering sites such that the particles are scattered many times within the system size.

We choose to concentrate on $nw^2 \leq 0.03$, which fulfills both criteria. Under this condition, the percolation threshold is less than $2.5 \times 10^{-4} \Delta$, which is smaller than the percolation threshold for three-dimensional (3D) speckle [27]. The system size and w are limited by experimental constraints such as optical power, imaging signal-to-noise ratio, and numerical aperture. For the rest of this paper, we choose to use an experimentally feasible disorder size $w = 400$ nm. When discussing proposed experiments, we assume that the disorder potential and the light used to create it are limited to a $100 \times 100 \mu\text{m}^2$ area in order to estimate the requisite laser power. We use $n = 0.2 \mu\text{m}^{-2}$ (corresponding to $nw^2 = 0.03$) for comparing the localization lengths predicted by scaling theory using either

the first Born approximation or the exact scattering differential cross section and for predicting a thermally averaged density profile. In these cases, we choose the highest possible n that avoids significant classical trapping in order to make AL effects as robust as possible. For comparing the results of scaling theory and a simulation of the time-dependent Schrödinger equation, we use $n = 0.08 \mu\text{m}^{-2}$ (corresponding to $nw^2 = 0.013$), which is the largest n compatible with our computational resources. For $n = 0.2$ and $n = 0.08 \mu\text{m}^{-2}$, there are 2000 and 800 disorder peaks within the proposed $100 \times 100 \mu\text{m}^2$ area, respectively.

While we have shown that pointlike disorder can avoid classical trapping, it must also lead to observable localization lengths to be a viable experimental option. In principle, atoms in an infinite two-dimensional system are localized by infinitesimal disorder [31], but only localization lengths smaller than the system size are physically meaningful and observable. Therefore, the rest of this paper is concerned with estimation of the localization length for pointlike disorder and its dependence on the disorder properties and particle energy.

III. LOCALIZATION LENGTHS: THE BORN APPROXIMATION

In this section, we determine analytic expressions for the localization length in the limit where the scattered wavefunction amplitude is small. Although we will show that this approach is inaccurate in the regime of interest, it is useful for developing physical insight. Analysis of pointlike disorder is particularly simple in this regime because the differential cross section for scattering from a single disorder barrier can be determined using the first-order Born approximation. This differential cross section can be used to determine transport properties in a potential consisting of many Gaussian potentials, provided that there is little spatial overlap. Our procedure has three steps: we first find the Born approximation for the differential scattering cross section $d\sigma/d\theta$ of a single potential barrier. We use $d\sigma/d\theta$ to determine the Boltzmann transport mean free path l_B , which characterizes the diffusive properties for particle transport in the disordered potential. Finally, we use scaling theory to estimate the localization length ξ from l_B .

In two dimensions, we write the (unnormalized) scattered wave function $\psi(\vec{x})$ as

$$\psi(\vec{x}) = e^{i\vec{k}\cdot\vec{x}} + f(\theta) \frac{e^{ikr}}{\sqrt{r}}, \quad (2)$$

where \vec{r} is the radial coordinate, \vec{k} is the incoming wave vector, $f(\theta)$ is the scattering amplitude, and θ is the scattering angle. We assume a free-particle dispersion so that $k = \sqrt{2m\epsilon_k}/\hbar$, where m is the mass of the particle, ϵ_k is the kinetic energy of the atom, and $\hbar = 2\pi\hbar$ is Planck's constant. Given the scattering amplitude in the Born approximation,

$$f(\theta) = -\frac{me^{i\frac{\pi}{4}}}{\hbar^2\sqrt{2\pi k}} \int e^{i(k\hat{r}-\vec{k})\cdot\vec{x}} V(\vec{x}) d^2\vec{x} \quad (3)$$

(where \hat{r} is a unit vector that points in the scattered direction), the differential cross section for a single Gaussian potential

$V(\vec{x}) = V_0 e^{-r^2/w^2}$ is

$$\begin{aligned} \frac{d\sigma}{d\theta} &= |f(\theta)|^2 \\ &= \frac{\pi}{8k} \left(\frac{2m}{\hbar^2} \right)^2 w^4 V_0^2 e^{-2w^2 k^2 \sin^2 \frac{\theta}{2}}, \end{aligned} \quad (4)$$

where θ is the scattering angle. We calculate the Boltzmann mean free path l_B , the distance over which the direction of momentum remains correlated [16], using Eq. (4) for the differential cross section and the density of scattering sites n :

$$l_B = l_s \left[1 - \int_0^{2\pi} \cos \theta \left(\frac{1}{\sigma} \frac{d\sigma}{d\theta} \right) d\theta \right]^{-1}, \quad (5)$$

where the elastic mean free path is $l_s = (n\sigma)^{-1}$ and the total cross section is $\sigma = \int_0^{2\pi} (d\sigma/d\theta) d\theta$. Combining Eqs. (4) and (5), we find

$$l_B = \frac{1}{\sqrt{2\pi^3}} \frac{1}{nw} \left(\frac{\hbar^2 k^2}{2m} \frac{1}{V_0} \right)^2 \quad (6)$$

for the Boltzmann mean free path.

The connection between l_B and the localization length ξ is given in the $(kl_B)^{-1} \ll 1$, $L \rightarrow \infty$ limit by scaling theory [31] as

$$\xi = l_B e^{\frac{2}{3} kl_B}. \quad (7)$$

Thus, given the properties of the disorder and atoms, we may calculate a localization length valid in these limits using the Born approximation. We choose to focus on an experimentally realistic situation. In an experiment in which the disorder is generated by the dipole force from a far-detuned laser, limited laser power constrains the maximum average potential energy, rather than the value of V_0 for individual potential barriers. Therefore, we investigate the case in which Δ is fixed, but the density of disorder sites n and V_0 vary inversely.

To get a concrete sense of these predictions, for disorder generated by a 2 W, 532 nm laser focused to a Gaussian envelope with a 170 μm waist (which has been employed in experiments on 3D AL [7]), realistic disorder parameters are $w = 400$ nm and average disorder strength $\Delta = k_B \times 1000$ nK. The peak potential V_0 is determined by the relation $V_0 = \Delta/\pi n w^2$. The resulting localization lengths, as a function of particle energy ϵ_k and n , are shown in Fig. 4 along with the percolation threshold. For the contour lines shown in Fig. 4, the value of kl_B varies from 0.05–0.3. A localization length of 100 μm , which would result in high imaging signal-to-noise ratio and minimal effects from the disorder envelope, can be well separated from classical trapping when there is less than approximately one potential barrier per square micron. Furthermore, a regime exists for $n < 0.25 \mu\text{m}^{-2}$ in which classical trapping is irrelevant and small localization lengths exist for experimentally accessible particle energies.

While this standard approach to determining localization lengths suggests that two-dimensional localization may be observable using ultracold atoms and pointlike disorder, it is unclear that the Born approximation will be valid in an experiment. Given the parameters explored in Fig. 4, accessible

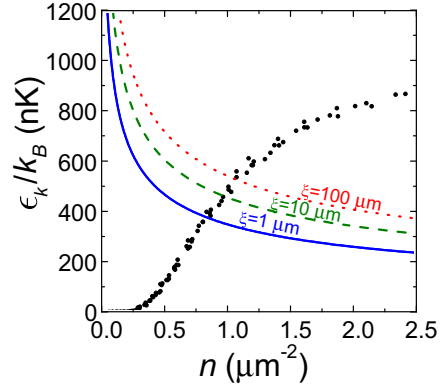


FIG. 4. (Color online) Localization lengths according to scaling theory within the Born approximation. Contour lines for three localization lengths are displayed using the experimental parameters described in the main text. The percolation threshold in terms of ϵ_k is shown using solid circles. If $\epsilon_k < E_{\text{th}}$, then AI will not be observable and the atoms will be classically trapped. Because the average disorder potential energy is fixed at $k_B \times 1000$ nK, V_0 varies according to $V_0 = k_B \times (1989/n [\mu\text{m}^{-2}])$ nK.

localization lengths necessarily involve $V_0 > \epsilon_k$, and thus the Born approximation is suspect. The precise limits of the Born approximation are not always obvious [36]. Unlike the three-dimensional case, the Born approximation is never valid in two dimensions as $k \rightarrow 0$. In two dimensions and for $kw \ll 1$, a simple analysis suggests that the Born approximation may be valid for

$$g = \frac{4mw}{\hbar^2} \frac{V_0}{k} \ll 1. \quad (8)$$

The smallest value for $g \approx 7.5$ occurs in the upper right-hand corner of Fig. 4, and thus the Born approximation is not satisfied for this range of parameters. Similar considerations hold for the high-energy (i.e., $kw \gg 1$) regime. Thus, while the Born approximation can supply physical insight, the localization lengths computed in this section may not be accurate.

Using the Born approximation will generally underestimate the localization length. The differential cross section in the Born approximation [Eq. (4)] depends quadratically on the strength V_0 of a scattering site, which accounts for the sharp decrease in localization length in Fig. 4 near $n = 0$, where the disorder potential is concentrated in few, very strongly scattering sites. However, once V_0 is much greater than the particle kinetic energy, further increasing V_0 must have diminishing effects on scattering. Underestimating the localization length is a critical problem because large localization lengths may not be observable in an experiment. We determine the precise deviation from the Born-approximation behavior using numerical simulation. As we will show in the next section, the Born approximation and scaling theory as applied here can underestimate the localization length by more than three orders of magnitude in the regime we propose to explore experimentally.

IV. BEYOND THE BORN APPROXIMATION

In this section, we implement numerical simulations of scattering and localization, and use them to determine improved estimates of localization lengths. We rely on two complementary approaches. The first, simplest approach is a single scattering simulation: we numerically determine the exact differential cross section for a single scattering event, and then use this in place of the analytic result [Eq. (4)] to compute l_B and ξ as in Sec. III. While the values obtained using this method remain valid only for $kl_B \gg 1$, they have two important advantages over the analytic solutions. First, the error is much less severe at low energy in practice. Second, the assumptions that entered into the scaling theory derivation are such that it provides an upper bound on the localization length [31]. The (dimensionless) ohmic conductance assumed at the microscopic cutoff length scale l_B in scaling theory is an upper bound, since weak-localization effects are ignored. The length scale at which the conductance vanishes in scaling theory, which is taken as the localization length, is therefore also an upper bound.

To apply this method, we numerically extract $d\sigma/d\theta$ by a straightforward application of scattering theory (Fig. 5).

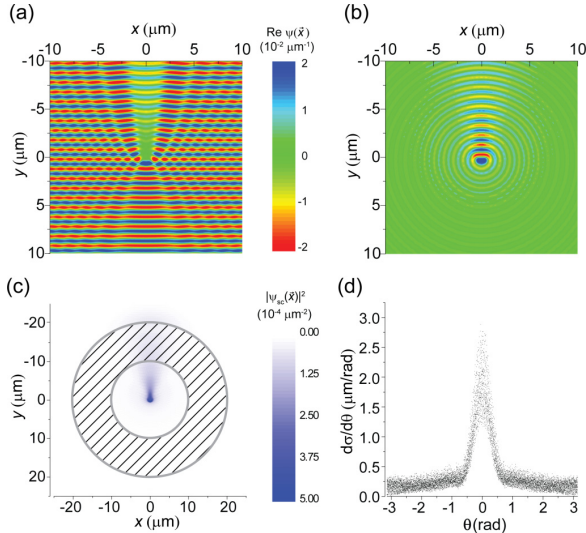


FIG. 5. (Color online) Process of extracting scattering properties from a simulating propagation of a plane wave for the time-dependent Schrödinger equation. The initial wave vector \vec{k} is in the y direction. (a) Real part of the wave function $\psi(\vec{x}, \tau)$ shown in false color. For all of the data shown in this figure, $\epsilon_k = k_B \times 240$ nK, $V_0 = k_B \times 1000$ nK, and $w = 400$ nm. Violation of the Born approximation is evident as significant distortion of the initial plane wave by the potential barrier at the origin (not pictured). (b) Real part of the scattered wave function $\psi_{sc}(\vec{x})$ obtained by subtracting a plane wave propagated in free space from the data shown in (a). The color bar applies to the simulated wave functions shown in (a) and (b). (c) The scattered probability density $|\psi_{sc}(\vec{x})|^2$ is shown as a density plot. The cross-hatched region is sampled to determine that differential cross section. (d) Differential cross section obtained from the data in (c). Points are shown at fixed θ and different r within the circular annulus.

We first simulate, via the split-step Fourier method [37], a plane-wave scattering from a single potential barrier (see Appendix A). A wave function $\psi(\vec{x}, t = 0) = e^{ik_y y} / L$ with energy $\epsilon_k = \hbar^2 k^2 / 2m$ and wave vector $k\hat{y}$ is prepared at initial time $t = 0$ in the simulation space, which has sides of length L . The wave function is propagated forward in time steps δt according to

$$\psi(\vec{x}, t + \delta t) = e^{-i\frac{\delta t}{\hbar}V(\vec{x}, t)} \times \mathcal{F}^{-1} \left\{ e^{-i\delta t \frac{\hbar k^2}{2m}} \mathcal{F} \left[e^{-i\frac{\delta t}{\hbar}V(\vec{x}, t)} \psi(\vec{x}, t) \right] \right\}, \quad (9)$$

where \mathcal{F} represents a Fourier transform. The time step δt is chosen to minimize numerical instability and such that $\delta t \times V/\hbar \ll 1$ and $\delta t \times \hbar k^2 / 2m \ll 1$.

While propagating the wave function forward in time, the Gaussian potential $V(\vec{x}, t) = V_0 e^{-r^2/w^2} (1 - e^{-t/0.2\tau})$ is slowly ramped on. We determined that the time over which the barrier was turned on did not significantly change the simulation results. After a total propagation time from $\tau = 1-7$ ms (depending on the group velocity), a wave function distorted by scattering from the potential barrier is produced, as shown in Fig. 5(a). For the V_0 and ϵ_k chosen in Fig. 5, the simulated wave is highly distorted, signaling a violation of the Born approximation.

The scattered wave $\psi_{sc} = \psi(\vec{x}, t) - \psi'(\vec{x}, t)$ is recovered using the unscattered wave $\psi'(\vec{x}, t)$, which is determined by repeating the simulation with $V(\vec{x}, t) = 0$. The scattering amplitude $f_r(\theta)$ at radius r is computed according to Eq. (2) as $f_r(\theta) = e^{-ikr} \sqrt{r} \psi_{sc}(\vec{x})$. As shown in Fig. 5, $f_r(\theta)$ is sampled in a circular annulus centered on the origin. The outer and inner radii of this annulus were set to minimize boundary effects and to achieve the asymptotic scattering regime. The differential cross section $d\sigma/d\theta$ —calculated by averaging $|f_r(\theta)|^2$ across all r within the annulus at fixed θ —is numerically integrated to produce the cross section σ .

A comparison between the total cross section σ determined using the exact $d\sigma/d\theta$ and using $d\sigma/d\theta$ from the Born approximation is shown in Fig. 6. The two approaches agree at high kinetic energy. At low energies, however, the Born approximation fails and underestimates the cross section.

An improved scaling-theory prediction for the localization length ξ using the exact differential cross section is shown in Fig. 7. We fix $n = 0.2 \mu\text{m}^{-2}$, which corresponds to a vertical slice in Fig. 4. The localization length predicted using the exact differential cross section exceeds the Born-approximation prediction by more than three orders of magnitude at all particle energies. Furthermore, the localization length is always larger than the characteristic length scales of the disorder, while the Born approximation predicts unphysical localization lengths much smaller than w and $1/\sqrt{n} \approx 2 \mu\text{m}$. For the disorder parameters explored here and a $100 \mu\text{m}$ system size, localization will be visible for pointlike disorder for particles with energies less than $k_B \times 20$ nK. While for a speckle potential with the same Δ the percolation threshold is $k_B \times 500$ nK, the percolation threshold for this pointlike disorder potential is approximately $k_B \times 0.25$ nK, and thus AL will be the dominant influence on transport.

As a second approach to determining localization lengths, we performed complete time-dependent simulations of a wave

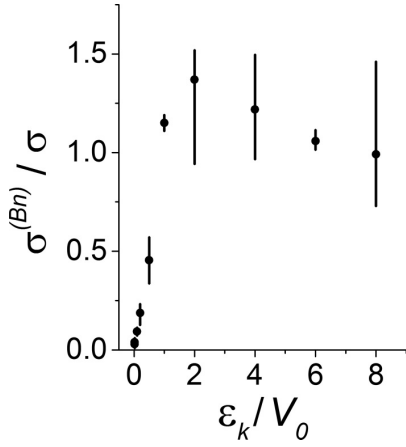


FIG. 6. Ratio of total-collision cross section determined from the Born approximation $\sigma^{(Bn)}$ to σ calculated using the exact differential cross section for $w = 400$ nm and $V_0 = k_B \times 50$ nK. The error bars show the spread in values determined across the inner and outer radii of the annulus displayed in Fig. 5(c) and include the effects of numerical errors and deviation from the far-field limit.

packet propagating through a pointlike disorder potential (see Appendix B). This approach is inspired by the method used to observe AL in 1D [5,6] and 3D [7–9] ultracold gases: atoms initially confined in a small region of space by a trap are

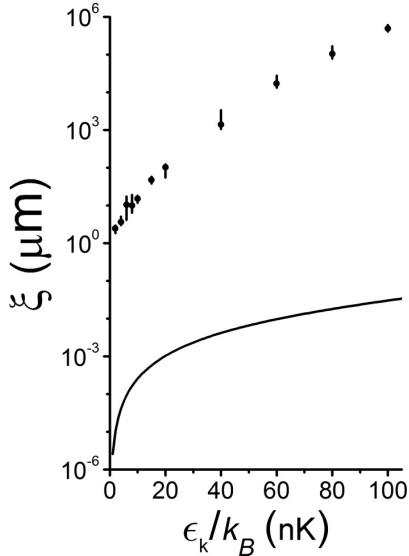


FIG. 7. Localization lengths predicted using scaling theory and the exact differential cross section (circles) and the Born approximation (solid line). The density for the disorder potential is $n = 0.2 \mu\text{m}^{-2}$, the average disorder potential energy $\Delta = k_B \times 1000$ nK, and the Gaussian barrier height $V_0 = k_B \times 9950$ nK. The error bars are determined using the spread in the differential cross section determined across the inner and outer radii of the annulus displayed in Fig. 5(c).

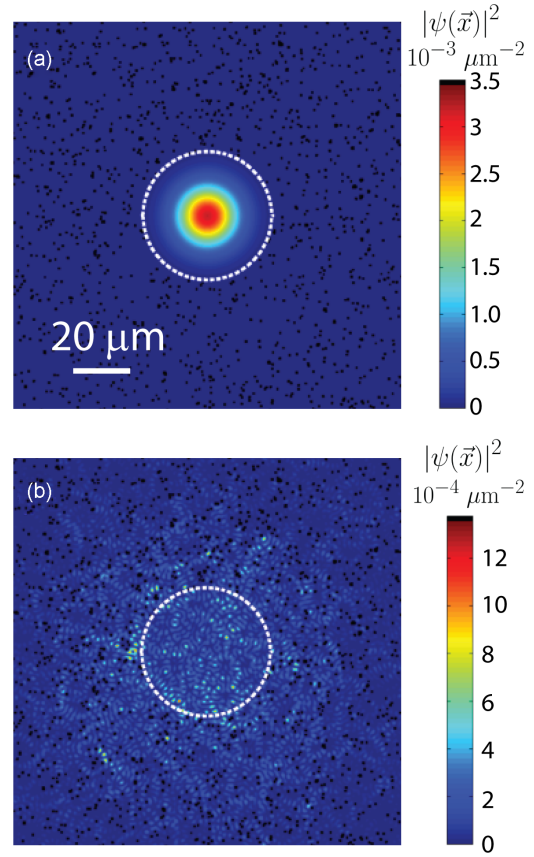


FIG. 8. (Color online) Simulated probability density distributions shown in false color from a time-dependent simulation of localization. A Gaussian wave packet initialized at $t = 0$ in the disorder-free region marked by the white dashed line is shown in (a). The wave function propagated forward in time for 146 ms is shown in (b). The potential barriers that constitute the disorder potential are magnified and marked in black for clarity. For these simulations, $\epsilon_k = k_B \times 25$ nK, $V_0 = k_B \times 1000$ nK, $w = 400$ nm, and $n = 0.08 \mu\text{m}^{-2}$.

allowed to expand into a disordered potential. The atoms propagate through the disorder potential and, through scattering, eventually adopt a localized profile. We numerically simulate independent realizations of a potential according to Eq. (1), with a disorder-free, circular region of radius R centered on the origin [see Fig. 8(a)]. As an initial condition, a Gaussian wave packet $\psi(\vec{x}, t = 0) \propto \exp[ikr - r^2/2(R/2.2)^2]$ with $kR \gg 1$ is prepared in the disorder-free region. The wave number k is varied from $0.07\text{--}0.4 \mu\text{m}^{-1}$, which corresponds to a kinetic energy from $k_B \times 3\text{--}100$ nK. The shift in the average kinetic energy of the wave packet resulting from the Gaussian envelope is less than 2% of ϵ_k .

The wave function is propagated according to Eq. (9) for total time $\tau = 146$ ms using time steps $\delta t = 14.6 \mu\text{s}$ in order to resolve the effects of the disorder potential energy on the wave function. During propagation, the wave packet disperses into the disorder potential, eventually forming a localized state

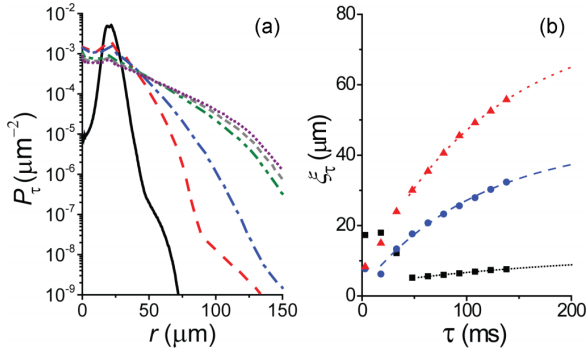


FIG. 9. (Color online) Procedure to determine ξ from the time-dependent simulations of localization. (a) Sample radial probability density showing the approach to a steady-state profile. The propagation times are $\tau = 3$ ms (solid black line), 15 ms (red dashed line), 30 ms (blue dot-dashed line), 90 ms (green dash-double-dotted line), 120 ms (short dashed line), and 150 ms (purple dotted line). For the data shown in this figure, $\epsilon_k = k_B \times 100$ nK, $V_0 = k_B \times 1000$ nK, $w = 400$ nm, and $n = 0.08 \mu\text{m}^{-2}$. (b) Fitted exponential decay lengths ξ_τ from data such as those in (a) for $\epsilon_k = k_B \times 100$ nK (red triangles), 35 nK (blue circles), and 3 nK (black squares). Only a fifth of the points generated for each value of ϵ_k are shown. The uncertainty in the points is too small to be visible. Fits of these data to an exponential function (lines) are used to extract the asymptotic value of the localization length ξ .

[Fig. 8(b)]. We perform an angular average of $|\psi(\vec{x}, \tau)|^2$ at fixed radius r , which is then averaged over multiple realizations of the disorder potential to produce the disorder-averaged radial probability density $P_r(r)$. Sample $P_r(r)$ for fixed disorder parameters $V_0 = k_B \times 1000$ nK, $w = 400$ nm, and $n = 0.08 \mu\text{m}^{-2}$ and kinetic energy $\epsilon_k = k_B \times 100$ nK are shown in Fig. 9(a). An exponential distribution at large r is rapidly achieved, which then expands and relaxes at long times to a static, localized state. We fit $P_r(r)$ to an exponential decay for $r = 43\text{--}50 \mu\text{m}$ for $\epsilon_k \leq k_B \times 10$ nK and $r = 57\text{--}68 \mu\text{m}$ for $\epsilon_k > k_B \times 10$ nK at each τ in order to determine the characteristic size ξ_τ of the propagated wave function. The asymptotic localization length ξ (that would be observed in an experiment probing atoms expanding through a disordered potential) is determined by fitting ξ_τ to an exponential function, discarding points at short times.

These numerical simulations enable us to benchmark the individual scattering technique against a calculation without any inherent approximations. A comparison is shown in Fig. 10. At the lowest energies, the single scattering approximation predicts localization lengths smaller than the de Broglie wavelength $2\pi/k$ of the particle, which occurs because $n\sigma < 2\pi/k$ and the approximation that $l_s = (n\sigma)^{-1}$ is violated. In contrast, the results of the time-dependent simulation always produce localization lengths greater than the de Broglie wavelength. For the regime in which $l_s = (n\sigma)^{-1}$ is a good approximation, the single scattering approximation provides an upper bound on the numerically determined localization length, as expected. At low energies, the single scattering approximation and results of the time-dependent simulations agree within an order of magnitude. The Born

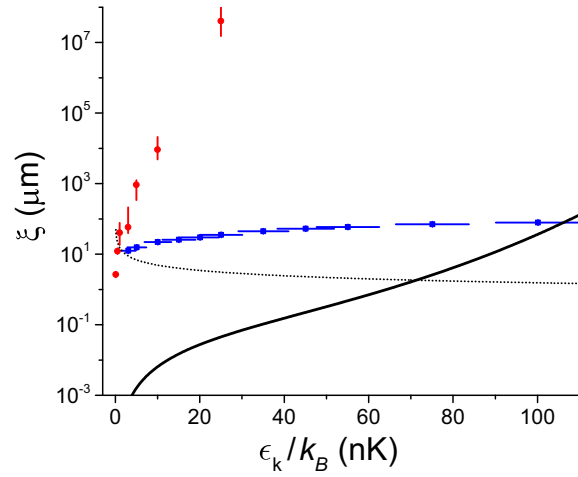


FIG. 10. (Color online) Comparison of localization lengths from a numerical simulation of the time-dependent Schrödinger equation (blue squares), from the perturbative correction to the independent scattering transport properties (red circles) and from the Born approximation (solid black line). For comparison, the de Broglie wavelength $2\pi/k$ is shown as a dotted line. The parameters used for this plot are $V_0 = k_B \times 1000$ nK, $w = 400$ nm, and $n = 0.08 \mu\text{m}^{-2}$. The error bars for the circles show the impact of the difference in the differential cross section across the inner and outer radii for the annulus shown in Fig. 5(c) and the standard deviation in the energy (resulting from the Gaussian envelope of the wave packet) for the squares.

approximation, however, is four orders of magnitude smaller than the numerically simulated ξ at low energies.

Finally, we calculate a localized density profile for a thermal gas of particles under conservative conditions (i.e., $n = 0.2 \mu\text{m}^{-2}$) using the simulated localization lengths from Fig. 7, corresponding to the single scattering approximation and exact scattering cross section. We assume that the density profile associated with each energy in the thermal ensemble is a radially symmetric exponential function centered at the origin with a decay length determined by a fit to the data in Fig. 7. The average density profile of a localized gas of 10 000 Maxwell-Boltzmann particles at temperature $T = 10$ nK is shown in Fig. 11. Dimensionality plays a helpful role since, unlike in three dimensions, the lowest particle energies (with the smallest localization lengths) are the most probable. Hence, most of the particles localize within a relatively small, experimentally accessible area. For example, at $T = 10$ nK, 90% of the particles are localized within a radius of $20 \mu\text{m}$. Furthermore, just 2.5% of the particles have energies below the percolation threshold and are classically trapped. A gas released into the disorder potential with a time-independent profile similar to that shown in Fig. 11 is straightforward to image with high signal-to-noise ratio and would provide a clear signature of two-dimensional AL. Since the single scattering approximation is an upper bound on the localization length observed in an expansion experiment, the localized thermal density profile should be smaller in extent than what is shown in Fig. 11.

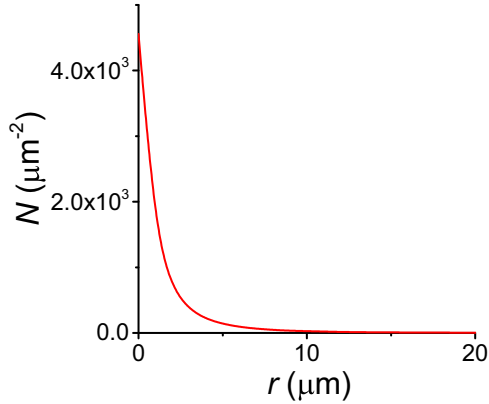


FIG. 11. (Color online) Thermal density profile for $V_0 = k_B \times 9947$ nK, $w = 400$ nm, $n = 0.2 \mu\text{m}^{-2}$, and $T = 10$ nK. Here, N is the two-dimensional number density for 10 000 particles.

V. CONCLUSION

We have identified an experimentally feasible approach to observation two-dimensional AL using ultracold atoms using pointlike disorder. Our approach requires nanoKelvin-scale temperatures in conjunction with a dilute, strongly scattering disordered potential. By using a single scattering approximation and exact numerical simulations, we predict observable localization lengths for realistic particle energies. This method can be extended to interacting systems such as a gas composed of two spin states of fermionic atoms, which may enable exploration of the analog of two-dimensional metal-insulator transitions [13–15].

ACKNOWLEDGMENTS

We thank W. Shirley for assistance with numerical simulations of wave-packet propagation. We acknowledge support from the NSF under Grant No. PHY12-05548 and from the ARO under Grant No. W9112-1-0462.

APPENDIX A: INDIVIDUAL SCATTERING SIMULATION

In simulations of scattering from a single Gaussian potential barrier, square grids were employed ranging from $L^2 = 3600$ to $10\,000 \mu\text{m}^2$ with discretization sizes of 0.01 to $0.25 \mu\text{m}$. The size of the time steps was scaled with the shorter of the two physical length scales in the system, the disorder width w , and the particle de Broglie wavelength $2\pi/k$, according to $\delta t = 50.1 \text{ ns}/\mu\text{m}$. Approximately 16 000 time steps were taken, which allowed the wave function initially at the center of the potential to scatter outward through roughly $L/2$, independent of the group velocity. Propagation for longer times resulted in significant errors induced by boundary and finite-size effects, manifest as a periodic modulation of the scattered wave. The scattered wave function was sampled between radii of 3–5 μm in order to determine the scattering amplitude.

APPENDIX B: TIME-DEPENDENT SIMULATION OF ANDERSON LOCALIZATION

We used a 1536×1536 discretization of the system area $349 \times 349 \mu\text{m}^2$ and populated the region $r > R$ with pointlike disorder given by

$$V(\vec{x}) = \sum_i V_0 e^{-\left(\frac{\vec{x}-\vec{x}_i}{w}\right)^2}, \quad (\text{B1})$$

where the coordinates \vec{x}_i are chosen randomly with the constraint that $r_i > R = 21.8 \mu\text{m}$. We choose $w = 400$ nm, $V_0 = k_B \times 1000$ nK, and $n = 0.08 \mu\text{m}^{-2}$, which corresponds to disorder strong enough to produce localization within the simulation space while remaining computationally tractable.

We include an imaginary potential component near the edges of the system grid in order to absorb a probability current approaching the periodic boundary. This enables dynamical simulations to continue for the long times necessary to observe localization. The absorbing boundary potential is given by

$$V = \begin{cases} -iB \frac{r}{r_{\text{max}}}, & |x|, |y| > 304 \mu\text{m} \\ 0 & \text{otherwise,} \end{cases} \quad (\text{B2})$$

with $r_{\text{max}} = 349 \mu\text{m}$ and $B = k_B \times (5 \times 10^{-5})$ nK.

-
- [1] P. W. Anderson, *Phys. Rev.* **109**, 1492 (1958).
 - [2] B. Kramer and A. MacKinnon, *Rep. Prog. Phys.* **56**, 1469 (1993).
 - [3] T. Schwartz, G. Bartal, S. Fishman, and M. Segev, *Nature (London)* **446**, 52 (2007).
 - [4] H. Hu, A. Strybulevych, J. H. Page, S. E. Skipetrov, and B. A. van Tiggelen, *Nat. Phys.* **4**, 945 (2008).
 - [5] J. Billy, V. Josse, Z. Zuo, A. Bernard, B. Hambrecht, P. Lugan, D. Clément, L. Sanchez-Palencia, P. Bouyer, and A. Aspect, *Nature (London)* **453**, 891 (2008).
 - [6] G. Roati, C. D’Errico, L. Fallani, M. Fattori, C. Fort, M. Zaccanti, G. Modugno, M. Modugno, and M. Inguscio, *Nature (London)* **453**, 895 (2008).
 - [7] S. S. Kondov, W. R. McGehee, J. J. Zirbel, and B. DeMarco, *Science* **334**, 66 (2011).
 - [8] F. Jendrzejewski, A. Bernard, K. Müller, P. Cheinet, V. Josse, M. Piraud, L. Pezzé, L. Sanchez-Palencia, A. Aspect, and P. Bouyer, *Nat. Phys.* **8**, 398 (2012).
 - [9] W. R. McGehee, S. S. Kondov, W. Xu, J. J. Zirbel, and B. DeMarco, *Phys. Rev. Lett.* **111**, 145303 (2013).
 - [10] M. Robert-de-Saint-Vincent, J.-P. Brantut, B. Allard, T. Plisson, L. Pezzé, L. Sanchez-Palencia, A. Aspect, T. Bourdel, and P. Bouyer, *Phys. Rev. Lett.* **104**, 220602 (2010).
 - [11] S. Krinner, D. Stadler, J. Meineke, J.-P. Brantut, and T. Esslinger, *Phys. Rev. Lett.* **110**, 100601 (2013).
 - [12] M. C. Beeler, M. E. W. Reed, T. Hong, and S. L. Rolston, *New J. Phys.* **14**, 073024 (2012).
 - [13] S. V. Kravchenko and M. P. Sarachik, *Int. J. Mod. Phys. B* **24**, 1640 (2010).

- [14] A. M. Goldman, *Int. J. Mod. Phys. B* **24**, 4081 (2010).
- [15] E. Abrahams, S. V. Kravchenko, and M. P. Sarachik, *Rev. Mod. Phys.* **73**, 251 (2001).
- [16] R. C. Kuhn, O. Sigwarth, C. Miniatura, D. Delande, and C. A. Mueller, *New J. Phys.* **9**, 161 (2007).
- [17] B. Shapiro, *J. Phys. A* **45**, 143001 (2012).
- [18] M. Piraud, L. Pezzé, and L. Sanchez-Palencia, *New J. Phys.* **15**, 075007 (2013).
- [19] J. W. Essam, *Rep. Prog. Phys.* **43**, 833 (1980).
- [20] K. S. Mendelson, *Phys. Rev. E* **56**, 6586 (1997).
- [21] R. Zallen and H. Scher, *Phys. Rev. B* **4**, 4471 (1971).
- [22] J. W. Goodman, *Speckle Phenomena in Optics: Theory and Applications* (Roberts, Greenwood Village, CO, 2007).
- [23] M. Pasienski, D. McKay, M. White, and B. DeMarco, *Nat. Phys.* **6**, 677 (2010).
- [24] S. S. Kondov, W. R. McGehee, W. Xu, and B. DeMarco, *Phys. Rev. Lett.* **114**, 083002 (2015).
- [25] B. Gadway, D. Pertot, J. Reeves, M. Vogt, and D. Schneble, *Phys. Rev. Lett.* **107**, 145306 (2011).
- [26] K. O'Holleran, M. R. Dennis, F. Flossmann, and M. J. Padgett, *Phys. Rev. Lett.* **100**, 053902 (2008).
- [27] S. Pilati, S. Giorgini, M. Modugno, and N. Prokof'ev, *New J. Phys.* **12**, 073003 (2010).
- [28] A. Weinrib, *Phys. Rev. B* **26**, 1352 (1982).
- [29] L. Pezzé, M. R. de Saint-Vincent, T. Bourdel, J.-P. Brantut, B. Allard, T. Plisson, A. Aspect, P. Bouyer, and L. Sanchez-Palencia, *New J. Phys.* **13**, 095015 (2011).
- [30] E. Abrahams, P. W. Anderson, D. C. Licciardello, and T. V. Ramakrishnan, *Phys. Rev. Lett.* **42**, 673 (1979).
- [31] P. A. Lee, *Rev. Mod. Phys.* **57**, 287 (1985).
- [32] E. R. Dufresne, G. C. Spalding, M. T. Dearing, S. A. Sheets, and D. G. Grier, *Rev. Sci. Instrum.* **72**, 1810 (2001).
- [33] M. Pasienski and B. DeMarco, *Opt. Express* **16**, 2176 (2008).
- [34] A. L. Gaunt and Z. Hadzibabic, *Sci. Rep.* **2**, 721 (2012).
- [35] S. Mertens and C. Moore, *Phys. Rev. E* **86**, 061109 (2012).
- [36] K. Gottfried and T. Yan, *Quantum Mechanics: Fundamentals*, Graduate Texts in Contemporary Physics (Springer, New York, 2003).
- [37] X. Xu and T. Taha, *J. Math. Model. Algorithms* **2**, 185 (2003).

Appendix D

Reprint: Correlated Spin-Flip Tunneling in a Fermi Lattice Gas

The following is a reprint of W. Xu, W. Morong, H.-Y. Hui, V.W. Scarola, and B. DeMarco, *Correlated spin-flip tunneling in a Fermi lattice gas*, Physical Review A, **98**, 023623 [200].

Correlated spin-flip tunneling in a Fermi lattice gasWenchao Xu,^{1,*} William Morong,¹ Hoi-Yin Hui,² Vito W. Scarola,² and Brian DeMarco^{1,†}¹*Department of Physics, University of Illinois at Urbana-Champaign, Urbana, Illinois 61801, USA*²*Department of Physics, Virginia Tech, Blacksburg, Virginia 24061, USA*

(Received 4 November 2017; published 20 August 2018)

We report the realization of correlated, density-dependent tunneling for fermionic ^{40}K atoms trapped in an optical lattice. By appropriately tuning the frequency difference between a pair of Raman beams applied to a spin-polarized gas, simultaneous spin transitions and tunneling events are induced that depend on the relative occupations of neighboring lattice sites. This correlated spin-flip tunneling (CSFT) is spectroscopically resolved using gases prepared in opposite spin states, and the inferred Hubbard interaction energy is compared with a tight-binding prediction. We measure the doublons created by the laser-induced correlated tunneling process using loss induced by light-assisted collisions. Furthermore, by controllably introducing vacancies to a spin-polarized gas, we demonstrate that correlated tunneling is suppressed when neighboring lattice sites are unoccupied. We explain how the CSFT quench implemented here prepares and evolves a large number of resonating-valence-bond (RVB) singlets in a Hubbard model, thus allowing exploration of RVB dynamics.

DOI: [10.1103/PhysRevA.98.023623](https://doi.org/10.1103/PhysRevA.98.023623)**I. INTRODUCTION**

Measurements on ultracold atoms trapped in optical lattices have emerged as a powerful approach to studying quantum phase transitions and dynamics in strongly correlated systems. Periodic driving forces and light-induced tunneling combined with optical lattices have enabled experiments to achieve physics beyond the minimal Hubbard model (see Ref. [1] for a recent review). For example, magnetic phase transitions have been probed [2,3], synthetic gauge fields realized [4–7], and nontrivial band structures [8] have been created using periodic driving and external fields in lattices.

In this work, we use applied laser fields to demonstrate and study the dynamics of correlated tunneling that depends on density and spin for fermionic atoms. Correlated tunneling, known in solids as a bond-charge interaction, has been proposed to play a role in high-temperature superconductivity [9] and lattice stiffening in polyacetylene [10,11]. The influence of correlated tunneling on transport properties has also been intensively investigated in quantum dots, where it can be manipulated by gate voltages and applied electromagnetic fields [12]. Beyond mimicking these effects in optical lattices, correlated tunneling for ultracold atoms has attracted theoretical interest for inducing occupation-dependent gauge fields [13], obtaining novel phases such as holon and doublon superfluids [14], and realizing anyonic Hubbard models [15]. Thus far, two-body correlated tunneling has been realized in double wells for bosons [16,17] and fermions [18]. However, many-body density-dependent tunneling has been directly observed only for bosonic atoms trapped in optical lattices [19,20].

Inspired by the theoretical proposals in Ref. [21], we implement an experimental approach to generate spin- and density-dependent tunneling for fermionic atoms. This technique is fundamentally different from those already used to realize intersite interactions in two key ways. First, prior approaches [16–20,22] conserve spin, whereas the spin flips induced via our method can lead to more exotic physics. Second, the intersite interaction generated in our work is between fermionic atoms and spans the entire lattice, which leads to challenging many-body physics due to the fermion sign problem [23]. Our method is therefore able to prepare quantum many-body steady and excited states beyond the scope of previous experiments and exceeding the capabilities of current unbiased numerical modeling tools in two and three spatial dimensions. Specifically, we show that CSFT effectively creates singlet pairs to dynamically build RVB correlations [24,25] in a Hubbard model. Prior work created RVB singlets in four-site plaquettes in an optical superlattice [26]. Here we demonstrate a method to build up RVB correlations in large numbers of singlet pairs, which can be used to explore the many-body RVB states proposed by Anderson in the context of lattice models of high-temperature superconductivity.

To implement spin- and density-dependent tunneling, we apply a pair of Raman beams to a spin-polarized gas, for which conventional tunneling is forbidden by the Pauli exclusion principle. The Raman beams flip the atomic spins and induce density-dependent tunneling. We spectroscopically resolve these CSFT events, and the corresponding increase in doubly occupied sites is measured using loss from light-assisted collisions. Moreover, by varying the filling fraction in the lattice, we directly verify the density dependence of spin transitions.

The paper is organized as follows. In Sec. II we discuss the experimental setup used to observe CSFT. In Sec. III we discuss modeling of CSFT in the leading order dynamics. In Sec. IV we present measurements of spin transfer fraction and

*Now at Department of Physics, Massachusetts Institute of Technology, 77 Massachusetts Ave, Cambridge, MA 02139, USA.

†bdemarco@illinois.edu

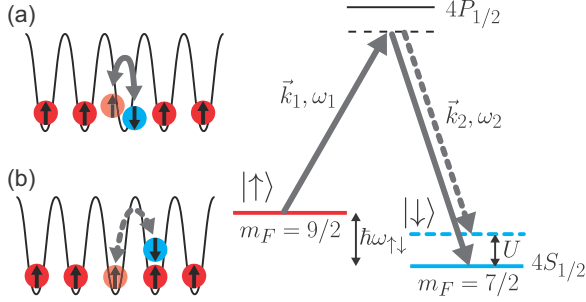


FIG. 1. Schematic diagram of Raman transitions. A pair of Raman beams, each detuned approximately 80 GHz from the $4S_{1/2} \rightarrow 4P_{1/2}$ transition, with frequencies $\omega_{1,2}$ and wave vectors $\vec{k}_{1,2}$ are applied to drive transitions between the $|\uparrow\rangle$ (red) and $|\downarrow\rangle$ (blue) states. The Raman wave-vector difference $\delta\vec{k} = \vec{k}_1 - \vec{k}_2$ lies along the $(-1, -1, 1)$ direction of the lattice. Selecting between two distinct processes is achieved by fixing the laser beam frequency ω_1 and tuning ω_2 . (a) If the frequency difference matches the Zeeman energy (i.e., $\Delta\omega = \omega_1 - \omega_2 = \omega_{\uparrow\downarrow}$), then atoms flip their spin and remain on the same site. (b) When the laser frequency difference accommodates the Hubbard interaction energy U ($\Delta\omega = \omega_{\uparrow\downarrow} - U/\hbar$), then CSFT occurs and atoms tunnel to neighboring occupied sites and flip their spin. For $|\downarrow\rangle$ as an initial state, the condition for resonant CSFT changes to $\Delta\omega = \omega_{\uparrow\downarrow} + U/\hbar$.

double occupancy to observe CSFT, and we summarize and discuss potential improvements to the experiment in Sec. V.

II. EXPERIMENTAL SETUP

These measurements are performed using a degenerate Fermi gas composed of ^{40}K atoms trapped in a cubic optical lattice in a regime described by a single-band Fermi-Hubbard model with tunneling energy t and interaction energy U (see Appendix A for details of the experimental sequence). We work in the $U/t \gtrsim 12$ regime, for which the ground state of a spin-mixed trapped gas possesses a Mott-insulator core [27]. Overall confinement is provided by a 1064 nm optical dipole trap. After cooling the gas in the dipole trap and before slowly superimposing the lattice, the gas is spin polarized in either the $|F = 9/2, m_F = 9/2\rangle$ or $|F = 9/2, m_F = 7/2\rangle$ state, which we label $|\uparrow\rangle$ and $|\downarrow\rangle$. The atom number and confinement are tuned so that the central density is approximately one atom per site, with the Fermi energy $E_F \approx 7t$. A pair of Raman beams with wave vectors \vec{k}_1 and \vec{k}_2 intersecting at approximately 30° are focused onto the gas and pulsed to drive spin transitions (Fig. 1). The frequency difference $\Delta\omega = \omega_1 - \omega_2$ between the Raman beams is tuned near to the $|\uparrow\rangle \rightarrow |\downarrow\rangle$ resonance. After a Raman pulse, the number of atoms in each band and spin state is measured using band mapping with a magnetic-field gradient applied during time-of-flight imaging. Atom number loss and heating induced by the Raman pulse are discussed in detail in Appendix A. We observe an approximately 20% atom loss during a (typical) 50 ms pulse due to off-resonant light scattering, which occurs at a relatively high rate because of the limited tuning range of the Raman laser. Heating from the Raman pulse is comparable with that from other sources, and we do not observe atoms excited to higher-energy bands.

The Raman beams can drive two resonant processes depending on $\Delta\omega$. If $\Delta\omega$ is tuned to the energy difference between spin states ($\Delta\omega = \omega_{\uparrow\downarrow}$), then on-site spin rotations occur without induced tunneling and changes in site occupancies Fig. 1(a). We define this process as the carrier transition. By tuning the frequency difference between the beams to include U ($\Delta\omega - \omega_{\uparrow\downarrow} = \pm U/\hbar$), density-dependent tunneling is driven as a sideband to the carrier [Fig. 1(b)]. Other processes, such as interband transitions, are far off resonant for the experimental parameters (see Appendix A).

III. CORRELATED SPIN-FLIP TUNNELING

To model the dynamics we consider an initially polarized band insulator with driven spin-flip tunneling events. Working in the large U limit, we use perturbation theory to find the effective Hamiltonian term describing CSFT:

$$H_{\text{CSFT}} = \sum_{i,j \in \text{n.n.}} K_{ij} n_{i\uparrow} (1 - n_{j\downarrow}) c_{j\uparrow}^\dagger c_{i\downarrow} + \text{H.c.} \quad (1)$$

(see Appendix B for derivation). Here, $i, j \in \text{n.n.}$ denotes a sum over nearest-neighboring sites and permutations, $c_{i\sigma}^\dagger$ ($c_{i\sigma}$) creates (removes) a particle on site i in spin state σ , and $n_{i\sigma}$ is the number of particles on site i in state σ .

CSFT arises as a spin-flip transition to a virtual state offset by U followed by a tunneling event. In contrast to the conventional tunneling term $-tc_i^\dagger c_j$ in the Fermi-Hubbard model, this laser-induced correlated spin-flip tunneling is density dependent and accompanied by a spin rotation. CSFT occurs only when neighboring sites are occupied by atoms in the same spin state or when a doublon (i.e., a $|\uparrow\rangle|\downarrow\rangle$ pair) is next to an empty site. Using a particle-hole transformation, we show (see Appendix B) that Eq. (1) effectively creates singlets to build RVB correlations [25].

The CSFT matrix element is complex and tunable. It is given by (Appendix B)

$$K_{ij} \approx \frac{t\Omega}{2U} (e^{-i\delta\vec{k}\cdot\vec{R}_j} - e^{-i\delta\vec{k}\cdot\vec{R}_i}), \quad (2)$$

where the ratio $t/U \approx 0.04\text{--}0.08$ is controlled by the lattice potential depth s , \vec{R}_i is the location of site i , and $\delta\vec{k}$ is the Raman wave-vector difference. For our lattice, $|\delta\vec{k} \cdot (\vec{R}_i - \vec{R}_j)| = \pi/2\sqrt{3}$ is the same for every lattice direction. The Rabi rate for the carrier transition $|\Omega|/\hbar \approx 2\pi \times 650$ Hz is controlled by the Raman laser intensity and measured via Rabi oscillations (Appendix B), and therefore $|K_{ij}|/\hbar \approx 2\pi \times 6\text{--}22$ Hz for our measurements.

Equation (1) is the leading order in a large U expansion and has been projected into the subspace connected to the initial spin-polarized $|\uparrow\rangle$ state by resonant CSFT. Other terms can, in principle, contribute to the dynamics. We have verified that the dynamics of the full tight-binding CSFT model (i.e., without the large U approximation) are reproduced by Eq. (1) by applying the time-evolving block decimation algorithm [28] to 1D chains (see Appendix B).

The site-dependent Raman phase in K_{ij} that arises from the Raman wave-vector difference is critical to allow tunneling to occur. When spin rotations are driven by long-wavelength radiation or copropagating Raman beams, this phase factor is absent, and tunneling is prevented. One reason for the absence

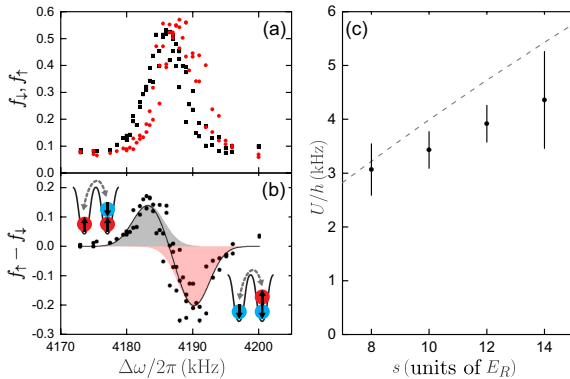


FIG. 2. Spectroscopy of CSFT. (a) The fraction of atoms transferred between spin states by a 50 m Raman pulse is shown for an initially $|\uparrow\rangle$ (black squares, f_{\uparrow}) and $|\downarrow\rangle$ (red circles, f_{\downarrow}) spin-polarized state at $s = 10 E_R$ for varied $\Delta\omega$. For these measurements, $N = 25400 \pm 3900$ atoms were cooled to $T/T_F = 0.24 \pm 0.08$ before turning on the lattice. Each data point is the result from a single experimental run, and the measurement uncertainty is not visible on this scale. Nonzero transfer at large detuning is due to off-resonant spontaneous Raman scattering. (b) The difference $f_{\uparrow} - f_{\downarrow}$ for pairs of points in (a) reveals the CSFT sidebands at approximately $\pm U$. The black line shows a fit to a sum of two Gaussian functions; the individual Gaussians are displayed as shaded regions. The peak at lower (higher) frequency corresponds to CSFT for an initially $|\uparrow\rangle$ ($|\downarrow\rangle$) spin-polarized state. (c) The interaction energy U inferred from fits to data such as those shown in (b) for varied s . The error bars are derived from the fit uncertainty. The dashed line is the value of U from a standard tight-binding calculation.

of tunneling in this scenario can be understood as destructive interference between multiple tunneling pathways caused by the antisymmetrization of the fermionic wave functions (see Appendix C). This effect is related to the behavior of clock shifts for fermionic atoms [29–31]. In our case, the Raman phase factor suppresses the destructive tunneling interference.

IV. OBSERVATION OF CORRELATED SPIN-FLIP TUNNELING

A. Transfer fraction spectroscopy

We spectroscopically resolve CSFT and distinguish it from on-site spin rotations by measuring the change in spin fraction after a 50 m Raman pulse, which is comparable to the CSFT π time. Sample data are shown in Fig. 2(a) for the fraction $f_{\downarrow, \uparrow}$ of atoms transferred between spin states at varied $\Delta\omega$ for $s = 10 E_R$, where $E_R = \hbar^2/8md^2$ is the recoil energy, m is the atomic mass, and $d \approx 390$ nm is the lattice spacing. Broadening of the carrier transition, which is consistent with contributions from magnetic field and Raman phase noise (see Appendix B), results in a feature that obscures CSFT. To isolate CSFT, we therefore subtract the data taken at identical $\Delta\omega$ with opposite initial spin configurations. Since the carrier frequency does not depend on the initial state, the contribution from the broad carrier feature is canceled out by this procedure. In contrast, the frequency offset of the CSFT sideband changes sign with the initial spin configuration and is not removed by

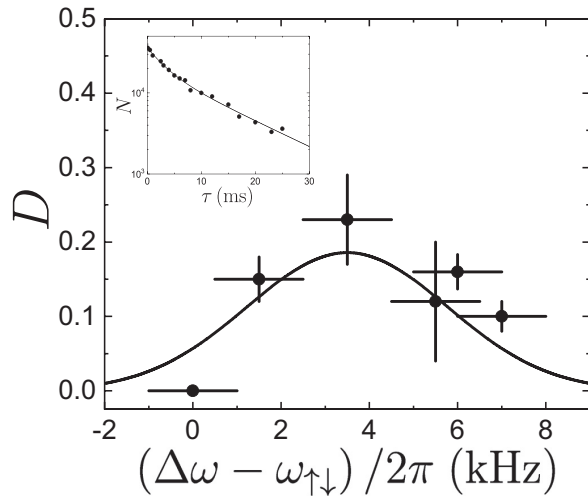


FIG. 3. Fraction of doubly occupied sites D measured after a 50 m Raman pulse at various detunings for $s = 10 E_R$. The inset shows sample LAC for $(\Delta\omega - \omega_{\uparrow\downarrow})/2\pi = 3.5$ kHz fit to a double-exponential decay with $\tau_D = 3.1 \pm 0.77$ ms and $\tau_S = 13.7 \pm 2.5$ ms. The vertical error bars in D are derived from fits to similar data acquired at different $\Delta\omega$, while the horizontal error bars show the estimated 0.5 kHz uncertainty in the carrier transition from magnetic-field drift. The solid line in the main panel is the fit from Fig. 2(a) for $|f_{\uparrow} - f_{\downarrow}|$ plotted on the same scale as D .

the subtraction. The resulting line shape for $f_{\uparrow} - f_{\downarrow}$ shown in Fig. 2(b) therefore reveals the CSFT sidebands as peaks offset at approximately $\pm U/\hbar \approx \pm 2\pi \times 3.5$ kHz from the carrier transition.

To compare with the predicted sideband frequency, we fit the $f_{\uparrow} - f_{\downarrow}$ line shape to a sum of two Gaussian functions with independent central frequencies and standard deviations as free parameters. The interaction energy U determined from this fit as half of the frequency separation of the peaks is shown in Fig. 2(c) for data taken at different lattice potential depths. The inferred U increases less rapidly with s than the tight-binding prediction, which is shown as a dashed line. A similar disagreement has been observed in other experiments [32]. The source of this discrepancy is unresolved and cannot be explained by renormalization of U by the Raman process, which is approximately a 1% effect (see Appendix B).

B. Double occupancy spectroscopy

To isolate CSFT from other dynamics, we measure changes in the doublon number. As doublon formation and decay are strongly suppressed at high interaction strength in the standard Hubbard model [33], doublon generation provides a signature of CSFT dynamics. We probe doublon creation using loss induced by light-assisted collisions (LAC) [34]. The carrier frequency $\omega_{\uparrow\downarrow}$ is estimated using a Gaussian fit to Raman spectroscopy taken using a 0.7 m pulse, which is too short to drive CSFT. The inset to Fig. 3 shows sample LAC data taken after a 50 m Raman pulse with $(\Delta\omega - \omega_{\uparrow\downarrow})/2\pi = 3.5$ kHz, which corresponds to the $+U$ CSFT sideband. Immediately following the Raman pulse, the lattice potential depth is rapidly

increased to $29 E_R$ to arrest further dynamics. We measure the number of atoms remaining after a laser pulse 50 MHz detuned from the $4S, F = 9/2 \rightarrow 5P_{3/2}, F = 11/2$ transition is applied to the gas. Two loss processes are evident as the duration τ of the resonant laser pulse is changed. The loss on a fast time scale τ_D corresponds to LAC removing atoms from doubly occupied sites, while the decay over a slower time scale τ_S results from single atoms ejected from the dipole trap via spontaneous scattering. These data are fit to a double exponential decay function $N(\tau) = N_D e^{-\tau/\tau_D} + (N - N_D) e^{-\tau/\tau_S}$ with $N, N_D, \tau_D,$ and τ_S as free parameters to determine the fraction of doubly occupied sites $D = N_D/N$.

Measurements of D as $\Delta\omega$ is changed show that a resonance for doublon creation is centered near the CSFT spectroscopy sideband peak at $(\Delta\omega - \omega_{\uparrow\downarrow}) \approx U/\hbar$ (Fig. 3). The doublon dynamics near the resonance agree with the rate predicted by H_{CSFT} (see Fig. 7 in Appendix B) and indicate that D has reached a steady state. We therefore compare the data with the fit from Fig. 2(b) to $|f_{\uparrow} - f_{\downarrow}|$, which can be interpreted as the fraction of atoms that flip their spin during CSFT events. The close agreement between the fit and D implies that each spin flip is associated with the creation of a doublon.

C. Vacancy dependence of transfer fraction

Finally, we demonstrate the sensitivity of CSFT to site occupancy by reducing the atom number and controllably introducing vacancies before a Raman pulse on the CSFT sideband (see Fig. 4 inset). Our technique involves three steps. After turning on the lattice to $s = 8 E_R$, atoms are transferred from a spin-polarized initial state (either $|\uparrow\rangle$ or $|\downarrow\rangle$), as in Fig. 2) to the $F = 7/2, m_F = 7/2$ state via adiabatic rapid passage (ARP) driven by a microwave-frequency magnetic field. The power of the microwave field (swept across 0.4 MHz in 0.5 m) is varied to control the probability of a transition between hyperfine states. The fraction δN of atoms that are not transferred to $F = 7/2$ are removed from the lattice with a 0.5 m pulse of light resonant with the $4S, F = 9/2 \rightarrow 5P_{3/2}, F = 11/2$ transition. A second ARP sweep (across 0.8 MHz in 1 m) returns all of the atoms shelved in the $F = 7/2$ manifold to the initial spin state.

After this procedure, unoccupied sites are randomly distributed through the spin-polarized atomic density distribution. The presence of holes suppresses CSFT, which can only occur when adjacent sites are occupied. We probe this effect by measuring changes in $|f_{\uparrow} - f_{\downarrow}|$ for a 40 m Raman pulse with $\Delta\omega$ fixed on the $\pm U$ peaks of the CSFT sideband (Fig. 4). Because the doublon population has saturated (see Fig. 7 in Appendix B), $|f_{\uparrow} - f_{\downarrow}|$ coincides with the number of nearest-neighbor pairs. As the number of atoms is reduced and the hole density increases, $|f_{\uparrow} - f_{\downarrow}|$ decreases, indicating that fewer atoms can participate in CSFT. The data shown in Fig. 4 show good agreement with a prediction of the probability for adjacent sites to be occupied (see Appendix D). For this calculation, the density profile is computed using entropy matching based on s , the overall confinement, and the measured N and T/T_F . The probability of adjacent sites being occupied is determined by averaging over configurations that involve randomly removing a fraction δN of atoms from the simulated density profile.

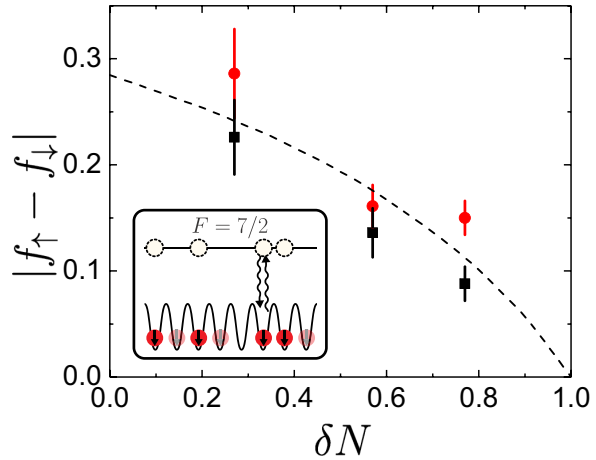


FIG. 4. Density dependence of CSFT. The CSFT spectroscopy signal taken with fixed $(\Delta\omega - \Delta\omega_{\uparrow\downarrow}) \approx \pm U/\hbar$ is shown for varied fraction δN of atoms randomly removed from an $s = 8 E_R$ lattice gas. For these data, $N = 47\,000\text{--}81\,000$, and the gas was cooled to $T/T_F \approx 0.35$ before turning on the lattice. Data obtained with the $+U$ sideband are shown as red circles and those for $-U$ as black squares. The sideband frequencies were determined using a double-Gaussian fit to CSFT spectroscopy data, as in Fig. 2(b). The dashed line is a prediction for the probability to find adjacent sites occupied based on a calculation of the density profile after the removal procedure. The inset shows the procedure for controllably introducing vacancies. Atoms (shown as transparent) that are not shelved in the $F = 7/2$ state via microwave transitions are removed using resonant light.

V. CONCLUSION

We have reported an observation of density-dependent tunneling in a many-body optical lattice Fermi-Hubbard model. In the future, the spontaneous scattering rate and associated heating and loss can be reduced by a factor of 50 (at constant K) and rendered insignificant by using a laser tuned to an optimal point between the $D1$ and $D2$ transitions, which for ^{40}K is at 768.67 nm [35]. Furthermore, reducing the sources of carrier-broadening technical noise by a factor of 3.5 or using a Feshbach resonance to enhance U would enable the CSFT and carrier transitions to be separately resolved.

The technique we have developed may be used to directly prepare and dynamically evolve RVB order or to observe other exotic states, such as bond-ordered waves, triplet pairing, and hole superconductivity [21]. The site-dependent phase of the bond-charge interaction the Raman lasers introduce also leads to a synthetic gauge field that was not explored in this work. The unique properties of the occupation-dependent gauge field created via this method can be used to simulate interacting relativistic quantum field theories and correlated topological insulators [21].

ACKNOWLEDGMENTS

W.X., W.M., and B.D. acknowledge support from the Army Research Office (Grant No. W911NF-17-1-0171) and National Science Foundation (Grant No. PHY 15-05468). V.W.S. and

H.H. acknowledge support from the Air Force Office of Scientific Research (Grant No. FA9550-11-1-0445) and the Army Research Office (Grant No. W911NF-16-1-0182).

APPENDIX A: EXPERIMENTAL SEQUENCE AND PARAMETERS

Ultracold gases composed of ground-state ^{40}K atoms in the $|F = 9/2, m_F = 9/2\rangle$ and $|F = 9/2, m_F = 7/2\rangle$ states are cooled to temperatures below the Fermi temperature T_F in a crossed-beam 1064 nm optical dipole trap using standard techniques. After evaporative cooling, the optical trap depth is increased to the same value for all the data presented in this paper. The resulting dipole trap frequencies are 7.9 ± 0.4 Hz, 98 ± 1 Hz, and 114 ± 2 Hz. A microwave-frequency swept magnetic field combined with a static magnetic-field gradient are used to remove all atoms in one hyperfine state, thereby preparing a spin-polarized gas with a purity of greater than 95% for either spin state. Following spin polarization, we ramp on the three pairs of lattice beams ($\lambda = 782.2$ nm) in 100 ms. The Raman beams are derived from a cavity-stabilized diode laser (Vortex II TLB-6900) and are 80 GHz red detuned from the $D1$ transition. The frequency and power of each beam are controlled using an acousto-optic modulator.

A 13 G magnetic field is used to lift the degeneracy of Zeeman transitions between different m_F states. The field provides a 27 kHz difference between the $m_F = 9/2 \rightarrow 7/2$ and $m_F = 7/2 \rightarrow 5/2$ transitions. No significant population of $m_F = 5/2$ atoms has been observed in our measurements. The drift in the magnetic field is about 10 mG from day to day and 3 mG over the course of a two-hour measurement run.

The magnetic field is reduced to 3 G for imaging. The lattice is ramped down over 100 μs to map band populations onto the momentum distribution [36], and then the dipole trap is turned off for time-of-flight expansion. An additional magnetic-field gradient is applied during time of flight to spatially separate the two spin components. A Gaussian distribution is used to fit the images of each spin component and determine the corresponding atom number.

The minimum band gap (at the band edge) in this work is 31 kHz. For the approximately 10 kHz Raman detunings (from the carrier transition) we sample, the probability for interband transitions is therefore negligible. Furthermore, we do not observe excited band population for any of the measurements discussed here.

We observe loss of atoms and heating caused by light scattering from the Raman beams. We characterized this process, which is not fully understood for strongly interacting systems,

using measurements at $s = 12 E_R$. The measured exponential decay constant for N at $s = 12 E_R$ for Raman-induced loss varied from 130 ± 20 ms to 310 ± 50 ms during the time period when data were acquired. The weighted average of the measured lifetime at $s = 12 E_R$ was 200 ± 10 ms, which is much longer than the Raman pulses used in this work. Heating is more difficult to measure, given that determining temperature for strongly correlated lattice gases is an outstanding problem. To estimate the heating rate, we measure the temperature in the dipole trap after slowly turning off the lattice. Using this method, we observed a 0.30 ± 0.02 nK/ms heating rate at $s = 12 E_R$. The measured heating rate without a Raman pulse is 0.13 ± 0.01 nK/ms. We conclude that heating from the Raman pulse is comparable to that from other sources. Furthermore, these data do not show a strong dependence of the heating rate on atom number: the temperature of the gas increases linearly in time, even though the atom number decays (for this measurement) from approximately 2.8×10^4 to 1.7×10^4 over 80 ms. We also note that the light scattering (and heating and loss rates) could be reduced by a factor of 50 (without changing the Raman Rabi rate) for ^{40}K atoms by using a different laser capable of tuning to 768.67 nm [35]. Moreover, using an atom with a different electronic structure could achieve scattering rates that are many orders of magnitude smaller.

For comparison to theory, U is determined from the lattice depth (as measured by lattice spectroscopy) [37] according to

$$U = \frac{4\pi\hbar^2 a_s}{m} \int |\psi_i(\vec{x})|^4 d^3\vec{x}, \quad (\text{A1})$$

where $a_s \approx 174a_0$ is the free-space scattering length between the spin states [38], m the atomic mass, and $\psi_i(\vec{x})$ the Wannier wave function derived from the tight-binding model. The uncertainty in U is estimated to be less than 2%, and we sample $U/t = 13\text{--}47$ in this work.

APPENDIX B: THEORETICAL DESCRIPTION OF EFFECTIVE CSFT HAMILTONIAN

1. Single-particle Hamiltonian

We first review the Raman-transition Hamiltonian in the absence of interactions and a lattice. Following the standard approach, we consider a three-level system and adiabatically eliminate the intermediate state. This procedure is valid in the $\Omega_{1,2} \ll \Delta_R$ and $\delta \ll \Delta_R$ limits (to be defined subsequently), both of which are well satisfied in our experiment.

The level diagram for the three-level atom is shown in Fig. 5. The Hamiltonian is

$$H_{3\text{-lev}} = \begin{pmatrix} \omega_{\uparrow\downarrow} & 0 & \frac{\Omega_1^*}{2} (e^{-i(\vec{k}_1 \cdot \vec{R} - \omega_1 t)} + \text{c.c.}) \\ 0 & 0 & \frac{\Omega_2^*}{2} (e^{-i(\vec{k}_2 \cdot \vec{R} - \omega_2 t)} + \text{c.c.}) \\ \frac{\Omega_1}{2} (e^{i(\vec{k}_1 \cdot \vec{R} - \omega_1 t)} + \text{c.c.}) & \frac{\Omega_2}{2} (e^{i(\vec{k}_2 \cdot \vec{R} - \omega_2 t)} + \text{c.c.}) & \omega_0 \end{pmatrix}, \quad (\text{B1})$$

which is written with respect to the $\{|\uparrow\rangle, |\downarrow\rangle, |3\rangle\}$ basis. Here, \vec{R} is the position of the atom, the laser frequencies satisfy $\omega_1 = \omega_0 - \Delta_R - \delta - \omega_{\uparrow\downarrow}$ and $\omega_2 = \omega_0 - \Delta_R$, and the individual Rabi rates $\Omega_{1,2} = -e\langle 3 | \vec{E}_{1,2} \cdot \vec{r} | \uparrow, \downarrow \rangle$ depend on the dipole

matrix elements for the atom-light (with electric field \vec{E}_i) interaction.

For the calculations in the main text and discussed in this document, we use a simplified model in which laser beam 1

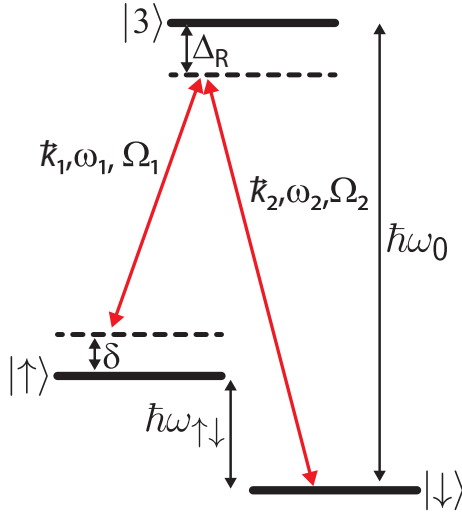


FIG. 5. Energy levels of three-level atoms with two lasers of frequencies ω_1 and ω_2 .

only couples $|\uparrow\rangle$ and $|3\rangle$, and laser beam 2 only couples $|\downarrow\rangle$ and $|3\rangle$. In the experiment, however, the polarizations of the Raman beams are such that both ground states are coupled to the (multilevel) excited state by both beams. The couplings that we neglect are far from any resonant Raman or single-photon transition and only lead to ac Stark shifts that can be absorbed into the definition of the ground spin states.

We make the rotating-wave approximation and a unitary transformation $H'_{3\text{-lev}} = e^{i \int^t V dt'} H_{3\text{-lev}} e^{-i \int^t V dt'} - V$ with

$$V = \begin{pmatrix} \omega_{\uparrow\downarrow} + \delta & 0 & 0 \\ 0 & 0 & 0 \\ 0 & 0 & \omega_0 - \Delta_R \end{pmatrix}, \quad (\text{B2})$$

which is similar to a transformation to a rotating frame. Projecting $H'_{3\text{-lev}}$ onto the subspace $\{|\uparrow\rangle, |\downarrow\rangle\}$, under the condition $|\Omega_1| \approx |\Omega_2| \ll \Delta_R$, yields

$$H_{2\text{-lev}} \approx \begin{pmatrix} \delta & \frac{\Omega}{2} e^{-i\vec{\delta}\vec{k}\cdot\vec{R}} \\ \frac{\Omega^*}{2} e^{i\vec{\delta}\vec{k}\cdot\vec{R}} & 0 \end{pmatrix}, \quad (\text{B3})$$

for an effective Hamiltonian, where $\Omega = -\Omega_1^* \Omega_2 / 2\Delta_R$ and $\vec{\delta}\vec{k} = \vec{k}_1 - \vec{k}_2$. This projection is equivalent to adiabatically eliminating the excited electronic state. These two levels act as the pseudospin basis used in the main part of the text.

2. Lattice and interaction effects

In the presence of an optical lattice, we project the Hamiltonian onto the lowest Bloch band of the lattice. We denote the Wannier function centered at the site located at \vec{R}_i as $\psi_i(\vec{r}) = \psi(\vec{r} - \vec{R}_i)$ and $c_{i\sigma}^\dagger$ as the operator that creates a fermion with spin σ at that site. The full tight-binding Hamiltonian is

$$\begin{aligned} H_0 = & -t \sum_{(ij)\sigma} (c_{i\sigma}^\dagger c_{j\sigma} + \text{H.c.}) \\ & + \sum_{(ij)} \left(\frac{\Omega}{2} e^{-i\vec{\delta}\vec{k}\cdot\frac{\vec{R}_i+\vec{R}_j}{2}} \Psi_{ij} c_{i\uparrow}^\dagger c_{j\downarrow} + i \leftrightarrow j + \text{H.c.} \right) \\ & + \sum_i \left(\frac{\Omega}{2} \Psi_0 e^{-i\vec{\delta}\vec{k}\cdot\vec{R}_i} c_{i\uparrow}^\dagger c_{i\downarrow} + \frac{\Omega^*}{2} \Psi_0 e^{i\vec{\delta}\vec{k}\cdot\vec{R}_i} c_{i\downarrow}^\dagger c_{i\uparrow} \right) \\ & + \frac{\delta}{2} \sum_i (n_{i\uparrow} - n_{i\downarrow}) + U \sum_i n_{i\uparrow} n_{i\downarrow}, \end{aligned} \quad (\text{B4})$$

where $n_{i\sigma} = c_{i\sigma}^\dagger c_{i\sigma}$, $\Psi_{ij} = \int d\vec{r} \psi_i^* e^{i\vec{\delta}\vec{k}\cdot(\vec{R}_i-\vec{R}_j)} \psi_j$ is a Debye-Waller factor, $\Psi_0 = \Psi_{00}$, and U is the strength of on-site interaction. The first term is the ordinary spin-conserving tunneling term. The second term is a spin-flip tunneling term akin to spin-orbit coupling in the lattice. The third term is an on-site spin-flip term, which can be understood as an effective Zeeman term in the x, y directions. The fourth term is an effective Zeeman energy. For the experimental parameters explored in this work, we find $\Psi_{ij} \approx \delta_{ij}$. The second term can therefore be safely ignored.

3. Effective Hamiltonian for $\delta \approx U$

To derive an effective Hamiltonian for CSFT, we work in the limit $U, \delta \gg t, \Omega$ and treat the first three terms of H_0 as perturbations. We consider the case $\delta \approx U$ and project the Hilbert space onto the subspace of states that have the same total Zeeman energy as the initial states. Other states are separated in energy by at least δ and are projected away. The virtual transitions involving these states lead to higher-order (in $1/\delta$) terms in the effective Hamiltonian of the retained states. Off-resonant processes that can take the state out of this subspace (for example, carrier transitions leading to sites occupied by a single spin-down atom) are ignored. This procedure isolates the CSFT dynamics from other aspects of the system. As described in the main text, we also experimentally isolate the CSFT behavior either by studying doublon dynamics or by performing differential spin measurements that remove the carrier contribution. This allows a comparison of only the CSFT portion of the dynamics with theory.

We therefore project our Hamiltonian onto such states where all sites are either empty or occupied by at least a spin-up fermion. Let $\mathcal{P} = \prod_i [1 - n_{i\downarrow}(1 - n_{i\uparrow})]$ be the projector onto this space. Second-order perturbation theory then gives

$$\begin{aligned} H_{\text{eff}} = & \mathcal{P} \left\{ -t \sum_{(ij)\sigma} (c_{i\sigma}^\dagger c_{j\sigma} + \text{H.c.}) - \frac{t\Psi_0}{2} \left(\frac{1}{U} + \frac{1}{\delta} \right) \sum_{(ij)} \left[\frac{\Omega^*}{2} (e^{i\vec{\delta}\vec{k}\cdot\vec{R}_i} - e^{i\vec{\delta}\vec{k}\cdot\vec{R}_j}) c_{i\downarrow}^\dagger c_{j\uparrow} + i \leftrightarrow j + \text{H.c.} \right] \right. \\ & \left. + \left(\frac{\delta}{2} + \frac{|\Omega|^2 \Psi_0^2}{4\delta} \right) \sum_i (n_{i\uparrow} - n_{i\downarrow}) + U \sum_i n_{i\uparrow} n_{i\downarrow} + \sum_{(ij)} \left(\frac{\Omega}{2} e^{-i\vec{\delta}\vec{k}\cdot\frac{\vec{R}_i+\vec{R}_j}{2}} \Psi_{ij} c_{i\uparrow}^\dagger c_{j\downarrow} + i \leftrightarrow j + \text{H.c.} \right) \right\} \end{aligned}$$

$$\begin{aligned}
& + \frac{2t^2}{U} \sum_{(ij)} (c_{i\uparrow}^\dagger c_{i\downarrow}^\dagger c_{j\downarrow} c_{j\uparrow} + \text{H.c.}) + \frac{2t^2}{U} \sum_{(ij)} [n_{i\uparrow} n_{i\downarrow} (1 - n_{j\uparrow}) (1 - n_{j\downarrow}) + i \leftrightarrow j] + \frac{t^2}{U} \sum_{(ij), (ij'), j \neq j'} n_{i\uparrow} c_{i\downarrow}^\dagger c_{j'\downarrow} c_{j\downarrow}^\dagger c_{i\downarrow} \\
& + \frac{t^2}{U} \sum_{(ij), (ij'), j \neq j'} (1 - n_{i\downarrow}) c_{j\uparrow}^\dagger c_{i\uparrow} c_{i\downarrow}^\dagger c_{j'\uparrow} - \frac{t^2}{U} \sum_{(ij), (ij'), j \neq j'} (c_{j\uparrow}^\dagger c_{j'\downarrow} c_{i\uparrow} c_{i\downarrow} + \text{H.c.}) \Big\} \mathcal{P}. \tag{B5}
\end{aligned}$$

Noting that $\Psi_{ij} \approx 0$ for $i \neq j$ and further ignoring higher-order interactions, this can be written as

$$H_{\text{eff}} = \mathcal{P} \left[-t \sum_{(ij)\sigma} (c_{i\sigma}^\dagger c_{j\sigma} + \text{H.c.}) + \sum_{(ij)} (K_{ij} c_{j\uparrow}^\dagger c_{i\downarrow} + K_{ji} c_{i\uparrow}^\dagger c_{j\downarrow} + \text{H.c.}) + \frac{\delta^*}{2} \sum_i (n_{i\uparrow} - n_{i\downarrow}) + U \sum_i n_{i\uparrow} n_{i\downarrow} \right] \mathcal{P} + O\left(\frac{t^2}{U}\right), \tag{B6}$$

where

$$K_{ij} = -t\Omega\Psi_0 \frac{e^{-i\delta k \cdot \vec{R}_i} - e^{-i\delta k \cdot \vec{R}_j}}{4} \left(\frac{1}{U} + \frac{1}{\delta} \right) \tag{B7}$$

and

$$\delta^* = \delta + \frac{|\Omega\Psi_0|^2}{2\delta}. \tag{B8}$$

H_{eff} governs the dynamics of fully polarized initial states discussed in the main text. The first term moves (but does not create) doublons and holes (e.g., $|\uparrow\downarrow, \downarrow\rangle \rightarrow |\downarrow, \uparrow\downarrow\rangle$). The second term is spin-flip tunneling, which due to the projectors \mathcal{P} is effective only if no sites with spin down are created. We can therefore rewrite the second term by explicitly inserting the projectors: $K_{ij} n_{i\uparrow} (1 - n_{j\downarrow}) c_{j\uparrow}^\dagger c_{i\downarrow} + i \leftrightarrow j + \text{H.c.}$. This term can create doublon-hole pairs out of the fully polarized initial state and dominates the dynamics to leading order.

4. Particle-hole transformation and singlet creation

The effective Hamiltonian (B6) can be recast using a particle-hole transformation into a Hubbard model with singlet creation. We perform the following canonical transformation on Eq. (B6):

$$\begin{aligned}
c_{i\uparrow}^\dagger & \rightarrow \tilde{c}_{i\uparrow}^\dagger, \\
c_{i\downarrow}^\dagger & \rightarrow (-1)^P \tilde{c}_{i\downarrow}, \tag{B9}
\end{aligned}$$

where, for the bipartite lattices we are considering, $(-1)^P$ takes on opposite signs for all pairs of nearest neighbors.

This results in a transformed effective Hamiltonian of the form

$$\begin{aligned}
\tilde{H}_{\text{eff}} = \tilde{\mathcal{P}} \Big\{ & -t \sum_{(ij)} (\tilde{c}_{i\uparrow}^\dagger \tilde{c}_{j\uparrow} + \tilde{c}_{i\downarrow}^\dagger \tilde{c}_{j\downarrow} + \text{H.c.}) \\
& + \sum_{(ij)} [(-1)^P K_{ij} (\tilde{c}_{i\uparrow}^\dagger \tilde{c}_{j\downarrow} - \tilde{c}_{i\downarrow}^\dagger \tilde{c}_{j\uparrow}) + \text{H.c.}] \\
& + \frac{\delta^*}{2} \sum_i (\tilde{n}_{i\uparrow} + \tilde{n}_{i\downarrow}) + U \sum_i \tilde{n}_{i\uparrow} (1 - \tilde{n}_{i\downarrow}) \Big\} \tilde{\mathcal{P}} \\
& + O\left(\frac{t^2}{U}\right), \tag{B10}
\end{aligned}$$

where $\tilde{\mathcal{P}} = \prod_i [1 - (1 - \tilde{n}_{i\downarrow})(1 - \tilde{n}_{i\uparrow})]$ and $\tilde{n}_{i\sigma} = \tilde{c}_{i\sigma}^\dagger \tilde{c}_{i\sigma}$. In this new basis, the initial state of the system is the fully

occupied state, where each site has two fermions. The projector $\tilde{\mathcal{P}}$ now restricts the Hilbert space to have at least one particle on each site.

Initialized with the fully filled state, the only effective term in the Hamiltonian [Eq. (B10)] is the second term, which is of the form $(\tilde{c}_{i\uparrow}^\dagger \tilde{c}_{j\downarrow} - \tilde{c}_{i\downarrow}^\dagger \tilde{c}_{j\uparrow})$. This operator creates a singlet on each pair of nearest-neighbor sites. We can therefore understand the state during the initial stage of the dynamics as a superposition of states consisting of singlet pairs. We also note that the second term effectively implements RVB correlations because the RVB order parameter is $\langle \tilde{c}_{i\uparrow}^\dagger \tilde{c}_{j\downarrow} - \tilde{c}_{i\downarrow}^\dagger \tilde{c}_{j\uparrow} \rangle$.

The second term in Eq. (B10) creates singlets in time evolution when acting on the initial state. To explain this behavior, we consider a four-site system. The evolution in the early stage can be schematically understood as follows:

$$\begin{aligned}
& \left| \overline{\uparrow\downarrow}, \overline{\uparrow\downarrow}, \overline{\uparrow\downarrow}, \overline{\uparrow\downarrow} \right\rangle \xrightarrow{1-i\tilde{H}_{\text{eff}}\delta t} \text{superposition of} \\
& \left| \overline{\uparrow\downarrow}, \overline{\uparrow\downarrow}, \overline{\uparrow\downarrow}, \overline{\uparrow\downarrow} \right\rangle, \left| \overline{\uparrow}, \overline{\downarrow}, \overline{\uparrow\downarrow}, \overline{\uparrow\downarrow} \right\rangle, \tag{B11} \\
& \left| \overline{\uparrow\downarrow}, \overline{\uparrow}, \overline{\downarrow}, \overline{\uparrow\downarrow} \right\rangle, \left| \overline{\uparrow\downarrow}, \overline{\uparrow\downarrow}, \overline{\uparrow}, \overline{\downarrow} \right\rangle,
\end{aligned}$$

where the outlined sites denote singlet pairs, i.e., $\left| \overline{\uparrow}, \overline{\downarrow} \right\rangle \equiv \frac{|\uparrow\downarrow\rangle - |\downarrow\uparrow\rangle}{\sqrt{2}}$, and δt is an infinitesimally small

time interval such that only the first-order effects of \tilde{H}_{eff} are important. The main dynamics in the early stages of time evolution are therefore the creation of entangled singlet pairs. A comparison between the two bases is tabulated in Table I.

5. Estimation of U using the resonance near $\delta = U$

The value of the Hubbard U is estimated experimentally via CSFT by finding the resonant δ at which doublon creation is most effective. As discussed in the main text, this procedure appears to undervalue U compared with the tight-binding prediction from independent measurements of the lattice potential depth. To understand how higher-order terms in H_{eff} may explain this discrepancy, we consider a two-site system with the three states $|\uparrow, \uparrow\rangle, |\uparrow\downarrow, 0\rangle, |0, \uparrow\downarrow\rangle$ and solve for the value of δ at which the doublon creation rate is maximized. Writing

TABLE I. Comparison between the original and the transformed basis. In the representation of states, we have used the notation where

$$\left| \begin{array}{c} \uparrow\downarrow \\ 0 \end{array} \right\rangle \equiv \frac{|\uparrow\downarrow, 0\rangle + |0, \uparrow\downarrow\rangle}{\sqrt{2}} \quad \text{and} \quad \left| \begin{array}{c} \uparrow \\ \downarrow \end{array} \right\rangle \equiv \frac{|\uparrow, \downarrow\rangle - |\downarrow, \uparrow\rangle}{\sqrt{2}}.$$

	Original basis	Transformed basis
Allowed states of each site	$ \uparrow\rangle, \uparrow\downarrow\rangle, 0\rangle$	$ \tilde{\uparrow}\tilde{\downarrow}\rangle, \tilde{\uparrow}\rangle, \tilde{\downarrow}\rangle$
CSFT term	$c_{j\uparrow}^\dagger c_{i\downarrow} - c_{i\uparrow}^\dagger c_{j\downarrow} + \text{H.c.}$	$\tilde{c}_{i\uparrow}^\dagger \tilde{c}_{j\downarrow} - \tilde{c}_{i\downarrow}^\dagger \tilde{c}_{j\uparrow} + \text{H.c.}$
Initial state	$ \uparrow, \uparrow, \uparrow, \uparrow\rangle$	$ \tilde{\uparrow}\tilde{\downarrow}, \tilde{\uparrow}\tilde{\downarrow}, \tilde{\uparrow}\tilde{\downarrow}, \tilde{\uparrow}\tilde{\downarrow}\rangle$
State after evolution to first order $(1 - i\tilde{H}_{\text{eff}}\delta t)$	Superposition of $ \uparrow, \uparrow, \uparrow, \uparrow\rangle, \left \begin{array}{c} \uparrow\downarrow \\ 0 \end{array} \right\rangle, \uparrow, \uparrow\rangle,$ $\left \begin{array}{c} \uparrow \\ \downarrow \end{array} \right\rangle, \left \begin{array}{c} \uparrow\downarrow \\ 0 \end{array} \right\rangle, \uparrow, \uparrow\rangle$	Superposition of $ \tilde{\uparrow}\tilde{\downarrow}, \tilde{\uparrow}\tilde{\downarrow}, \tilde{\uparrow}\tilde{\downarrow}, \tilde{\uparrow}\tilde{\downarrow}\rangle, \left \begin{array}{c} \tilde{\uparrow} \\ \tilde{\downarrow} \end{array} \right\rangle, \tilde{\uparrow}\tilde{\downarrow}, \tilde{\uparrow}\tilde{\downarrow}\rangle,$ $\left \begin{array}{c} \tilde{\uparrow} \\ \tilde{\downarrow} \end{array} \right\rangle, \left \begin{array}{c} \tilde{\uparrow}\tilde{\downarrow} \\ 0 \end{array} \right\rangle, \tilde{\uparrow}\tilde{\downarrow}, \tilde{\uparrow}\tilde{\downarrow}\rangle$

H_{eff} in this basis,

$$H_{\text{eff}}^{(2)} = \begin{pmatrix} \delta + \frac{\Psi_0^2 |\Omega|^2}{2\delta} & K_{12} & -K_{21} \\ K_{12}^* & U + \frac{2t^2}{U} & \frac{2t^2}{U} \\ -K_{21}^* & \frac{2t^2}{U} & U + \frac{2t^2}{U} \end{pmatrix} = U^\dagger \begin{pmatrix} \delta + \frac{\Psi_0^2 |\Omega|^2}{2\delta} & \sqrt{2}K_{12} & 0 \\ \sqrt{2}K_{12}^* & U + \frac{4t^2}{U} & 0 \\ 0 & 0 & U \end{pmatrix} U, \quad (\text{B12})$$

where U transforms the basis to $\{|\uparrow, \uparrow\rangle, \frac{|\uparrow\downarrow, 0\rangle + |0, \uparrow\downarrow\rangle}{\sqrt{2}}, \frac{|\uparrow\downarrow, 0\rangle - |0, \uparrow\downarrow\rangle}{\sqrt{2}}\}$ and the equality $K_{ij} = -K_{ji}$ has been used. The first two states have the same energy (and hence doublon creation is most effective) when

$$\delta \approx U + \frac{4t^2 - |\Omega|^2 \Psi_0^2 / 2}{U} + \frac{2t^2 |\Omega|^2 \Psi_0^2}{U^3}. \quad (\text{B13})$$

Here we see that the resonant condition for maximal doublon creation is not exactly at $\delta = U$, but instead shows higher-order corrections. These corrections contribute to the deviation between the measured and predicted U discussed in the main text. However, the predicted 1% deviation is too small to explain the observed discrepancy.

6. Validating the CSFT effective Hamiltonian

The effective model H_{eff} is a perturbative result, in comparison to the full tight-binding Hamiltonian H_0 . To test the validity of the doublon dynamics predicted by H_{eff} , we compare the time evolution of the doublon population in both models. This allows us to benchmark the effective Hamiltonian against an exact numerical simulation.

The dynamics of H_0 cannot be solved exactly in large systems with dimension higher than one. We therefore consider doublon dynamics in one dimension. We initialize a one-dimensional infinite system with one spin-up fermion in each state, and evolve it with infinite time-evolving block decimation (iTEBD) [28]. The evolution of doublon fraction, defined as $D = \langle n_{i\uparrow} n_{i\downarrow} \rangle / \langle n_{i\uparrow} + n_{i\downarrow} \rangle$, is plotted in Fig. 6(a). The simulations performed with H_0 and H_{eff} are both presented.

Here we see that the effective model captures the qualitative features of the full Hamiltonian. The doublon creation rate at short times is essentially the same for both models. Furthermore, the long-time steady-state reveals approximately the same doublon fraction. In both models the time scale of equilibration is roughly set by $\hbar/|K_{(ij)}| = 14$ ms. We therefore see that the effective CSFT model H_{eff} captures the essential features of the full tight-binding model H_0 in one dimension.

7. CSFT time scale: Theory-experiment comparison

We measure the Rabi rate of the carrier $\Psi_0|\Omega|/\hbar = 2\pi \times 650$ Hz using resonant Rabi oscillations. The carrier frequency $\omega_{\uparrow\downarrow}$ is determined using a fit of the spin transition probability vs Raman detuning $\Delta\omega$ for a 0.7 m pulse, which is too short to drive CSFT.

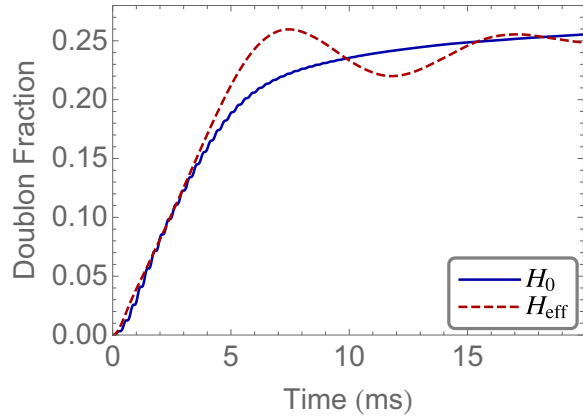


FIG. 6. Evolution of doublon fraction $\langle n_{i\uparrow} n_{i\downarrow} \rangle / \langle n_{i\uparrow} + n_{i\downarrow} \rangle$ from a numerical simulation with constant Ω . The solid lines show the simulation with the full Hamiltonian H_0 , while the dashed line shows that with the effective Hamiltonian H_{eff} derived from second-order perturbation theory. The states are initialized with one spin-up fermion on every site, and the parameters are determined by experiment: $t/\hbar = 0.25$ kHz, $U/\hbar = 3.22$ kHz, $\Omega = 0.1U$, and $\delta\vec{k} \cdot \vec{d} = \pi/2\sqrt{3}$, where \vec{d} is a lattice vector.

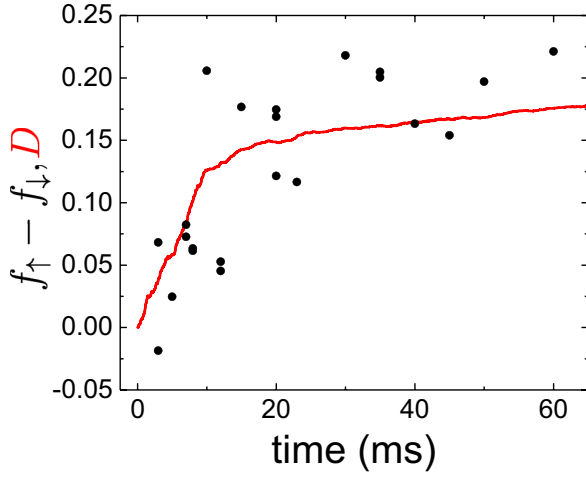


FIG. 7. CSFT signal for varied Raman pulse time. The Raman detuning for these measurements is fixed to the $+U$ CSFT sideband. The measurements are shown using black circles and a theoretical simulation is displayed as a red line. The simulation is performed with Ω in H_0 replaced with $\Omega e^{i\phi(t)}$, where $\langle \phi(t)^2 \rangle = 8$, and the characteristic time scale of the fluctuations in $\phi(t)$ is 2 ms. The dynamics has been averaged (indicated by the notation $\langle \rangle$) over five realizations of $\phi(t)$. For these parameters, the carrier Rabi oscillations are not strongly perturbed.

Measuring the slower rate for CSFT requires a longer time scale. We eliminate the background contribution from the broadened carrier feature using the same procedure as for Fig. 4 in the main text. After locating the carrier frequency $\omega_{\uparrow\downarrow}$, we perform two measurements with the same Raman pulse time at $\Delta\omega = \omega_{\uparrow\downarrow} + U/\hbar$, but with different initial spin polarization. The difference between these two measurements $f_{\uparrow} - f_{\downarrow}$ reflects only the CSFT process. Figure 7 shows the measured CSFT signal for different Raman pulse times at $s = 8 E_R$ lattice depth.

The measured CSFT time scale is approximately a factor of five larger than that of the numerical simulations shown in Fig. 6, which use the experimentally determined carrier Rabi rate. The uncertainty in t and U (which determine K_{ij} and the CSFT time scale) from measurements of the lattice potential depth are too small to support this difference.

A potential source of this discrepancy is phase noise between the Raman laser beams, which translates into fluctuations in the complex phase of Ω in H_{eff} . Such noise can arise from, for example, differential acoustic vibrations of the optomechanics or fibers in the physically distinct and spatially separated Raman beam paths or the separate optical power servos we use for each beam. Phase noise with a nonuniform frequency spectrum is required to explain the inconsistency we observe, since the predicted CSFT time dependence shown in Fig. 6 is constrained by all the experimental parameters, including the independent measurement of $|\Omega|$ using the carrier transition. In order to differentially affect the carrier and CSFT transitions, the phase-noise spectral density must be frequency dependent.

To explore this, we carry out iTEBD numerical simulations with a time-dependent $\Omega e^{i\phi(t)}$. The result, plotted as the solid line in Fig. 7, shows better agreement with the experimental result. The noise we introduce in this simulation is generally consistent with experimental sources of phase instability between the Raman beams. This phase noise may also explain the broadening of the CSFT peaks evident in Fig. 2 in the main text. We reserve a detailed discussion of the noise and comparison with experiment to future work [39].

APPENDIX C: RAMAN PHASE GRADIENT AND FERMIONIC STATISTICS

As discussed in the main text, the spatially dependent Raman phase that arises because the Raman beams intersect at an angle plays a key role in enabling CSFT. We use a two-site, two-atom toy model to explain how the Raman phase disrupts destructive interference between multiple tunneling pathways that is induced by antisymmetrization of the wave function.

Considering a two-site, two-fermion system, there are six possible configurations, which we label according to the site and spin occupancy in each well: $|\uparrow, \uparrow\rangle_W$, $|\downarrow, \downarrow\rangle_W$, $|\uparrow\downarrow, 0\rangle_W$, $|0, \uparrow\downarrow\rangle_W$, $|\uparrow, \downarrow\rangle_W$, and $|\downarrow, \uparrow\rangle_W$. In this well-specific basis, $|\downarrow, \uparrow\rangle_W$ means that a $|\downarrow\rangle$ atom is in the left well (located at position \vec{R}_1) and an $|\uparrow\rangle$ atom is in the right well (located at position \vec{R}_2), for example.

Using a Slater determinant to explicitly write down properly symmetrized (un-normalized) two-atom wave functions, we have

$$|\uparrow, \uparrow\rangle_W = (|LR\rangle - |RL\rangle)|\uparrow\uparrow\rangle, \quad (\text{C1})$$

$$|\downarrow, \downarrow\rangle_W = (|LR\rangle - |RL\rangle)|\downarrow\downarrow\rangle, \quad (\text{C2})$$

$$|\uparrow\downarrow, 0\rangle_W = |LL\rangle(|\uparrow\downarrow\rangle - |\uparrow\downarrow\rangle), \quad (\text{C3})$$

$$|0, \downarrow\uparrow\rangle_W = |RR\rangle(|\uparrow\downarrow\rangle - |\uparrow\downarrow\rangle), \quad (\text{C4})$$

$$|\uparrow, \downarrow\rangle_W = (|LR\rangle - |RL\rangle)(|\uparrow\downarrow\rangle + |\uparrow\downarrow\rangle) + (|LR\rangle + |RL\rangle)(|\uparrow\downarrow\rangle - |\uparrow\downarrow\rangle), \quad (\text{C5})$$

$$|\downarrow, \uparrow\rangle_W = (|LR\rangle - |RL\rangle)(|\uparrow\downarrow\rangle + |\uparrow\downarrow\rangle) - (|LR\rangle + |RL\rangle)(|\uparrow\downarrow\rangle - |\uparrow\downarrow\rangle), \quad (\text{C6})$$

where the spatial part of the wave function is written in the basis of $|L\rangle$ and $|R\rangle$, which are single-particle states on either the left or the right well, and the spin component is denoted as $|\uparrow\rangle$ and $|\downarrow\rangle$. For example, in this basis, $|LR\rangle|\uparrow\downarrow\rangle$ means that atom 1 is in the left well in the $|\uparrow\rangle$ state and atom 2 is in the right well in the $|\downarrow\rangle$ state. The key point for this discussion is that the $|\uparrow, \downarrow\rangle_W$ and $|\downarrow, \uparrow\rangle_W$ states consist of spin singlet and triplet components. Furthermore, the relative sign between the spin and triplet components is opposite for these two states.

We focus on resonant CSFT with $\Delta\omega = U/\hbar$. An initially spin-polarized state $|\uparrow, \uparrow\rangle_W$ (as in the experiment) can transition to a virtual state $|\uparrow, \downarrow\rangle_W$ or $|\downarrow, \uparrow\rangle_W$ via a Raman transition (see Fig. 8). The amplitude for this process is suppressed by a factor of $1/U$ because of the energy mismatch. The phase of the virtual state depends on which atom undergoes

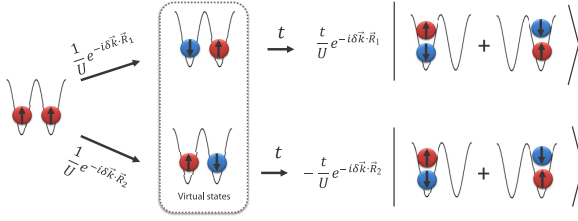


FIG. 8. Schematic diagram showing CSFT for a two-site two-fermion system. CSFT happens as a two-step process via a virtual state. Two possible channels between the initial state $|\uparrow, \uparrow\rangle_W$ and the final state $|\uparrow\downarrow, 0\rangle_W + |0, \uparrow\downarrow\rangle_W$ happen simultaneously but with amplitudes carrying opposite signs. The probability to observe a doublon-hole pair is affected by interference between these channels.

a spin flip, since $\vec{\delta k} \neq 0$. Therefore, the Raman phase enters as either $e^{\delta\vec{k}\cdot\vec{R}_1}$ or $e^{\delta\vec{k}\cdot\vec{R}_2}$, where \vec{R}_1 and \vec{R}_2 differ by a lattice vector \vec{d} . After the virtual state is formed, tunneling completes the CSFT process and a doublon is formed. Via tunneling, the sign difference between Eqs. (C5) and (C6) is converted into an overall sign difference between the wave functions for each doublon-formation pathway. This π relative phase between the wave functions can be computed from the tunneling matrix elements $\langle\uparrow\downarrow, 0|_W t(c_i^\dagger c_{i+1} + \text{H.c.})|\uparrow, \uparrow\rangle_W$ and $\langle\uparrow\downarrow, 0|_W t(c_i^\dagger c_{i+1} + \text{H.c.})|\downarrow, \uparrow\rangle_W$.

The transition between the initial state $|\uparrow, \uparrow\rangle_W$ and the final doublon-hole state happens via these two possible channels simultaneously. The final state is a superposition of these two pathways, with a wave function proportional to $(e^{-i\delta\vec{k}\cdot\vec{R}_1} - e^{-i\delta\vec{k}\cdot\vec{R}_2})(|\uparrow\downarrow, 0\rangle + |0, \uparrow\downarrow\rangle)$. The probability to observe a doublon-hole state is thus proportional to $[1 - \cos(\delta\vec{k}\cdot\vec{d})]$. Without the Raman phase gradient (i.e., $\delta\vec{k} = 0$ or $\delta\vec{k}\cdot\vec{d} = 0$), destructive interference prevents tunneling and doublons will not be formed. Ultimately, this interference arises from the different signs between the triplet and singlet components in Eqs. (C5) and (C6)—it is absent for bosons, for instance.

APPENDIX D: SIMULATION OF CSFT SENSITIVITY TO VACANCIES

We developed a simple numerical simulation (shown in Fig. 4 in the main text) to determine the sensitivity of CSFT to vacancies in the lattice. We compute a density distribution in the noninteracting limit and determine the probability that neighboring sites are occupied as atoms are randomly removed. The density distribution after turning on the lattice is generated according to $n(r_x, r_y, r_z) = \int \frac{d^3\vec{q}}{\hbar^3} \frac{1}{e^{\beta[V(r_x, r_y, r_z) + \epsilon(\vec{q}) - \mu]} + 1}$, where $V(r_x, r_y, r_z)$ is the total harmonic potential imposed by optical trap and lattice beams, μ is the chemical potential, $\beta = 1/k_B \tilde{T}$, $\epsilon(\vec{q}) = 2t(3 - \cos \pi q_x/q_B - \cos \pi q_y/q_B - \cos \pi q_z/q_B)$ is the lattice dispersion, $q_B = \hbar\pi/d$, and \tilde{T} is the effective temperature in the lattice. Both μ and \tilde{T} are solved by matching the entropy and number of atoms N to the corresponding values in the dipole trap. Noninteracting thermodynamics (including the tight-binding lattice dispersion and confining potential) are solved to relate the entropy to N and \tilde{T} . Each site in the

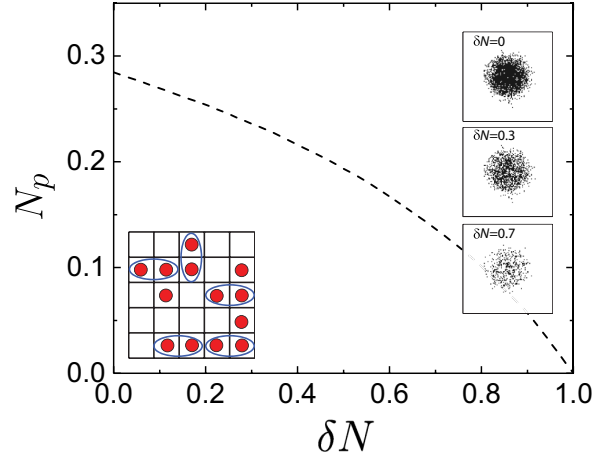


FIG. 9. Fraction of atoms with nearest neighbors at various removal fractions δN for $N = 61\,000$ and $S/N = 2.89 k_B$, which corresponds to $k_B \tilde{T} = 9.7t$ and chemical potential $\mu = 6.4t$ in the lattice. The insets at the right show sample occupation profiles (with one black dot per atom) through a central slice of the gas. The inset at bottom left schematically illustrates the procedure for counting pairs.

simulated lattice is computed as occupied by a single atom or empty based on comparing a random number in the interval $[0, 1]$ to $n(r_x, r_y, r_z)$.

Atoms are randomly removed from the simulated density profile according to a probability δN , which corresponds to the average fraction of atoms discarded. The fraction N_p of atoms in adjacent occupied sites remaining after this removal procedure is counted. As shown in an inset to Fig. 9, atoms are only counted once if they participate in any nearest-neighbor pair. Results from this simulation for the fraction of atoms N_p are shown in Fig. 9 for $N = 61\,000$ and entropy per particle $S/N = 2.89 k_B$ in the lattice. This curve is plotted in Fig. 4 in the main text.

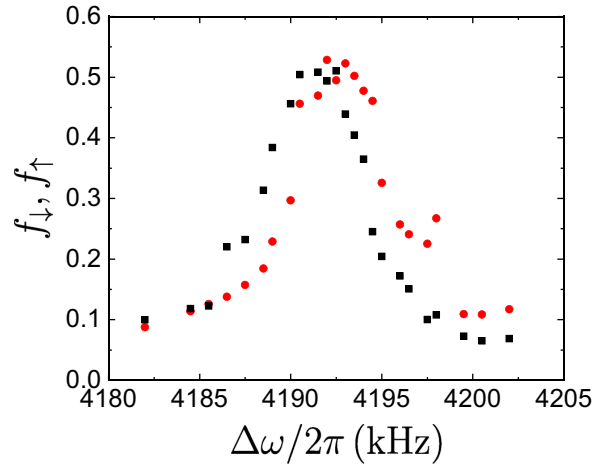


FIG. 10. Measurements of f_\downarrow (black squares) and f_\uparrow (red circles) for varied Raman detuning $\Delta\omega$ taken using the same procedure as for Fig. 2 in the main text. For these data, $\delta N \approx 0.57$.

Our simulation includes the Raman-induced atom loss in δN . For the measurements in Fig. 4 in the main text, the initial conditions before the controlled removal procedure are $N = 80\,900 \pm 3940$ and $T/T_F = 0.29 \pm 0.04$, $N = 54800 \pm 12500$ and $T/T_F = 0.34 \pm 0.04$, and $N = 47200 \pm 2810$ and $T/T_F = 0.38 \pm 0.08$ from high to low δN . After removal and loss induced by the Raman beams, the atom

number is 59200 ± 2660 , 23700 ± 1830 , and 10900 ± 5180 , from high to low δN .

The procedure described in the main text for determining how D depends on δN involves measurements of f_\uparrow and f_\downarrow . We observe that the CSFT spectrum is not altered qualitatively by changes in N for the range of δN sampled in Fig. 4 in the main text. Sample data are shown in Fig. 10 for $\delta N \approx 0.57$.

-
- [1] A. Eckardt, *Rev. Mod. Phys.* **89**, 011004 (2017).
 [2] C. V. Parker, L.-C. Ha, and C. Chin, *Nat. Phys.* **9**, 769 (2013).
 [3] J. Struck, C. Ölschläger, R. Le Targat, P. Soltan-Panahi, A. Eckardt, M. Lewenstein, P. Windpassinger, and K. Sengstock, *Science* **333**, 996 (2011).
 [4] Y.-J. Lin, R. L. Compton, A. R. Perry, W. D. Phillips, J. V. Porto, and I. B. Spielman, *Phys. Rev. Lett.* **102**, 130401 (2009).
 [5] M. Aidelsburger, M. Atala, M. Lohse, J. T. Barreiro, B. Paredes, and I. Bloch, *Phys. Rev. Lett.* **111**, 185301 (2013).
 [6] H. Miyake, G. A. Siviloglou, C. J. Kennedy, W. C. Burton, and W. Ketterle, *Phys. Rev. Lett.* **111**, 185302 (2013).
 [7] J. Struck, C. Ölschläger, M. Weinberg, P. Hauke, J. Simonet, A. Eckardt, M. Lewenstein, K. Sengstock, and P. Windpassinger, *Phys. Rev. Lett.* **108**, 225304 (2012).
 [8] G. Jotzu, M. Messer, R. Desbuquois, M. Lebrat, T. Uehlinger, D. Greif, and T. Esslinger, *Nature (London)* **515**, 237 (2014).
 [9] J. Hirsch, *Physica C* **158**, 326 (1989).
 [10] W. P. Su, J. R. Schrieffer, and A. J. Heeger, *Phys. Rev. Lett.* **42**, 1698 (1979).
 [11] D. K. Campbell, J. T. Gammel, and E. Y. Loh, *Phys. Rev. B* **42**, 475 (1990).
 [12] W. G. Van der Wiel, S. De Franceschi, J. M. Elzerman, T. Fujisawa, S. Tarucha, and L. P. Kouwenhoven, *Rev. Mod. Phys.* **75**, 1 (2002).
 [13] S. Greschner, G. Sun, D. Poletti, and L. Santos, *Phys. Rev. Lett.* **113**, 215303 (2014).
 [14] Á. Rapp, X. Deng, and L. Santos, *Phys. Rev. Lett.* **109**, 203005 (2012).
 [15] S. Greschner and L. Santos, *Phys. Rev. Lett.* **115**, 053002 (2015).
 [16] S. Fölling, S. Trotzky, P. Cheinet, M. Feld, R. Saers, A. Widera, T. Müller, and I. Bloch, *Nature (London)* **448**, 1029 (2007).
 [17] Y.-A. Chen, S. Nascimbène, M. Aidelsburger, M. Atala, S. Trotzky, and I. Bloch, *Phys. Rev. Lett.* **107**, 210405 (2011).
 [18] R. Desbuquois, M. Messer, F. Görg, K. Sandholzer, G. Jotzu, and T. Esslinger, *Phys. Rev. A* **96**, 053602 (2017).
 [19] R. Ma, M. E. Tai, P. M. Preiss, W. S. Bakr, J. Simon, and M. Greiner, *Phys. Rev. Lett.* **107**, 095301 (2011).
 [20] F. Meinert, M. J. Mark, K. Lauber, A. J. Daley, and H.-C. Nägerl, *Phys. Rev. Lett.* **116**, 205301 (2016).
 [21] A. Bermudez and D. Porras, *New J. Phys.* **17**, 103021 (2015).
 [22] M. Di Liberto, C. E. Creffield, G. I. Japaridze, and C. Morais Smith, *Phys. Rev. A* **89**, 013624 (2014).
 [23] M. Troyer and U.-J. Wiese, *Phys. Rev. Lett.* **94**, 170201 (2005).
 [24] P. Anderson, *Science* **235**, 1196 (1987).
 [25] G. Baskaran, Z. Zou, and P. Anderson, *Solid State Commun.* **88**, 853 (1993).
 [26] S. Nascimbène, Y.-A. Chen, M. Atala, M. Aidelsburger, S. Trotzky, B. Paredes, and I. Bloch, *Phys. Rev. Lett.* **108**, 205301 (2012).
 [27] D. McKay and B. DeMarco, *Rep. Prog. Phys.* **74**, 054401 (2011).
 [28] G. Vidal, *Phys. Rev. Lett.* **98**, 070201 (2007).
 [29] S. Gupta, Z. Hadzibabic, M. Zwierlein, C. Stan, K. Dieckmann, C. Schunck, E. Van Kempen, B. Verhaar, and W. Ketterle, *Science* **300**, 1723 (2003).
 [30] A. M. Rey, A. V. Gorshkov, and C. Rubbo, *Phys. Rev. Lett.* **103**, 260402 (2009).
 [31] E. L. Hazlett, Y. Zhang, R. W. Stites, K. Gibble, and K. M. O'Hara, *Phys. Rev. Lett.* **110**, 160801 (2013).
 [32] R. Jördens, N. Strohmaier, K. Günter, H. Moritz, and T. Esslinger, *Nature (London)* **455**, 204 (2008).
 [33] N. Strohmaier, D. Greif, R. Jördens, L. Tarruell, H. Moritz, T. Esslinger, R. Sensarma, D. Pekker, E. Altman, and E. Demler, *Phys. Rev. Lett.* **104**, 080401 (2010).
 [34] M. T. DePue, C. McCormick, S. L. Winoto, S. Oliver, and D. S. Weiss, *Phys. Rev. Lett.* **82**, 2262 (1999).
 [35] R. Ozeri, W. M. Itano, R. B. Blakestad, J. Britton, J. Chiaverini, J. D. Jost, C. Langer, D. Leibfried, R. Reichle, S. Seidelin, J. H. Wesenberg, and D. J. Wineland, *Phys. Rev. A* **75**, 042329 (2007).
 [36] D. McKay, M. White, and B. DeMarco, *Phys. Rev. A* **79**, 063605 (2009).
 [37] D. Jaksch, C. Bruder, J. I. Cirac, C. W. Gardiner, and P. Zoller, *Phys. Rev. Lett.* **81**, 3108 (1998).
 [38] S. Falke, H. Knöckel, J. Friebe, M. Riedmann, E. Tiemann, and C. Lisdat, *Phys. Rev. A* **78**, 012503 (2008).
 [39] H.-Y. Hui, W. Xu, W. Morong, B. DeMarco, and V. Scarola (unpublished).

References

- [1] P. W. Anderson, *Science* **177**, 393 (1972).
- [2] I. Bloch, J. Dalibard, and S. Nascimbène, *Nature Physics* **8**, 267 (2012).
- [3] R. P. Feynman, *International Journal of Theoretical Physics* **21**, 467 (1982).
- [4] P. A. Lee, N. Nagaosa, and X.-G. Wen, *Reviews of Modern Physics* **78**, 17 (2006).
- [5] J. Hubbard, *Proceedings of the Royal Society A: Mathematical, Physical and Engineering Sciences* **276**, 238 (1963).
- [6] G. Kotliar, in *Metal-insulator transitions revisited*, edited by P. P. Edwards and C. N. R. Rao (Taylor and Francis, 1995) Chap. 17, pp. 317–342.
- [7] N. F. Mott, *Proceedings of the Physical Society. Section A* **62**, 416 (1949).
- [8] V. Dobrosavljević, in *Conductor-Insulator Quantum Phase Transitions*, edited by V. Dobrosavljević, N. Trivedi, and J. M. Valles Jr. (Oxford University Press, 2012) Chap. 1, pp. 3–63.
- [9] P. W. Anderson, *Physical Review* **109**, 1492 (1958).
- [10] E. Abrahams, P. W. Anderson, D. C. Licciardello, and T. V. Ramakrishnan, *Physical Review Letters* **42**, 673 (1979).
- [11] A. Lagendijk, B. V. Tiggelen, and D. S. Wiersma, *Physics Today* **62**, 24 (2009).
- [12] B. A. van Tiggelen, *Diffuse Waves in Complex Media*, edited by J.-P. Fouque (Springer Netherlands, Dordrecht, 1999).
- [13] P. A. Lee, *Reviews of Modern Physics* **57**, 287 (1985).
- [14] R. Weaver, *Wave Motion* **12**, 129 (1990).
- [15] M. Segev, Y. Silberberg, and D. N. Christodoulides, *Nature Photonics* **7**, 197 (2013).
- [16] K. Byczuk, W. Hofstetter, and D. Vollhardt, *International Journal of Modern Physics B* **24**, 1727 (2010).
- [17] D. Semmler, J. Wernsdorfer, U. Bissbort, K. Byczuk, and W. Hofstetter, *Physical Review B* **82**, 235115 (2010).
- [18] A. Georges, G. Kotliar, W. Krauth, and M. J. Rozenberg, *Reviews of Modern Physics* **68**, 13 (1996).
- [19] P. J. H. Denteneer, R. T. Scalettar, and N. Trivedi, *Physical Review Letters* **83**, 4610 (1999).
- [20] K. Byczuk, W. Hofstetter, and D. Vollhardt, *Physical Review Letters* **94**, 056404 (2005).
- [21] T. Maier, M. Jarrell, T. Pruschke, and M. H. Hettler, *Reviews of Modern Physics* **77**, 1027 (2005).
- [22] W. Xu, *Dynamics in a Fermi lattice gas*, Ph.D. thesis (2017).

- [23] W. R. McGehee, *Transport and Disorder-Induced Localization of Ultracold Fermi Gas*, Ph.D. thesis (2015).
- [24] S. Kondov, *Ultracold Fermionic Atoms in Disordered Potentials*, Ph.D. thesis (2013).
- [25] B. Demarco, *Quantum Behavior of an Atomic Fermi Gas*, Ph.D. thesis (2001).
- [26] T. D. Lee, K. Huang, and C. N. Yang, *Physical Review* **106**, 1135 (1957).
- [27] R. Grimm, M. Weidemüller, and Y. B. Ovchinnikov, in *Advances in Atomic, Molecular and Optical Physics Vol. 42* (Elsevier Inc., 2000) pp. 95–170.
- [28] T. G. Tiecke, “Properties of Potassium,” (2010), url: <http://www.tobiastiecke.nl/>.
- [29] M. White, *Ultracold atoms in a disordered optical lattice*, Ph.D. thesis (2009).
- [30] D. Jaksch, C. Bruder, J. I. Cirac, C. W. Gardiner, and P. Zoller, *Physical Review Letters* **81**, 3108 (1998).
- [31] S. Q. Zhou and D. M. Ceperley, *Physical Review A* **81**, 013402 (2010).
- [32] M. Greiner, *Ultracold quantum gases in three-dimensional optical lattice*, Ph.D. thesis (2003).
- [33] M. White, M. Pasienski, D. McKay, S. Q. Zhou, D. Ceperley, and B. DeMarco, *Physical Review Letters* **102**, 055301 (2009).
- [34] C. Meldgin, U. Ray, P. Russ, D. Chen, D. M. Ceperley, and B. DeMarco, *Nature Physics* **12**, 646 (2016).
- [35] V. W. Scarola and B. DeMarco, *Physical Review A* **92**, 053628 (2015).
- [36] C. J. Foot, *Atomic Physics* (Oxford University Press, 2005).
- [37] C. Regal, *Experimental realization of BCS-BEC crossover physics with a Fermi gas of atoms*, Ph.D. thesis (2006).
- [38] C. J. Pethick and H. Smith, *Bose–Einstein Condensation in Dilute Gases* (Cambridge University Press, Cambridge, 2008).
- [39] C. Chin, R. Grimm, P. Julienne, and E. Tiesinga, *Reviews of Modern Physics* **82**, 1225 (2010).
- [40] C. Shkedrov, Y. Florshaim, G. Ness, A. Gandman, and Y. Sagi, *Physical Review Letters* **121**, 093402 (2018).
- [41] S. Falke, H. Knöckel, J. Friebe, M. Riedmann, E. Tiemann, and C. Lisdat, *Physical Review A* **78**, 012503 (2008).
- [42] C. A. Regal, M. Greiner, and D. S. Jin, *Physical Review Letters* **92**, 083201 (2004).
- [43] C. A. Regal, C. Ticknor, J. L. Bohn, and D. S. Jin, *Nature* **424**, 47 (2003).
- [44] T. Köhler, K. Góral, and P. S. Julienne, *Reviews of Modern Physics* **78**, 1311 (2006).
- [45] E. Hodby, S. T. Thompson, C. A. Regal, M. Greiner, A. C. Wilson, D. S. Jin, E. A. Cornell, and C. E. Wieman, *Physical Review Letters* **94**, 120402 (2005).
- [46] J. P. Gaebler, *Photoemission Spectroscopy of a Strongly Interacting Fermi Gas*, Ph.D. thesis (2010).
- [47] Z. Fu, L. Huang, Z. Meng, P. Wang, X.-J. Liu, H. Pu, H. Hu, and J. Zhang, *Physical Review A* **87**, 053619 (2013).
- [48] A. B. Bardou, *Dynamics of a Unitary Fermi Gas*, Ph.D. thesis (2014).

- [49] T. Busch, B.-G. Englert, K. Rzazewski, and M. Wilkens, *Foundations of Physics* **28**, 549 (1998).
- [50] T. Stöferle, H. Moritz, K. Günter, M. Köhl, and T. Esslinger, *Physical Review Letters* **96**, 1 (2006).
- [51] J. J. Zirbel, *Ultracold Fermionic Feshbach Molecules*, Ph.D. thesis (2008).
- [52] M. H. Anderson, J. R. Ensher, M. R. Matthews, C. E. Wieman, and E. A. Cornell, *Science* **269**, 198 (1995).
- [53] M. Köhl, H. Moritz, T. Stöferle, K. Günter, and T. Esslinger, *Physical Review Letters* **94**, 080403 (2005).
- [54] D. McKay, M. White, and B. DeMarco, *Physical Review A* **79**, 063605 (2009).
- [55] L. W. Cheuk, M. A. Nichols, K. R. Lawrence, M. Okan, H. Zhang, E. Khatami, N. Trivedi, T. Paiva, M. Rigol, and M. W. Zwierlein, *Science* **353**, 1260 (2016).
- [56] A. Mazurenko, C. S. Chiu, G. Ji, M. F. Parsons, M. Kanász-Nagy, R. Schmidt, F. Grusdt, E. Demler, D. Greif, and M. Greiner, *Nature* **545**, 462 (2017).
- [57] T. A. Hilker, G. Salomon, F. Grusdt, A. Omran, M. Boll, E. Demler, I. Bloch, and C. Gross, *Science* **357**, 484 (2017).
- [58] M. A. Nichols, L. W. Cheuk, M. Okan, T. R. Hartke, E. Mendez, T. Senthil, E. Khatami, H. Zhang, and M. W. Zwierlein, *Science* **363**, 383 (2019).
- [59] P. T. Brown, D. Mitra, E. Guardado-Sanchez, R. Nourafkan, A. Reymbaut, C.-D. Hébert, S. Bergeron, A.-M. S. Tremblay, J. Kokalj, D. A. Huse, P. Schauß, and W. S. Bakr, *Science* **363**, 379 (2019).
- [60] P. J. Lee, B. B. Blinov, K. Brickman, L. Deslauriers, M. J. Madsen, R. Miller, D. L. Moehring, D. Stick, and C. Monroe, *Optics Letters* **28**, 1582 (2003).
- [61] G. K. Woodgate, *Elementary Atomic Structure* (Oxford science publications, 1980).
- [62] D. Steck, “Rubidium 87 D Line Data,” (2003), url: <https://steck.us/alkalidata/>.
- [63] W. Ketterle, K. B. Davis, M. A. Joffe, A. Martin, and D. E. Pritchard, *Physical Review Letters* **70**, 2253 (1993).
- [64] G. D. Bruce, E. Haller, B. Peaudecerf, D. A. Cotta, M. Andia, S. Wu, M. Y. H. Johnson, B. W. Lovett, and S. Kuhr, *Journal of Physics B: Atomic, Molecular and Optical Physics* **50**, 095002 (2017).
- [65] C. Ravensbergen, V. Corre, E. Soave, M. Kreyer, E. Kirilov, and R. Grimm, *Physical Review A* **98**, 063624 (2018).
- [66] G. Salomon, L. Fouché, S. Lepoutre, A. Aspect, and T. Bourdel, *Physical Review A* **90**, 033405 (2014).
- [67] B. S. Marangoni, C. R. Menegatti, and L. G. Marcassa, *Journal of Physics B: Atomic, Molecular and Optical Physics* **45**, 175301 (2012).
- [68] D. Mitra, *Exploring attractively interacting fermions in 2D using a Quantum Gas Microscope*, Ph.D. thesis (2018).
- [69] A. M. Steane, M. Chowdhury, and C. J. Foot, *Journal of the Optical Society of America B* **9**, 2142 (1992).
- [70] S. J. M. Kuppens, K. L. Corwin, K. W. Miller, T. E. Chupp, and C. E. Wieman, *Physical Review A* **62**, 013406 (2000).
- [71] A. di Stefano, D. Wilkowski, J. Müller, and E. Arimondo, *Applied Physics B* **69**, 263 (1999).
- [72] M. Vangeleyn, P. F. Griffin, E. Riis, and A. S. Arnold, *Optics Express* **17**, 13601 (2009).

- [73] H. J. Metcalf and P. van der Straten, *Laser Cooling and Trapping*, Graduate Texts in Contemporary Physics (Springer New York, New York, NY, 1999).
- [74] C. Simonelli, E. Neri, A. Ciamei, I. Goti, M. Inguscio, A. Trenkwalder, and M. Zaccanti, (2019), arXiv:1904.01965 .
- [75] J. Vijayan, P. Sompet, G. Salomon, J. Koepsell, S. Hirthe, A. Bohrdt, F. Grusdt, I. Bloch, and C. Gross, (2019), arXiv:1905.13638 .
- [76] D. Husmann, M. Lebrat, S. Häusler, J.-P. Brantut, L. Corman, and T. Esslinger, Proceedings of the National Academy of Sciences **115**, 8563 (2018).
- [77] S. A. Hartnoll, Nature Physics **11**, 54 (2014).
- [78] S. Krinner, D. Stadler, J. Meineke, J.-P. Brantut, and T. Esslinger, Physical Review Letters **110**, 100601 (2013).
- [79] K. Zhao, H. Lin, X. Xiao, W. Huang, W. Yao, M. Yan, Y. Xing, Q. Zhang, Z.-X. Li, S. Hoshino, J. Wang, S. Zhou, L. Gu, M. S. Bahrany, H. Yao, N. Nagaosa, Q.-K. Xue, K. T. Law, X. Chen, and S.-H. Ji, Nature Physics (2019), 10.1038/s41567-019-0570-0.
- [80] W. Xu, W. R. McGehee, W. N. Morong, and B. DeMarco, Nature Communications **10**, 1588 (2019).
- [81] D. Pines and P. Nozieres, *The theory of quantum liquids, 1: Normal Fermi Liquids* (W. A. Benjamin, Inc., New York, 1966).
- [82] G. D. Mahan, *Many-Particle Physics* (Springer US, Boston, MA, 2000).
- [83] A. J. Schofield, Contemporary Physics **40**, 95 (1999).
- [84] H. K. Pal, V. I. Yudson, and D. L. Maslov, Lithuanian Journal of Physics **52**, 142 (2012).
- [85] J. Rammer, in *Quantum Transport Theory* (CRC Press, 2004) Chap. 3, pp. 129–157.
- [86] A. Ioffe and A. Regel, in *Progress in Semiconductors, Vol. 4*, edited by R. Burgess and F. Kroger (Heywood & Co., London, 1960) pp. 239–243.
- [87] N. E. Hussey, K. Takenaka, and H. Takagi, Philosophical Magazine **84**, 2847 (2004).
- [88] N. F. Mott, Philosophical Magazine **26**, 1015 (1972).
- [89] O. Gunnarsson, M. Calandra, and J. E. Han, Reviews of Modern Physics **75**, 1085 (2003).
- [90] D. J. Thouless, Philos. Mag. **32**, 877 (1975).
- [91] G. De Filippis, V. Cataudella, A. de Candia, A. S. Mishchenko, and N. Nagaosa, Phys. Rev. B **90**, 014310 (2014).
- [92] J. A. N. Bruin, H. Sakai, R. S. Perry, and A. P. Mackenzie, Science **339**, 804 (2013).
- [93] V. J. Emery and S. A. Kivelson, Physical Review Letters **74**, 3253 (1995).
- [94] A. Legros, S. Benhabib, W. Tabis, F. Laliberté, M. Dion, M. Lizaire, B. Vignolle, D. Vignolles, H. Raffy, Z. Z. Li, P. Auban-Senzier, N. Doiron-Leyraud, P. Fournier, D. Colson, L. Taillefer, and C. Proust, Nature Physics (2018), 10.1038/s41567-018-0334-2.
- [95] P. Giraldo-Gallo, J. A. Galvis, Z. Stegen, K. A. Modic, F. F. Balakirev, J. B. Betts, X. Lian, C. Moir, S. C. Riggs, J. Wu, A. T. Bollinger, X. He, I. Božović, B. J. Ramshaw, R. D. McDonald, G. S. Boebinger, and A. Shekhter, Science **361**, 479 (2018).
- [96] R. Jaramillo, S. D. Ha, D. M. Silevitch, and S. Ramanathan, Nature Physics **10**, 304 (2014).

- [97] W. Xu, K. Haule, and G. Kotliar, *Physical Review Letters* **111**, 036401 (2013).
- [98] P. W. Anderson, *Physics Today* **66**, 9 (2013).
- [99] H. Liu, *Physics Today* **65**, 68 (2012).
- [100] B. Keimer, S. A. Kivelson, M. R. Norman, S. Uchida, and J. Zaanen, *Nature* **518**, 179 (2015).
- [101] S. Naqib, J. Cooper, J. Tallon, and C. Panagopoulos, *Physica C: Superconductivity* **387**, 365 (2003).
- [102] K. Limtragoon and P. Phillips, *Physical Review B* **92**, 155128 (2015).
- [103] D. M. Broun, *Nature Physics* **4**, 170 (2008).
- [104] M. M. Qazilbash, K. S. Burch, D. Whisler, D. Shrekenhamer, B. G. Chae, H. T. Kim, and D. N. Basov, *Physical Review B* **74**, 205118 (2006).
- [105] S. D. Gensemer and D. S. Jin, *Physical review letters* **87**, 173201 (2001).
- [106] M. P. Marder, *Condensed Matter Physics* (John Wiley & Sons, Inc., Hoboken, NJ, USA, 2010).
- [107] B. J. DeSalvo, K. Patel, G. Cai, and C. Chin, *Nature* **568**, 61 (2019).
- [108] M. Zaghoo, T. R. Boehly, J. R. Rygg, P. M. Celliers, S. X. Hu, and G. W. Collins, *Physical Review Letters* **122**, 085001 (2019).
- [109] E. Perepelitsky, A. Galatas, J. Mravlje, R. Žitko, E. Khatami, B. S. Shastry, and A. Georges, *Physical Review B* **94**, 235115 (2016).
- [110] H. Kajueter, G. Kotliar, and G. Moeller, *Physical Review B* **53**, 16214 (1996).
- [111] X. Deng, J. Mravlje, R. Žitko, M. Ferrero, G. Kotliar, and A. Georges, *Physical Review Letters* **110**, 086401 (2013).
- [112] N. Pakhira and R. H. McKenzie, *Physical Review B* **91**, 075124 (2015).
- [113] J. Kokalj, *Physical Review B* **95**, 041110 (2017).
- [114] E. W. Huang, R. Sheppard, B. Moritz, and T. P. Devereaux, (2018), arXiv:1806.08346 .
- [115] O. Parcollet, M. Ferrero, T. Ayril, H. Hafermann, I. Krivenko, L. Messio, and P. Seth, *Computer Physics Communications* **196**, 398 (2015).
- [116] M. Aichhorn, L. Pourovskii, P. Seth, V. Vildosola, M. Zingl, O. E. Peil, X. Deng, J. Mravlje, G. J. Kraberger, C. Martins, M. Ferrero, and O. Parcollet, *Computer Physics Communications* **204**, 200 (2016).
- [117] C. H. Mousatov, I. Esterlis, and S. A. Hartnoll, *Physical Review Letters* **122**, 186601 (2019).
- [118] M. Blake, R. A. Davison, and S. Sachdev, *Physical Review D* **96**, 106008 (2017).
- [119] Y. Gu, A. Lucas, and X.-L. Qi, *SciPost Physics* **2**, 018 (2017).
- [120] R. A. Davison, K. Schalm, and J. Zaanen, *Physical Review B* **89**, 245116 (2014).
- [121] J. Zaanen, *SciPost Physics* **6**, 061 (2019).
- [122] P. K. Kovtun, D. T. Son, and A. O. Starinets, *Physical Review Letters* **94**, 111601 (2005).
- [123] C. Cao, E. Elliott, J. Joseph, H. Wu, J. Petricka, T. Schäfer, and J. E. Thomas, *Science (New York, N.Y.)* **331**, 58 (2011).

- [124] A. Adams, L. D. Carr, T. Schäfer, P. Steinberg, and J. E. Thomas, *New Journal of Physics* **14**, 115009 (2012).
- [125] E. Abrahams and C. M. Varma, *Proceedings of the National Academy of Sciences of the United States of America* **97**, 5714 (2000).
- [126] P. A. Casey and P. W. Anderson, *Physical Review Letters* **106**, 097002 (2011).
- [127] S. Gupta, Z. Hadzibabic, M. W. Zwierlein, C. a. Stan, K. Dieckmann, C. H. Schunck, E. G. M. Van Kempen, B. J. Verhaar, and W. Ketterle, *Science (New York, N.Y.)* **300**, 1723 (2003).
- [128] J. T. Stewart, J. P. Gaebler, and D. S. Jin, *Nature* **454**, 744 (2008).
- [129] P. T. Brown, E. Guardado-Sanchez, B. M. Spar, E. W. Huang, T. P. Devereaux, and W. S. Bakr, (2019), arXiv:1903.05678 .
- [130] R. Anderson, F. Wang, P. Xu, V. Venu, S. Trotzky, F. Chevy, and J. H. Thywissen, *Physical Review Letters* **122**, 153602 (2019).
- [131] P. W. Anderson, *Science* **235**, 1196 (1987).
- [132] D. Belitz and T. R. Kirkpatrick, *Reviews of Modern Physics* **66**, 261 (1994).
- [133] F. Evers and A. D. Mirlin, *Reviews of Modern Physics* **80**, 1355 (2008).
- [134] J. Billy, V. Josse, Z. Zuo, A. Bernard, B. Hambrecht, P. Lugan, D. Clément, L. Sanchez-Palencia, P. Bouyer, and A. Aspect, *Nature* **453**, 891 (2008).
- [135] S. S. Kondov, W. R. McGehee, J. J. Zirbel, and B. DeMarco, *Science* **334**, 66 (2011).
- [136] F. Jendrzejewski, A. Bernard, K. Müller, P. Cheinet, V. Josse, M. Piraud, L. Pezzé, L. Sanchez-Palencia, A. Aspect, and P. Bouyer, *Nature Physics* **8**, 398 (2012).
- [137] S. R. Finch, *Mathematical Constants* (Cambridge University Press, 2003).
- [138] R. C. Kuhn, O. Sigwarth, C. Miniatura, D. Delande, and C. A. Mueller, *New Journal of Physics* **9**, 33 (2007).
- [139] E. Fratini and S. Pilati, *Physical Review A* **92**, 063621 (2015).
- [140] T. Vojta, F. Epperlein, and M. Schreiber, *Physical Review Letters* **81**, 4212 (1998).
- [141] D. Heidarian and N. Trivedi, *Physical Review Letters* **93**, 126401 (2004).
- [142] E. Z. Kuchinskii, I. A. Nekrasov, and M. V. Sadovskii, *Journal of Experimental and Theoretical Physics* **106**, 581 (2007).
- [143] H. Bragança, M. C. O. Aguiar, J. Vučićević, D. Tanasković, and V. Dobrosavljević, *Physical Review B* **92**, 125143 (2015).
- [144] S. V. Kravchenko and M. Sarachik, *Reports on Progress in Physics* **67**, 1 (2004).
- [145] E. Lahoud, O. N. Meetei, K. B. Chaska, A. Kanigel, and N. Trivedi, *Physical Review Letters* **112**, 206402 (2014).
- [146] Z. Wang, Y. Okada, J. O’Neal, W. Zhou, D. Walkup, C. Dhital, T. Hogan, P. Clancy, Y.-J. Kim, Y. F. Hu, L. H. Santos, S. D. Wilson, N. Trivedi, and V. Madhavan, *Proceedings of the National Academy of Sciences* **115**, 11198 (2018).
- [147] D. Basko, I. Aleiner, and B. Altshuler, *Annals of Physics* **321**, 1126 (2006).
- [148] R. Nandkishore and D. A. Huse, *Annual Review of Condensed Matter Physics* **6**, 15 (2015).

- [149] M. Serbyn, Z. Papić, and D. A. Abanin, *Physical Review Letters* **111**, 127201 (2013).
- [150] D. A. Huse, R. Nandkishore, and V. Oganesyan, *Physical Review B* **90**, 174202 (2014).
- [151] T. B. Wahl, A. Pal, and S. H. Simon, *Nature Physics* **15**, 164 (2019).
- [152] M. Schreiber, S. S. Hodgman, P. Bordia, H. P. Lüschen, M. H. Fischer, R. Vosk, E. Altman, U. Schneider, and I. Bloch, *Science* **349**, 842 (2015).
- [153] H. P. Lüschen, P. Bordia, S. S. Hodgman, M. Schreiber, S. Sarkar, A. J. Daley, M. H. Fischer, E. Altman, I. Bloch, and U. Schneider, *Physical Review X* **7**, 011034 (2017).
- [154] H. P. Lüschen, P. Bordia, S. Scherg, F. Alet, E. Altman, U. Schneider, and I. Bloch, *Physical Review Letters* **119**, 260401 (2017).
- [155] P. Bordia, H. Lüschen, S. Scherg, S. Gopalakrishnan, M. Knap, U. Schneider, and I. Bloch, *Physical Review X* **7**, 041047 (2017).
- [156] S. S. Kondov, W. R. McGehee, W. Xu, and B. DeMarco, *Physical Review Letters* **114**, 083002 (2015).
- [157] L. Fallani, J. E. Lye, V. Guarrera, C. Fort, and M. Inguscio, *Physical Review Letters* **98**, 130404 (2007).
- [158] B. Deissler, M. Zaccanti, G. Roati, C. D’Errico, M. Fattori, M. Modugno, G. Modugno, and M. Inguscio, *Nature Physics* **6**, 354 (2010).
- [159] C. D’Errico, E. Lucioni, L. Tanzi, L. Gori, G. Roux, I. P. McCulloch, T. Giamarchi, M. Inguscio, and G. Modugno, *Physical Review Letters* **113**, 095301 (2014).
- [160] B. Gadway, D. Pertot, J. Reeves, M. Vogt, and D. Schneble, *Physical Review Letters* **107**, 145306 (2011).
- [161] M. Pasienski, D. McKay, M. White, and B. DeMarco, *Nature Physics* **6**, 677 (2010).
- [162] J.-y. Choi, S. Hild, J. Zeiher, P. Schauss, A. Rubio-Abadal, T. Yefsah, V. Khemani, D. A. Huse, I. Bloch, and C. Gross, *Science* **352**, 1547 (2016).
- [163] A. Rubio-Abadal, J.-y. Choi, J. Zeiher, S. Hollerith, J. Rui, I. Bloch, and C. Gross, (2018), arXiv:1805.00056 .
- [164] M. P. A. Fisher, P. B. Weichman, G. Grinstein, and D. S. Fisher, *Physical Review B* **40**, 546 (1989).
- [165] R. Sensarma, D. Pekker, E. Altman, E. Demler, N. Strohmaier, D. Greif, R. Jördens, L. Tarruell, H. Moritz, and T. Esslinger, *Physical Review B* **82**, 224302 (2010).
- [166] J. Eisert, M. Friesdorf, and C. Gogolin, *Nature Physics* **11**, 124 (2015).
- [167] S. Smale, P. He, B. A. Olsen, K. G. Jackson, H. Sharum, S. Trotzky, J. Marino, A. M. Rey, and J. H. Thywissen, *Science Advances* **5**, eaax1568 (2019).
- [168] M. Prüfer, P. Kunkel, H. Strobel, S. Lannig, D. Linnemann, C.-M. Schmied, J. Berges, T. Gasenzer, and M. K. Oberthaler, *Nature* **563**, 217 (2018).
- [169] S. Erne, R. Bücker, T. Gasenzer, J. Berges, and J. Schmiedmayer, *Nature* **563**, 225 (2018).
- [170] C. Eigen, J. A. P. Glidden, R. Lopes, E. A. Cornell, R. P. Smith, and Z. Hadzibabic, *Nature* **563**, 221 (2018).
- [171] N. Strohmaier, D. Greif, R. Jördens, L. Tarruell, H. Moritz, T. Esslinger, R. Sensarma, D. Pekker, E. Altman, and E. Demler, *Physical Review Letters* **104**, 080401 (2010).

- [172] R. Sensarma, D. Pekker, A. M. Rey, M. D. Lukin, and E. Demler, *Physical Review Letters* **107**, 145303 (2011).
- [173] A. L. Chudnovskiy, D. M. Gangardt, and A. Kamenev, *Physical Review Letters* **108**, 085302 (2012).
- [174] D. Hansen, E. Perepelitsky, and B. S. Shastry, *Physical Review B* **83**, 205134 (2011).
- [175] M. Ligges, I. Avigo, D. Golež, H. U. R. Strand, Y. Beyazit, K. Hanff, F. Diekmann, L. Stojchevska, M. Kalläne, P. Zhou, K. Rossnagel, M. Eckstein, P. Werner, and U. Bovensiepen, *Physical Review Letters* **120**, 166401 (2018).
- [176] M. Schecter and A. Kamenev, *Physical Review A* **85**, 043623 (2012).
- [177] M. Schiró and M. Fabrizio, *Physical Review B* **83**, 165105 (2011).
- [178] M. Eckstein, M. Kollar, and P. Werner, *Physical Review Letters* **103**, 056403 (2009).
- [179] K. Winkler, G. Thalhammer, F. Lang, R. Grimm, J. Hecker Denschlag, A. J. Daley, A. Kantian, H. P. Büchler, and P. Zoller, *Nature* **441**, 853 (2006).
- [180] R. Jördens, N. Strohmaier, K. Günter, H. Moritz, and T. Esslinger, *Nature* **455**, 204 (2008).
- [181] R. Jördens, *Metallic and Mott-insulating phases in fermionic quantum gases*, Ph.D. thesis (2010).
- [182] J. C. Phillips, *Reports on Progress in Physics* **59**, 1133 (1996).
- [183] T. Stöferle, H. Moritz, C. Schori, M. Köhl, and T. Esslinger, *Physical Review Letters* **92**, 130403 (2004).
- [184] C. Kollath, A. Iucci, T. Giamarchi, W. Hofstetter, and U. Schollwöck, *Physical Review Letters* **97**, 050402 (2006).
- [185] V. Guarrera, L. Fallani, J. E. Lye, C. Fort, and M. Inguscio, *New Journal of Physics* **9**, 107 (2007).
- [186] C. Kollath, A. M. Läuchli, and E. Altman, *Physical Review Letters* **98**, 180601 (2007).
- [187] P. Russ, *private communication*.
- [188] O. L. Acevedo, A. Safavi-Naini, J. Schachenmayer, M. L. Wall, R. Nandkishore, and A. M. Rey, *Physical Review A* **96**, 033604 (2017).
- [189] W. Morong, S. Muleady, I. Kimchi, R. Nandkishore, A. M. Rey, and B. DeMarco, *in preparation*.
- [190] S. Chiesa, P. B. Chakraborty, W. E. Pickett, and R. T. Scalettar, *Physical Review Letters* **101**, 086401 (2008).
- [191] S. Johri, R. Nandkishore, and R. N. Bhatt, *Physical Review Letters* **114**, 117401 (2015).
- [192] V. Dobrosavljević, D. Tanasković, and A. A. Pastor, *Physical Review Letters* **90**, 016402 (2003).
- [193] K. Agarwal, S. Gopalakrishnan, M. Knap, M. Müller, and E. Demler, *Physical Review Letters* **114**, 160401 (2015).
- [194] A. C. Potter, R. Vasseur, and S. A. Parameswaran, *Physical Review X* **5**, 031033 (2015).
- [195] D. J. Luitz, N. Laflorencie, and F. Alet, *Physical Review B* **93**, 060201 (2016).
- [196] S. Gopalakrishnan and D. A. Huse, *Physical Review B* **99**, 134305 (2019).
- [197] M. Yan, H.-Y. Hui, M. Rigol, and V. W. Scarola, *Physical Review Letters* **119**, 073002 (2017).
- [198] J. Smith, A. Lee, P. Richerme, B. Neyenhuis, P. W. Hess, P. Hauke, M. Heyl, D. A. Huse, and C. Monroe, *Nature Physics* **12**, 907 (2016).

[199] W. Morong and B. DeMarco, Physical Review A **92**, 023625 (2015).

[200] W. Xu, W. Morong, H.-Y. Hui, V. W. Scarola, and B. DeMarco, Physical Review A **98**, 023623 (2018).